



University of Kentucky
UKnowledge

University of Kentucky Doctoral Dissertations

Graduate School

2009

VISUALIZATION AND CHARACTERIZATION OF ULTRASONIC CAVITATING ATOMIZER AND OTHER AUTOMOTIVE PAINT SPRAYERS USING INFRARED THERMOGRAPHY

Nelson Kudzo Akafuah
University of Kentucky, nkakaf2@uky.edu

[Right click to open a feedback form in a new tab to let us know how this document benefits you.](#)

Recommended Citation

Akafuah, Nelson Kudzo, "VISUALIZATION AND CHARACTERIZATION OF ULTRASONIC CAVITATING ATOMIZER AND OTHER AUTOMOTIVE PAINT SPRAYERS USING INFRARED THERMOGRAPHY" (2009). *University of Kentucky Doctoral Dissertations*. 792.
https://uknowledge.uky.edu/gradschool_diss/792

This Dissertation is brought to you for free and open access by the Graduate School at UKnowledge. It has been accepted for inclusion in University of Kentucky Doctoral Dissertations by an authorized administrator of UKnowledge. For more information, please contact UKnowledge@lsv.uky.edu.

ABSTRACT OF DISSERTATION

Nelson Kudzo Akafuah

The Graduate School
University of Kentucky
2009

VISUALIZATION AND CHARACTERIZATION OF ULTRASONIC CAVITATING
ATOMIZER AND OTHER AUTOMOTIVE PAINT SPRAYERS USING INFRARED
THERMOGRAPHY

ABSTRACT OF DISSERTATION

A dissertation submitted in partial fulfillment of the
requirements for the degree of Doctor of Philosophy in the
College of Engineering
at the University of Kentucky

By
Nelson Kudzo Akafuah

Lexington, Kentucky

Co-Director: Dr. Kozo Saito, Professor of Mechanical Engineering
and Dr. Abraham J. Salazar, Associate Research Professor of
Mechanical Engineering

Lexington, Kentucky

2009

Copyright © Nelson K. Akafuah 2009

ABSTRACT OF DISSERTATION

VISUALIZATION AND CHARACTERIZATION OF ULTRASONIC CAVITATING ATOMIZER AND OTHER AUTOMOTIVE PAINT SPRAYERS USING INFRARED THERMOGRAPHY

The disintegration of a liquid jet emerging from a nozzle has been under investigation for several decades. A direct consequence of the liquid jet disintegration process is droplet formation. The breakup of a liquid jet into discrete droplets can be brought about by the use of a diverse forcing mechanism. Cavitation has been thought to assist the atomization process. Previous experimental studies, however, have dealt with cavitation as a secondary phenomenon assisting the primary atomization mechanism. In this dissertation, the role of the energy created by the collapse of cavitation bubbles, together with the liquid pressure perturbation is explicitly configured as a principal mechanism for the disintegration of the liquid jet. A prototype of an atomizer that uses this concept as a primary atomization mechanism was developed and experimentally tested using water as working fluid.

The atomizer fabrication process and the experimental characterization results are presented. The parameters tested include liquid injection pressure, ultrasonic horn tip frequency, and the liquid flow rate. The experimental results obtained demonstrate improvement in the atomization of water.

To fully characterize the new atomizer, a novel infrared thermography-based technique for the characterization and visualization of liquid sprays was developed. The technique was tested on the new atomizer and two automotive paint applicators. The technique uses an infrared thermography-based measurement in which a uniformly heated background acts as a thermal radiation source, and an infrared camera as the receiver. The infrared energy emitted by the source in traveling through the spray is attenuated by the presence of the droplets. The infrared intensity is captured by the receiver showing the attenuation in the image as a result of the presence of the spray.

The captured thermal image is used to study detailed macroscopic features of the spray flow field and the evolution of the droplets as they are transferred from the applicator to the target surface. In addition, the thermal image is post-processed using

theoretical and empirical equations to extract information from which the liquid volume fraction and number density within the spray are estimated.

KEYWORDS: Atomization, Cavitation, Infrared Thermography,
Volume Fraction, Number Density.

Nelson K. Akafuah

09/21/2009

VISUALIZATION AND CHARACTERIZATION OF ULTRASONIC CAVITATING
ATOMIZER AND OTHER AUTOMOTIVE PAINT SPRAYERS USING INFRARED
THERMOGRAPHY

By

Nelson Kudzo Akafuah

Dr. Kozo Saito

Co-Director of Dissertation

Dr. Abraham J. Salazar

Co-Director of Dissertation

Dr. L. Scott Stephens

Director of Graduate Studies

09/21/2009

RULES FOR THE USE OF DISSERTATIONS

Unpublished dissertations submitted for the Doctor's degree and deposited in the University of Kentucky Library are as a rule open for inspection, but are to be used only with due regard to the rights of the authors. Bibliographical references may be noted, but quotations or summaries of parts may be published only with the permission of the author, and with the usual scholarly acknowledgments.

Extensive copying or publication of the dissertation in whole or in part also requires the consent of the Dean of the Graduate School of the University of Kentucky.

A library that borrows this dissertation for use by its patrons is expected to secure the signature of each user.

NameDateThis image shows a full page of white paper with horizontal black lines, resembling notebook paper. The lines are evenly spaced and run across the width of the page. There are no margins, text, or other markings on the paper.

DISSERTATION

Nelson Kudzo Akafuah

The Graduate School
University of Kentucky
2009

VISUALIZATION AND CHARACTERIZATION OF ULTRASONIC CAVITATING
ATOMIZER AND OTHER AUTOMOTIVE PAINT SPRAYERS USING INFRARED
THERMOGRAPHY

DISSERTATION

A dissertation submitted in partial fulfillment of the
requirements for the degree of Doctor of Philosophy in the
College of Engineering
at the University of Kentucky

By
Nelson Kudzo Akafuah

Lexington, Kentucky

Co-Director: Dr. Kozo Saito, Professor of Mechanical Engineering
and Dr. Abraham J. Salazar, Associate Research Professor of
Mechanical Engineering

Lexington, Kentucky

Copyright © Nelson K. Akafuah 2009

To my wife, Rhoda

Your enduring love and endless encouragement have been my continuous source of inspiration. You have been my truest friend, my trusted companion through some difficult times. You have caused me to realize how remarkable is the truth found in ***Proverbs 18:22, “He who finds a wife finds what is good and receives favor from the LORD.”***

You are and always will be the love of my life.

ACKNOWLEDGEMENTS

I wish to express my sincere gratitude to my academic advisor Dr. Kozo Saito for his support and invaluable guidance throughout this research work. I am also greatly indebted to my co-advisor Dr. Abraham Salazar for his invaluable insights and constructive criticisms. I have greatly benefited from his numerous comments and helpful discussions. I am also greatly thankful to the external examiner Dr. Rick Honaker and the entire dissertation committee: Dr. Eric Grulke, Dr. Cidambi Srinivasan, and Dr. Dusan Sekulic for their invaluable insights.

I would also like to thank my colleagues in the IR4TD group: Dr. Tianxiang Li, Dr. Keng Chuah, Dr. Belal Gharaibeh, Mrs. Allison Hehemann, Mr. Mark Pittman, Mr. Ahmad Salaimeh, Mr. Churn Poh, Ms. Brittany Adam, and Mr. Marc Harik for their company and the many different ways they made this PhD experience manageable.

Finally, I would like to thank my friends and family, especially my wife Rhoda who served as my cheerleader and so patiently understanding throughout the time of writing of this dissertation. To my father whose passing early last year left a scar in my heart, I hope I can still make you proud. To my mother Grace, I say thank you for teaching me to love people and be respecting of others views.

TABLE OF CONTENTS

ACKNOWLEDGEMENTS.....	iii
TABLE OF CONTENTS.....	iv
LIST OF TABLES	viii
LIST OF FIGURES	ix
NOMENCLATURE	xv
CHAPTER ONE	1
1.0 Introduction.....	1
1.1 Research Objective	2
1.2 Literature Review.....	4
1.2.1 Spray Atomization	4
1.2.1.1 The Phenomenon of Liquid Jet Breakup.....	5
1.2.1.2 Effect of Cavitation on Liquid Jet Breakup.....	8
1.2.1.3 Effect of Oscillating Pressure Field on Liquid Jet Breakup.....	11
1.2.2 Spray Characterization.....	16
1.2.2.1 Droplet Size Distribution in Sprays.....	16
1.2.2.2 Droplet Sampling Technique.....	24
1.2.2.3 Droplet Size Measurement Techniques.....	27
1.2.2.3.1 Optically-Based Droplet Size Measurement Techniques	28
1.2.3 Spray Visualization.....	32
1.2.4 Infrared Thermography.....	36
1.2.4.1 Historical Background of Infrared	37
1.2.4.2 Principles of Infrared Thermography	39
1.2.4.3 Applications of Infrared Thermography on Thermo-Fluid Dynamics	43
CHAPTER TWO	48
2.0 Theoretical Formulation.....	48
2.1 Theoretical Study of Cavitation	48
2.1.1 Some Consideration of the Liquid State	49

2.1.2	The Phenomenon Called Cavitation	51
2.1.3	Inception of Cavitation and Turbulence Effects	52
2.1.4	Equation of Cavitation Bubble Dynamics	54
2.1.5	Influence of Oscillating Pressure Fields	54
2.1.6	Ultrasonic Cavitation Atomization	60
2.1.6.1	The Ultrasonic Horn	62
2.1.6.1.1	Ratio of Horn Tip Diameter to Horn Stroke Length.....	63
2.1.6.1.2	Position of the Horn Relative to the Nozzle Exit.....	63
2.1.6.1.3	Frequency of Oscillating Horn.....	64
2.1.6.1.4	Shape of the Horn Surface	65
2.1.6.1.5	Amplitude of the Horn Motion	66
2.1.6.1.6	Shape of the Horn	66
2.1.6.2	The Interior Nozzle Geometry	66
2.1.6.3	Liquid Parameters.....	69
2.2	Mathematical Treatment of Infrared Spray Visualization and Characterization ..	70
2.2.1	The Radiation Model	71
2.2.1.1	Infrared Radiation Formulation.....	73
2.2.1.2	Two-Dimensional Infrared Image Analysis	75
2.2.1.2.1	Estimation of the Spray Depth at each Pixel Location	81
2.2.1.2.2	Extinction Efficiency	82
2.2.1.2.3	Estimation of D_{30} and D_{20} using Empirical Formulation.....	84
CHAPTER THREE		87
3.0	Experimental Apparatus.....	87
3.1	Apparatus for the Infrared Visualization and Characterization Technique.....	87
3.1.1	Infrared Camera	87
3.1.2	Background Radiation Source	89
3.1.3	Droplet Size Analyzer.....	90
3.2	Fabrication of the Ultrasonic Cavitating Atomizer	92
3.2.1	Ultrasonic Horn.....	92
3.2.2	The Piezoelectric Actuator.....	94
3.2.3	UCA Nozzle and Nozzle Housing	96

3.3 Other Automotive Paint Spray Atomizers.....	100
3.3.1 High-Speed Rotary Bell Atomizer.....	100
3.3.2 High Volume Low Pressure Air-Assisted Atomizer	103
CHAPTER FOUR.....	106
4.0 Experimental Procedures and Discussion Of Results.....	106
4.1 Characterization of the Ultrasonic Cavitating Atomizer	106
4.1.1 The UCA Prototype Characterization Results	108
4.1.1.1 Macroscopic Features of the UCA Prototype Spray	109
4.1.1.2 Droplet Size and Size Distribution Within the UCA Spray	111
4.2 Infrared Visualization and Characterization.....	120
4.2.1 Experimental Setup.....	120
4.2.2 Infrared Visualization Results.....	122
4.2.2.1 High-Speed Rotary Bell Atomizer Visualization Results	123
4.2.2.2 High Volume Low Pressure Air-Assisted Atomizer Visualization Results.....	133
4.2.2.3 Ultrasonic Cavitating Atomizer Results.....	139
4.2.3 Volume Fraction and Number Density Results	142
4.2.3.1 The Volume Fraction and the Number Density Results for High- Speed Rotary Bell Atomizer.....	142
4.2.3.2 Volume Fraction and Number Density Results for High Volume Low Pressure Air-Assisted Atomizer	147
4.2.3.3 Comparison Between the High-Speed Rotary Bell Atomizer and the HVLV Air-Assisted Atomizer	149
4.2.3.4 Volume Fraction and Number Density Results for the Ultrasonic Cavitating Atomizer	150
CHAPTER FIVE	154
5.0 Conclusions and Recommendations	154
5.1 Ultrasonic Cavitation Atomizer Fabrication and Characterization	154
5.2 Infrared Characterization and Visualization Technique	156
5.3 Contribution of this Dissertation.....	157

APPENDICES	159
Appendix A: Detail Diagram and Dimensions of the Ultrasonic Cavitating Atomizer	159
Appendix B: Some Research Areas for Infrared Visualization Technique	166
REFERENCES	171
VITA.....	192

LIST OF TABLES

Table 1.1	Mean droplet diameters and their applications	22
Table 1.2	Definitions of representative droplet diameters	24
Table 1.3	Measurement techniques for droplet size	28
Table 3.1	The UCA nozzle dimensions	97

LIST OF FIGURES

Figure 1.1	A measurement volume for the spatial distribution.....	26
Figure 1.2	A measurement cross-section for the flux distribution.....	26
Figure 1.3	The electromagnetic spectrum showing the subdivision of the infrared spectral band.....	36
Figure 2.1	A typical phase diagram.....	50
Figure 2.2	A radius-time curve of the influence of imposed perturbation frequency on a gas-filled bubble.....	57
Figure 2.3	A radius-time curve of the influence of initial bubble radius on the vapor bubble dynamics.....	57
Figure 2.4	The bubble resonant frequency in water at 300 K.....	60
Figure 2.5	Cavitation cluster generation at the ultrasonic horn tip.....	62
Figure 2.6	The nozzle interior geometry.....	67
Figure 2.7	A concept of the residence chamber.....	68
Figure 2.8	A schematic of the infrared visualization model.....	72
Figure 2.9	The interaction between electromagnetic waves and spherical particles.....	73
Figure 2.10	A schematic of the attenuation map of the spray.....	76
Figure 2.11	The computation of the spray depth b : (a) the cross-section of the UCA and the high-speed rotary bell atomizer spray, (b) the cross-section of the HVLP air-assisted atomizer spray.....	82
Figure 2.12	The Mie efficiencies for water.....	84
Figure 3.1	The ThermoVision SC4000 infrared camera.....	88
Figure 3.2	The IR-150/301 blackbody system.....	90
Figure 3.3	A schematic of the Spraytec measurement system.....	91
Figure 3.4	The ultrasonic horn.....	93
Figure 3.5	The ultrasonic horn dimensions.....	94

Figure 3.6	The piezo-electric actuator and the ultrasonic horn assembly.....	96
Figure 3.7	The dimensions of the nozzle interior geometry.....	97
Figure 3.8(a)	The UCA atomizer assembly.....	98
Figure 3.8(b)	The UCA atomizer assembly.....	99
Figure 3.9	A picture of the UCA atomizer assembly.....	99
Figure 3.10	The high-speed rotary bell atomizer.....	102
Figure 3.11	A schematic of the cross-section of the high-speed rotary bell cup.	102
Figure 3.12	A schematic of the cross-section of the nozzle of HVLP air- assisted atomizer.....	103
Figure 3.13	HVLP air-assisted atomization.....	104
Figure 3.14	A picture of the HVLP air-assisted atomizer.....	105
Figure 4.1	A schematic of the UCA experimental setup with the Malvern Spraytec system.....	107
Figure 4.2	Image of the UCA spray for a liquid flow rate of 100 cc/min with an increasing liquid injection pressure.....	110
Figure 4.3	Image of the UCA spray for a liquid flow rate of 200 cc/min with an increasing liquid injection pressure.....	110
Figure 4.4 (a)	The volume frequency vs. the droplet diameter, for a liquid flow rate of 100 cc/min, at an ultrasonic frequency of 60 kHz, and a liquid injection pressure of 4.1 MPa.....	112
Figure 4.4 (b)	The volume frequency vs. the droplet diameter, for a liquid flow rate of 100 cc/min, at an ultrasonic frequency of 60 kHz, and a liquid injection pressure of 4.8 MPa.....	113
Figure 4.4 (c)	The volume frequency vs. the droplet diameter, for a liquid flow rate of 100 cc/min, at an ultrasonic frequency of 60 kHz, and a liquid injection pressure of 5.5 MPa.....	113
Figure 4.4 (d)	The volume frequency vs. the droplet diameter, for a liquid flow rate of 100 cc/min, at an ultrasonic frequency of 60 kHz, and a liquid injection pressure of 6.2 MPa.....	114

Figure 4.5	The sauter mean diameter vs the liquid injection pressure at a liquid flow rate of 100 cc/min and ultrasonic frequencies of zero and 60 kHz.....	114
Figure 4.6 (a)	The volume frequency vs. the droplet diameter, for a liquid flow rate of 200 cc/min, at an ultrasonic frequency of 60 kHz, and a liquid injection pressure of 4.1 MPa.....	115
Figure 4.6 (b)	The volume frequency vs. the droplet diameter, for a liquid flow rate of 200 cc/min, at an ultrasonic frequency of 60 kHz, and a liquid injection pressure of 4.8 MPa.....	115
Figure 4.6 (c)	The volume frequency vs. the droplet diameter, for a liquid flow rate of 200 cc/min, at an ultrasonic frequency of 60 kHz, and a liquid injection pressure of 5.5 MPa.....	116
Figure 4.6 (d)	The volume frequency vs. the droplet diameter, for a liquid flow rate of 200 cc/min, at an ultrasonic frequency of 60 kHz, and a liquid injection pressure of 6.2 MPa.....	116
Figure 4.7	The Sauter Mean Diameter vs the liquid injection pressure at a liquid flow rate of 200 cc/min and ultrasonic frequencies of zero and 60 kHz.....	117
Figure 4.8	Sauter mean diameter vs ultrasonic frequency at a liquid flow rate of 100 cc/min and a liquid injection pressure of 5.5 MPa.....	118
Figure 4.9	The time history of Sauter mean diameter with and without ultrasonic frequency of 60 kHz.....	119
Figure 4.10	A schematic of the experimental setup for the infrared visualization and characterization technique.....	122
Figure 4.11(a)	The infrared visualization of the high-speed rotary bell atomizer showing increasing bell cup rotation speed for a liquid flow rate of 100 cc/min.....	124
Figure 4.11 (b)	The infrared visualization of the high-speed rotary bell atomizer showing increasing bell cup rotation speed for a liquid flow rate of 200 cc/min.....	125
Figure 4.11 (c)	The infrared visualization of the high-speed rotary bell atomizer showing increasing bell cup rotation speed for a liquid flow rate of 300 cc/min.....	125
Figure 4.11 (d)	The infrared visualization of the high-speed rotary bell atomizer showing increasing bell cup rotation speed for a liquid flow rate of 400 cc/min.....	126

Figure 4.12	A schematic of the droplet trajectory in the high-speed rotary bell atomizer.....	126
Figure 4.13	The Sauter mean diameter of the high-speed rotary bell atomizer for a liquid flow rate of 100 cc/min at various bell cup rotation speeds.....	127
Figure 4.14	The droplet size distribution of the high-speed rotary bell atomizer for a liquid flow rate of 100 cc/min at various bell cup rotation speeds.....	128
Figure 4.15	The infrared visualization of the high-speed rotary bell atomizer spray at a bell cup rotation speed of 40,000 rpm, showing increasing liquid flow rate.....	129
Figure 4.16	The Sauter mean diameter of the high-speed rotary bell atomizer spray at a bell cup rotation speed of 40,000 rpm, showing increasing liquid flow rate.....	130
Figure 4.17	The cross-sectional area of the high speed rotary bell atomizer spray.....	131
Figure 4.18	A detailed structure of the toroid shape inside the high speed rotary bell atomizer spray.....	131
Figure 4.19	The infrared image showing vortex shedding from the toroid shaped vortex tube.....	132
Figure 4.20	A high speed visual image of the high-speed rotary bell atomizer showing increasing bell cup rotation speed for a liquid flow rate of 200 cc/min.....	133
Figure 4.21	A schematic of the cross section of the flat spray and the measurement orientation: (a) orientation for long axis, (b) orientation for short axis.....	134
Figure 4.22	The infrared themographic images of the long axis of the HVLP air-assisted atomizer, with increasing liquid flow rate at a fixed air pressure of 0.4 MPa.....	136
Figure 4.23	The infrared themographic images of the short axis of the HVLP air-assisted atomizer, with increasing liquid flow rate at a fixed air pressure of 0.4 MPa.....	136
Figure 4.24	The Sauter mean diameter of the HVLP air-assisted atomizer with increasing liquid flow rate.....	137

Figure 4.25	The droplet size distribution of the HVLP air-assisted atomizer at various flow rates.....	137
Figure 4.26	The infrared themographic images of the long axis of the HVLP air-assisted atomizer, with increasing liquid flow rate at a fixed air pressure of 0.4 MPa showing increasing spray angle.....	138
Figure 4.27	A schematic explanation of the expansion and necking in the infrared images along the short axis of the HVLP air-assisted atomizer: (a) the infrared image showing the bottleneck, (b) schematics explaining the phenomenon.....	139
Figure 4.28	The infrared visualization of the UCA spray with increasing liquid injection pressure at a liquid flow rate of 100 cc/m.....	140
Figure 4.29	The infrared visualization of the UCA spray with increasing liquid injection pressure at a liquid flow rate of 200 cc/min.....	141
Figure 4.30	A comparison of the liquid volume fraction and the Sauter mean diameter for the high-speed rotary bell atomizer showing increasing bell cup rotation speed for a liquid flow rate of 100 cc/min.....	144
Figure 4.31	A comparison of the droplet number density and the Sauter mean diameter for the high-speed rotary bell atomizer showing increasing bell cup rotation speed for a liquid flow rate of 100 cc/min.....	144
Figure 4.32	A comparison of the liquid volume fraction and the Sauter mean diameter for the high-speed rotary bell atomizer showing increasing bell cup rotation speed for a liquid flow rate of 400 cc/min.....	145
Figure 4.33	A comparison of the droplet number density and the Sauter mean diameter for the high-speed rotary bell atomizer showing increasing bell cup rotation speed for a liquid flow rate of 400 cc/min.....	145
Figure 4.34	A comparison of the liquid volume fraction and the Sauter mean diameter for the high-speed rotary bell atomizer showing increasing liquid flow rate for a fixed bell cup ration speed of 40,000 rpm.....	146
Figure 4.35	A comparison of droplet number density and the Sauter mean diameter for the high-speed rotary bell atomizer showing increasing liquid flow rate for a fixed bell cup ration speed of 40,000 rpm.....	147

Figure 4.36	A comparison of the liquid volume fraction and the Sauter mean diameter for HVLP air-assisted atomizer showing increasing liquid flow rate at a fixed air pressure of 0.4 MPa.....	148
Figure 4.37	A comparison of the droplet number density and the Sauter mean diameter for HVLP air-assisted atomizer showing increasing liquid flow rate at a fixed air pressure of 0.4 MPa.....	149
Figure 4.38	A comparison of the liquid volume fraction and the Sauter mean diameter for the UCA atomizer showing increasing liquid injection pressure at a fixed liquid flow rate of 100 cc/min.....	151
Figure 4.39	A comparison of the droplet number density and the Sauter mean diameter for the UCA atomizer showing increasing liquid injection pressure at a fixed liquid flow rate of 100 cc/min.....	152
Figure 4.40	A comparison of the liquid volume fraction and the Sauter mean diameter for the UCA atomizer showing increasing liquid injection pressure at a fixed liquid flow rate of 200 cc/min.....	152
Figure 4.41	A comparison of the droplet number density and the Sauter mean diameter for the UCA atomizer showing increasing liquid injection pressure at a fixed liquid flow rate of 200 cc/min.....	153

NOMENCLATURE

$E_{\lambda b}$	Blackbody monochromatic radiation intensity,
\bar{D}_{sg}	Geometric surface means droplet diameter
\dot{n}	Droplet number generation rate
\bar{D}_{ng}	Geometric mean droplet diameter
S_g^2	Geometric variance
\bar{D}_{vg}	Geometric volume means droplet diameter
q''	Heat flux, W/m^2
\dot{m}	Mass flow rate
\bar{D}	Mean value of diameter
S_n^2	Variance
a	Absorption coefficient
a_n, b_n	Mie coefficients
b	Local thickness of the scattering medium (spray)
C	Electromagnetic cross-section
c	inter-particle clearance
C_1	First radiation constant
C_2	Second radiation constant
D	Diameter, μm
D_{10}	Arithmetic mean diameter, μm
D_{20}	Surface mean diameter, μm
D_{30}	volume mean diameter, μm

D_{32}	Sauter Mean Diameter, μm
f	Frequency
$f(D)$	Number distribution function
f_v	Liquid droplet volume fraction
G	Geometric cross-section
h	Convective heat transfer Coefficient, $W/m^2 \cdot K$
I	Radiative intensity
K	Cavitation Number
m	complex refractive index, $n - ik$
N	Number of droplet, number of pixel
$n,$	Refractive index, number of particles per unit volume, number of moles
P	image pixel, Pressure
Q	Radiation interaction efficiency
R	Universal Gas Constant
s	Distance traveled into the medium
S	Surface Tension
S_g	Geometric standard deviation
S_n	Standard deviation
T	Absolute temperature, K
U	Velocity
V	Volume

Greek Letters

Φ	Particle phase function, Attenuation volume
--------	---

ε_{λ}	Spectral emissivity coefficient
μ	Dynamic Viscosity (ν/ρ)
κ	Extinction coefficient
λ	Wavelength of the radiation being considered
ν	Kinetic Viscosity
ρ	Density
σ	Stefan-Boltzmann constant, scattering coefficient
τ	Optical thickness
χ	Particle size parameter
Ω	Scattering albedo
ω	Solid angle, angular frequency

Subscripts

∞	Far from surface under consideration
<i>abs</i>	Absorption
<i>b</i>	Blackbody
<i>B</i>	Bubble
<i>d</i>	Droplet
<i>ext</i>	Extinction
<i>l,L</i>	Liquid
<i>max</i>	Based on the maximum value
<i>min</i>	Based on the minimum value
<i>sca</i>	scattering
<i>sur</i>	Surface under consideration

CHAPTER ONE

1.0 INTRODUCTION

The automotive coating process requires fine atomization to ensure an outstanding coated surface finished quality, higher paint transfer efficiency, and reduction in volatile organic compound (VOC) emission (Im et al., 2001). The atomization process determines the quality of a finished surface. The appearance (color, gloss, and texture) of a coated surface greatly affects a customer's perception of product quality (McKnight and Martin, 1997). Moreover, customer expectations for the attributes given by the appearance of coatings increase continually as manufacturers compete to provide those surfaces that offer enhanced surface characteristics. Coating composition, together with application procedures, film formation processes, and coated surface characteristics determine the appearance of a coating film (Bruan and Fields, 1994).

Automotive coatings are generally applied in the form of paint sprays, using spray atomizers. Paint sprays are droplet systems which consist of a large number of paint droplets dispersed in a carrier gas, often air or a mixture of air and the vapor of the volatile components of the paint. The liquid paint droplet distribution in the gas phase during transfer from the applicator to the target surface influences film-build consistency. This needs to be maintained to minimize paint applicator-related coating defects. The distribution of the liquid and gas phases in the time-spaced domain is described by the liquid volume fraction f_v (Frohn and Roth, 2000). The liquid volume fraction f_v is defined as the ratio of equivalent volume of the liquid to a given volume of the gas and

liquid mixture (Sirignano, 1999). The droplet number density is defined as the number of liquid droplets per unit volume.

Understanding the atomization process and how the paint droplets are transferred from the applicator to the target surface helps in the improvement of the paint application process with the prevention and reduction in paint application-related defect. Ensuring increased transfer efficiency and improvement in coated surface quality require continuous improvement in the application process and reformulation of the paint, especially for metallic paints to satisfy consumer demands. The solutions for these problems require multiple approaches—such as new paint formulation, operation optimization, new paint applicator designs, and improved understanding of the paint droplet transfer process. The ability to visualize the internal structures of the paint spray transfer process is vital to understanding the role that the atomization mechanisms have on the evolution of the paint droplets as they travel from the paint applicator to the target surface. This dissertation, therefore, seeks to address some of these issues by focusing on a new paint applicator design and the visualization and characterization of the paint spray transfer process.

1.1 RESEARCH OBJECTIVE

The main objective of this dissertation is to tackle two of the issues related to the efficacy of automotive paint spray mentioned above, namely a new paint atomizer design and a paint spray transfer process visualization and characterization. The new paint atomizer known as Ultrasonic Cavitating Atomizer (UCA) uses the energy generated by

the collapse of cavitation bubbles together with pressure modulation of the exiting liquid jet to produce droplets. This dissertation identifies the role that the energy created by the collapse of ultrasonically generated cavitation bubbles plays in the disintegration of liquid jets and the development and fabrication of an atomizer that uses ultrasonically driven cavitation to enhance liquid jet disintegration.

Secondly, a novel thermography-based visualization and characterization technique was developed. The technique allows the visualization of the internal structures and the macroscopic features of the paint spray transfer process. In addition, the paint droplet volume fraction and the paint droplet number density inside the spray are computed by the new technique. This provides quantitative information about the droplet distribution inside the continuous gas phase. The novel visualization and characterization technique was applied to the new atomizer and two other automotive paint applicators. These two automotive paint applicators, which are currently in use in most automotive painting processes, consist of a high-speed rotary bell atomizer and a High Volume Low Pressure (HVLP) air-assisted atomizer.

The high-speed rotary bell atomizer and the UCA both produce axisymmetric sprays. The HVLP air-assisted atomizer, however, produces a fan-shaped spray. Centrifugal forces are the main atomization mechanism of the high-speed rotary bell atomizer. The UCA uses pressure forces in addition to pressure modulation and the energy created by the collapse of cavitation bubbles to achieve atomization. The HVLP air-assisted atomizer utilizes air pressure forces to achieve atomization.

1.2 LITERATURE REVIEW

Spray atomization, spray characterization, spray visualization, and infrared thermography have been studied for decades and much has been written about these subjects. The literature review is thus grouped as follows: spray atomization is presented in section 1.2.1, which includes the phenomenon of liquid jet breakup, effects of nozzle cavitation, and oscillating pressure field on the liquid jet breakup. In Section 1.2.2, the characterization of liquid spray is presented, which includes droplet size distribution, sampling, and measurement techniques. Section 1.2.3 reviews spray visualization methods, and section 1.2.4 reviews infrared thermography and its principles and applications in thermo-fluid dynamics.

1.2.1 SPRAY ATOMIZATION

A spray is generally considered as a system of droplets immersed in a gaseous continuous phase (Lefebvre, 1989). There are many occurrences of spray phenomena in power and propulsion applications, industrial applications, and nature (Sirignano, 1993). Sprays are produced as a result of atomization, which is defined as the disintegration of liquid into droplets (Lefebvre, 1989; Liu, 2000). Atomization of a liquid into discrete droplets can be brought about by the use of diverse mechanism like aerodynamic, mechanical, ultrasonic, or electrostatic forces. For example, the breakup of a liquid into droplets can be achieved by the impingement with a gas in two-fluid atomization, by centrifugal forces in rotary atomization, by ultrasonic vibration utilizing a piezoelectric

transducer in ultrasonic atomization, or by electrostatic/electromagnetic fields in electrostatic/electromagnetic atomization.

Atomization processes may also be classified according to the energy used to produce the instability on the liquid element. For example, pressure energy in the case of pressure atomization, centrifugal energy for rotary atomization, gaseous/fluid energy for two fluid atomization, and vibratory energy for ultrasonic or acoustic atomization (Lefebvre, 1989; Liu, 2000).

When a liquid is sprayed, it forms ligaments due to the interaction of the surface tension and the air resistance (Lefebvre, 1989). The surface tension breaks the liquid jet into individual droplets that are capable of holding themselves together at their velocities. Very large droplets once formed will split further if the surrounding ambient resistance overcomes the surface tension. In the vast majority of industrial processes air assisted atomizers are used, where compressed air supplies the required energy for atomizing the liquid.

1.2.1.1 THE PHENOMENON OF LIQUID JET BREAKUP

The phenomenon of the breakup of a liquid jet emerging from a nozzle has been under investigation for several decades. The breakup of a liquid jet is the process whereby a mass of liquid is accelerated through a small orifice (nozzle) into a continuous gas phase. The jet is dynamically broken up into a large number of tiny droplets. The complexity of the jet breakup process is due to the large number of parameters which

influence it, including the physical properties of both the liquid and the gas phases, the velocities and temperature of the fluid, and the nozzle geometry (Reitz, 1978).

Because of the importance of sprays in many technological applications, a vast amount of literature has accumulated on the subject including several extensive reviews which are available via (Ranz, 1956; DeJuhasz, 1960; Lapple et al., 1967; Tate, 1969; Lin and Reitz, 1998; Lasheras, and Hopfinger, 2000; Smallwood and Omer, 2000) and numerous books focused upon the subject of sprays (Giffen and Muraszew, 1953; Levich, 1962; Orr, 1966; Borodin et al., 1967; Lefebvre, 1989; Bayvel and Orzechowski, 1993; Kuo, 1995; Sirignano, 1999; Liu, 2000; Nasr et al., 2000).

When a liquid is forced to flow through a smooth circular orifice into a chamber of quiescent gas, four main regimes of jet disintegration are observed—Rayleigh jet breakup regime, first wind induced breakup regime, second wind induced breakup regime, and atomization regime (Reitz, 1978). The liquid jet atomization regimes were attributed to several factors presented in the studies by Reitz (1978), and Reitz and Bracco (1986).

The atomization mechanism of liquid jet has been attributed, among other things, to aerodynamic interaction effects, liquid turbulence, jet velocity profile rearrangement effects, cavitation phenomena, and the liquid injection pressure oscillation (Reitz and Bracco, 1982). Castleman (1931, 1932) hypothesized that the liquid jet breakup is as a result of aerodynamic interaction between the liquid and gas phase, arguing that the interaction of aerodynamic forces with the liquid phase leads to the formation of ligaments. Drawing upon the experimental results from Sauter (1929), Castleman (1932)

proposed that the formation and lifetimes of the ligaments decrease, and smaller droplets are produced with greater gas phase velocity contribution.

After analyzing the forces involved in the breakup and energy expended in the ligament model, Ranz (1956) concluded that the ligament diameters, and thus the droplet sizes, were related to the wavelengths of unstable aerodynamically-induced surface waves growing on the core of the liquid jet. However, various authors questioned the model, arguing that aerodynamically induced wave growth takes time to develop, and thus, the model cannot explain the experimental results which demonstrated jet disintegration in the immediate exit of a jet into a chamber against the postulates of Ranz (1956). Earlier DeJuhasz (1931), proposed that the liquid jet disintegration process possibly occurs within the nozzle itself. With some experimental evidences, DeJuhasz (1931) suggested that liquid turbulence may have a significant role in the liquid jet breakup process. Schweitzer (1937) noted the existence of a radial component of velocity in turbulent pipe flows and argued that this radial flow could cause the disruption of the liquid jet surface as soon as the jet emerged from the nozzle unbounded.

The problem of liquid jet disintegration was first investigated in the simple configuration of a single drop immersed in a flow moving relatively to itself (Hinze, 1949; Kolmogorov, 1949; Lane, 1951). It was realized that the relevant parameter for the drop breakup criterion is the Weber Number (Weber 1931), constructed as the ratio of the drag, aerodynamic pressure $\rho_2(u_2-u_1)^2$, and the capillary restoring pressure S/d as $We = \rho_2(u_2-u_1)^2 d / S$, where ρ_2 denotes the density of the destabilizing flow; $(u_2 - u_1)$ is the contrast of velocity between the flow and the droplet; d signifies its diameter, and S represent the liquid surface tension. The critical Weber Number above which the droplet

disintegrates is about 10 (Hanson, et al., 1963) and is somewhat smaller when the destabilizing flow is turbulent (Hinze 1955).

The detailed breakup mechanism reveals a very rich spectrum of phenomena (Pilch and Erdman, 1987). At moderate Weber Numbers, the droplet deforms in a pancake shape which flattens in a bag membrane eventually breaking into very small droplets (originating from the membrane itself) and into larger droplets (emerging from the membrane rim). At higher Weber Numbers, the droplet is no longer deformed as a whole, but is rather ‘stripped’ at its surface, forming liquid fibers, or ligaments which produce the stable droplets (Ranger and Nicholls, 1969; Krzeczowski, 1980; Joseph et al., 1999). The same qualitative succession of atomization regimes is observed when a liquid jet flows in a faster coaxial stream (Farago’ and Chigier, 1992; Zaleski et al., 1996), except that there is no critical Weber Number for the jet disintegration since its circular geometry suffers a capillary-driven instability (Plateau, 1873); (Rayleigh, 1879).

Two other phenomena, cavitation and the liquid injection pressure oscillation, have been noted to influence the liquid jet disintegration. These are covered in some detail in the next two sections.

1.2.1.2 EFFECT OF CAVITATION ON LIQUID JET BREAKUP

Cavitation in nozzles of liquid atomizer is known to affect the atomization of a liquid jet. The subject has been well investigated by many researchers including (Bergwerk, 1959; Hiroyasu et al., 1991; Chaves et al., 1991; Soteriou et al., 1995; Schmidt, 1997; Sou et al., 2006, 2007; Tamaki, 2009). Bergwerk (1959), in studying the

liquid flow field within the nozzle and its influence on the liquid jet breakup process coupled with turbulent interactions, observed the presence of liquid cavitation regions within the nozzles. From these observations, he concluded that the liquid cavitation phenomena may play a role in the liquid jet atomization mechanism. Bergwerk (1959) also found that nozzles with short length-diameter ratios and sharp edged inlet sections allowed complete detachment of the liquid flow from the nozzle walls under certain conditions. The jets obtained showed no tendency to disintegrate. In the case of attached flows, the experiments revealed local cavitation regions within the nozzles. The emerging jet into atmospheric air then had a ruffled appearance. This behavior was also collaborated by Northrup (1951) and Nurick (1976). Bergwerk (1959) surmised that the reattachment of the flow beyond the cavitation zone created large amplitude of turbulent disturbances which were responsible for the waviness of the liquid jet surface seen in the vicinity of the nozzle exit. Bergwerk (1959) hypothesized that cavitation bubbles, which are formed in the cavitation region and swept along with the flow, may influence the liquid jet break up process.

As a consequence of vast experiments conducted by many researchers, it has been determined that strong turbulence in the nozzle hole induced by the cavitation phenomena, contributed immensely to the disintegration of the liquid jet. Arcoumanis et al. (1998) performed experiments to characterize the spray based on the internal nozzle flow structure and obtained results which strongly indicate the influence of cavitation on the spray structure. They proposed the liquid core atomization model and a cavitation-induced atomization model, wherein the cavitation bubble collapse energy as an induced force opposes the surface tension, thus enhancing the liquid jet breakup.

The cavitation-induced atomization model represents the effect of hole cavitation on the disintegration of the emerging liquid jet by assuming that its breakup is caused by the collapsing of the cavitation bubbles formed within the hole. Since the pressure in the cavitating bubbles is much lower than ambient pressure, bubbles collapse either before reaching the surface of the liquid jet or immediately after. The condition in which the bubbles collapse after reaching downstream of the nozzle exit is termed as supercavitation. Water jet cutting technology such as cavitating interrupted jets employ this technique for using traveling cavitation bubbles in water jets for erosive action on metals. Various authors hinted at the influence of cavitation appearing as turbulent quantities enhancing the jet breakup, which lead to a series of experiments on the influence of cavitation on jet breakup and atomization. Reitz and Bracco (1986) studied various atomization mechanisms with the inclusion of cavitation phenomena. They observed wider spray cone angle with the nozzle cavitating. They also observed hydraulic flips, when the liquid flow detaches itself from the wall, and hence, cavitation occurrence is wiped out. Park et al., (2008), and Suh et al., (2008), made similar observations while investigating the influence of cavitation on the fuel flow and atomization characteristics of diesel and biodiesel fuel. They noticed that supercavitation formation along the internal nozzle wall influences the external flow pattern and droplet formation.

Fujimoto (1994) performed experiments on the modeling of atomization and vaporization process in flash boiling sprays where he considered the effect of vapor bubble nucleation to enhance atomization. Tamaki et al. (1998), in studying the effects of cavitation and internal flow on the atomization of a liquid jet, observed that when cavitation takes place in a nozzle, there is a considerable reduction in the breakup length

of the jet. Instability analysis performed by Shkadov (1998) showed that velocity profile relaxation can generate surface waves of growing amplitude, and their growth rate increases as the velocity gradient below the liquid surface increases. Leroux et al. (1996), in studying the stability of Newtonian liquid jets, confirmed that the jet atomization is strongly influenced by the fastest growing wavelength in the radial direction. Tomita et al. (1975) predicted the impulse pressure accompanying the collapse of an isolated cavitation bubble which indicated that its strength decaying inversely over the radial distance. Hence, for smaller jet diameters, the pressure pulse resulting from the cavitation bubble collapse can trigger a growth wave leading to rapid atomization.

1.2.1.3 EFFECT OF OSCILLATING PRESSURE FIELD ON LIQUID JET BREAKUP

The effects of high amplitude, high frequency mechanical vibration on the break-up characteristics of a liquid jet have been thoroughly documented in the literature (Lang, 1962; Peskin and Raco, 1963; Crane et al., 1964; McCormack et al., 1965; Elrod et al., 1989; Lin and Woods, 1991; Sindayihebura and Bolle, 1998). By the application of mechanical vibration in the appropriate frequency range, velocity modulation can be induced inside the nozzle. These forced liquid jets would carry with them a well defined modulation amplitude and frequency. Crane et al. (1964) experimented with the effect of modulations on the breakup of cylindrical water jets in air and found out that under high frequency vibrations, inertial effects dominate the surface tension induced displacements.

McCormack et al. (1965) extended the work of Crane et al. (1964) by carrying out further experimental and theoretical analysis on velocity modulated jets. In their

experiments, velocity modulation was realized by pressure variation upstream of the injector. They concluded that the application of mechanical vibration in the appropriate frequency range and at small vibration acceleration values can induce minute pressure fluctuations and trigger a capillary instability. With higher acceleration values, appreciable “bunching” effect in the liquid jet was observed. The term “bunching” denotes the radial velocity of liquid due to the relative velocity of adjacent particles in the jet. Formation of discs due to strong liquid bunching was evident (Crane et al., 1964). However, no details of the aerodynamic interaction and the resulting spreading mechanism were discussed. Mass concentration appeared with definite periodicity equal in comparison to the imposed wavelength of modulation.

A modulated liquid jet issuing from a nozzle goes from a state of high shear inside the nozzle to a state of free shear in the nozzle exterior. The liquid bulk in the exterior domain of the nozzle is subjected to the aerodynamic forces which interact with the surface forces leading to a liquid-gas interfacial instability. As the liquid jet enters the gas domain, shear layers are generated because of the velocity difference between the liquid and gas phases. The viscous interaction of the two fluids, in addition to the shear layer instability, contributes to the enhancement of liquid surface wave instabilities. In the case of modulated liquid jets, local mass accumulation occurs at finite periodicity resulting from the transient variation in liquid velocity and as a result of momentum conservation, which was analyzed by Meier et al. (1997).

In studying unsteady liquid jets, Meier et al. (1997) showed that the conservation of initial momentum is one of the governing effects in jet instability and decomposition. They formulated the mass distribution along the axis of a modulated liquid jet without the

effect of liquid properties such as surface tension and liquid viscosity. For large amplitudes and low frequencies of modulation, the jets are decomposed in very peculiar shapes, which can be very simply explained by the collision of packets of concentrated mass on the axis of the jet motion. Meier et al. (1997) worked on large diameter and high velocity jets neglecting the effect of surface tension forces. However, it is well known that liquid properties such as surface tension and viscosity are crucial in deciding the magnification/suppression of the initial disturbances (Reitz, 1978). In different experiments with water jets, Meier et al. (1997) demonstrated breakup of very low velocity liquid jets with the effects of modulations. Formations of disc-like water-films were observed when a liquid jet was imposed with large amplitude distortions and concluded the existence of bowl shaped films. The instabilities occurring in such a system were found replicable.

More recently, fundamental research on the disintegration of a sinusoidally forced liquid jet was performed by Geschner et al. (2001, 2004). Their experimental setup assured fewer turbulence effects, swirl, or any related effects inside the nozzle so that an unperturbed jet is made available for investigation in the nozzle exterior. In their investigation a wide range of jet morphology was obtained by varying the modulation characteristics, amplitude and frequency, along with the mean jet velocity, and liquid-gas density ratios. Classification of the disintegration of harmonically excited round liquid jets revealed surface waves, upstream directed bells, discs, downstream directed bells, multiple chains of droplets, and phase jump phenomena. When turbulent conditions existed inside the nozzle, stochastic atomization process was observed. Geschner et al.

(2001, 2004) created a non-dimensional map for the appearance of spray structures of a periodically excited round liquid jet.

The influence of modulation parameters on the detection of variety of highly reproducible structures ranging from discs to droplet chains indicate that spray formation can be controlled as a deterministic process. The experimental investigations on the modulated jets provide us with a global understanding of the phenomena. In order to identify and comprehend the basic underlying mechanism, details on the non-linear interaction between various forces involved in free shear flows of round liquid jets needs further clarification.

Modulated free jets discharge has the particular property that the slow and fast stream portions of each discharge cycle tend to flow together or bunch in the free stream. Seno et al. (1997) used same fluid jet to address the coherent structures generated by controlled stimulation of axisymmetric jets. They observed formation of vortex rings and their coalescence in a reproducible fashion and identified the influence of modulation parameters on these structure formations. By modulating a liquid stream, structure formation is forced into the liquid phase which then results in gas phase structures due to interfacial matching conditions. The free stream thus becomes a train of bunches of water which eventually separate depending on the inlet conditions and aerodynamic interactions. Bunch diameter increases with downstream distance until the axial velocity becomes uniform with each bunch.

An issuing modulated liquid jet is always under the influence of aerodynamic forces present in the surroundings. These aerodynamic effects promote the growth of modulation bunching because gas (air) pressure deficiency or suction is produced at any

jet surface protrusion, such as bunch edges, whereas increased pressure is obtained in surface depressions between bunches. This effect depends, in a relatively complex manner, on aerodynamic pressure, air acoustic speed, and surface disturbance size and shape. In general, however, the aerodynamic pressures should help produce percussive jets. On the other hand, gas (air) drag acts to dissipate jets. The interaction of surface tension of the liquid and the aerodynamic forces result in droplet formation. This mechanism of droplet formation by modulated jets has been reported to be of deterministic nature (Geschner et al., 2001, 2004). The droplet sizes have been observed to be consistent and the entire process, repetitive. This mechanism indicated that a truly deterministic process of spray formation with controllable droplet size distribution is achievable.

In the experiments performed by Geschner et al. (2001), they identified different possible jet structures such as waves, discs, upstream directed bells, downstream directed bells, touching bells, droplet chains, stochastic disintegration, and a phase jump. Geschner et al. (2004) observed that the basic parameter is the modulation amplitude which is representative of the structures that are formed.

It is important to understand the basic physical process underlying the creation of liquid droplets. Several researchers have worked on droplet formation from a liquid jet ejected from a nozzle. The basic theories behind the creation of these droplets lead to the instability in the jet emanating from a nozzle. There have been relations derived which were based on the fluid parameters to the droplet characteristics generated by the nozzle. In this dissertation, the new atomizer that was developed utilizes cavitation mechanism as a very crucial enhancing factor in the process of atomization. The phenomena of

cavitation can be expressed as the formation of vapor pockets (or bubble) as a result of lowering pressure in a liquid. A detailed mechanism of the cavitation phenomenon and its influence on liquid jet atomization are presented in a later section together with the new atomizer development and fabrication.

1.2.2 SPRAY CHARACTERIZATION

Practical atomizers do not generally produce sprays of uniform droplet size at any given operating condition; instead the spray can be regarded as a spectrum of droplet sizes distributed about some arbitrary defined mean value (Schick, 1997). In order to accurately assess and understand droplet size data, all of the key variables such as nozzle type, pressure, capacity, liquid properties, and spray angle have to be taken into consideration (Lefebvre, 1989). The droplet size testing method should also be fully understood. The measurement techniques, the type of droplet size analysis technique, the data analysis, and the reporting methods all have a strong influence on the results (Schick, 1997).

1.2.2.1 DROPLET SIZE DISTRIBUTION IN SPRAYS

Accurate knowledge of droplet size distribution as a function of the conditions of the spray system is a prerequisite for the fundamental analysis on the transport of mass, heat, and phase separation in dispersed systems (Mugele and Evans, 1951). Detailed characterization of sprays is critical in optimizing injector design and validating

mathematical modeling predictions. Spray characteristics include the droplet size and velocity distribution, spray pattern, spray coverage, and spray angle. Sprays are multiphase flows which are generally a complex system commonly consisting of droplets which have a range of properties. This property range almost always includes droplet diameter, velocity, and concentration, which usually includes non-sphericity, mass/heat transfer, and temperature variations. In addition, other properties that are commonly present in some regions of the spray include droplet break-up, physical property variations, and coalescence. At the most basic level, multiphase flows may be characterized by an average spray length scale. However, there are a number of definitions, and this is a source of much confusion. Standard texts (Lefebvre, 1989; Liu, 2000) offer definitions, and the two most commonly used are D_{10} and D_{32} .

The linear average diameter (D_{10}) is defined as the diameter of a uniform droplet set with the same number and sum of diameters as the real set, providing a simple ‘average’ measure with which to compare different sprays. However, most multiphase processes involve heat and/or mass transfer, and the representative length scale used here is the Sauter Mean Diameter, expressed as SMD or D_{32} , which is the diameter of a uniform droplet set with the same total volume to total surface area ratio as the real set.

Spray characterization techniques normally record data that are typically in the form of number count per class size. The data are arranged into a mathematical representation referred to as a droplet size distribution. The mathematical representation is most often dependent on the characterization techniques used. Some of the most common droplet size distribution functions used in industry include normal, log-normal, root normal, Nukiyama-Tanasawa, Rosin-Rammler, and upper-limit distribution function

(Lefebvre, 1989; Liu, 2000). It should be noted that no single distribution function can characterize all experimental measurement data of droplets sizes, and none of these functions is universally superior to any other for representing droplet size distribution (Liu, 2000).

Many droplet size distributions in random droplet generation processes follow Gaussian, or normal distribution pattern. In the normal distribution, a number distribution function $f(D)$ may be used to determine the number of droplets of diameter D :

$$f(D) = \frac{dN}{dD} = \frac{1}{\sqrt{2\pi}s_n} \exp\left[-\frac{1}{2s_n^2}(D - \bar{D})^2\right] \quad (1.1)$$

where S_n is the standard deviation, a measure of the deviation values of D from the mean value \bar{D} , and S_n^2 is the variance. A plot of the distribution function is the so-called standard normal curve. The area under the standard normal curve from $-\infty$ to $+\infty$ equals 1. The integral of the standard normal distribution function is the cumulative standard number distribution function $F(D)$:

$$F(D) = \frac{1}{\sqrt{2\pi}} \int_{-\infty}^D \exp\left[-\frac{1}{2}\left(\frac{D - \bar{D}}{S_n}\right)^2\right] d\left(\frac{D - \bar{D}}{S_n}\right). \quad (1.2)$$

Plotting the droplet size data on an arithmetic-probability graph paper will generate a straight line if the data follow normal distribution. Thus, the mean droplet diameter and standard deviation can be determined from such a plot (Liu, 2000).

Many droplet size distributions in natural droplet formulation and liquid metal atomization processes conform to log-normal distribution:

$$f(D) = \frac{dN}{dD} = \frac{1}{\sqrt{2\pi}DS_g} \exp \left[-\frac{1}{2S_g^2} (\ln D - \ln \bar{D}_{ng})^2 \right] \quad (1.3)$$

where \bar{D}_{ng} is the number geometric mean droplet diameter and S_g is the geometric standard deviation. Plotting droplets size data on a log-probability graph paper will generate a straight line if the data follow log-normal distribution (Liu, 2000).

Log-normal distribution functions based on surface and volume respectively are (Liu, 2000):

$$f(D^2) = \frac{dN}{dD} = \frac{1}{\sqrt{2\pi}DS_g} \exp \left[-\frac{1}{2S_g^2} (\ln D - \ln \bar{D}_{sg})^2 \right] \quad (1.4)$$

and

$$f(D^3) = \frac{dN}{dD} = \frac{1}{\sqrt{2\pi}DS_g} \exp \left[-\frac{1}{2S_g^2} (\ln D - \ln \bar{D}_{vg})^2 \right] \quad (1.5)$$

where \bar{D}_{sg} and \bar{D}_{vg} are the geometric surface and volume means droplet diameters, respectively. These diameters can be determined once the number of the geometric mean droplets' diameters and the geometric standard deviation are known:

$$\ln \bar{D}_{sg} = \ln \bar{D}_{ng} + 2S_g^2 \quad (1.6)$$

$$\ln \bar{D}_{vg} = \ln \bar{D}_{ng} + 3S_g^2 \quad (1.7)$$

$$\ln SMD = \ln \bar{D}_{ng} + 2.5S_g^2. \quad (1.8)$$

In many atomization processes of normal liquids, droplet size distribution fairly follow root-normal distribution pattern (Liu, 2000):

$$f(D) = \frac{dN}{dD} = \frac{1}{\sqrt{2\pi}S_s} \exp \left[-\frac{1}{2S_s^2} \left((D/MMD)^{1/2} - 1 \right)^2 \right] \quad (1.9)$$

where S_s is the standard deviation, and MMD is the mass mean diameter.

The Nukiyama and Tanasawa distribution function (Nukiyama and Tanasawa, 1939) is given by:

$$f(D) = \frac{dN}{dD} = aD^p \exp[-bD^q] \quad (1.10)$$

where a , b , and p are constants, and q is the dispersion coefficient which is a constant for a given nozzle design. The value of q usually varies from 1/6 to 2 and is determined by trial and error. A graphical method to determine a and b has been proposed by Mugele and Evans (1951). In the Nukiyama-Tanasawa distribution equation, $p = 2$, such that:

$$f(D) = \frac{dN}{dD} = aD^2 \exp[-bD^q]. \quad (1.11)$$

Rearranging Equation 1.11 yields

$$\ln \left(\frac{1}{D^2} \frac{dN}{dD} \right) = \ln a - bD^q. \quad (1.12)$$

Plotting $\ln(1/D^2 (dN/dD))$ vs. D^q based on experimental data and an assumed value of q yields a straight line if the assumed value of q is correct. The values of a and b can then be determined from the plot.

The Rosin-Rammler distribution function is given by the following relations; it is perhaps the most widely used at present:

$$Q = 1 - \exp\left[-\frac{D}{X}\right]^q \quad (1.13)$$

where Q is the fraction of total volume of droplets smaller than D , and X and q are constants. The exponent q is a measure of the spread of droplet sizes; a larger value of q corresponds to a more uniform droplet size.

Mugele and Evan (1951) proposed the upper-limit distribution function based upon their analysis of various distribution functions and comparisons of experimental data. This is a modified form of the log-normal distribution function, and for volume distribution it is expressed as:

$$\frac{dV}{dy} = \delta \exp\left[-\frac{1}{\sqrt{\pi}} \delta^2 y^2\right] \quad (1.14)$$

Where V is volume; $y = \ln\left[aD/(D_{\max} - D)\right]$; δ is a factor related to the standard deviation of droplet size; a is a dimensionless constant, and D_{\max} is the maximum droplet diameter. The SMD is formulated as:

$$\text{SMD} = \frac{D_{\max}}{1 + a \exp(a/4\delta^2)}. \quad (1.15)$$

The upper-limit distribution function assumes a realistic spray of finite minimum and maximum droplet sizes. However, similar to other distribution functions, it is difficult to

integrate, and in addition requires many trials to determine a most suitable value for a maximum droplet size.

In many applications, a mean droplet size is a factor of foremost concern. Mean droplet size can be taken as a measure of the quality of an atomization process. It is also convenient to use only mean droplet size in calculations involving discrete droplets, such as multiphase flow and mass transfer processes (Lefebvre, 1989). Various definitions of mean droplet size have been employed in different applications, as summarized in Table 1.1, adopted from (Liu, 2000).

Table 1.1: Mean Droplet Diameters and their Applications (Liu, 2000)

Symbol	Common Name	a	b	Definition	Application
D_{10}	Arithmetic Mean (Length)	1	0	$\frac{\sum N_i D_i}{\sum N_i}$	Comparison
D_{20}	Surface Mean (Surface Area)	2	0	$\left[\frac{\sum N_i D_i^2}{\sum N_i} \right]^{1/2}$	Surface Area Controlling
D_{30}	Volume Mean (Volume)	3	0	$\left[\frac{\sum N_i D_i^3}{\sum N_i} \right]^{1/3}$	Volume Controlling (Hydrology)
D_{21}	Length Mean (Surface Area-Length)	2	1	$\frac{\sum N_i D_i^2}{\sum N_i D_i}$	Absorption
D_{31}	Length Mean (Volume Length)	3	1	$\left[\frac{\sum N_i D_i^3}{\sum N_i D_i} \right]^{1/2}$	Evaporation, Molecular Diffusion
D_{32}	Sauter Mean (Volume-Surface)	3	2	$\frac{\sum N_i D_i^3}{\sum N_i D_i^2}$	Mass Transfer Reaction
D_{43}	Herdan Mean (De Brouckere or Herdan) (Weight)	4	3	$\frac{\sum N_i D_i^4}{\sum N_i D_i^3}$	Combustion, Equilibrium

The expressions for the mean droplet diameters as shown in Table 1.1 takes the form of a generalized equation as follows:

$$D_{ab} = \left[\frac{\int_{D_{\min}}^{D_{\max}} D^a \left(\frac{dN}{dD} \right) dD}{\int_{D_{\min}}^{D_{\max}} D^b \left(\frac{dN}{dD} \right) dD} \right]^{1/(a-b)}, \text{ or } D_{ab} = \left[\frac{\sum N_i D_i^a}{\sum N_i D_i^b} \right]^{1/(a-b)} \quad (1.16)$$

where D_{\min} and D_{\max} are the minimum and maximum droplet diameters respectively, and a and b take any value according to the effects considered in Table 1.1. SMD is perhaps the most widely used. It represents the diameter whose ratio of volume to surface area is the same as that of the entire droplet sample.

In characterizing the droplet size distribution, at least two parameters are typically necessary, i.e., a representative droplet diameter, (e.g. mean droplet size) and a measure of droplet size range (e.g. standard deviation or q). Many representative droplet diameters have been used in specifying distribution functions. The definitions of these diameters and the relevant relationships are summarized in Table 1.2. The relationships are derived on the basis of the Rosin-Rammler distribution function (Equation 1.13).

Many authors (Li and Tankin, 1987, 1988; Semio et al., 1996; Dumouchel and Boyaval, 1999; Ayres et al., 2001; Cao, 2002) have used maximum entropy formalism to derive probability density function for the prediction of droplet size distribution. Lui (2000) provided a detailed summary of empirical and analytical correlations for droplet size distribution.

Table 1.2: Definition of Representative Droplet Diameters (Liu, 2000)

Symbol	Definition	Position in Q-D plot	Relationship
$D_{0.1}$	10% of total volume of droplets are of smaller diameter than this value	$Q = 10\%$	$\frac{D_{0.1}}{X} = (0.1051)^{1/q},$ $\frac{D_{0.1}}{MMD} = (0.152)^{1/q}.$
$D_{0.5}$ (MMD)	Mass Mean Diameter 50% of total volume of droplets are of smaller diameter than this value	$Q = 50\%$ Left-hand or right hand side of D_{peak} for $q > \text{or} < 3.2584$	$\frac{MMD}{X} = (0.693)^{1/q},$ $\frac{MMD}{SMD} = (0.963)^{1/q} \Gamma\left(1 - \frac{1}{q}\right).$
$D_{0.632}$	Characteristic diameter 63.2% of total volume of droplets are of smaller diameter than this value	$Q = 63.2\%$	X (X in the Rosin-Rammler Distribution Function)
$D_{0.9}$	90% of total volume of droplets are of smaller diameter than this value	$Q = 90\%$	$\frac{D_{0.9}}{X} = (2.3025)^{1/q},$ $\frac{D_{0.9}}{MMD} = (3.32)^{1/q}.$
$D_{0.999}$	Maximum Diameter 99.9% of total volume of droplets are of smaller diameter than this value	$Q = 99.9\%$	$\frac{D_{0.999}}{MMD} = (9.968)^{1/q}.$
D_{peak}	Peak diameter value of D corresponding to peak of droplet size frequency distribution curve	Peak point corresponding to $d^2Q/dD^2 = 0$	$\frac{D_{peak}}{X} = \left(1 - \frac{1}{q}\right)^{1/q},$ $\frac{D_{peak}}{MMD} = \left(1.4428 - \frac{1.4428}{q}\right)^{1/q},$ $\frac{D_{peak}}{SMD} = \left(1 - \frac{1}{q}\right)^{1/q} \Gamma\left(1 - \frac{1}{q}\right).$

1.2.2.2 DROPLET SAMPLING TECHNIQUE

There are two different types of droplet size sampling techniques: spatial and flux also called temporal (Schick, 1997). The spatial technique is implied when a collection of droplets occupying a given volume is sampled instantaneously. Generally, spatial

measurements are collected with the aid of holographic means such as high-speed photography or light scattering instruments. This type of measurement is sensitive to the number density in each class size and the number of particles per unit volume.

The flux technique occurs when individual droplets pass through the cross section of a sampling region and are examined during an interval of time. Flux measurements are generally collected by optical instruments that are capable of sensing individual droplets. This type of measurement is sensitive to the particle flux. The sampling technique is critical for understanding droplet size data. Typically, nozzles measured using the spatial technique will report droplets smaller on average than nozzles measured using the flux technique. When comparing data from different sources, it is important to identify the differences in sampling techniques. This should help resolve many data discrepancies.

The sampling technique used can also be application-driven. For example, gas conditioning, cooling, or similar processes would be better served with a spatial sampling technique. According to Schick (1997), in applications requiring accurate spray deposition such as painting and agricultural spraying, a flux sampling technique would be more appropriate. Flux methods are more sensitive to individual droplet sizes and velocity and provide the additional detail required by some applications. The two sampling techniques are depicted in Figures 1.1 and 1.2.

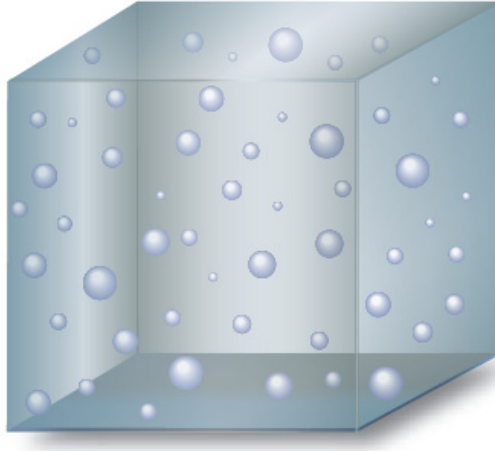


Figure 1.1: The measurement volume for the spatial distribution (Schick, 1997).

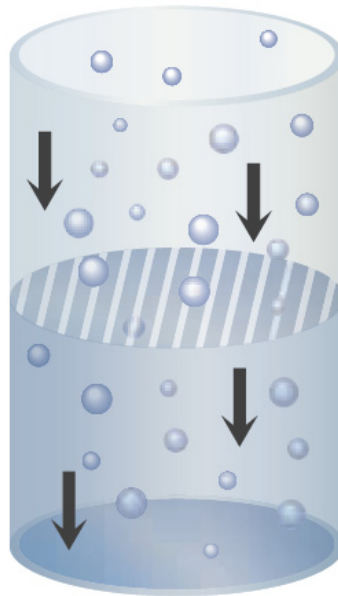


Figure 1.2: The measurement cross-section for the flux distribution (Schick, 1997).

1.2.2.3 DROPLET SIZE MEASUREMENT TECHNIQUES

Various measurement techniques have been developed and applied with different degrees of success. For the measurement of droplet properties in sprays, non-intrusive techniques are often desired (Liu, 2000). The measurement should not create disturbance to the spray pattern. An ideal measurement technique should have large range of capability to measure both the spatial and temporal distribution. Such a technique should tolerate wide variations in droplet properties at some extreme conditions present in sprays in various engineering applications. An appropriate technique should also be able to acquire sufficient representative samples to ensure reasonable measurement accuracy. Rapid sampling and data processing means are hence needed for the analysis of measurement results. The sampling, data acquisition, and processing system must be fast enough to record every droplet passing through the measurement volume when measuring the number density of the spray (Liu, 2000).

The measurement techniques for droplet sizing may be grouped conveniently into four primary categories: (a) mechanical methods, (b) electrical methods, (c) optical methods and (d) acoustical methods. Mechanical methods are relatively simple and low cost. Droplets are collected in either liquid or frozen state, followed by microscopic or sieving analysis. Electrical methods involve the detection and analysis of electronic pulses generated by droplets in a measurement volume or on a wire. The electronic signals are then converted into digital data and calibrated to produce information on droplet size distribution. Optical methods have been developed in recent years and are finding an increasing range of applications. Some of the optical methods are capable of simultaneously measuring droplet size and velocity, as well as velocity and number

density (Lefebvre, 1989). An acoustical method has been evaluated for the measurements of fine droplets. Table 1.3 summarizes the droplet measurement techniques (Liu, 2000).

Table 1.3: Measurement Techniques for Droplet Size (Liu, 2000)

Categories	Methods	Size range (μm)
Mechanical	Collection of droplets on slides or in cells	$\geq \sim 3$
	Cascade impactor	$\geq \sim 3$
	Molten-wax and frozen-droplet techniques	
	Mechanical sieving of metal powder	
Electrical	Pulse counting technique	
	Charged wire technique	
	Hot wire technique	1 – 600
Optical	Imaging	
	Photography	$\geq \sim 5$
	Videography	
	Holography	5 – 1000
	Non-Imaging	
	Light-scattering interferometry	5 – 3000
	Phase-Doppler Anemometry	0.5 – 3000
	Light intensity deconvolution technique	0.2 – 200
	Light scattering technique	10 – 250
	Malvern particle analyzer	1 – 900
	Polarization ratio particle sizer	
	Intensity ratio method	
	Phase optical-microwave method	
	Dual-cylindrical wave laser technique	
Acoustical		5 – 30

1.2.2.3.1 OPTICALLY-BASED DROPLET SIZE MEASUREMENT TECHNIQUES

In this section we focus our attention on optically-based droplet size measurement techniques and provide a brief review of three of the most widely used. A wide range of optically-based droplet size measurement techniques have been developed and are in use.

Although each measurement technique has its own advantages and limitations, most optical methods have an important, common attribute of allowing droplet size measurements to be made without disturbing the flow field being measured. The optical methods generally fall into one of two categories: Imaging or Non-Imaging. The most important sub-class is the single droplet counting method of which Black et al. (1996, 2001) provides an extensive review. Other methods include ensemble light scattering methods of droplet sizing, which integrates in one dimension (Swithenbank et al., 1976), and more recently Domann and Hardalupas, (2000) which focuses upon planar methods.

Phase Doppler Anemometry (PDA) (Durst and Zare, 1975; Manasse et al., 1992, 1993; Bachalo, 1994) is generally considered the most accurate method for spray characterization despite its high capital cost and the requirement for skilled operation in order to optimize the system set-up and subsequent data interpretation. PDA is a Laser-Doppler Velocimeter (LDV) based method for non-intrusive, simultaneous measurements of the diameter and velocity of spherical particles (Manasse et al., 1992, 1993). The technique relies on measuring the time delay that occurs when the light scattered by a droplet traversing the intersection of two coherent laser beams arrives at two spatially separated photo detectors. Through good design and proper set-up, the method has the potential to gather accurate data at extremely high data rates with good statistical certainty. However, measurement accuracy is dependent upon a number of factors including laser power, optical configuration, droplet homogeneity, sphericity, and concentration. It also requires skilled set-up and operation to obtain accurate results.

One of the fundamental limitations of PDA is the inability to accurately measure non-spherical droplets (Damaschke et al., 1997). Such conditions are observed at the

interface where an initial liquid sheet breaks up into ligaments subsequently forming initially large and often non-spherical droplets; therefore PDA is an inherently unsuitable instrument to characterize near-orifice flows. This is an unfortunate limitation since the near-orifice region is where the spray is defined and the process of atomization is occurring. This creates particular problems for data certainty since only a small fraction of the spray mass is spherical in the near-orifice region. In addition, the best optical geometry is specific and may not be available in the experiment. Curved window surfaces need complex optical corrections to be employed which, while valid for LDA work, are difficult to extend to PDA (Stieglmeier et al., 1989; Pitcher and Wigley, 1992, 1994).

The Malvern Particle Analyzer is another widely used particle analyzer. It is based on the Fraunhofer diffraction of a parallel beam of monochromatic light by a moving droplet. When a droplet interacts with a parallel beam of light, a diffraction pattern is formed. For monodisperse spray, the diffraction pattern is of the Fraunhofer form. It comprises a series of alternate light and dark concentric rings whose spacing is related to the droplet size. For a polydisperse spray, the diffraction pattern comprises a number of the Fraunhofer pattern with series of overlapping diffraction rings, each of which is produced by a different group of droplets sizes (Hirleman, 1988). The Fourier transform receiver lens focuses the diffraction patterns onto a multi-element photodetector that measures the light energy distribution. The photodetector consists of 31 semicircular photosensitive rings surrounding a central circle. Each ring is most sensitive to a particular small range of droplet sizes. The output of the photodetector is multiplexed through an analog-digital converter. The measured light energy distribution is then converted to the droplet size distribution. The measured data may be either

analyzed in terms of a histogram with 15 size classes or presented in the format of normal, log-normal, Rosin-Rammler, or other modes that are independent of the known models.

Imaging is probably one of the most accurate and least expensive techniques for measuring droplet size and velocity. It has the potential of measuring droplets in dense, fast-moving sprays that are of particular interest in power generation (Liu, 2000). In the imaging method, an image of the droplets is taken with a light pulse of sufficient intensity and sufficient short duration to yield a sharp image of the droplets. The major advantage is that a visual record of the spray under investigation provides a simple means to check what is and (more importantly) is not being measured and the ability to quantify arbitrarily shaped objects. Until recently, the error and time required for manual analysis of the images (Herbst, 2001) has been the reason why imaging methods have not been more prevalent.

One of the most common image analysis methods available in the market is the Particle/Droplet Image Analysis (PDIA) technique by Oxford Lasers Inc. In the PDIA technique the object diameter is based upon the measured area/perimeter rather than local object curvatures as is the case of PDA. The PDIA technique, as reported by Whybrew et al. (1999), uses an automated segmentation thresholding algorithm for the quantitative analysis of droplet or particle images. This method is based upon the original approach adopted by Yule et al. (1978), in terms of determining the degree of image focus from the edge gradient intensity of a droplet image. In a preliminary study, Kashdan et al. (2000) examined probability density function correction schemes to account for edge contact correction and depth of field (DOF) biasing effects which are diameter dependent.

1.2.3 SPRAY VISUALIZATION

Spray visualization is generally carried out to give qualitative information of the spray flow field. It also provides information of the geometric features of the spray which includes spray pattern, spray cone angle, and spray coverage. Traditionally, spray visualization has been achieved by several optical methods, including but not limited to, high speed photography, schlieren technique, shadowgraph technique, and holography.

High speed photography is the most common spray visualization technique. This imaging technique requires two main components: a light source to illuminate the spray and an imaging device. The illumination for high speed photography can roughly be divided into three modes namely: Laser Light Sheet (LLS), stroboscopic lighting, and backlighting or front lighting. For laser light sheet illumination of the spray for imaging, the laser light is passed through a cylindrical lens to create the laser sheet which is expanded to penetrate the entire spray vertically to illuminate the center vertical plane. The imaging device or camera is positioned normal to the plane of the laser light sheet to acquire images of the spray structure.

For stroboscopic lighting, the stroboscope must be synchronized with the imaging device or camera for recording. The system consists of a flashing strobe light and an imaging device or camera with an open shutter. Stroboscopic images must be taken in darkness so that every time the strobe flashes, a still image is taken of a moving object at that instant. Another illumination method is backlighting, where the light source and the imaging device are placed at opposite sides of the object to be imaged while facing each other. There are several combinations of the above three illumination methods in high speed photography.

Im et al. (2001) and Wang et al. (2003) used high speed photography for spray visualization in which laser light sheet generated by a copper-vapor laser was used to illuminate the spray. Domnick and Thieme (2006) used stroboscopic lighting with a nanolight of 18 ns flash to capture images of liquid disintegration process at the bell cup edge of a high speed rotary bell atomizer using a video camera. The flash is synchronized with the video camera yielding a frame rate of 25 frames per second. Settles (1997) used two visualization approaches; one is stroboscopic lighting with a xenon flash of about 1 μ s duration for illumination and Super Video Home System (S-VHS) videotape at standard 30 Hz frame rate. The second is a Continuous Wave (CW) Argon-ion laser beam which was spread into a sheet by a glass rod for illumination.

To investigate spray propagation in a gas turbine combustor, Schober et al. (2002) used the LLS technique for detail and effective two-dimensional characterization of liquid fuel spray. Lee et al. (2005) used backlight scattering to capture spray images which were analyzed by measuring spray penetration, spray angle, and total spray volume of dimethyl ether fuel spray. A strobe light was used as the backlight in this case. Versteeg et al. (2006) used a copper-vapor laser as the illumination source in conjunction with a Kodak HS4540 high speed digital camera for image recording. The laser provided a pulsed light source with a frequency of 9 kHz. Fiber-optic light delivery was used to provide front and backlighting.

A second method commonly used for spray visualization is the schlieren technique. The schlieren technique is based on the deflection of a collimated light beam crossing gradients of the index of refraction in a transparent medium (i.e. it provides images of the refractive-index-gradient fields). It is, therefore, suited for applications in

which deviations of light are intended to be visualized as they appear, e.g., at the refraction-gradient due to density-discontinuities in a fluid (Mayinger and Feldmann, 2001). Settles (2001) and Settles et al. (1995) used the schlieren technique in the visualization of a combustion driven High-Velocity Oxy-Fuel (HVOF) thermal spray torch utilized to apply metallic coatings to surfaces. The hot supersonic jet produced by this equipment spreads rapidly and vigorously entrains the surrounding air. This visualization is critical to understand the process since direct visual observation belies its true character.

Shadowgraph technique is a companion of schlieren, and is also based on light refractions. While the schlieren image displays the deflection angle, shadowgraph displays the ray displacement resulting from the deflection. There are three main differences between schlieren and shadowgraph techniques. First the shadowgram is not a focus optical image; it is a mere shadow. The schlieren image, however, is what it purports to be: an optical image formed by a lens, and thus it is bearing a conjugate optical relationship to the schlieren object. Second, schlieren methods require a knife-edge or some other cutoff from the refracted light, where no such cutoff is needed or allowed in shadowgraphy. Finally, the luminance level in a schlieren image responds to the first spatial derivative of the refractive index in the schlieren, e.g. $\partial n / \partial x$. However, the shadowgram response is the second spatial derivative, or Laplacian, e.g. $\partial^2 n / \partial x^2$ (Settles, 2001). Bellofiore et al. (2007) used a flash shadowgraph technique for the visualization of a dense spray of water and kerosene. Bae et al. (2002) utilized shadowgraph, and Mie Scattering observed the spray from a Valve-Covered-Orifice (VCO) nozzle and a Start-On-Injection (SOI) nozzle. In their setup for shadowgraph

visualization, Bellofiore et al. (2007) used a Xenon flash lamp with 15 μ s pulse length, a Pulnix TM-6710 digital camera (to acquire 8-bit 640x200 pixel frames at 240 Hz), and a BNC delay generator for time-based generation synchronization.

A fourth visualization technique is holography. It is a technique that allows the light scattered from an object to be recorded and later reconstructed so that it appears as if the object is in the same position relative to the recording medium as it was when originally recorded. The image changes as the position and orientation of the viewing system changes in exactly the same way as if the object were still present, thus making the recorded image (hologram) appear three-dimensional (Mayinger and Feldmann, 2001). Feldmann et al. (1998) used short time holography for the visualization of both sub-cooled and superheated sprays generated in a flat spray nozzle.

The spray visualization and characterization technique developed in this work is an infrared thermography-based technique in which a thermal radiation source in the form of a uniformly heated blackbody background as the emitter and an infrared camera as the receiver are employed. As a result of the presence of the spray, the infrared energy emitted by the source is attenuated as it passes through the spray before reaching the receiver. The infrared detector, therefore, receives a damped signal as a result of the attenuation of the emitted intensity. This damped image is recorded to provide an attenuation map of the spray, which is post-processed using theoretical and empirical equations to extract information about the liquid volume fraction and droplet number density.

1.2.4 INFRARED THERMOGRAPHY

Infrared thermography transforms the thermal energy emitted by an object in the infrared spectral band of the electromagnetic spectrum into a visible image. It is known that any object at a temperature above absolute zero, that is 0 K ($-273.16\text{ }^{\circ}\text{C}$) emits electromagnetic radiation in the form of rays which fall in the infrared spectral band of the electromagnetic spectrum. Within the infrared spectral band of the electromagnetic spectrum at the short-wavelength end, the boundary of the limit of visual perception lies in the deep red. At the long-wavelength end, it merges with the microwave radio wavelength in the millimeter range. The infrared spectral band of the electromagnetic spectrum ranges from 1 to $1000\text{ }\mu\text{m}$. This band is further subdivided into four smaller bands, the boundaries of which are arbitrarily chosen. They include: the near infrared ($0.75\text{-}3\mu\text{m}$), the middle infrared ($3\text{-}6\text{ }\mu\text{m}$), the far infrared ($6\text{-}15\text{ }\mu\text{m}$), and the extreme infrared ($15\text{-}1000\text{ }\mu\text{m}$). You will find this illustrated in Figure 1.3.

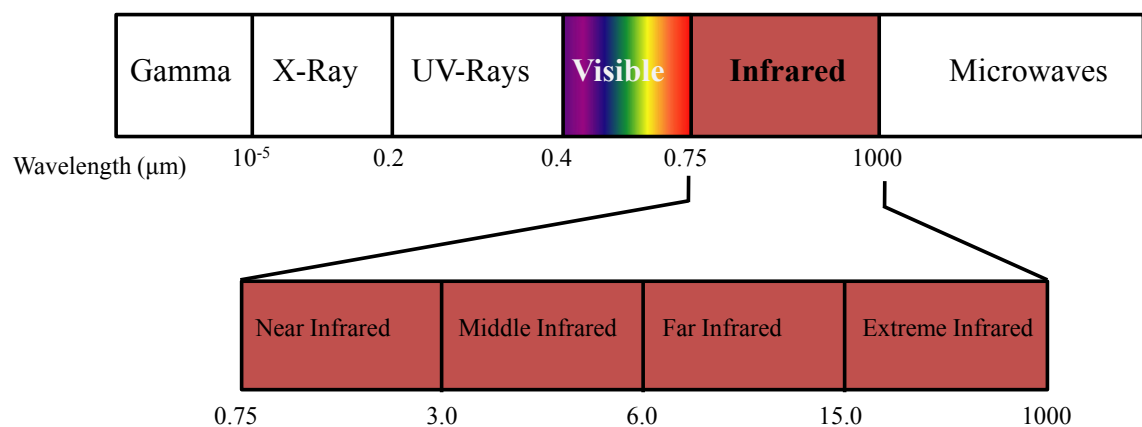


Figure 1.3: The electromagnetic spectrum showing the subdivision of the infrared spectral band.

Infrared thermography is a non-contact, non-intrusive technique, which enables us to see thermal energy. The energy emitted by a body is mainly a function of its surface temperature, and consequently, infrared thermography may be considered a two-dimensional technique of temperature measurement. Thus infrared thermography is the science of detecting and measuring variations in heat emitted by an object and transforming them into visible images.

1.2.4.1 HISTORICAL BACKGROUND OF INFRARED

The origin of infrared thermography comes from the early 1800s when William Herschel discovered thermal radiation outside the deep red in the visible spectrum. The invisible light was later called “infrared”. Herschel was involved in a search for a solution to an astronomical problem. In order to facilitate his studies of sunspots, he was seeking some filtering technique which would give adequate light for seeing, without undesirable heating.

Herschel first step toward the design of such a filter was to undertake a careful survey of the distribution of thermal energy in the visible solar spectrum. To do this he formed a prismatic spectrum on a table top in a dark room and placed one of two identical sensitive thermometers at various positions in the spectrum, in each case comparing the equilibrium temperature reached with that of the other thermometer which was not illuminated. He found that the thermometer readings increased as he went from the violet to the red, and I quote, “it appears that the maximum of illumination has little more than half the heat of the full red; and from other experiments, I likewise conclude,

that the full red falls still short of the maximum of heat; which perhaps lies even a little beyond visible refraction. In this case, radiant heat will at least partly, if not chiefly, consist, if I may be permitted the expression, of invisible light” (Herschel, 1800 a, p. 272).

Immediately following this report you will find the first paper devoted to an infrared investigation (Herschel, 1800 b). This paper discusses the measurements he made in the region adjoining the red end of the spectrum which led him to the conclusion that the radiation found there was of the same nature as visible light. The methodical thoroughness that was so characteristic of Herschel impelled him to go further into the matter, and he undertook a comprehensive study of the radiation from a candle, from a hearth fire, and from a red hot-poker to supplement his solar measurements (Herschel, 1800 c, d).

During the thirty years which followed Herschel’s discovery of the infrared region in 1800, a number of researchers—among whom may be mentioned Brewster, Davy, Englefield, Leslie and Ritchie in England; Berard and Provost in France; and Ritter, Ruhland, Seebeck and Wunsch in Germany—did random probing in the field with results which did little to advance it, although useful bits of information appeared, such as Seebeck’s discovery of the important role played by the material of the prism, in 1820 (Cornell, 1938 a). As pointed out by Cornell, experimental work was handicapped by the lack of a more sensitive detector than the liquid in-glass thermometer. Even the nature of the radiation under study was in dispute, despite the opinion expressed by Young (1802) that it seems highly probable that light differs from heat only in the frequency of its undulations or vibrations; those undulations which are within certain limits, with respect

to frequency, being capable of affecting the optic nerve, and constituting light and those which are slower, and probably stronger, constituting heat only. A historical account on the work of Sir William Herschel was presented by Barr (1961). In a follow up paper, Barr (1962) presented the works of Macedonio Melloni.

In a historical account, Cornell (1936) presented some of the earlier studies in radiant heat which were carried out before Herschel. He followed with two other papers (Cornell, 1938 a, b) which documented the research work on radiant heat spectrum from William Herschel (1800) to Macedonio Melloni. Following the work of William Herschel, Macedonio Melloni and their contemporaries, many other scientists, notable among them, Gustav Kirchhoff, James Clerk Maxwell, Joseph Stefan, Ludwig Boltzmann, and Max Planck all contributed immensely to make infrared thermography a useful technique of surface temperature mapping.

1.2.4.2 PRINCIPLES OF INFRARED THERMOGRAPHY

Infrared thermography basically includes a camera, equipped with series of changeable optics, and a computer. The core of the camera is the infrared detector, which absorbs the infrared energy emitted by the object and converts it into electrical voltage or current. The law that describes the spectral distribution of the radiation intensity from a blackbody was derived by Max Planck (1901). He showed by quantum argument and experimental verification that for a blackbody, the spectral distributions of hemispherical emissive power and radiant intensity in a vacuum are expressed as a function of wavelength and the blackbody absolute temperature as follows:

$$E_{\lambda b} = \frac{C_1}{\lambda^5 (e^{C_2/\lambda T} - 1)} \quad (1.17)$$

In the above equation, $E_{\lambda b}$ is the blackbody monochromatic radiation intensity; C_1 and C_2 are the first and second radiation constants respectively; λ is the wavelength of the radiation being considered, and T is the absolute temperature of the blackbody. By differentiating Planck's Law with respect to λ and taking the maximum radiation intensity, Wien's Displacement Law is obtained (Wien, 1894),

$$\lambda_{\max} = 2898/T \quad (1.18)$$

which mathematically expresses the common observation that colors vary from red to orange to yellow, as the temperature of a thermal radiator increases. By integrating Planck's Law over the entire spectrum ($\lambda = 0 - \infty$), the total hemispherical radiation intensity is obtained,

$$E_b = \sigma T^4 \quad (1.19)$$

where σ is the Stefan-Boltzmann constant.

It has to be pointed out that Equation (1.17) describes the radiation emitted from a blackbody which is the maximum value radiated by a body at a given temperature. Real objects almost never comply with this law although they may approach the behavior of a blackbody in certain spectral intervals. The energy emitted by a real object, E_λ , generally emit only a part of the radiation emitted by a blackbody at the same temperature and at the same wavelength. By introducing the quantity,

$$\varepsilon_{\lambda} = \frac{E_{\lambda}}{E_{\lambda b}} \quad (1.20)$$

which is called the spectral emissivity coefficient, Equation (1.17) can be rewritten for real bodies by simply multiplying it by ε_{λ} .

Infrared instruments are often classified as total-radiation radiometers and are thought to be based on the Stefan-Boltzmann Law even if their detectors sense radiation in a limited bandwidth of the infrared spectrum. Measurements are generally performed in two different windows: short wave (SW) and long wave (LW). Therefore, measurements made with infrared radiometers must be generally based on Planck's Law.

Infrared thermography may be successfully exploited in many industrial and/or research fields. Each field or area of potential use of infrared thermography presents specific characteristics and requirements which entail a specific choice of infrared system, test procedure, and data analysis.

The first choice for infrared thermography is the imaging system where one chooses between scanner and Focal Plane Array (FPA), which could operate in a short- or long-wave window. Scanner systems use a single detector. To achieve two-dimensionality, rotating mirrors or oscillating refractive elements (such as prisms) which scan the Field-Of-View (FOV) in both vertical and horizontal directions are used. FPA systems include a matrix of detectors to resolve the FOV. The detectors mostly used are photon ones in which the release of electrons is directly associated with photon absorption. Their main characteristic is a short response time and a limited spectral response.

Such detectors generally require cooling well below the ambient temperature to allow for rapid scanning, high sensitivity, and low noise. The sensor is often located in the wall of a Dewar chamber which is filled with liquid nitrogen (77 K). This may represent a limit in applications where a horizontal surface has to be viewed; but this drawback may be eliminated by viewing the surface via a mirror placed at 45°. In addition, a demand flow Joule–Thompson cryostat using high-pressure nitrogen (or argon) gas, or a closed-cycle cryogenic refrigerator, can also be employed. However, in the latest system generation, temperature around 70 K is easily achievable by miniature Stirling coolers.

Infrared devices generally perform measurements in two different windows: the short wave (SW) 3–6 μm and the long wave (LW) 8–12 μm . The main workhorse in the field of photon detectors is mercury cadmium telluride (HgCdTe), which is used in both SW and LW. Indium antimonide (InSb) is also used for the SW case.

The performance of an infrared system is conventionally evaluated in terms of thermal sensitivity, scan speed, image resolution, and intensity resolution. The sensitivity is generally expressed as the Noise-Equivalent Temperature Difference (NETD) that represents the difference of temperature, at two points of the image, which corresponds to a signal equal to the background noise of the camera. Some new FPA systems are able to detect temperature differences of less than 20 mK at ambient temperature. The scan speed represents the rate at which a complete image is updated and, at least for old interlaced systems, is expressed as scan rate per line and scan rate per field; non-interlaced systems of the new generation are characterized by high acquisition speeds higher than 1600 Hz.

The image resolution, which is the capability of a system to measure the surface temperature of small objects, is generally defined as the Instantaneous Field of View (IFOV) of the detector. Actually, the thermal image is digitized into pixels smaller than the resolution element corresponding to the detector size. Modern systems are able to produce images composed of several tens of thousands of pixels. The intensity resolution, or dynamic range, is expressed in terms of the number of grey shades (or digital levels of intensity) of which the thermal image is composed. The latest generation of cameras provides 14-bit recording and allows small temperature variations to be distinguished in a very hot ambient environment.

The standard instantaneous output of each thermal image is generally represented by a matrix of data of the order of 20,000-60,000 elements or more; consequently, a treatment of the data by numerical techniques is compulsory. The temperature range which can generally be measured spans from -20°C up to $+1500^{\circ}\text{C}$, but it can be extended to higher values by using filters.

1.2.4.3 APPLICATIONS OF INFRARED THERMOGRAPHY IN THERMO-FLUID DYNAMICS

Infrared thermography has found application in many industries, included but not limited to medicine, agriculture, production processes, environmental technology, maintenance, non-destructive testing and turbomachinery. The focus here is the application of infrared thermography in thermo-fluid dynamics. Recent advances in infrared imaging systems allow for thermal images with high thermal and spatial

resolution to be obtained. In most thermo-fluid applications of infrared thermography the major goal is not an absolute measurement of temperature but the qualitative temporal and spatial distribution of thermal radiation intensity.

Since the mid-sixties, infrared thermography has been applied as a measurement technique. Primarily, this method was used in space missions where the protection of vehicles in the re-entry phase was of prime importance. In recent years thermography has become one of the most advanced non-intrusive measurement techniques.

When a solid is located in a flow, heat is transferred by means of convection, conduction, and radiation. Radiation heat transfer represents the main heat transfer mode, because it is directly measured by an infrared thermographic system. Under steady state conditions, the contribution of radiation is balanced by the convection heat transfer between the body and the fluid (Desideri et al., 2004). At each point where there is a temperature difference between the fluid and the body, convective heat transfer takes place according to the Newton's Law of Cooling

$$q'' = h(T_{sur} - T_{\infty}). \quad (1.21)$$

Since the heat transfer coefficient changes in laminar or turbulent flow, a different temperature will be measured after the flow transitions from laminar to turbulent (Gartenberg et al., 1989; Balageas and Bouchardy, 1993). This understanding is fundamental to the use of infrared thermography in fluid flow experimental studies. As a result of laminar-turbulent transition on the surface of solid body, it is possible to observe a detectable temperature gradient on the transitions borders, with different temperatures corresponding to the areas where turbulent or laminar conditions are present. This

allowed Desideri et al. (2004) to measure the heat transfer coefficient along an airfoil using infrared thermography.

Schulz (2000) used infrared thermography to perform a comprehensive film cooling study on the effectiveness of film cooling holes on gas turbine components. Two-dimensional mapping of the film cooling effectiveness in the near field of a single scaled-up film cooling hole with and without exit expansions were presented. Meola and Carlomagno (2004) provided a review of recent advances in the use of infrared thermography, particularly in thermo-fluid dynamics. In their paper, they presented the use of infrared thermography in the measurement and visualization of the diffusion of a hot water jet released into a stagnant water body. They also offered the visualization of jet impingement cooling, where they measured both the adiabatic wall temperature and the wall temperature using an infrared camera. The variation of the adiabatic wall temperature with the Mach number was presented as an infrared thermographic image. They also offered the visualization of a jet discharging normal to a cross-flow and the surface temperature mapping of aerodynamic bodies at an angle of attack using infrared thermography.

The non-intrusive, non-contact nature of infrared thermography makes it a very useful tool in the visualization of thermo-fluid flow fields. Polidori et al. (2003) used the technique to visualize the transient free convection from a vertical surface with mounted large scale obstacles and observed from their study that the thermal plumes measured with the infrared camera coincide exactly with the flow wake. Generally, measurement of heat flux rates, and/or of convection heat transfer coefficients from a surface to a stream, is more difficult to perform than other current thermo-fluid dynamic quantities. Astarita

et al. (2000) reviewed the use of infrared thermography in convective heat transfer measurement together with some particular aspects linked to its use. Ay et al. (2002) used thermography to monitor temperature distribution over a plate-fin surface inside the plate finned-tube heat exchanger. Following the temperature value identified at each pixel, the local convective heat transfer coefficients over the fins are determined by means of a control volume-based finite difference formulation. Astarita and Cardone (2008) used infrared thermography for flow visualization and the heat transfer measurement on a rotating disk, with a relatively small centered jet impinging upon it. From the infrared thermographic flow visualization, they observed a strong interaction between the turbulent jet and the laminar boundary layer over the rotating disk.

Infrared thermography was used for shear stress field measurement in flows by Malerba et al. (2006 a). Reynolds' Analogy was introduced with the possibility of using high sensitivity thermographic systems in order to analyze the distribution of shear stress on the surface of solid bodies immersed in fluid knowing the temperature of the examined body surfaces. Malerba et al. (2006 b) performed qualitative fluid-dynamic analysis of wing profile by thermographic technique.

A careful look at the literature demonstrates the great potential of infrared thermography for thermo-fluid visualization. Despite the widespread use of infrared thermography in surface flow visualization, few researchers have visualized the fluid flow field using infrared thermography. Narayanan et al. (2003) were among the first few researchers to use infrared thermography to visualize fluid flow using sulfur hexafluoride (SF_6) gas as tracer gas which has a high emissive peak in the infrared wavelength of the camera used. As far as the literature is concerned, little or no work has been done in using

infrared thermography to visualize a two-phase flow system like a spray. The current work seeks to exploit the potential of infrared thermography in the study and understandings of a two-phase system, particularly paint spray.

Copyright © Nelson K. Akafuah 2009

CHAPTER TWO

2.0 THEORETICAL FORMULATION

The second chapter discusses the theoretical formulation of the ultrasonic cavitation atomization, the infrared thermography-based characterization, and visualization technique developed in this dissertation. The chapter covers these mathematical formulations in two parts: Section 2.1 focuses on the theoretical formulation of vibratory cavitation and its influence on atomization. The second part of chapter two, specifically Section 2.2, covers the theoretical development of the use of infrared thermography in liquid spray characterization and visualization.

2.1 THEORETICAL STUDY OF CAVITATION

When a body of liquid is heated under constant pressure, or when its pressure is reduced at a constant temperature by static or dynamics means, an ultimate state is reached at which vapor or gas- and vapor-filled bubbles or cavities become visible and grow. The bubbles growth may be at a nominal rate if it occurs as the result of diffusion of dissolved gasses into the cavity or merely by expansion of the gas content with temperature rise or pressure reduction. Bubble growth will be “explosive” if it is caused primarily as the result of vaporization into the cavity. This condition is known as boiling if it is caused by temperature rise and cavitation if it is triggered by dynamic-pressure reduction at essentially constant temperature (Knapp et al., 1970).

The theory of cavitation cannot be discussed without a brief examination of the liquid and gaseous state. A simple kinetic theory understanding of the gaseous state is sufficient. However, for the liquid state a little more detailed discussion is necessary, and the next section offers a brief analysis of this topic.

2.1.1 SOME CONSIDERATION OF THE LIQUID STATE

In analyzing the liquid state, the approach by Brennen (1995) is followed. We will begin with typical phase diagrams, which though idealized, are relevant to many practical substances. Figure 2.1 shows typical graphs of pressure, p ; temperature, T , and specific volume, V , in which the state of the substance is indicated. The triple point is that point in the phase diagram at which the solid, liquid, and vapor states coexist; that is to say, the substance has three alternative stable states. The saturated liquid/vapor line (or binodal) extends from this point to the critical point. Thermodynamically it is defined by the fact that the chemical potentials of the two coexisting phases must be equal.

On the binodal line the vapor and liquid states represent two limiting forms of a single "amorphous" state, one of which can be obtained from the other by isothermal volumetric changes leading through intermediate but unstable states. Owing to this instability, the actual transition from the liquid state to the gaseous one and vice versa takes place, not along a theoretical isotherm (Figure 2.1 b), but along a horizontal isotherm (solid line) corresponding to the splitting up of the original homogeneous substance into two different coexisting phases (Frenkel, 1955). The critical point is that

point at which the maxima and minima in the theoretical isotherm vanish and the discontinuity disappears.

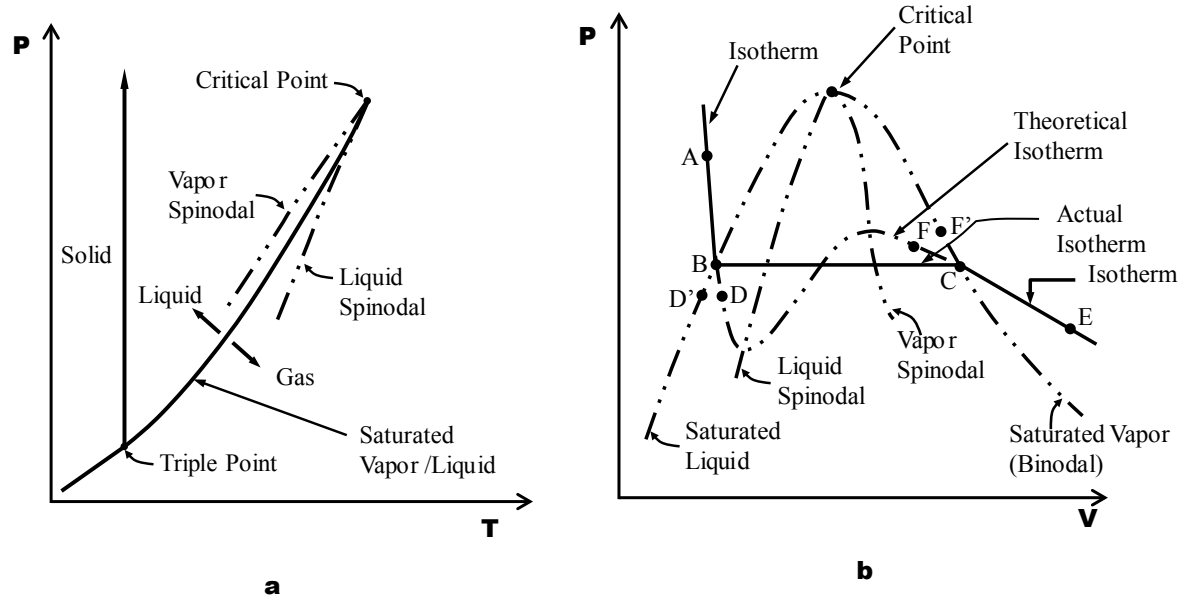


Figure 2.1: A typical phase diagram (Brennen, 1995).

The line joining the maxima in the theoretical isotherms is called the vapor spinodal line, and the line joining the minima is called the liquid spinodal line. Clearly both spinodals end at the critical point. The two regions between the spinodal lines and the saturated (or binodal) lines are of particular interest because the conditions represented by the theoretical isotherm within these areas can be realized in practice under certain special conditions. If, for example, a pure liquid at the state *A* (Figure 2.1 b) is depressurized at constant temperature, then several things may happen when the pressure is reduced below that of point *B* (the saturated vapor pressure). If sufficient numbers of nucleation sites of sufficient size are present the liquid will become vapor as

the state moves horizontally from B to C , and at a pressure below the vapor pressure, the state will come to equilibrium in the gaseous region at a point such as E . However, if no nucleation sites are present, the depressurization may lead to continuation of the state down the theoretical isotherm to a point such as D , called a “metastable state” since imperfections may lead to instability and transition to point E .

A liquid at a point such as D is said to be in tension, the pressure difference between B and D being the magnitude of the tension. Of course one could also reach a point like D by proceeding along an isobar from a point such as D' by increasing the temperature. Then an equivalent description of the state at D is to call it superheated and to refer to the difference between the temperatures at D and D' as superheat. In an analogous way one can visualize cooling or pressurizing a vapor that is initially at a state such as F and proceeding to a metastable state such as F' , where the temperature difference between F and F' is the degree of subcooling of the vapor.

2.1.2 THE PHENOMENON CALLED CAVITATION

As discussed in section 2.1.1, the tensile strength of a liquid can be manifested in at least two ways: one is boiling, and the other is cavitation. A liquid at constant temperature could be subjected to a locally decreasing pressure, p , which falls below the saturated vapor pressure, p_V . The value of $(p_V - p)$ is called the tension, Δp , and the magnitude at which rupture occurs is the tensile strength of the liquid, Δp_C . The process of rupturing a liquid by decrease in pressure at roughly constant liquid temperature is

termed as cavitation (Brennen, 1995). The degree of cavitation can be estimated with the aid of a non-dimensional parameter typically referred to as cavitation number, K .

$$K = \frac{p_{\infty} - p_v}{\frac{1}{2} \rho_L U_{\infty}^2} \quad (2.1)$$

where p_{∞} is the absolute static pressure at some reference location, p_v the vapor pressure, U_{∞} the reference velocity, and ρ_L the liquid density.

Any flow, whether cavitating or not, has some value of K . With reduction in K , the first occurrence of nucleation is incepted at some particular value of K called the incipient cavitation number (K_i). Further reduction in K below K_i causes an increase in the cavitation number and extent of vapor bubbles. Different types of cavitation are observed depending on the flow conditions and geometry. Major types of cavitation are: Traveling cavitation, fixed cavitation, vortex cavitation, and vibratory cavitation (Knapp et al., 1970; Furness and Hutton, 1975; Kubota et al., 1989).

2.1.3 INCEPTION OF CAVITATION AND TURBULENCE EFFECTS

Most flows are naturally turbulent and highly unsteady. Vortices occur because they are inherent in turbulence (Batchelor, 2000). This has important consequences for cavitation inception because the pressure in the center of a vortex may be significantly lower than the mean pressure in the flow (Brennen, 1995; Knapp et al., 1970). Although the cavitation number indicates the point at which some cavitation nuclei is expected to appear, in real circumstances the actual cavitation number might vary from the calculated cavitation number due to various factors (Kawanami et al., 1997).

In summary, there are a number of reasons for K_i (calculated) to be different from the value of K_c (actual) that might be calculated from the knowledge of the pressures in the single-phase liquid flow: (1) the existence of tensile strength can cause the reduction in K_i ; (2) the residence time effects can cause a reduction in K_i ; (3) the existence of contaminant gas can cause an increase in K_i ; (4) the steady viscous effect as a result of the dependency of K_c on Re can cause K_i to be a function of Re , and (5) the turbulence effects, characterized by highly random flow velocity components, augments K_i (Brennen, 1995).

If it were not for these effects, the prediction of cavitation would be a straightforward matter of determining K_c . Unfortunately, these effects can cause large departures from the criterion, $K_i=K_c$, with important engineering consequences in many applications. Furthermore, the above discussion identifies the parameters that must be controlled or at least measured in systematic experiments on cavitation inception (Brennen, 1995): (1) the cavitation number, K_c ; (2) the Reynolds number, Re ; (3) the liquid temperature, T_∞ , (4) the liquid quality-details of free stream nuclei available, dissolved gas component etc., and (5) the quality of the solid surfaces such as its roughness, pit population, porosity etc contributes to variation in cavitation inception.

Since this is a tall order, and many of the effects such as the interaction of turbulence and cavitation inception have only recently been identified (Brennen, 1995), it is not surprising that the individual effects are not readily isolated from many of the experiments performed in the past. Nevertheless, some discussion of these experiments is important for practical implementations in many fluidic devices. With this fundamental

background on cavitation, we continue to identify the subsequent dynamics of bubble growth and collapse.

2.1.4 EQUATION OF CAVITATION BUBBLE DYNAMICS

The dynamics of bubble growth and collapse are covered in detailed in the literature (Brennen, 1995; Knapp et al., 1970). The dynamics of the motion of the bubble is characterized to a first approximation by the Rayleigh-Plesset Equation. A generalized Rayleigh-Plesset Equation derived from the Navier Stokes Equation for a Newtonian liquid is given by:

$$R \frac{d^2 R}{dt^2} + \frac{3}{2} \left(\frac{dR}{dt} \right)^2 = \frac{p_B(R) - p_\infty(t)}{\rho_L} - \frac{4\nu_L dR}{Rdt} - \frac{2S}{\rho_L R} \quad (2.2)$$

where R is the radius of the bubble; P_∞ is the pressure at a reference location far from the bubble; P_B the pressure of the bubble; ν_L is the kinematic viscosity of the liquid; ρ_L the density of the liquid, and S is the liquid surface tension.

2.1.5 INFLUENCE OF OSCILLATING PRESSURE FIELDS

The response of a bubble to a continuous oscillating pressure field has been extensively covered in the literature (Neppiras and Noltingk, 1950, 1951; Flynn, 1964; Plesset and Prosperetti 1977; Crum, 1979; Neppiras, 1980; Prosperetti, 1982, 1984; Young, 1989). Frequently, vapor/gas bubbles are found immersed in a fluid flow environment. The translatory motion of the bubble affects its response to the local

pressure fluctuations by either increasing the energy content or by draining it. Various other parameters associated with flow field characterization such as vorticity and gradients impose severe constraints on the bubble dynamics (Brennen, 1995; Knapp et al., 1970). In the presence of oscillating pressure waves generated by an acoustic field, existing bubbles or cavities are subjected to both expansion and contraction (Neppiras, 1980).

To formulate the effects of oscillating pressure fields on a bubble, it is assumed that the bubble is filled with permanent gas obeying the ideal gas law $p(4\pi R^3/3) = nRT$. Ignoring the heat and mass transfer across the bubble interface, we can use the adiabatic relation $p(4\pi R^3/3)^\gamma = \text{constant}$ and $p_B(R) = (p_a + 2S/R_o)(R_o/R)^{3\gamma}$, since at $t = 0$ where $R = R_o$, the gas pressure in the bubble is just $(p_a + 2S/R_o)$. Equation 2.2 then becomes:

$$R \frac{d^2 R}{dt^2} + \frac{3}{2} \left(\frac{dR}{dt} \right)^2 = \frac{1}{\rho_L} \left[\left(p_a + \frac{2S}{R_o} \right) \left(\frac{R_o}{R} \right)^{3\gamma} - \frac{4\mu_L dR}{Rdt} - \frac{2S}{R} - p_\infty(t) \right]. \quad (2.3)$$

In the presence of an oscillating pressure field, the external liquid pressure at infinity, p_∞ , is modified to carry an added ultrasonic pressure wave such that

$$p_\infty = p_a - p_o \sin \omega t \quad (2.4)$$

where p_o is the amplitude of ultrasonic pressure wave with a frequency of $\omega/2\pi$ superimposed on a pressure field p_a . Substituting Equation (2.4) into (2.3) we obtain

$$R \frac{d^2 R}{dt^2} + \frac{3}{2} \left(\frac{dR}{dt} \right)^2 = \frac{1}{\rho_L} \left[\left(p_a + \frac{2S}{R_o} \right) \left(\frac{R_o}{R} \right)^{3\gamma} - \frac{4\mu_L dR}{Rdt} - \frac{2S}{R} - (p_a - p_o \sin \omega t) \right]. \quad (2.5)$$

Equation (2.5) without the viscous term was first derived by Noltingk and Neppiras (1950, 1951); the viscous term was later investigated by Poritsky (1952). Equation 2.3 and 2.5 are valid for an isothermal condition in which case $\gamma = 1$.

To investigate how a bubble will grow and collapse under an oscillating pressure condition, a simple inviscid, isothermal case was considered following the approach by Noltingk and Neppiras (1950). For the inviscid and isothermal condition, Equation 2.5 becomes

$$R \frac{d^2 R}{dt^2} + \frac{3}{2} \left(\frac{dR}{dt} \right)^2 = \frac{1}{\rho_L} \left[\left(p_a + \frac{2S}{R_o} \right) \left(\frac{R_o}{R} \right)^3 - \frac{2S}{R} - (p_a - p_o \sin \omega t) \right]. \quad (2.6)$$

Equation 2.6 is solved with imposed angular frequencies (ω) of 3×10^7 and 9×10^7 . The mean pressure, p_a , is taken as 10^5 Pa with an initial bubble size of $80 \mu\text{m}$. The liquid under investigation is water at Standard Temperature and Pressure (STP). The results were obtained numerically by Srinivasan (2006) shown in Figure 2.2. Similar results were earlier obtained by Neppiras and Noltingk, (1951).

The influence of the bubble's initial radius on its dynamics is also investigated where the frequency of imposed oscillation is maintained constant along with other liquid and vapor parameters. Since, no collapse was observed with a frequency of $\omega = 9 \times 10^7$ (Figure 2.2), this frequency value is assumed while two initial bubble radii $R_o = 80$ and $100 \mu\text{m}$ are used. The calculated results are shown in Figure 2.3. Notice from Figure 2.3, that a small change in the initial radius of the bubble results in an out of phase peaking of the bubble radius. This portrays the complex behavior of bubble mixtures wherein a wide range of bubble sizes exist and mutually affect one another.

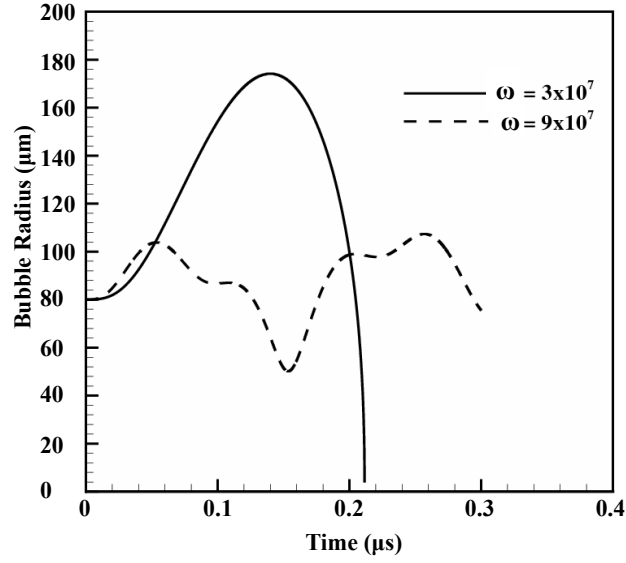


Figure 2.2: A radius-time curve of the influence of imposed perturbation frequency on a gas-filled bubble.

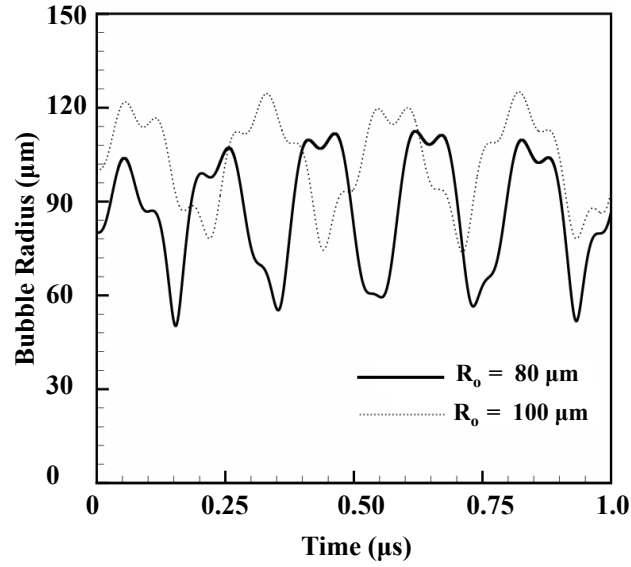


Figure 2.3: A radius-time curve of the influence of initial bubble radius on the vapor bubble dynamics.

For the frequency of 3×10^7 in Figure 2.2, events of collapse occur within $0.2 \mu\text{s}$ while with increase in the frequency of the pressure wave, the collapse is averted and a non-linear bubble evolution behavior is obtained. Neppiras and Noltingk, (1951) inferred

that for each impressed frequency on the pressure wave there exists a maximum bubble size that can give rise to cavitation. As the frequency is raised, they concluded, this limit becomes smaller and smaller. As a result of this, by sufficiently increasing the ultrasonic frequency, with other parameters remaining the same, the expected intensity of cavitation can be reduced to vanishing point (Brennen, 1995). For the imposed pressure wave frequency $p_o \ll p_a$, Neppiras and Noltingk, (1951) derived the resonant frequency of the bubble, f , as

$$(2\pi f)^2 = \frac{3\gamma(p_a + 2S/R_o)}{\rho R_o^2} \quad (2.7)$$

where γ is the polytropic constant. With a wide range of computations performed using different bubble equilibrium radii and pressure wave parameters, Neppiras and Noltingk, (1951) concluded that the pressure field, p , is fundamentally governed by the ultrasonic amplitude, p_o . In this configuration, p_B is the pressure of the gas inside the bubble at its maximum radius, with an initial bubble radius R_o . They showed that the maximum bubble radius reached during the evolution of the cavitation bubble is inversely proportional to the imposed angular frequency ω . Following this, all cavitation effects will be expected to fall off with increasing frequency and disappear completely in the range

$$f = \frac{1}{2\pi R_o} \left[\frac{3\gamma}{\rho} \left(p_a + \frac{2S}{R_o} \right) \right]^{\frac{1}{2}}. \quad (2.8)$$

The response of the vapor/gas bubbles to perturbations in the surrounding pressure fields vary as a function of the magnitude of such fluctuations. As a result of the

nonlinearities in the governing equations, particularly the Rayleigh-Plesset Equation 2.2, the response of a bubble will begin to be affected by these nonlinearities as the amplitude of oscillation is increased (Feng and Leal, 1997). A given set of operating parameters, such as the pressure difference across the bubble, the equilibrium radius, and the properties of the liquid and vapor (such as surface tension, viscosity etc.), determine the frequency ranges in which the bubble response would be critical (Neppiras and Noltingk, 1951). Considering the viscous effects, the peak frequency is calculated as

$$\omega = \left[\frac{3\gamma(p_\infty - p_v)}{\rho_L R_E^2} + \frac{2(3\gamma - 1)S}{\rho_L R_E^3} - \frac{8\nu_L^2}{R_E^4} \right]^{\frac{1}{2}} \quad (2.9)$$

where R_E is the bubble equilibrium radius.

The bubble peak frequency is an important quantity in any bubble dynamic problem. From Equation 2.10, it is clear that for larger bubbles the viscous terms become negligible, and the peak frequencies are driven by the pressure difference term. Typical peak frequencies for a water bubble, under varying equilibrium radii are plotted in Figure 2.4 (Brennen, 1995).

For no damping, neglecting viscous effects, the natural angular frequency of oscillations of the bubbles is given by

$$\omega_n = \left[\frac{1}{\rho_L R_E^2} \left(3\gamma(p_\infty - p_v) + 2(3\gamma - 1) \frac{S}{R_E} \right) \right]^{\frac{1}{2}}. \quad (2.10)$$

In the range of typical nuclei found in water (1-100 μ m), the natural frequencies are of the order 5-25 kHz. For example, if a given sample of water requires cavitation

using an imposed acoustic pressure field, then the frequencies that will be most effective in producing a substantial concentration of large cavitation bubbles will be in the frequency range as demonstrated in the Figure 2.4.

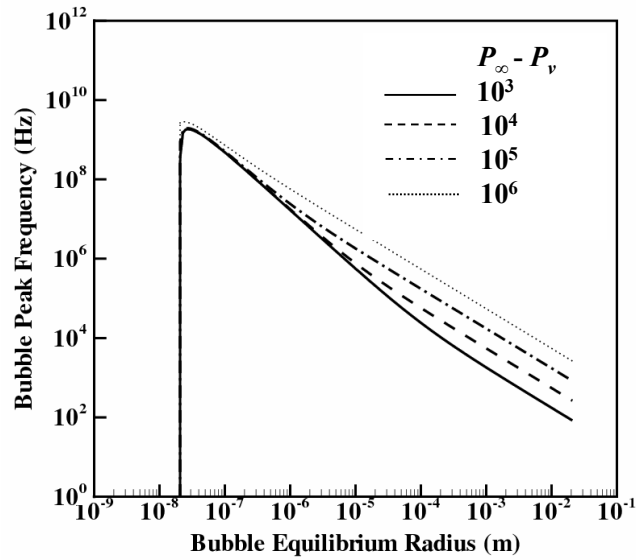


Figure 2.4: The bubble resonant frequency in water at 300K (Brennen, 1995).

2.1.6 ULTRASONIC CAVITATION ATOMIZATION

This section discusses the mechanism of cavitation collapse energy generated as a result of imposed ultrasonic pressure oscillation in the disintegration of a liquid jet. As discussed in earlier sections, cavitation collapse energy is known to significantly influence the disintegration of a liquid jet. Hence, an atomizer that uses this mechanism for atomization is considered. In designing such an atomizer, two components must be carefully considered. These are the design of the ultrasonic horn and the interior nozzle geometry that houses the ultrasonic horn. The design of these two components is important to ensuring the cavitation cluster generation, growth, and collapse in a manner

that assist the liquid jet disintegration without detrimental effects on the nozzle wall material.

The ultrasonic horn motion creates a low pressure region at the horn tip, depending on its location, which results in the activation of cavitation nuclei. The design of the nozzle interior geometry is crucial in maintaining a sufficient low pressure region for the growth of cavitation nuclei. The cavitation bubbles, once generated at the horn tip, are convected by the accelerating liquid flow toward the nozzle exit. The bubbles collapse on reaching the nozzle exit because of the increased pressure content in the nozzle exterior environment. In the near nozzle exit regions, the pressure perturbations generated by collapsing cavitation bubbles act as a strong deformation force within the liquid jet against the liquid surface tension forces, resulting in the enhancement of the atomization of the liquid.

The design concept is illustrated in Figure 2.5, where the initial forward motion of the ultrasonic horn tip (Figure 2.5a) followed by a sudden retraction (Figure 2.5b) creates a low pressure region at the ultrasonic horn tip. This low pressure region, if it falls below the vapor pressure of the liquid, causes the creation of cavitation nuclei. The subsequent forward motions of the horn (Figure 2.5c) together with the accelerating liquid flow, sweeps the cavitation bubble toward the nozzle exit. The converging nozzle ensured the acceleration of the liquid assisting the transport of the cavitation nuclei toward the nozzle exit. The bubble cluster upon reaching the nozzle exit grows and implodes as a result of the increased pressure on the nozzle exterior environment. This implosion generates the pressure wave which increases the turbulence in the liquid jet and thus assists its disintegration.

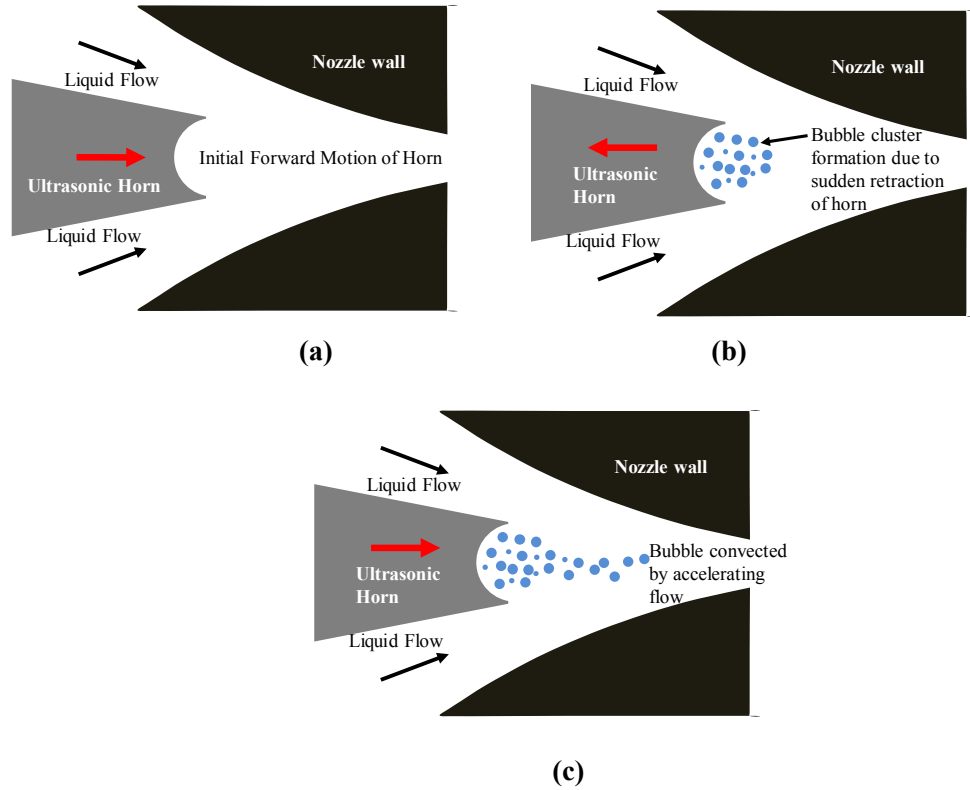


Figure 2.5: Cavitation cluster generation at ultrasonic horn tip: (a) initial forward motion of the horn, (b) sudden retraction of the horn, and (c) forward motion of the horn.

2.1.6.1 THE ULTRASONIC HORN

The ultrasonic horn is a critical component of the new atomizer design. The details of the ultrasonic horn design are shown below. The following are considered and presented: the ratio of the horn tip diameter to the horn stroke length, the horn tip position relative to the nozzle exit, the horn tip frequency, the shape of the horn surface, the amplitude of the horn motion, and the shape of the horn.

2.1.6.1.1 RATIO OF HORN TIP DIAMETER TO HORN STROKE LENGTH

The ratio of the horn tip diameter to the amount of displacement it performs has a profound influence on the cavitation dynamics and the flow structure. For a given displacement magnitude by the horn tip at any instant of time, the volume of liquid displaced per unit time is proportional to the square of the frontal horn surface diameter times the displacement. The fluctuation in flow rate influences the flow turbulence and velocity relaxation at the nozzle exit.

The behavior of the two-phase flow mixture, developed as a result of the presence of the cavitation bubbles, is highly stochastic (Brennen, 1995). From a numerical parametric study (Srinivasan, 2006), a horn tip diameter of 150 μm with a stroke length of 20 μm operating at a maximum frequency of 60 kHz, or a stroke length of 40 μm operating at 30 kHz, was considered to be the optimum operating condition for cavitation cluster generation. This gives the ratio of horn tip diameter to horn stroke length of 7.50 and 3.75 for frequencies of 60 kHz and 30 kHz respectively.

2.1.6.1.2 POSITION OF THE HORN RELATIVE TO THE NOZZLE EXIT

The nominal location of the horn tip inside the nozzle has a dominating influence on the translation of cavitation bubble clusters. Besides altering the cavitation dynamics, the relative position of the horn also carries with it the ability to control the pressure pulse propagation superimposed on the fluid flow pressure (Hansson and Morch, 1979; Kedrinskii, 1993). That is, the closer that the movement the horn is towards the nozzle

exit, the greater the influence it will have on the jet modulation as compared to moving it farther away because of the dissipation process.

It should be noted that the presence of the horn in the flow region inside the nozzle acts as a constriction to the free flowing liquid. And, moving the horn closer to the nozzle exit will decrease the effective area of cross section available for the flow to reach the exit, and hence, severe vortex structures may be triggered in addition to high velocities accompanied by rapidly changing flow rate due to horn motion. This effective change in flow structure changes the pressure fields which is tightly coupled to the cavitation dynamics. To obtain favorable conditions for cavitation cluster generation, the oscillating horn tip is placed at a position within the nozzle where the horn surface takes approximately one-third of the flow cross-sectional area.

2.1.6.1.3 FREQUENCY OF OSCILLATING HORN

The frequency of oscillation of the horn tip is very critical not only in controlling the bubble population but also in achieving the necessary perturbation to be imposed on the liquid jet. The magnitude of the frequency summarizes the amount of energy that is being supplied to the liquid to create the cavitation regions. Increasing the frequency directly relates to the increase in the energy applied to overcome the cohesive liquid forces leading to cavitation bubble cluster (Hansson and Morch, 1979 a, b; Kedrinskii, 1993; Hansson et al., 1982).

The compressibility of the two-phase medium is determined mainly by the compressibility of the gas phase, and the nonlinearity of the process is due to the bubble

dynamics. It is, therefore, appropriate to simplify the system of equations assuming further that the liquid is incompressible, and the number of bubbles per unit volume is constant. By neglecting the nonlinear terms in the mass conservation and the momentum equations, then the momentum equation for a one-dimensional two-phase medium can be written as

$$\frac{\partial u}{\partial t} + \frac{1}{\rho} \frac{\partial P}{\partial x} = 0. \quad (2.11)$$

If the motion of the horn is sinusoidal, the pressure gradient relates to the angular frequency as

$$\rho \frac{\partial P}{\partial x} = ap_h = \Gamma \omega^2 \sin(\omega t) \quad (2.12)$$

where ρ is the density; ap_h is the horn acceleration; Γ is the amplitude, and $\omega = 2\pi f$, where f is the frequency of the oscillating horn.

2.1.6.1.4 SHAPE OF THE HORN SURFACE

According to the discussions on the cavitation generation techniques, the bubble population is substantially enhanced if the energy of the oscillations is well focused in a given area. This is achieved by use of concave surface at the tip of the oscillating horn. Horn surface concavity increases the power density of the bubble formation (Vijay, 1992) and enhances high frequency pulsing to the liquid downstream.

2.1.6.1.5 AMPLITUDE OF THE HORN MOTION

Another critical parameter in the present design is the horn amplitude which directly dictates the amplitude of transient pressure field, the bubble population, and hence the droplet size distribution. From Equation (2.12), note that the pressure gradient is governed in a linear fashion by the horn amplitude. Increased amplitude results in formation of extended vapor region and consequent convection downstream. Amplitude, in conjunction with the frequency, is decisive in designing the horn tip to enhance cavitation. Designs with high amplitude of oscillation can lead to intensified cavitation regions (Hansson and Morch, 1979 a; Kedrinskii, 1993).

2.1.6.1.6 SHAPE OF THE HORN

Ultrasonic horns can be classified into exponential, catenoidal, conical, parabolic, hyperbolic, and stepped forms according to the decreasing rate of their cross sectional area (Woo et al., 2006). The solid ultrasonic horn acts as a vibration amplifier. Catenoidal and exponential shaped horns have been considered for such designs as the one by Vijay (1992). The ultrasonic horn increases the power density of the transducer. For the prototype in this work, a parabolic horn shape was employed.

2.1.6.2 THE INTERIOR NOZZLE GEOMETRY

The axial cross section of the nozzle interior geometry is illustrated in Figure 2.6. The cross section shows schematics of the converging section and the backward facing

step section of the nozzle. The residence chamber and the flow modulation inducer are illustrated in Figure 2.7.

The expansion chamber of the nozzle section acts as a residence chamber where the cluster is formed, and its subsequent transient evolution occurs. This residence chamber seeks to increase the cavitation cluster mixing with the bulk flow, a straightforward consequence of utilizing the backward facing step profile (Armaly et al., 1983). The increased turbulent production and increased shear layer contribution increases the perturbations within the liquid-vapor mixture flow which is then accelerated using a flow modulation inducer section, Figure 2.7.

Figure 2.6: The nozzle interior geometry.

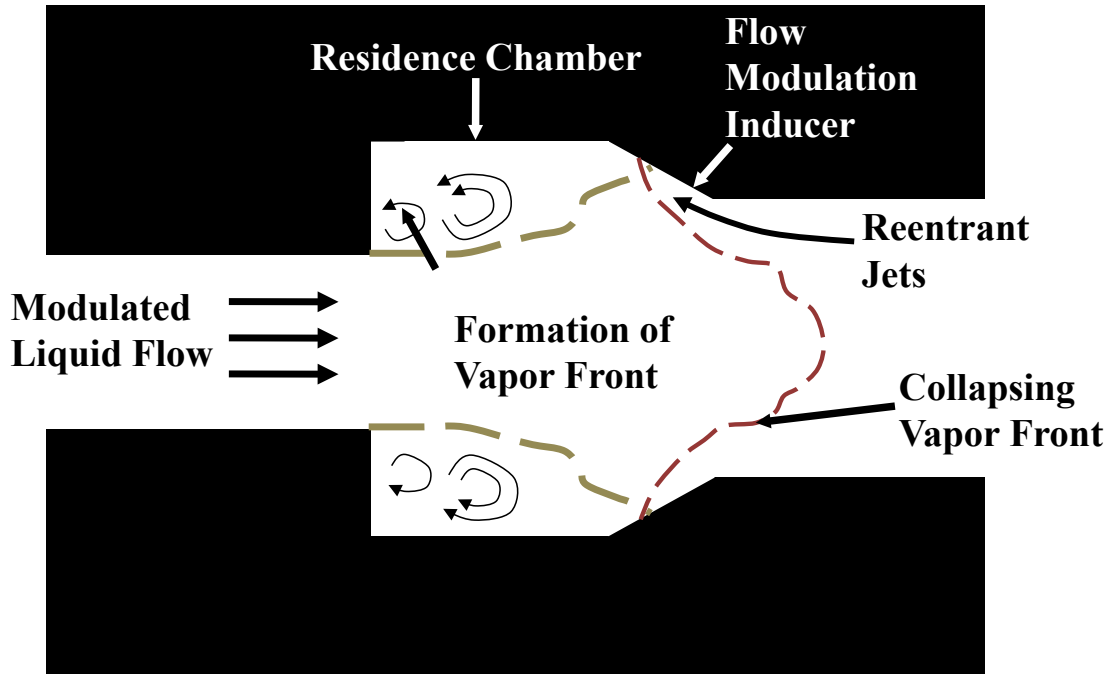


Figure 2.7: A concept of residence chamber.

There are two competing forces acting on the mixture flow near the entrance of the flow modulation inducer: the impingement of the cavitating liquid increases the stagnation pressure leading to the collapse of the vapor clusters and at the same instant, the flow modulation region acts against this pressure increase by accelerating the fluid. As a result of these dominating mechanisms, some cavitation clusters survive the expansion section and propagate into the constant diameter section. Meanwhile, because of the geometric curvature, a strong reverse pressure gradient acts near the corners of the section joining the flow modulation inducer and the constant diameter chamber leading to the separation of cavitation clusters from the nozzle walls (Armaly et al., 1983). Hence, the concentration of cavity clusters into the core of the bulk flow is achieved.

Mechanisms of vortex stretching and rollup contribute to the mixing of the vapor phase with the main liquid flow leading to increased perturbation of the exiting liquid jets (Armaly et al., 1983; Barkley et al, 2002). The presence of cavitation within a turbulent shear flow can potentially alter the dynamics of the flow through both local and global methods. The existence of developed cavitation can lead to overall flow changes through a reduction in mean flow density, an increase in the overall flow volume, or as a result of the modification of the mean pressure field.

Cavitation can also modify the vortical flow locally (Baur and Kongeter, 1998). Belahadji et al. (1995) have suggested that cavitation in the cores of vortices will affect the process of vortex stretching by the decoupling of the vortex strain and rotation rate. Gopalan and Katz (2000) demonstrated that significant flow–vapor interactions exist in the cavitating shear flow downstream of a partial cavity. Furthermore, Laberteaux and Ceccio (2001 a, b) showed how the growth and collapse of dispersed cavitation bubbles lead to the production of small-scale turbulence in the wake of partial cavities.

2.1.6.3 LIQUID PARAMETERS

The formation of cavitation bubbles within the liquid is greatly dependent on the type of liquid. This results from the cavitation mechanism which is greatly influenced by the liquid parameters such as its viscosity, surface tension, compressibility effects, solid contents, miscibility of components, and the specific rheological and dynamic behavior of a liquid. The elementary concept of cavitation inception is the formation of cavities at the instant the local pressure drops to the vapor pressure of the liquid. But, there are

deviations of various degrees with both water and other liquids that are not reconcilable with the vapor-pressure concept (Knapp et al., 1970).

The vapor pressure is defined as the equilibrium pressure at a specific temperature of the liquid's vapor which is in contact with an existing free surface. If a cavity is to be created in a homogeneous liquid, the liquid must be ruptured, and the stress required to do this is not measured by the vapor pressure but the tensile strength of the liquid at that temperature. Consequently, it is important that the parameters of the liquid under investigation are well known.

2.2 MATHEMATICAL TREATMENT OF INFRARED SPRAY VISUALIZATION AND CHARACTERIZATION

The Infrared thermography-based visualization and characterization technique introduced in this dissertation is an optical method which uses infrared imaging to characterize and visualize the entire flow field of a liquid spray. The technique employs an emitter which is a uniformly heated blackbody background as a thermal radiation source, and a receiver which is an infrared detector. The method provides a two-dimensional image in which the value is associated to each pixel on an intensity scale. This value accounts for the amount of infrared energy emitted by the source which then travels through the spray. As a result of the presence of the spray, the infrared energy emitted by the source is attenuated.

For a given fluid, this attenuation is a function of droplet size, spray density, and the complex refractive index ($m = n - ik$) of the material being sprayed. The infrared

detector, therefore, receives a damped signal as a result of the attenuation of the emitter intensity. This damped image is recorded to provide an attenuation image of the spray. This image is post-processed using theoretical and empirical equations to extract information about the spray volume fraction, number density, and macroscopic information.

2.2.1 THE RADIATION MODEL

In this section, consider a spray visualization system consisting of a radiative source of uniform or known intensity distribution and a camera or similar device capable of detecting the attenuation of the radiative intensity caused by the presence of any obstacle within a certain wavelength range. Radiative intensity is defined as radiative energy transferred per unit time, solid angle, spectral variable, and area normal to the pencil of rays. This radiative energy travels in the form of electromagnetic waves with a certain wavelength. The camera detects the attenuation of the radiative energy as it travels through a participating media consisting of a liquid spray made up of droplets with a certain size distribution. The spray is generated by a nozzle or similar atomization device. A schematic of the concept is shown in Figure 2.8.

The scattering and absorption coefficients of a group of droplets are directly related to the droplet number density and their effective cross-sectional areas. These effective areas are called the scattering and absorption cross-sections, $C_{sca\lambda}$ and $C_{abs\lambda}$ (Tien and Drolen, 1987). Generally $C_{sca\lambda}$ and $C_{abs\lambda}$ are a function of the particle orientation, the complex refractive index ($m = n - ik$), the particle size relative to the

wavelength, and the polarization of the incoming radiative beam. It is assumed that the bulk of the spray is made up of spherical droplets, and orientation is of no concern. Likewise, only unpolarized light is considered since this is a good approximation for most heat transfer processes (Tien and Drolen, 1987).

Considering the microscopic view of the spray, an electromagnetic wave or photon passing through the immediate vicinity of spherical particles or droplets will be absorbed, scattered, or both. The scattering is attributable to three separate phenomena namely diffraction, reflection at the particle surface, and refraction in a particle. Figure 2.9 illustrates the interaction between electromagnetic waves and spherical particles (Modest, 1993).

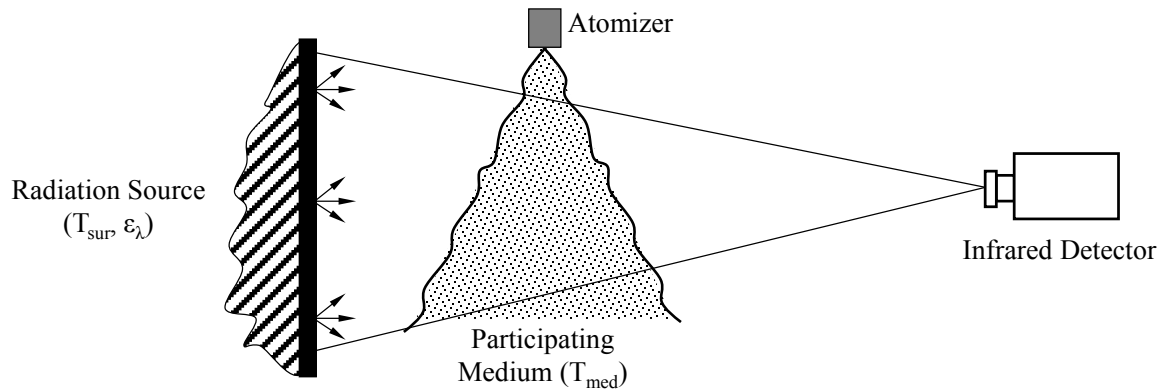


Figure 2.8: A schematic of the infrared visualization model.

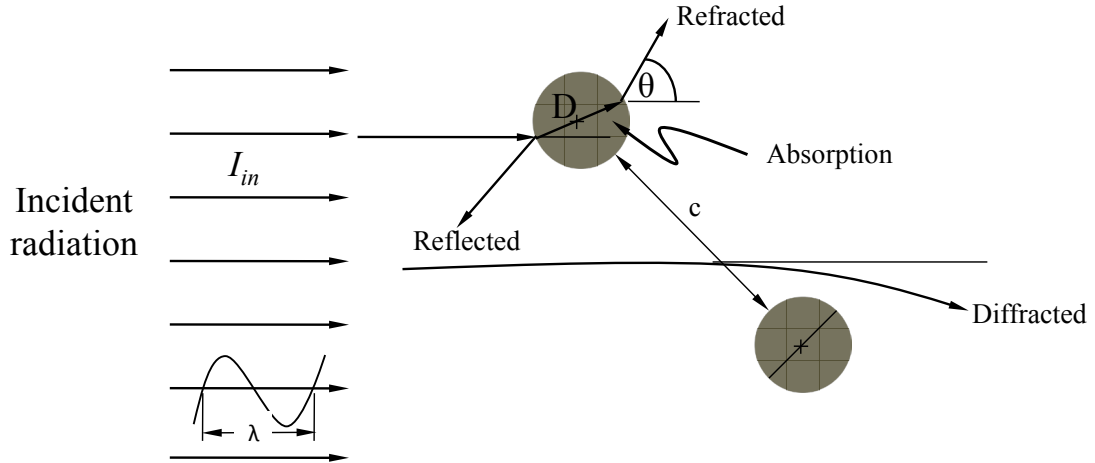


Figure 2.9: The Interaction between Electromagnetic Waves and Spherical Particles (Modest, 1993).

2.2.1.1 INFRARED RADIATION FORMULATION

It is now appropriate to focus attention upon the incoming radiant beam with intensity $I_{in\lambda}$ impinging upon an absorbing, emitting, and scattering particulate medium. As the beam traverses the medium, its intensity is attenuated by absorption and by out-scattering of energy into other directions. The intensity of the beam is enhanced by the in-scattering of radiation from other directions into the direction of propagation or by emitted energy from the particles. The variation of intensity in the medium is described by the equation of transfer (Siegel and Howell, 2001),

$$\frac{dI_{\omega\lambda}(s)}{ds} = -a_{\lambda}I_{\omega\lambda}(s) + a_{\lambda}I_{\omega\lambda b}[s, T(s)] - \sigma_{\lambda}I_{\omega\lambda}(s) + \frac{\sigma_{\lambda}}{4\pi} \int_{4\pi} I_{\omega\lambda}(s) \Phi_{\lambda}(\omega_i \rightarrow \omega) d\omega_i \quad (2.13)$$

where $I_{\omega\lambda}$ is the directional spectral intensity; s is the distance traveled in the medium, and a_λ and σ_λ are the absorption and scattering coefficients, respectively. Equation (2.13) also includes the emitted energy of the particles $I_{\omega\lambda b}$, from the Planck's Distribution evaluated at the particle temperature T , and the scattering phase function from direction ω_i into the direction ω , $\Phi_\lambda(\omega_i \rightarrow \omega)$. By introducing the definitions of the optical thickness τ_λ and the scattering albedo Ω_λ the following expressions are obtained

$$\tau_\lambda = \int_0^s (\sigma_\lambda + a_\lambda) ds, \quad \Omega_\lambda = \frac{\sigma_\lambda}{\sigma_\lambda + a_\lambda}. \quad (2.14)$$

The equation of radiative transfer, Equation (2.13), can be rewritten as:

$$\frac{dI_{\omega\lambda}(\tau_\lambda)}{d\tau_\lambda} = -I_{\omega\lambda}(\tau_\lambda) + (1 - \Omega_\lambda) I_{\omega\lambda b}[\tau_\lambda, T(\tau_\lambda)] + \frac{\Omega_\lambda}{4\pi} \int_{4\pi} I_{\omega\lambda}(\tau_\lambda) \Phi_\lambda(\omega_i \rightarrow \omega) d\omega_i. \quad (2.15)$$

Appropriate boundary conditions have to be introduced in order to make the formulation complete and well posed. Transparent boundaries are assumed at all sides of the problem. On the face radiated by the main source, a known diffuse irradiation may be taken into account (Collin et al., 2005)

$$I_{\omega\lambda}(\tau_\lambda = 0) = I_{0\lambda}(\omega). \quad (2.16)$$

Throughout the rest of the analysis we make the simplifying assumptions that the local emission of and the scattering of the electromagnetic waves into the direction of propagation is negligible. We also assume that there is no evaporation of the liquid droplets. The vapor phase attenuation is neglected in our analysis. Under these

assumptions, the source term in Equation (2.15) is negligible. Thus, the equation of transfer reduces to:

$$\frac{dI_{\omega\lambda}(\tau_\lambda)}{d\tau_\lambda} = -I_{\omega\lambda}(\tau_\lambda). \quad (2.17)$$

The solution of Equation (2.17) with boundary condition Equation (2.16) becomes

$$I_\lambda(\tau_\lambda) = I_{0\lambda}(0) \exp(-\tau_\lambda). \quad (2.18)$$

This indicates that the intensity of the propagating beam simply decays exponentially with optical distance travelled. Solving for the optical thickness from Equation (2.18) yields

$$\tau_\lambda = -\ln\left(\frac{I_\lambda(\tau_\lambda)}{I_{0\lambda}(0)}\right). \quad (2.19)$$

Thus, the optical thickness in the direction of propagation can be computed based on the attenuation of the radiative intensity acquired by the detector.

2.2.1.2 TWO-DIMENSIONAL INFRARED IMAGE ANALYSIS

When a captured two-dimensional digital image of a spray showing the attenuation of the radiant intensity is examined as a result of the presence of the spray droplets, the image contains a finite sequence of pixels $p(x, y)$, for $1 \leq x \leq N_x$ and $1 \leq y \leq N_y$, where N_x and N_y are the number of pixels in the x - and y - directions, respectively. The pixel size is $\Delta x \Delta y$, where Δx and Δy are usually constant throughout the image and may

be equal (i.e. $\Delta x = \Delta y$). Each pixel $p(x, y)$ is a two-dimensional view of an attenuation volume $\phi(x, y)$ with an effective attenuation depth $b(x, y)$, corresponding to the depth of the spray in a direction normal to the image at the location of the pixel $p(x, y)$. Therefore, the dimensions of each attenuation volume or voxel can be expressed as $\Delta x \Delta y b(x, y)$ (Figure 2.10). Within each attenuation volume, there exists a finite number of droplets $n(x, y)$ with a corresponding droplet size distribution.

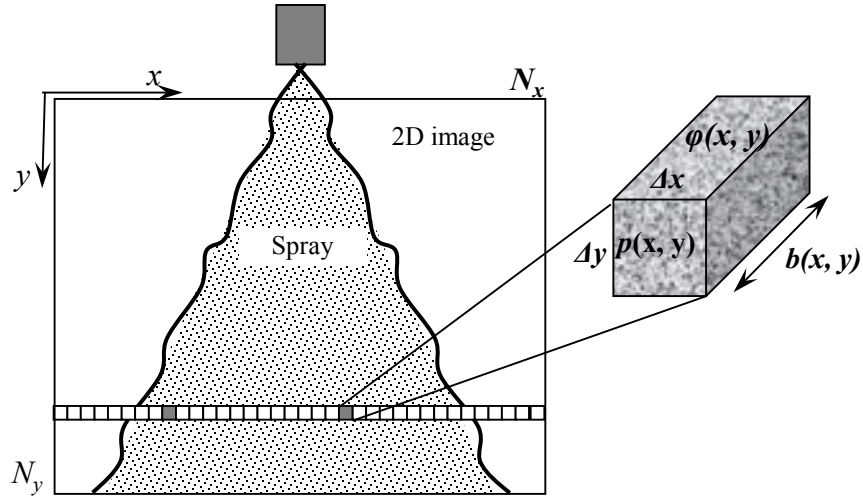


Figure 2.10: A schematic of the attenuation map of the spray.

It is assumed that the attenuation of the Infrared energy in the air surrounding the spray is negligible. That is, the attenuation of the rays occurs only within the attenuation volume $\phi(x, y)$. The optical thickness defined in Equation (2.14) is rewritten in terms of the extinction coefficient $\kappa_\lambda(x, y)$ as:

$$\tau_\lambda(x, y) = \int_0^{b(x, y)} (\sigma_\lambda(x, y) + a_\lambda(x, y)) d\zeta = \int_0^{b(x, y)} \kappa_\lambda(x, y) d\zeta. \quad (2.20)$$

Equation (2.20) can be integrated to yield the optical thickness expressed in terms of the effective extinction coefficient $\bar{\kappa}_\lambda(x, y)$ and the physical path length $b(x, y)$ as follows:

$$\tau_\lambda(x, y) = \int_0^{b(x, y)} \kappa_\lambda(x, y) d\mathfrak{s} = \bar{\kappa}_\lambda(x, y) b(x, y). \quad (2.21)$$

Despite the fact that the droplets in the integration path $b(x, y)$ exhibit a size distribution and can be concentrated unevenly along it, the effective extinction coefficient $\bar{\kappa}_\lambda(x, y)$ is considered independent on both the droplet size distribution and the droplet concentration. Therefore, the extinction coefficient can be expressed as:

$$\bar{\kappa}_\lambda(x, y) = \begin{cases} \frac{\tau_\lambda(x, y)}{b(x, y)} & \text{for } b(x, y) \neq 0 \\ 0 & \text{for } b(x, y) = 0 \end{cases}. \quad (2.22)$$

The scattering and absorption coefficients are defined as the fraction of the total propagating energy which is scattered out of, or absorbed from, a radiant beam per length of travel, respectively. The scattering and absorption coefficients of a group of particles (or droplets) as presented by Tien and Drolen (1987) are directly related to the number density of these particles (or droplets) and their effective cross-sectional areas. These effective areas are called the scattering and absorption cross-sections, $C_{scal}(x, y)$ and $C_{abs\lambda}(x, y)$.

The size parameter χ , is defined as the ratio between the droplet circumference and the light wavelength, i.e., $\chi = \pi D_m / \lambda$. The geometric cross section of the droplet m is given by $G_m(x, y) = \pi D_m^2(x, y) / 4$. For $\chi > 10$, light scattering can be approximated by

geometric optics (Van de Hulst, 1981), the extinction cross-section, which is the sum of $C_{sca\lambda}(x, y)$ and $C_{abs\lambda}(x, y)$, which would equal the physical cross-section $G_m(x, y)$ evaluated using the surface-based average droplet size $D_{20}(x, y)$ of the spray. Therefore, for each pixel in the image we obtain a value of $G_m(x, y)$ that contains information relevant to the integration path $b(x, y)$ along the attenuation volume $\phi(x, y)$. This gives us

$$G(x, y) = \pi D_{20}^2(x, y) / 4 \quad (2.23)$$

where $D_{20}(x, y)$ is defined as,

$$D_{20}(x, y) = \left(\frac{\sum_{m=1}^n n_m(x, y) D_m^2(x, y)}{\sum_{m=1}^n n_m(x, y)} \right)^{1/2} \quad (2.24)$$

which means that the scattering and absorption of all droplets contained within the attenuation volume $\phi(x, y)$ are equivalent to those of $n(x, y)$ droplets of an equivalent diameter $D_{20}(x, y)$.

The absorption and extinction cross-section can be non-dimensionalized using the physical cross-section of the droplets. The resulting parameters presented by Tien and Drolen (1987) are called scattering, absorption, and extinction efficiencies,

$$Q_{sca\lambda}(x, y) = \frac{C_{sca\lambda}(x, y)}{G(x, y)}; \quad Q_{abs\lambda}(x, y) = \frac{C_{abs\lambda}(x, y)}{G(x, y)}; \quad Q_{ext\lambda}(x, y) = \frac{C_{ext\lambda}(x, y)}{G(x, y)}. \quad (2.25)$$

With this notation, the scattering and absorption coefficients are given by,

$$\begin{aligned}
\sigma_{\lambda}(x, y) &= n(x, y) C_{sca\lambda}(x, y) = G(x, y) n(x, y) Q_{sca\lambda}(x, y) \\
a_{\lambda}(x, y) &= n(x, y) C_{abs\lambda}(x, y) = G(x, y) n(x, y) Q_{abs\lambda}(x, y) \quad . \\
\bar{\kappa}_{\lambda}(x, y) &= n(x, y) C_{ext\lambda}(x, y) = G(x, y) n(x, y) Q_{ext\lambda}(x, y)
\end{aligned} \tag{2.26}$$

Within each pixel (or attenuation volume $\varphi(x, y)$) there are $n(x, y)$ droplets with a droplet size distribution with diameters varying from $D_{min}(x, y)$ to $D_{max}(x, y)$. Define an effective diameter based on the total volume occupied by the droplets within the attenuation volume $\varphi(x, y)$ as

$$D_{30}(x, y) = \left(\frac{\sum_{m=1}^n n_m(x, y) D_m^3(x, y)}{\sum_{m=1}^n n_m(x, y)} \right)^{1/3} . \tag{2.27}$$

This equation signifies that the volume of droplets within each control volume can be represented by $n(x, y)$ droplets of equivalent diameter $D_{30}(x, y)$. These are related to the liquid volume fraction $f_v(x, y)$ of the droplets within the attenuation volume $\varphi(x, y)$.

Using Equation 2.27, the volume fraction $f_v(x, y)$ is defined as

$$f_v(x, y) = \frac{\pi n(x, y) D_{30}^3(x, y)}{6} \tag{2.28}$$

where $n(x, y)$ is the number of droplets per unit volume expressed as

$$n(x, y) = \frac{6 f_v(x, y)}{\pi D_{30}^3(x, y)} . \tag{2.29}$$

Substituting for of $G(x, y)$ (Equation 2.23) and $n(x, y)$ (Equation 2.29) into Equation (2.26) yields

$$\bar{\kappa}_\lambda(x, y) = \left(\frac{\pi D_{20}^2(x, y)}{4} \right) \left(\frac{6f_v(x, y)}{\pi D_{30}^3(x, y)} \right) Q_{ext\lambda}(x, y) = \left(\frac{3}{2} \right) \frac{f_v(x, y) Q_{ext\lambda}(x, y)}{D_{32}(x, y)} \quad (2.30)$$

where $D_{32}(x, y) = D_{30}^3(x, y) / D_{20}^2(x, y)$ is commonly known as the surface area moment mean or the Sauter Mean Diameter (SMD), and represents the diameter of a droplet that has the same ratio of area to volume as that of the droplets contained within the attenuation volume $\varphi(x, y)$. Substituting Equation (2.24) into (2.30), the liquid volume fraction can be expressed as a function of Sauter Mean Diameter,

$$f_v(x, y) = \begin{cases} \left(\frac{2\tau_\lambda(x, y)}{3Q_{ext\lambda}(x, y)b(x, y)} \right) D_{32}(x, y), & \text{for } b(x, y) \neq 0 \\ 0, & \text{for } b(x, y) = 0 \end{cases} \quad (2.31)$$

An expression for the droplet number density per unit volume can be obtained by introducing the formulas for $D_{30}(x, y)$ (Equation 2.27) and $D_{20}(x, y)$ (Equation 2.24) into Equation (2.31), which yields

$$n(x, y) = \begin{cases} \frac{4\tau_\lambda(x, y)}{\pi Q_{ext\lambda}(x, y)b(x, y)D_{20}^2(x, y)}, & b(x, y) \neq 0 \\ 0, & b(x, y) = 0 \end{cases} \quad (2.32)$$

For the droplet number density and the liquid volume fraction to be computed, the depth $b(x, y)$ of the spray at each pixel location and the extinction efficiency $Q_{ext\lambda}(x, y)$

needs to be known. To compute the droplet number density, the values of D_{30} and D_{20} need to be estimated.

2.2.1.2.1 ESTIMATION OF THE SPRAY DEPTH AT EACH PIXEL LOCATION

The value of $b(x, y)$, which is the depth of the spray in a direction normal to the image at each pixel $p(x, y)$ location, is computed as illustrated in Figure 2.11. The high-speed rotary bell atomizer and the UCA sprays have circular cross-sectional areas as illustrated in Figure 2.11(a). The HVLP air-assisted atomizer has an elliptical cross-sectional area as shown in Figure 2.11(b). For the high-speed rotary bell and the UCA sprays using edge detection methods, the radius R at each cross-sectional location along the image of the spray are estimated from which the values of $b(x, y)$ are computed using Equation 2.33. Note that the spray produced by the high-speed rotary bell atomizer starts-off as a hollow spray with an annular cross-sectional area. But, the spray becomes a solid spray with a circular cross-sectional area as it approaches the target surface. Consequently, a circular cross-sectional area is assumed for simplicity.

For the HVLP air-assisted atomizer, the major axes of the spray are estimated at each cross-sectional location along the image of the spray using edge detection methods. Thus for the HVLP air-assisted atomizer, two images are captured for each condition tested. An image is captured for the long axis and a second image is captured for the short axis. From the captured images, the values of $b(x, y)$ are computed using Equation 2.34.

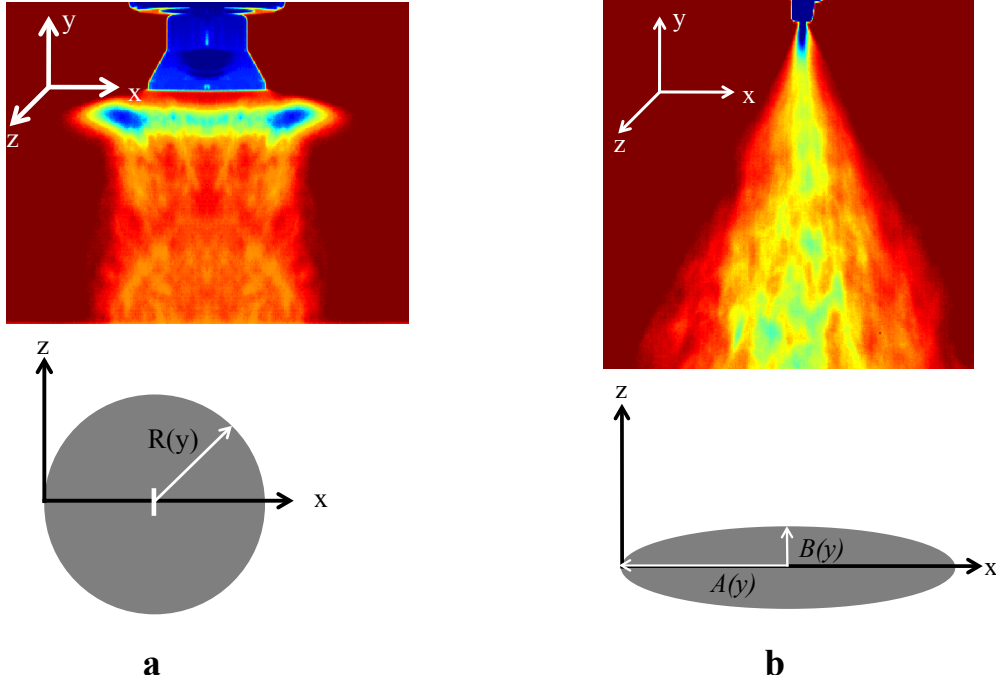


Figure 2.11: Computation of the spray depth $b(x, y)$: **(a)** the cross-section of the high-speed rotary bell atomizer and the UCA Spray, **(b)** the cross-section of the HVLP air-assisted atomizer spray.

$$b(x, y) = 2 \left[R(y)^2 - \{x - R(y)\}^2 \right]^{\frac{1}{2}} \quad (2.33)$$

$$b(x, y) = 2 \frac{B(y)}{A(y)} \left[A(y)^2 - \{x - A(y)\}^2 \right]^{\frac{1}{2}} \quad (2.34)$$

2.2.1.2.2 EXTINCTION EFFICIENCY

To solve for the extinction efficiency, the numerical solution of Matzler (2002) was followed. The extinction efficiency Q_{ext_λ} is given by the following expression:

$$Q_{ext_\lambda} = \frac{2}{\chi^2} \sum_{n=1}^{N_{\max}} (2n+1) \cdot \text{Re}[a_n + b_n] \quad (2.35)$$

where a_n and b_n are Mie coefficients defined as:

$$a_n = \frac{\left[D_n(m\chi)/m + n/\chi \right] \psi_n(\chi) - \psi_{n-1}(\chi)}{\left[D_n(m\chi)/m + n/\chi \right] \zeta_n(\chi) - \zeta_{n-1}(\chi)} \quad (2.36)$$

$$b_n = \frac{\left[mD_n(m\chi) + n/\chi \right] \psi_n(\chi) - \psi_{n-1}(\chi)}{\left[mD_n(m\chi) + n/\chi \right] \zeta_n(\chi) - \zeta_{n-1}(\chi)} \quad (2.37)$$

where ψ_n and ζ_n are the Ricatti-Bessel functions, and

$$N_{\max} = \max(\chi + 4\chi^{1/3} + 2). \quad (2.38)$$

The scattering efficiency is similarly defined as:

$$Q_{sca\lambda} = \frac{2}{\chi^2} \sum_{n=1}^{N_{\max}} (2n+1) \cdot \left[|a_n|^2 + |b_n|^2 \right] \quad (2.39)$$

and the absorption efficiency is obtained by satisfying the energy conservation as:

$$Q_{abs\lambda} = Q_{ext\lambda} - Q_{sca\lambda}. \quad (2.40)$$

Following the numerical solution by Matzler (2002) using MATLAB, the Mie efficiencies are obtained for water, using a complex refractive index of $1.33+0.00001i$. A plot of the Mie efficiency values is shown in Figure 2.11 for water. The value for the extinction efficiency (Q_{ext}) from the numerical solution asymptotically approaches 2.1. Thus constant value of 2.1 is assumed for the extinction efficiency in our analysis.

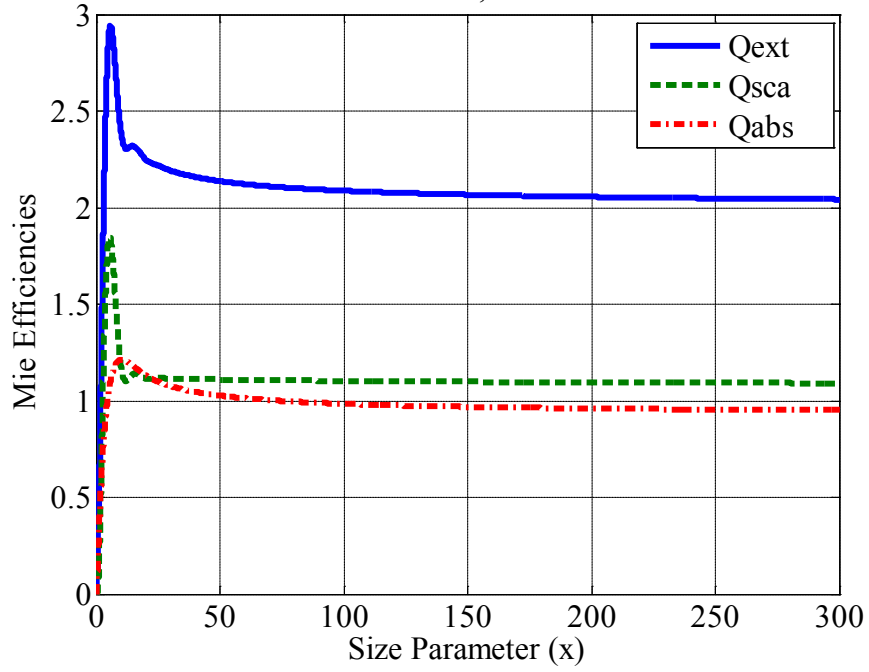


Figure 2.12: The Mie efficiencies for water.

With the Mie extinction efficiency obtained, the droplet volume fraction can be computed once the SMD (D_{32}) is known. The D_{32} values are obtained from experimental measurements using the Malvern Spraytec Particle Analyzer.

2.2.1.2.3 ESTIMATION OF D_{30} AND D_{20} USING EMPIRICAL FORMULATION

To compute the droplet number density using Equation 2.32, we compute D_{30} and D_{20} by employing the Nukiyama-Tanasawa Distribution Function (Nukiyama and Tanasawa, 1939).

$$\frac{dN}{dD} = BD^2 \exp(-CD^q) \quad (2.41)$$

where N is the normalized number distribution of droplets; B is a constant; C is the size parameter; q is a distribution parameter; and D is the droplet diameter. In effect B , C and q are constants that are adjusted to best fit the experimental data (Li and Tankin, 1987, 1988; Semio et al., 1996; Dumouchel and Boyaval, 1999; Ayres et al., 2001; Cao, 2002). Li and Tankin (1987), using information entropy and by taking the limits of the droplet size to be zero and infinity, found the distribution function to be:

$$\frac{dN}{dD} = \frac{\pi}{2} \frac{\rho_l \dot{n}}{\dot{m}_l} D^2 \exp\left(-\frac{\pi}{6} \frac{\rho_l \dot{n}}{\dot{m}_l} D^3\right) \quad (2.42)$$

where ρ_l is the liquid density, \dot{m}_l the liquid mass flow rate, and \dot{n} the droplet number density per unit time. This is a form of the Nukiyama-Tanasawa Distribution Function where distribution parameter (q) is no longer a free variable, but equal to 3.

From the definition of SMD given by the following expression,

$$D_{32} = \frac{\int_0^\infty \left(D^3 \frac{dN}{dD}\right) dD}{\int_0^\infty \left(D^2 \frac{dN}{dD}\right) dD} \quad (2.43)$$

and substituting Equation (2.42) into (2.43) we have an expression of the SMD in terms of the liquid density, the liquid mass flow rate, and the droplet number density per unit time as follow:

$$D_{32} = \frac{1}{\Gamma\left(\frac{5}{3}\right)} \left(\frac{6}{\pi} \frac{\dot{m}_l}{\rho_l \dot{n}}\right)^{\frac{1}{3}}. \quad (2.44)$$

Similarly from the definition of D_{30} (Equation 2.27), we obtain the expression of D_{30} in terms of the liquid density, the liquid mass flow rate, and the droplet number density per unit time as follow:

$$D_{30} = \left(\frac{6}{\pi} \frac{\dot{m}_l}{\rho_l \dot{n}} \right)^{\frac{1}{3}}. \quad (2.45)$$

From Equations (2.45) and (2.44), we obtain an expression of D_{30} in terms of D_{32} , from which the value for D_{30} can be obtained once D_{32} is measured from the experiment.

$$D_{30}(x, y) = \Gamma\left(\frac{5}{3}\right) D_{32}(x, y). \quad (2.46)$$

Similarly D_{20} is solved from its definition (Equation 2.24), yielding

$$D_{20}(x, y) = \left[\Gamma\left(\frac{5}{3}\right) \right]^{\frac{1}{2}} D_{30}(x, y) = \left[\Gamma\left(\frac{5}{3}\right) \right]^{\frac{1}{2}} \Gamma\left(\frac{5}{3}\right) D_{32}(x, y). \quad (2.47)$$

With an expression obtained for D_{20} and D_{30} in terms of D_{32} , one only needs to know D_{32} from which the values of D_{20} and D_{30} can be estimated using these relations. The droplet number density can then be obtained using Equation 2.32.

Copyright © Nelson K. Akafuah 2009

CHAPTER THREE

3.0 EXPERIMENTAL APPARATUS

The experimental apparatus is presented in three sections as follows: in Section 3.1, the basic apparatus for the infrared characterization and visualization technique developed in this dissertation are presented. Section 3.2 presents the fabrication of the new atomizer (ultrasonic cavitating atomizer). And lastly, Section 3.3 presents a brief description of the high-speed rotary bell atomizer and the High Volume Low Pressure (HVLP) air-assisted atomizer.

3.1. APPARATUS FOR THE INFRARED VISUALIZATION AND CHARACTERIZATION TECHNIQUE

The basic experimental apparatus for the infrared visualization and characterization technique comprises an imaging device (infrared camera), a thermal radiation source, and a droplet size analyzer. Brief descriptions of each of these apparatus are provided below.

3.1.1 INFRARED CAMERA

The imaging device utilized in this study to capture the spray flow field was an infrared camera, Flir ThermoVision™ SC4000, pictured in Figure 3.1. The SC4000 has a 320 x 256 pixels Indium Antimonide (InSb) detector, which operates in a 3.0 to 5.0 μm

spectral range of the electromagnetic spectrum. The ThermoVision SC4000 FPA incorporates a read-out technology in the form of a Complementary-Metal-Oxide-Semiconductor (CMOS) readout integrated circuit (ROIC) with $20\ \mu\text{m}$ pitch. FPA systems include a matrix of detectors to resolve the FOV. The detectors require cooling well below the ambient temperature to allow for rapid scanning, high sensitivity, and low noise. The cooling is achieved by an integrated miniature Stirling cooler, capable of achieving temperature around 70 K. In the SC4000, the pixel size of the detector is $30\ \mu\text{m}$.

The SC4000 has a dynamic range of 14-bit. The dynamic range in infrared thermography describes the ratio between the maximum and minimum measurable infrared radiant intensities. It has a typical Noise Equivalent Temperature Difference (NETD) or Noise Equivalent Irradiance (NEI) of 18 mK (FLIR Systems, 2009).



Figure 3.1: The ThermoVision SC4000 infrared camera (FLIR Systems, 2009).

NETD is a measure of the sensitivity of a detector of thermal radiation in the infrared band of the electromagnetic spectrum. For an infrared FPA imaging device, NETD is usually used to characterize the sensitivity of FPAs. NETD is the temperature change of a scene, required to produce a signal equal to the root mean square (rms) noise. It is a system level limit that depends on parameters such as the f -number (sometimes called focal ratio, f -ratio, or relative aperture) of the optics used. For low background applications, noise equivalent power (NEP), or noise equivalent irradiance (NEI) is usually used as a figure of merit. NEI is the radiant flux power necessary to produce a signal equal to the rms noise (Meimei, 2000).

3.1.2 BACKGROUND RADIATION SOURCE

The infrared camera is generally capable of mapping surface temperature. To visualize a multiphase fluid flow system such as liquid spray which is at room temperature, it is necessary to provide a temperature contrast. To achieve this, a uniformly heated background is utilized. This approach is similar to backlighting in high speed photography. In this dissertation this background serves two purposes; on one hand, it provides the needed temperature contrast to visualize the spray flow field. On the other hand, it provides the thermal radiation source, needed for the studies of scattering and absorption. By using Mie Theory in analyzing the scattering and absorption, some detail quantitative information about the spray flow field is deduced.

The background radiation source used is an IR-160/301TM Blackbody System from Infrared Systems Development (2009). The IR-160/301 Blackbody System is an

extended area type flat plate emitter with special high emissivity coating providing 0.96 average emissivity. The emitter size is 304.8 mm by 304.8 mm. The system has a temperature controller with 0.1°C set point resolution. The temperature range of the system is ambient to 350°C and a wavelength range of 1 to 99 μm . Temperature sensing in the system is provided by means of a Platinum Resistance Temperature Detector (RTD) and a Type *T* (copper-constantan) thermocouple. The blackbody and controller system are shown in Figure 3.2.

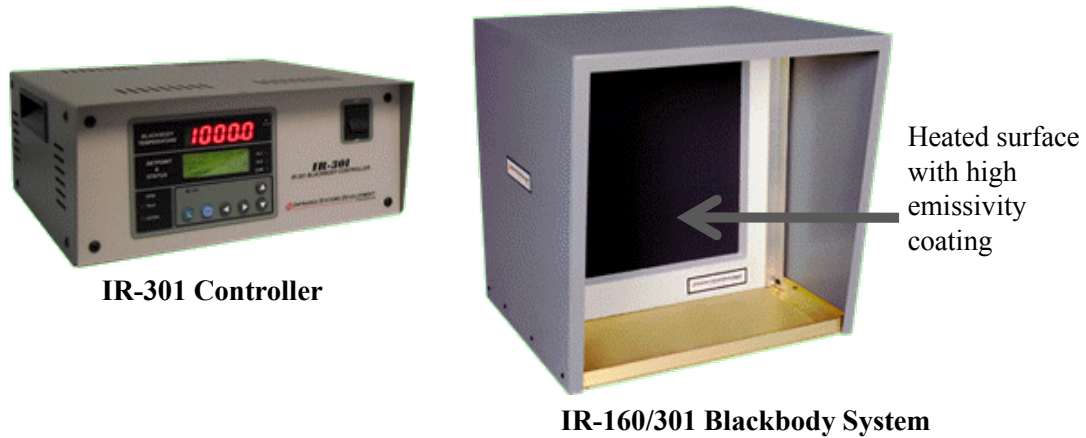


Figure 3.2: The IR-150/301 blackbody system (Infrared Systems Development, 2009).

3.1.3 DROPLET SIZE ANALYZER

To estimate the droplet number density and the liquid volume fractions from the infrared characterization and visualization technique developed in this dissertation, the droplet size information need to be known. To measure the droplet size and size distribution, a Malvern Spraytec particle sizing system was utilized.

The Malvern Spraytec particle sizing system (Figure 3.3) was used for droplet size measurement. The Spraytec particle sizing system yields a 0.1 to 900 μm size range with a 300 mm receiving lens. The measurement volume of the Spraytec has a diameter of 9 mm. Spraytec uses the full Mie Theory which completely solves the equations for interaction of light with matter. The system requires prior knowledge of the refractive index for the material being sprayed and the medium into which the material is sprayed. For this study water was used as the working fluid and was injected into air. The refractive indices of both water and air are well known.

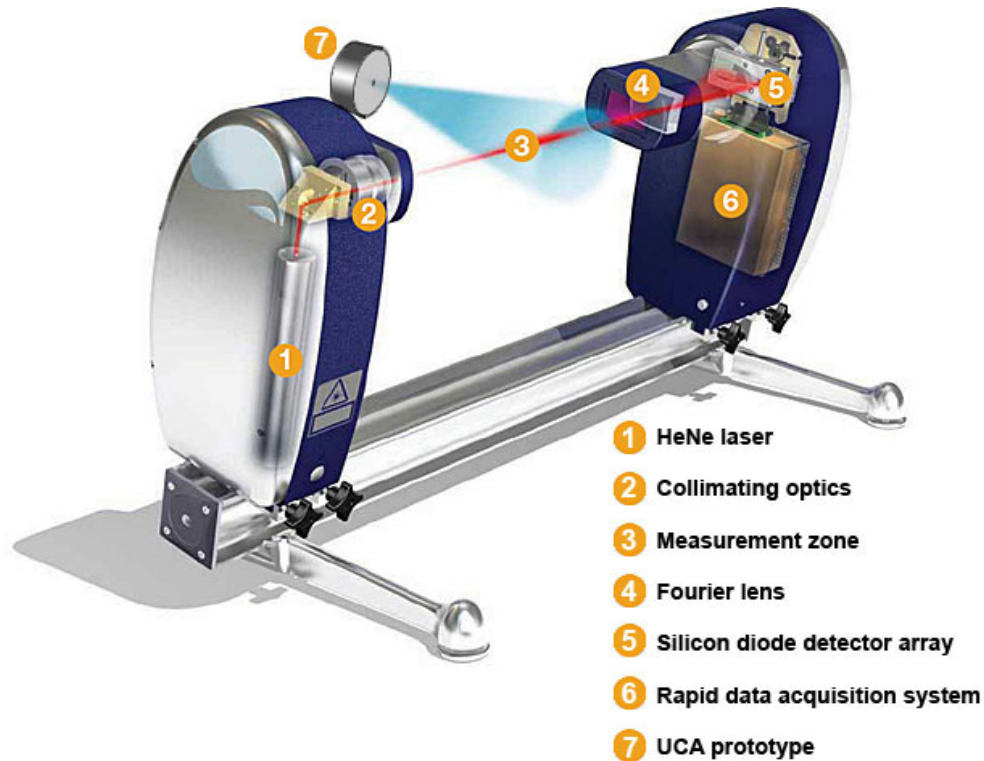


Figure 3.3: A schematic of the Spraytec measurement system (Malvern Instruments Ltd, 2005).

3.2 FABRICATION OF THE ULTRASONIC CAVITATING ATOMIZER

The ultrasonic cavitating atomizer (UCA) is a new atomizer design which uses ultrasonically generated cavitation collapse energy together with imposed oscillatory pressure field to produce droplets. Details of the fabrication process are offered in this section. The component presented includes herein the ultrasonic horn, the piezoelectric actuator, and the nozzle and nozzle housing.

3.2.1 ULTRASONIC HORN

The UCA uses an ultrasonic horn for the cavitation cluster generation and for the modulation of the exiting liquid jet. The cavitation bubble population is substantially enhanced if the energy of the oscillations is well focused in a given area. This is achieved by use of a concave surface at the tip of the oscillating horn. The horn surface concavity increases the power density of the bubble formation (Vijay, 1992, 1998) and enhances high frequency pulsing to the liquid downstream. Figure 3.4 shows the ultrasonic horn and a close-up view of the concave tip.

The ultrasonic horn has a base with a diameter of 10.00 mm and 5.00 mm in length. The horn tip has a diameter of 0.15 mm with a concave surface of radius 0.075 mm. The horn's longitudinal surface profile starts as a circular profile with radius of 16.40 mm from and base and merges into a conical section, 2.00 mm from the horn tip. Detail dimensions and construction of the horn is shown in Figure 3.5. The ultrasonic horn is made of stainless steel, with the base surface mirror finished for attachment to the piezoelectric actuator. The horn displacement is 20 μm , and thus, it is very important to

minimize any gap that may exist between the horn base surface and the surface of the piezoelectric actuator to which it is attached.

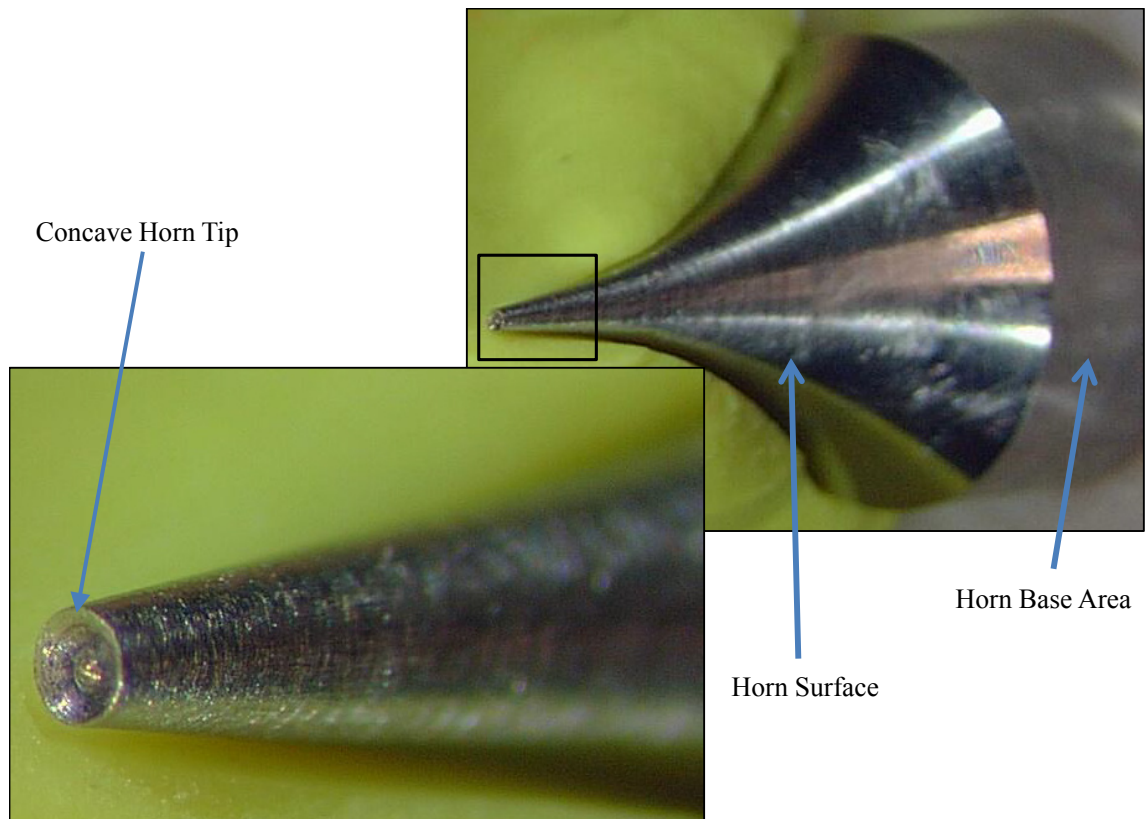


Figure 3.4: The ultrasonic horn.

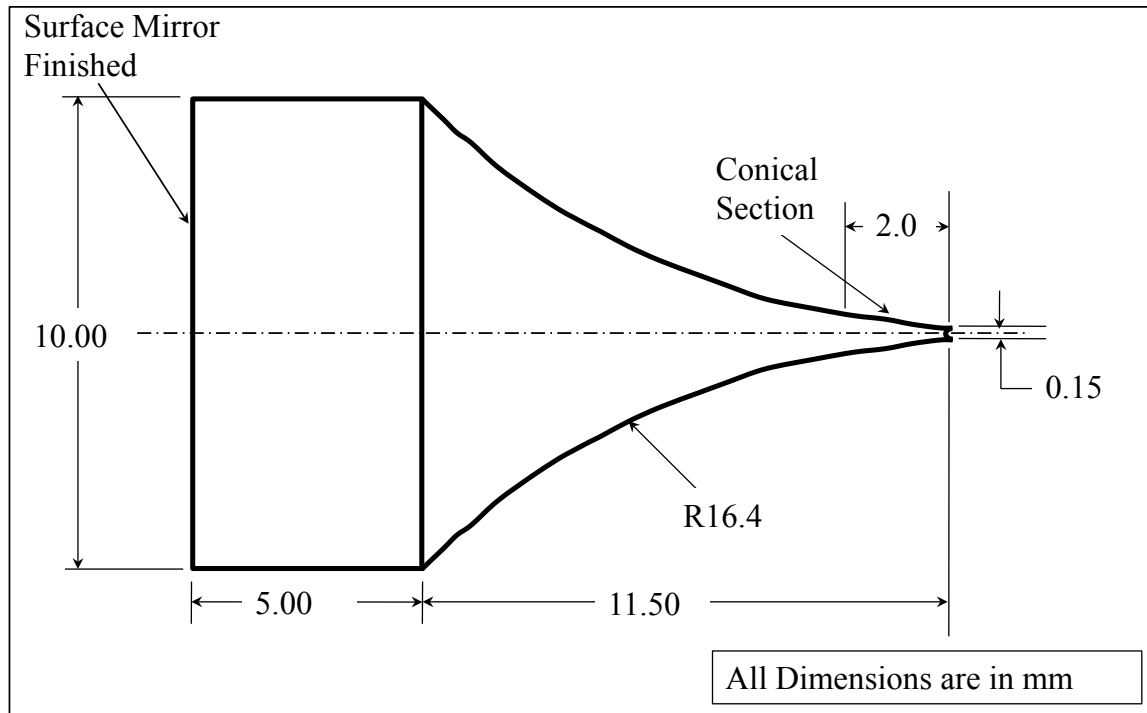


Figure 3.5: The ultrasonic horn dimensions.

3.2.2 THE PIEZOELECTRIC ACTUATOR

The piezoelectric actuator provides the ultrasonic frequency and the energy to the horn needed to generate cavitation bubbles and to provide the oscillatory pressure field in the fluid. The actuator is made of piezoelectric ceramic material, Lead Zirconate Titanate (PZT) disks, stacked together and enclosed in a stainless steel housing to allow immersion in a dielectric fluid. Piezoelectric actuator stacks are capacitors that change shape when charged with high voltage. Increasing voltage increases the length of the stack up to a maximum strain of approximately 0.1% for typical maximum voltage of 1000 V. The relationship between voltage and movement is approximately linear.

The piezoelectric actuator produces a nominal displacement of $24\ \mu\text{m}$ with a frequency of 68 kHz at full drive voltage of 1000 V. A high voltage linear amplifier is used to drive the piezoelectric actuator. The piezoelectric actuator fast response (high bandwidth) depends on the amplifier current and power. The rapid mechanical displacement requires fast electrical charging and discharging of the piezoelectric capacitor. The peak current output of the drive amplifier determines the voltage rise time in the capacitor, which determines the motion response. It must be noted that Mechanical resonance of the piezoelectric actuator and the mechanical system may also limit bandwidth. Physical response is limited by the speed of sound, which determines the system resonant frequency.

The oscillation of the transducer is intensified by the ultrasonic horn creating pressure waves in the liquid. This action forms microscopic bubbles (cavities), which expand during the negative pressure excursion, and implode violently during the positive excursion. It is this phenomenon, referred to as cavitation that produces the powerful shearing action at the horn tip, and causes the molecules in the liquid to become intensely agitated. The PZT disk stack is illustrated in Figure 3.6 together with the piezoelectric actuator and the ultrasonic horn assembly.

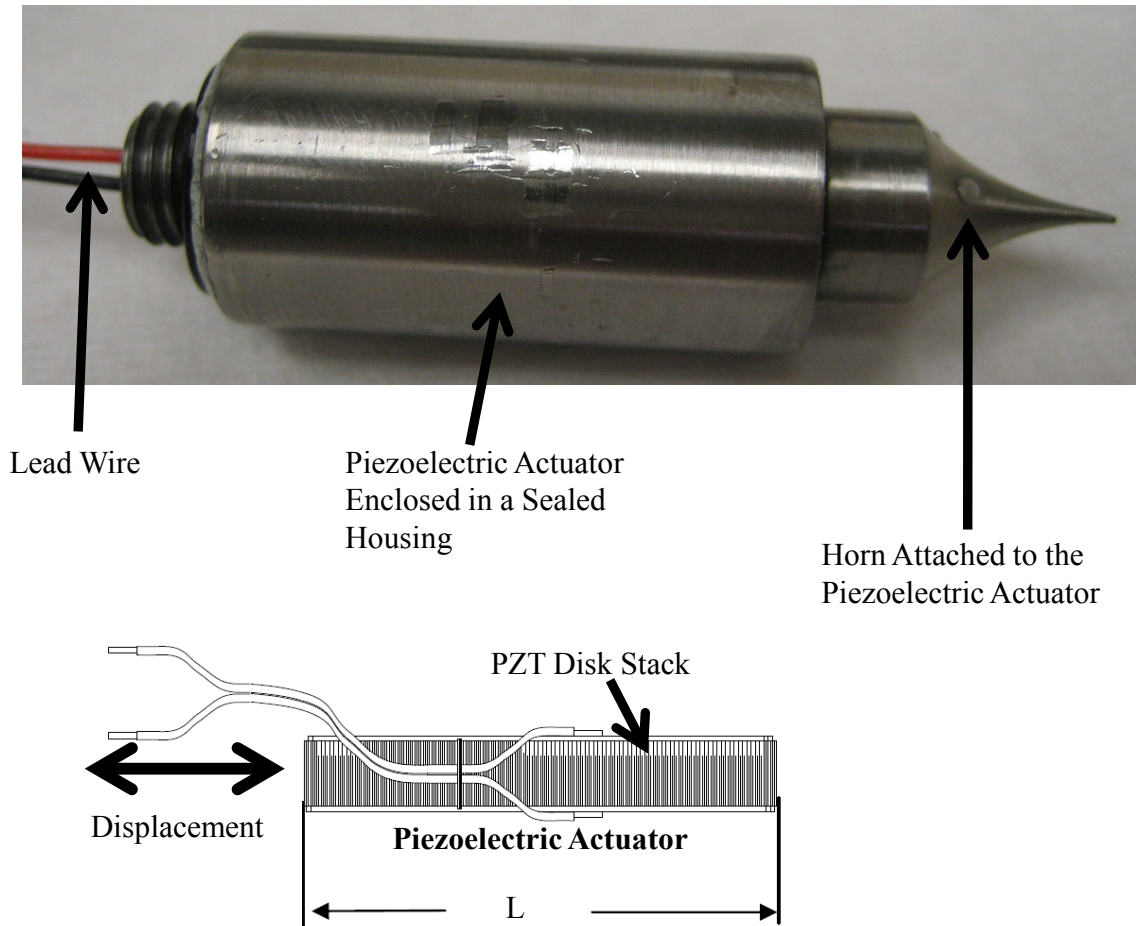


Figure 3.6: The piezoelectric actuator and the ultrasonic horn assembly.

3.2.3 UCA NOZZLE AND NOZZLE HOUSING

The interior geometry of the nozzle section of the atomizer is very crucial in ensuring cavitation bubble growth and collapse. The profile and detail dimensions of the axial cross-section of the nozzle interior geometry are shown in Figure 3.7. The dimensions of the nozzle interior profile are also tabulated in Table 3.1. The interior profile shows a precise nominal positioning of the ultrasonic horn tip to allow a horn

stroke length of 20 μm at a horn oscillation frequency of 60 kHz. The nominal position of the horn tip is at a cross section inside the nozzle such that the horn tip covers one-third of the cross-section of the liquid flow area.

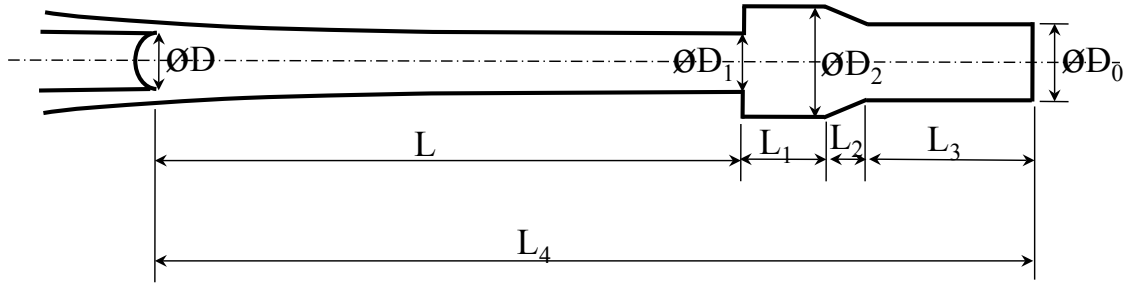


Figure 3.7: The dimensions of the nozzle interior geometry.

TABLE 3.1: UCA Nozzle Dimensions.

Nozzle Dimensions (mm)			
D	0.15	L	1.20
D ₀	0.23	L ₁	0.15
D ₁	0.15	L ₂	0.075
D ₂	0.30	L ₃	0.30
L ₄	1.725		

For ease of construction, the atomizer nozzle is constructed in five different parts namely: part 1-cap, part 2-nozzle, part 3- body, part 4-support, and part 5-end cap. The three-dimensional drawings of the parts are illustrated in Figure 3.8 a and b. Detailed

drawings and dimensions of the five parts are shown in Appendix A: part 1-cap comprises of L_1 , L_2 , and L_3 shown in Figure 3.7. Part 2-nozzle is comprised of L in Figure 3.7 and the main nozzle section of the atomizer. Part 3-body is the main atomizer body. Part 4-support is the support structure that holds the piezoelectric-horn assembly in place. Part 5-end cap houses the inlet port and is screwed onto the piezoelectric actuator and horn assembly.

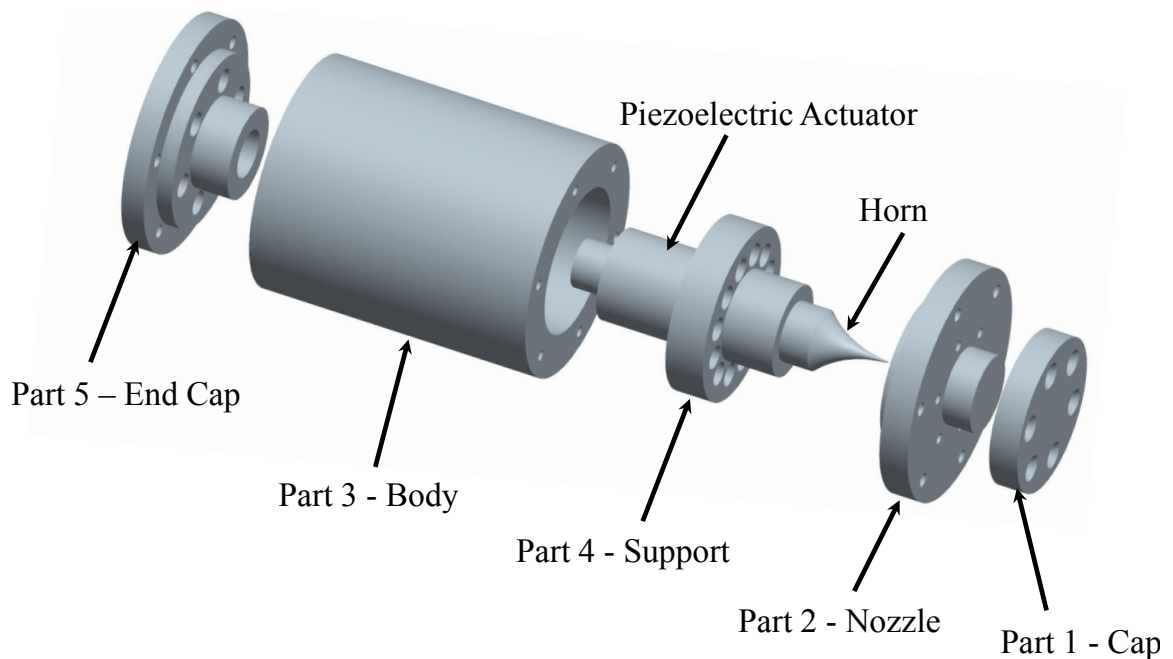


Figure 3.8 a: The UCA nozzle assembly.

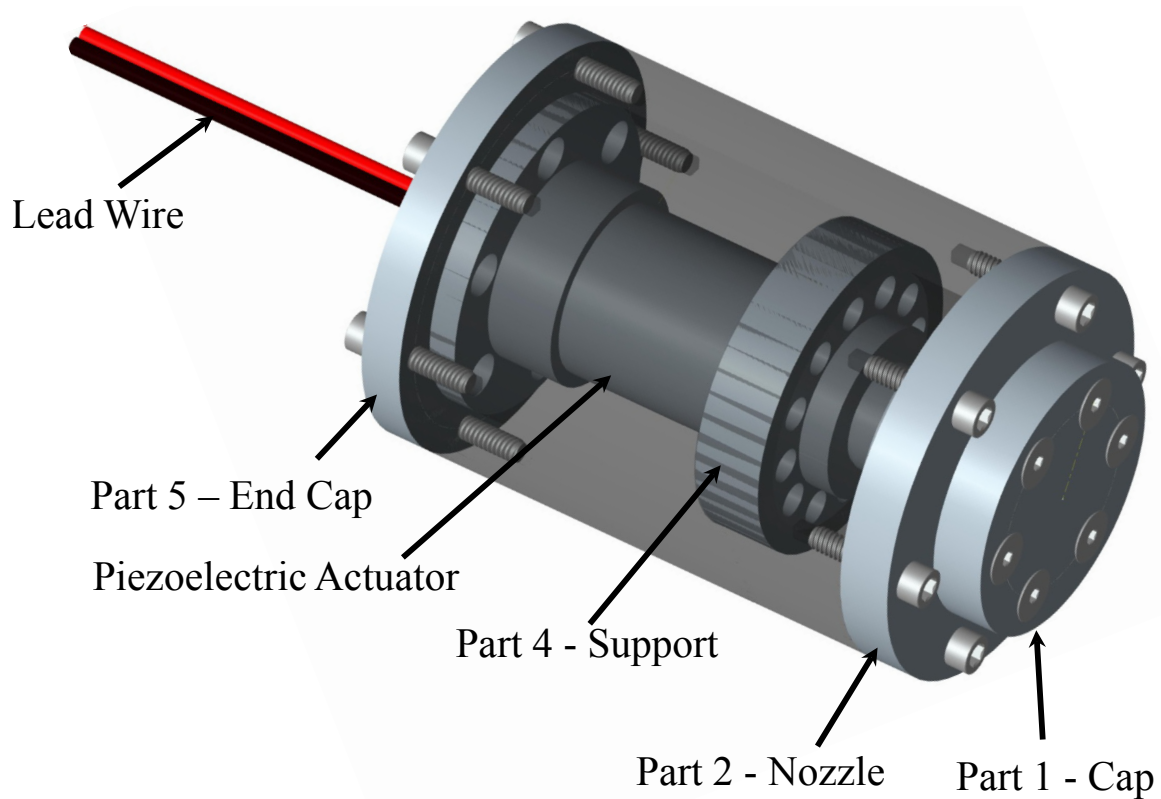


Figure 3.8 b: The UCA nozzle assembly.

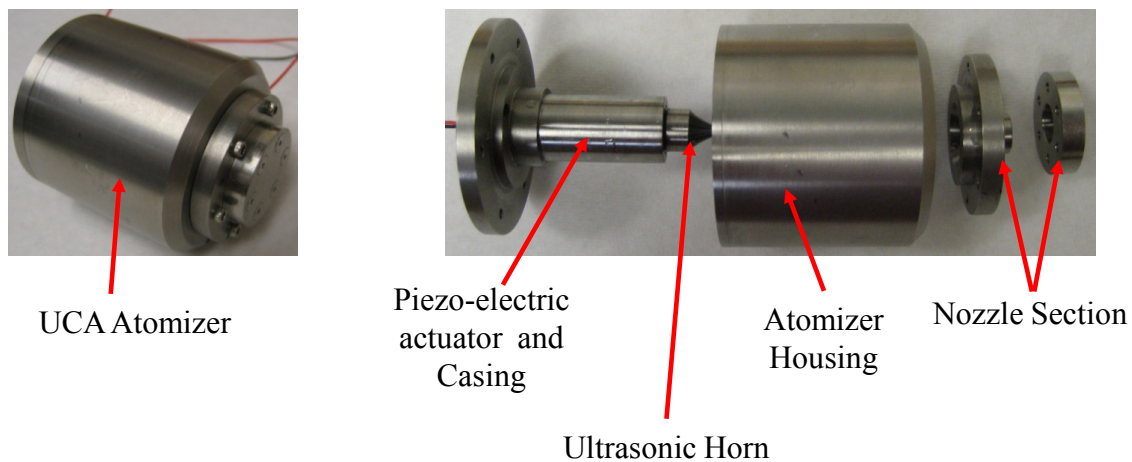


Figure 3.9: A picture of the UCA atomizer assembly.

A picture of the actual nozzle is shown in Figure 3.9. The nozzle holes were drilled by chemical etching. O-rings are placed between the cap and the main body as well as between the end cap and main body to seal in the liquid and prevent leakage.

3.3 OTHER AUTOMOTIVE PAINT SPRAY ATOMIZERS

This section provides a brief description of the other two automotive paint atomizers: the high-speed rotary bell and the High Volume Low Pressure (HVLP) air-assisted atomizer. The following provides summary of these two atomizers.

3.3.1 HIGH-SPEED ROTARY BELL ATOMIZER

A high-speed rotary bell atomizer is generally a device in which liquid is supplied to the center of the rotating bell cup. The friction between the liquid and the bell cup wall causes the liquid to rotate at roughly the same speed as the bell cup. This rotary motion creates centrifugal forces within the liquid that induces it to flow radially outward toward the rim of the bell cup. If the rotational speed of the bell cup is sufficiently high, the liquid will arrive at the rim in a thin continuous film. The mechanism of disintegration of the film into droplets is affected by the size and geometry of the bell cup, its rotational speed, the liquid flow rate, and the physical properties of the liquid (Lefebvre, 1989; Im et al., 2001, 2004; Dominick and Thieme, 2006).

The high-speed rotary bell atomizer pictured in Figure 3.10 has a 75 mm diameter bell cup with a serrated edge. Figure 3.11 shows a cut-off section of the rotary bell cup

with some details of the serrated cup lip. It has a wide range of operating conditions, but in these experiments the following conditions were tested: liquid flow rates of 100, 200, 300, and 400 cc/min. For each liquid flow rate the bell cup rotation speeds of 20,000, 30,000, 40,000, and 50,000 rpm were tested. The shaping airflow was not varied between trials, and electrostatic charging was not applied in these experiments.

The liquid is supplied to the atomizer ring by the ring gap and moves toward the bell cup edge owing to the centrifugal and Coriolis forces created by the rotating bell cup. Many of the available bell cup variants have a similar means of paint flow division; 80% of the paint quantity is supplied to the atomizer rim by the ring gap. The remaining 20% of the volume flow passes through the central drilled hole on the front side of the distributor ring to effect a permanent rinsing of the bell cup surface and to prevent paint deposits on the distributor ring. Serration or circumferential knurls along the edge of the bell cup permit the paint film flowing over the surface of the bell disk to be divided into defined individual flows and ligaments that eventually break up into droplets (Im et al., 2001).

Turbine housing protects the drive unit of the high-speed rotary atomizer which is driven by compressed air. Behind the rotary bell cup, shaping air exits from about 40 holes annularly arranged on the stationary housing. Shaping air is used primarily to support the transport of paint droplets, to stabilize the flow conditions around the atomizer, and to permit a precise alignment of the spray pattern by limiting the atomizing cone.

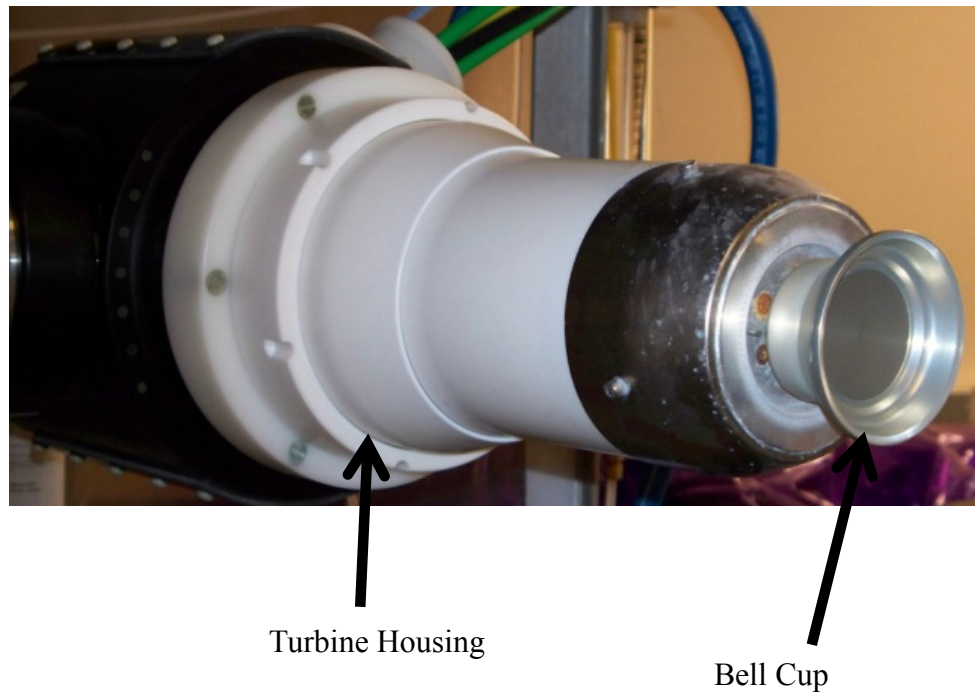


Figure 3.10: The high-speed rotary bell atomizer.

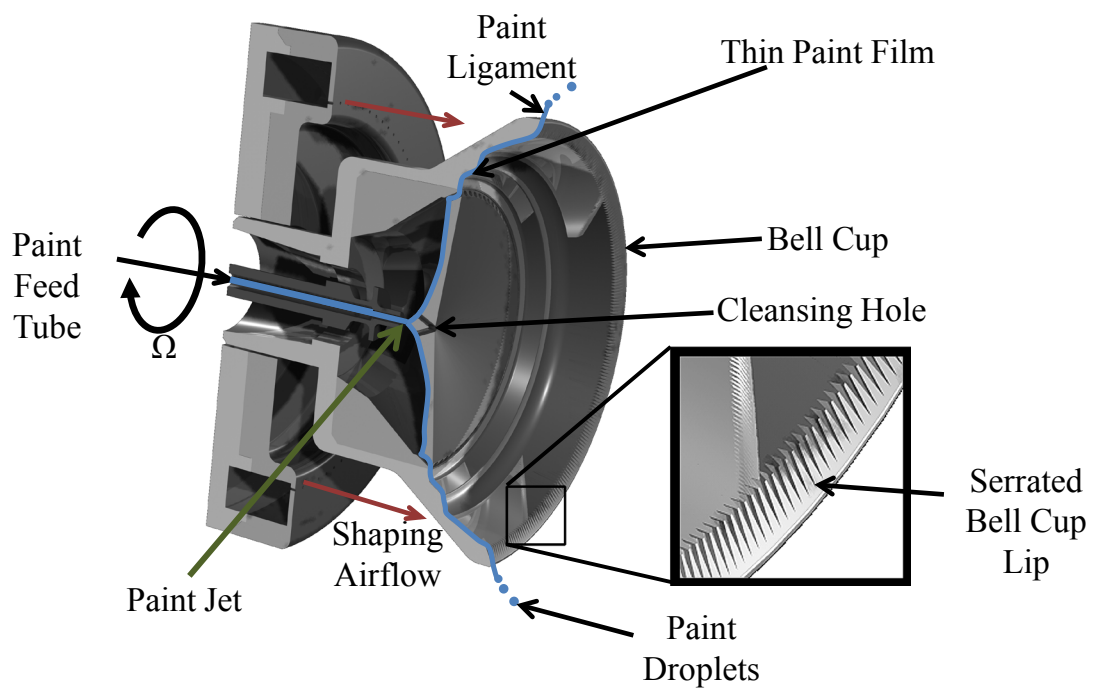


Figure 3.11: A schematic of the cross-section of the high-speed rotary bell cup.

3.3.2 HIGH VOLUME LOW PRESSURE AIR-ASSISTED ATOMIZER

The HVLP air-assisted atomizer used is 'MICRO COAT' Model MGB14 by Asahi Sunac Corporation of Japan. It is a twin fluid atomizer which uses the kinetic energy of the flowing air stream to shatter the paint into ligaments and then into droplets. The HVLP air-assisted atomizer is an external mixing type. In the external mixing type of spray guns, a paint nozzle opening and an atomizing air dispensing annulus release outwardly from the atomizing head (Figure 3.12). The liquid paint flow dispensed through the paint dispensing nozzle is dispersed and atomized by the airflow which is diffused and blown around the paint flow.

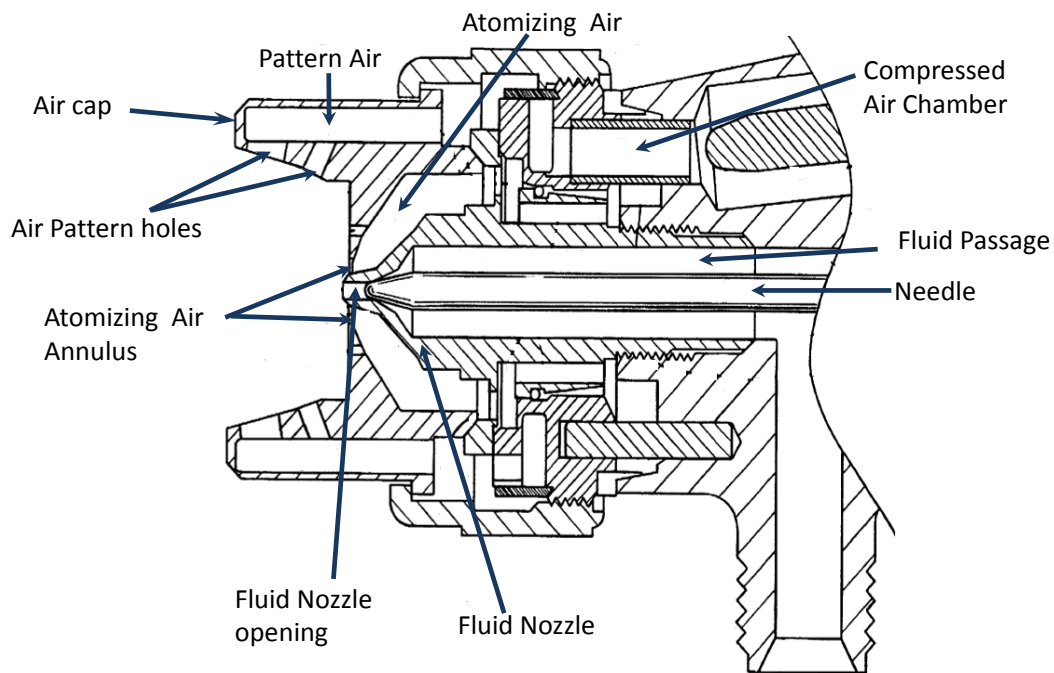


Figure 3.12: A schematic of the cross-section of the nozzle of HVLP.

The paint nozzle opening is located at the center facing to the outside of the atomizing head. An annular air hole is provided around the nozzle hole, and compressed air is blown at a pressure of 0.05-0.63 MPa as it surrounds the paint flow from the nozzle hole. The paint and the compressed air are dispensed separately and are mixed and atomized in front of and outside the atomizing head (Figure 3.13).

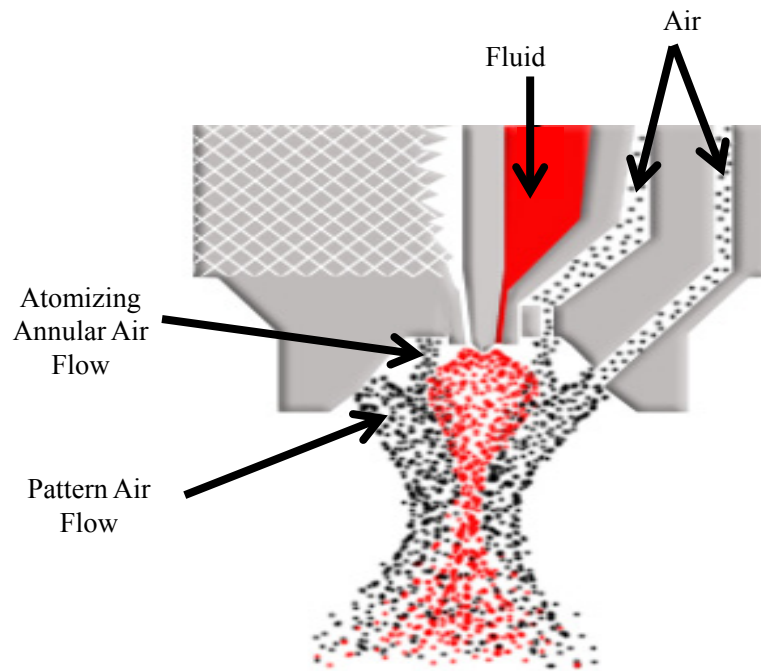


Figure 3.13: HVLP air-assisted atomization.

The HVLP air-assisted atomizer has lateral air holes provided on both sides, and compressed air is supplied from both sides to the spray flow in order to adjust the shape of the spray pattern (Figure 3.13). Consequently, a spray flow sprayed in a circular pattern at the center may be flattened by changing the airflow pressure and quantity from

the lateral air holes. In the case of this spray gun, better atomization is achieved when compressed air quantity (or pressure) is increased, such that the painted surface is provided with a higher quality finish as a consequence of the spraying of finer particles. A picture of the MICRO COAT HVLP air-assisted atomizer with explanation of major components is illustrated in Figure 3.14.



Figure 3.13: A picture of the HVLP air-assisted atomizer.

Copyright © Nelson K. Akafuah 2009

CHAPTER FOUR

4.0 EXPERIMENTAL PROCEDURES AND DISCUSSION OF RESULTS

Chapter four examines the experimental procedures and results. A detailed analysis of the experimental procedure used in characterizing the Ultrasonic Cavitating Atomizer (UCA) prototype and the spray characterization results are offered in Section 4.1. The experiment procedure and results for the novel infrared visualization and characterization technique for a liquid spray are presented in Section 4.2 for all three atomizers studied.

4.1 CHARACTERIZATION OF THE ULTRASONIC CAVITATING ATOMIZER

The UCA prototype was studied for a limited liquid injection pressure range of 600-900 psi (4.1-6.2 MPa). The atomizer was tested at the liquid injection pressure settings of 600 psi (4.1 MPa), 700 psi (4.8 MPa), 800 psi (5.5 MPa), and 900 psi (6.2 MPa). In addition, two liquid flow rate settings of 100 and 200 cc/min were considered under each liquid injection pressure setting.

An experimental setup comprising of an in-house fluid delivery system was built for the testing of the UCA prototype. The fluid delivery system has a fluid reservoir, which contains the working fluid (in this case, water). The fluid system is affixed with a flow controller, a flow meter, a pressure gauge, and a filter. A schematic of the experimental setup is illustrated in Figure 4.1. The setup includes the piezoelectric

actuator driver which is a linear amplifier and a function generator. An input voltage of 10 V was supplied to the amplifier which amplifies the input voltage signal to 1000 V. This was used to drive the piezoelectric actuator to which the ultrasonic horn is attached, providing the required ultrasonic frequency. A pressure gauge and a filter which filters out anything larger than 40 μm was installed in the fluid supply line. Figure 4.1 also illustrates the setup with the Malvern Spraytec system which was used to measure the droplet size and the droplet size distribution.

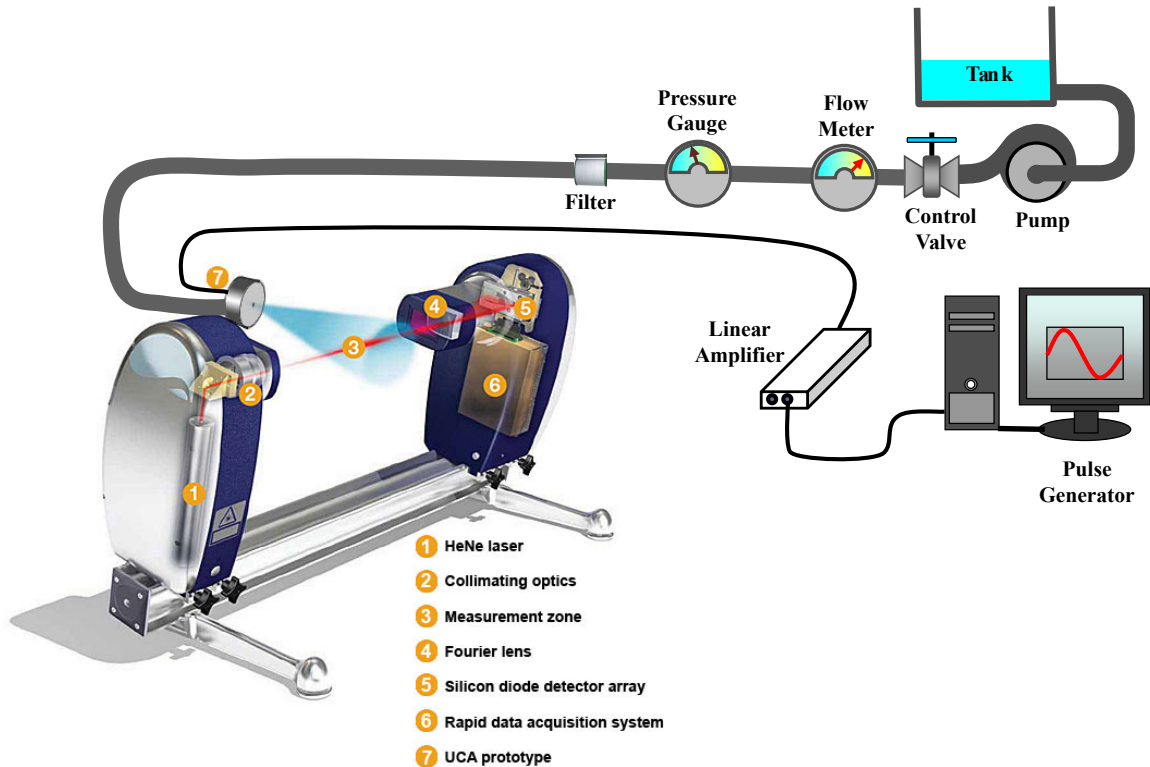


Figure 4.1: A schematic of the UCA prototype experimental setup with the Malvern Spraytec system.

The Malvern Spraytec particle analyzer measures droplet size distributions using the technique of laser diffraction. This requires the angular intensity of light scattered

from a spray to be measured as it passes through a laser beam. The recorded scattering pattern is then analyzed using an appropriate optical model to yield a size distribution.

The measurement process involves the following steps:

1. The spray generated by the atomizing device is delivered between the two functional modules of the instrument, the transmitter and the receiver modules, then travels through the laser beam forming a measurement zone.
2. The transmitter module uses a He-Ne (Helium-Neon) laser to produce a laser beam that passes through the spray delivered to the measurement zone.
3. Detecting optics in the receiver module senses the light diffraction pattern produced by the spray, converting the detected light into electrical signals.
4. These signals are processed by analogue and digital electronics boards and passed to the analysis software.
5. The light diffraction pattern is analyzed using an appropriate scattering model to calculate the spray size distribution.

4.1.1 THE UCA PROTOTYPE CHARACTERIZATION RESULTS

The characterization results for the UCA prototype are offered in two sections as follows: Section 4.1.1.1 presents the external or macroscopic features of the spray produced by the UCA. This includes the description of the external spray features—such as the spray angle, spray pattern, and spray cross-section. Section 4.1.1.2 offers

microscopic features of the spray, which includes droplet size and droplet size distribution within the spray.

4.1.1.1 MACROSCOPIC FEATURES OF THE UCA PROTOTYPE SPRAY

The UCA prototype is a pressure atomizer which uses the energy created by the collapse of cavitation bubbles in concert with liquid pressure modulation to produce droplets. The UCA spray produces a full conical spray, with a circular cross section. The characteristic of the flow in pressure atomizers has been studied by several researches. Their results demonstrate that the spray angle is influenced by nozzle dimensions, liquid properties, and the density of the medium into which the liquid is sprayed (Lefebvre, 1989). In these experiments, the working fluid is water, and the medium into which it was sprayed is ambient air.

Upon application of an ultrasonic frequency of 60 kHz, the UCA prototype spray yields cone angles between 14° and 21° for a liquid flow rate of 100 cc/min and spray cone angles between 16° and 24° for a liquid flow rate of 200 cc/min. Under both flow rate conditions, the smallest cone angles were observed at 4.1 MPa and the largest at 6.2 MPa. The image of the UCA spray illustrating the cone angles for all liquid injection pressure settings are shown for the liquid flow rate of 100 cc/min in Figure 4.2 and for the liquid flow rate of 200 cc/min in Figures 4.3.

For comparison, for each injection pressure and flow rate tested, two cases were considered: one with the piezoelectric actuator on at 60 kHz and the other with the actuator off.

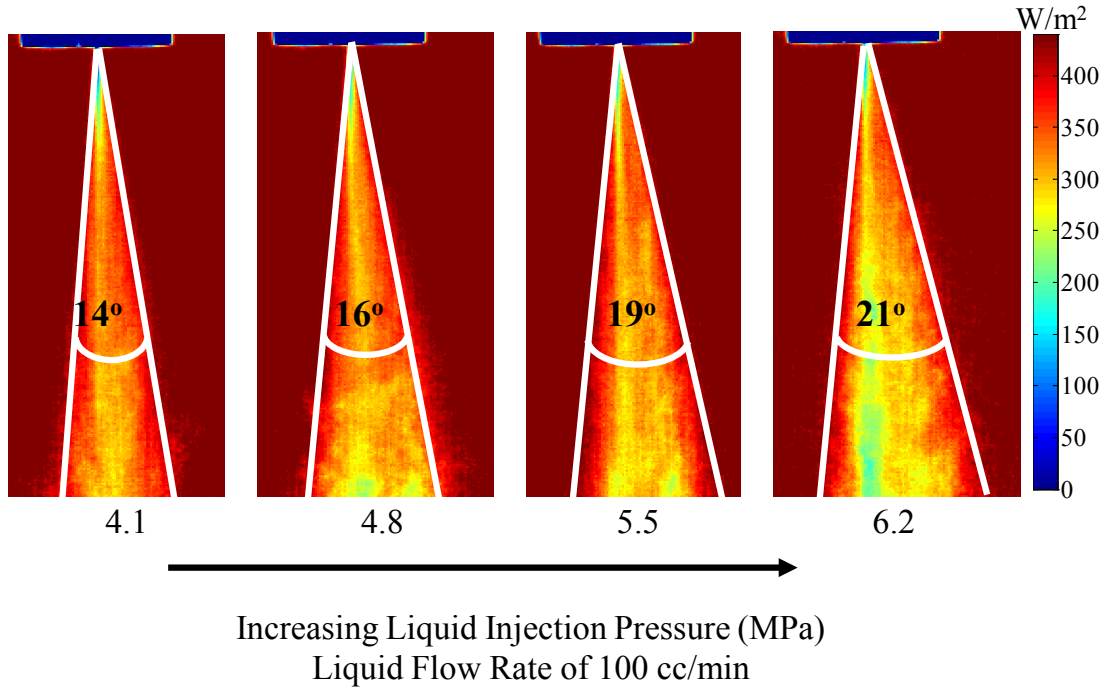


Figure 4.2: The image of the UCA spray for a liquid flow rate of 100 cc/min with increasing liquid injection pressure at an ultrasonic frequency of 60 kHz.

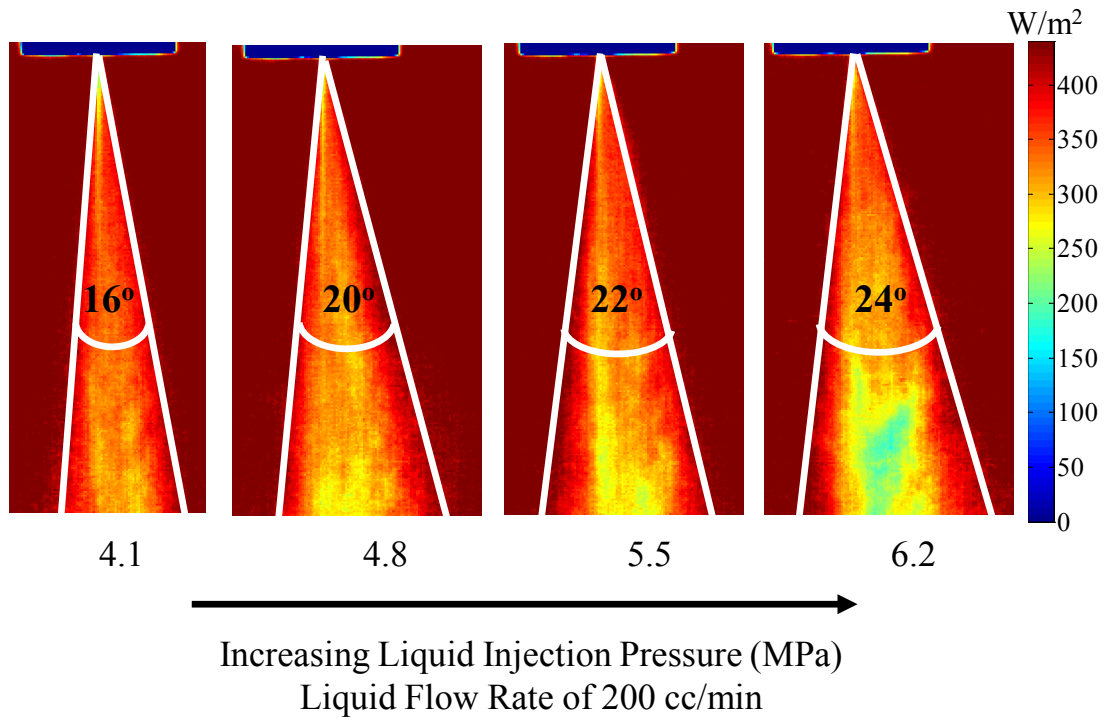


Figure 4.3: The image of the UCA spray for a liquid flow rate of 200 cc/min with increasing liquid injection pressure at an ultrasonic frequency of 60 kHz.

4.1.1.2 DROPLET SIZE AND SIZE DISTRIBUTION WITHIN THE UCA SPRAY

The droplet size distribution within the spray generated by the UCA prototype are illustrated in Figure 4.4 for the liquid flow rate of 100 cc/min. Figures 4.4a, 4.4b, 4.4c, and 4.4d correspond to the liquid injection pressures of 4.1, 4.8, 5.5, and 6.2 MPa, respectively. The corresponding SMD is shown in Figure 4.5. The plot for the droplet size distribution for a liquid flow rate of 200 cc/min is illustrated in Figure 4.6, with the corresponding SMD in Figure 4.7. Figure 4.6a, 4.6b, 4.6c, and 4.6d are the droplet size distributions for the liquid injection pressures of 4.1, 4.8, 5.5, and 6.2 MPa, respectively. The error bars in Figures 4.5 and 4.7 represent the standard deviation of the data.

Figure 4.5 point out that under all four liquid injection pressure conditions at zero ultrasonic frequency there is an average standard deviation of about 0.9 indicating significant statistical variation of the SMD with time. Upon application of 60 kHz ultrasonic frequency, the standard deviation is still on the average about 0.9 for the liquid injection pressures of 4.1 and 4.8 MPa. On the other hand, this value decreased to about 0.3 for both 5.5 and 6.2 MPa, indicating the stabilization of the spray. The energy created by the collapse of the cavitation bubble together with the oscillation of the exiting liquid jet, reduces the SMD, stabilized the spray, and minimized the variation in the SMD over time. On the average there is about a 9% drop in the SMD with the application of 60 kHz ultrasonic frequency to the flow. It is 10% for both 5.5 and 6.2 MPa liquid injection pressures. Similar observations were made for the liquid flow rate of 200 cc/min, with the largest reduction in the SMD about 12% at 5.5 MPa. Overall, there is on the average,

a 10% reduction in the SMD upon the application of the ultrasonic frequency of 60 kHz for a liquid flow rate of 200 cc/min.

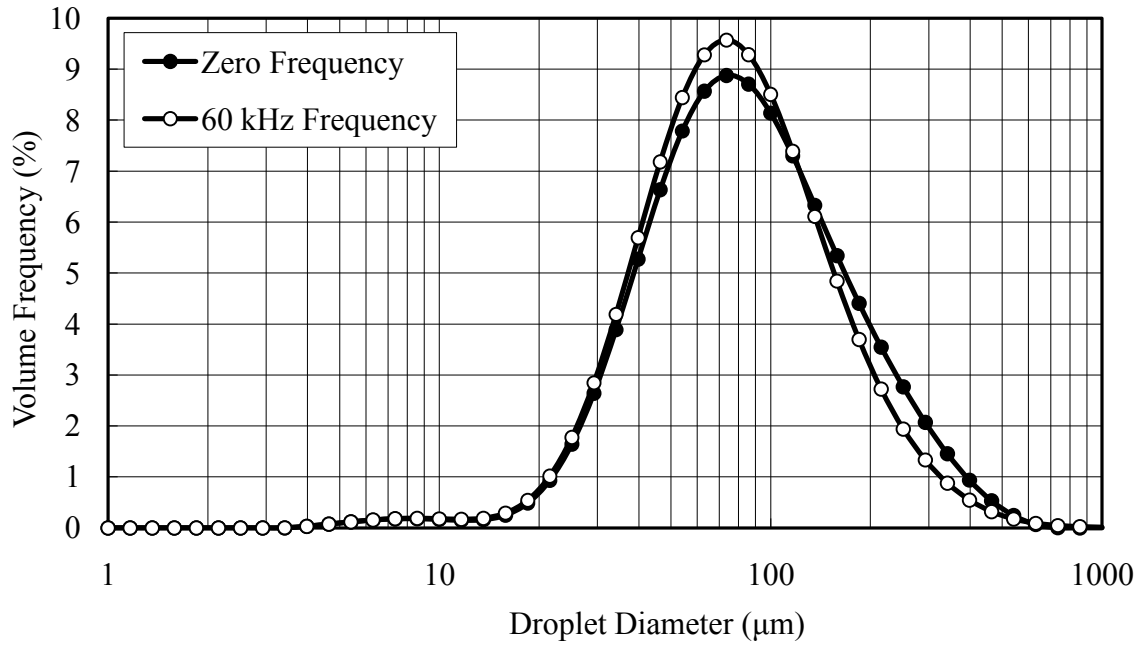


Figure 4.4a: The volume frequency vs. the droplet diameter at a liquid flow rate of 100 cc/min, with an ultrasonic frequency of 60 kHz, and a liquid injection pressure 4.1 MPa.

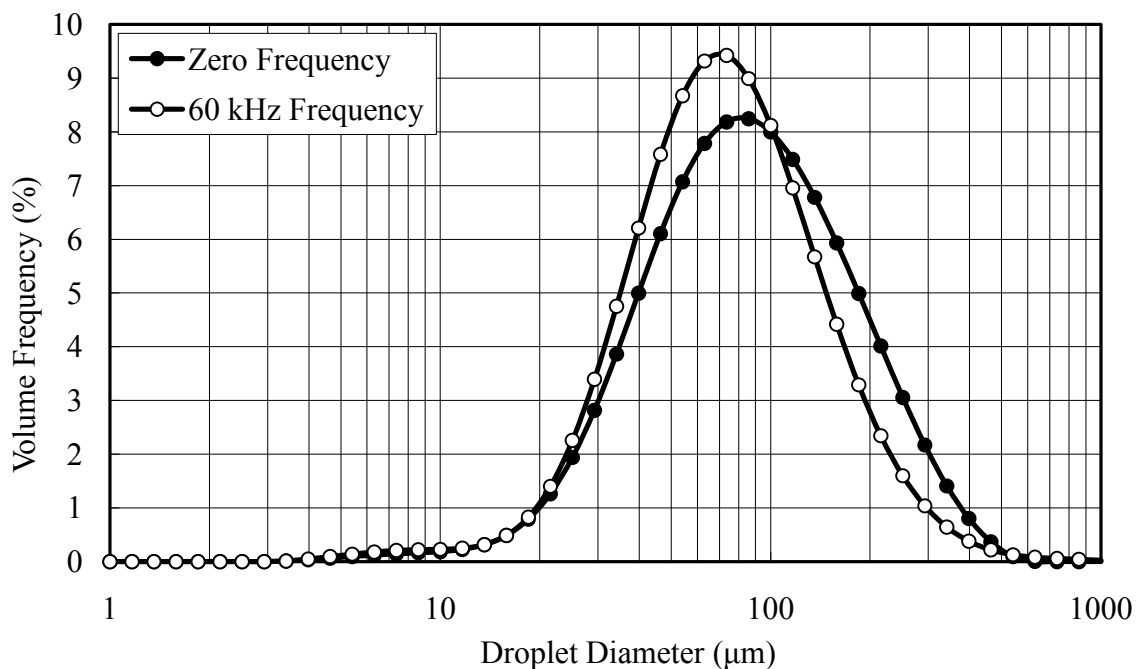


Figure 4.4b: The volume frequency vs. the droplet diameter at a liquid flow rate of 100 cc/min, with an ultrasonic frequency of 60 kHz, and a liquid injection pressure 4.8 MPa.

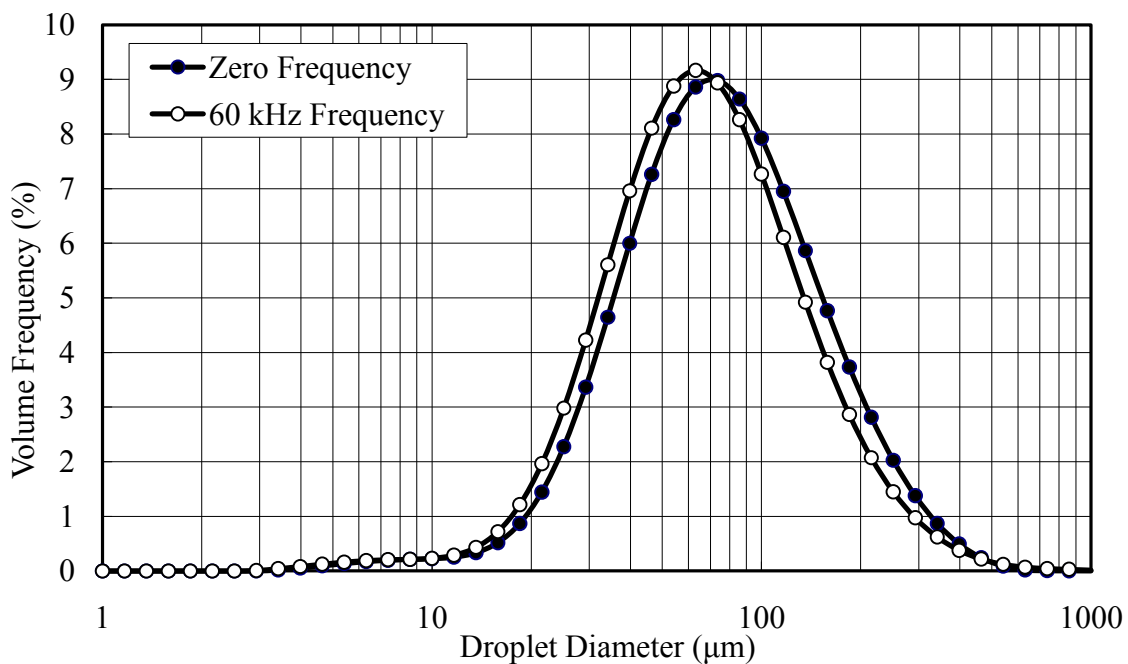


Figure 4.4c: The volume frequency vs. the droplet diameter at a liquid flow rate of 100 cc/min, with an ultrasonic frequency of 60 kHz, and a liquid injection pressure 5.5 MPa.

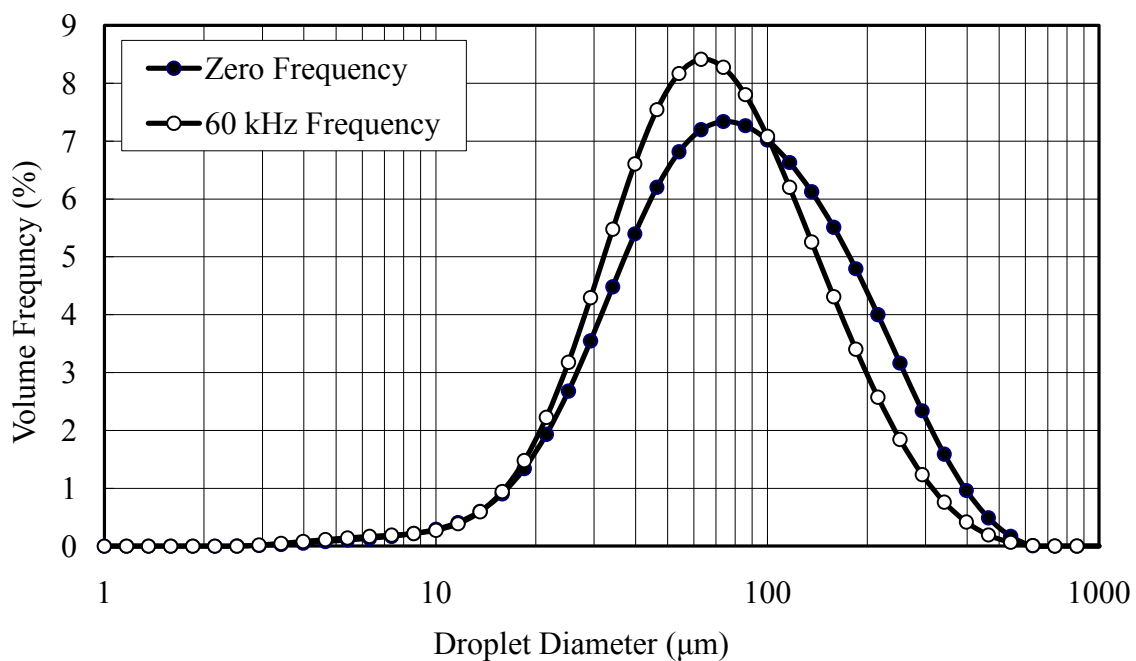


Figure 4.4d: The volume frequency vs. the droplet diameter at a liquid flow rate of 100 cc/min, with an ultrasonic frequency of 60 kHz, and a liquid injection pressure 6.2 MPa.

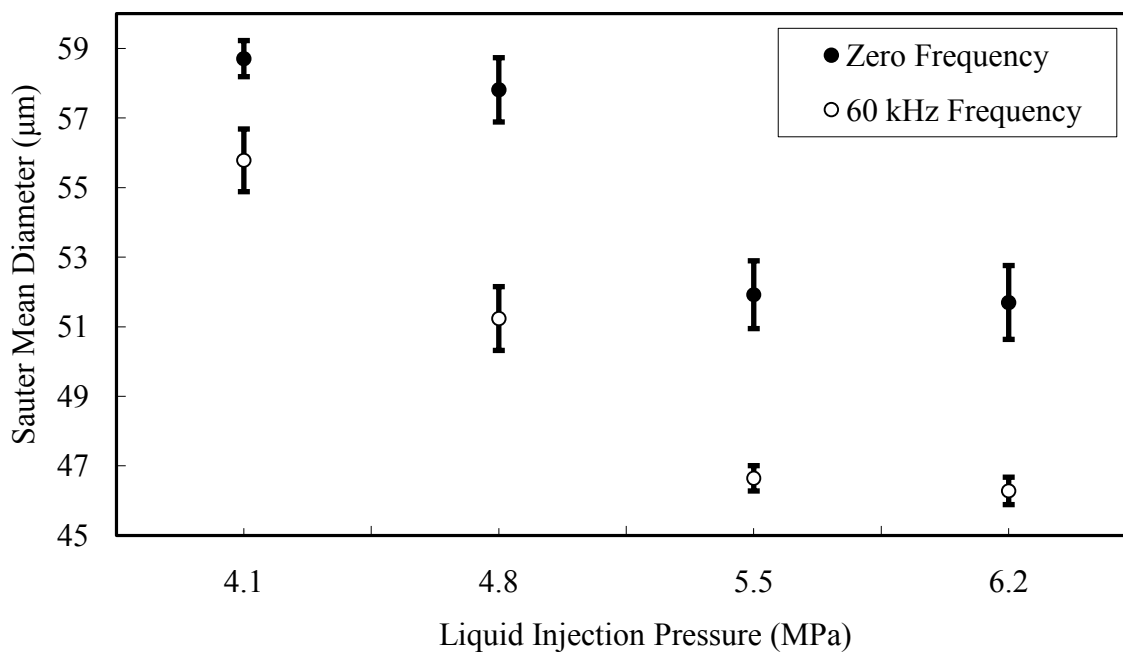


Figure 4.5: The sauter mean diameter vs the liquid injection pressure at a liquid flow rate of 100 cc/min and ultrasonic frequencies of zero and 60 kHz.

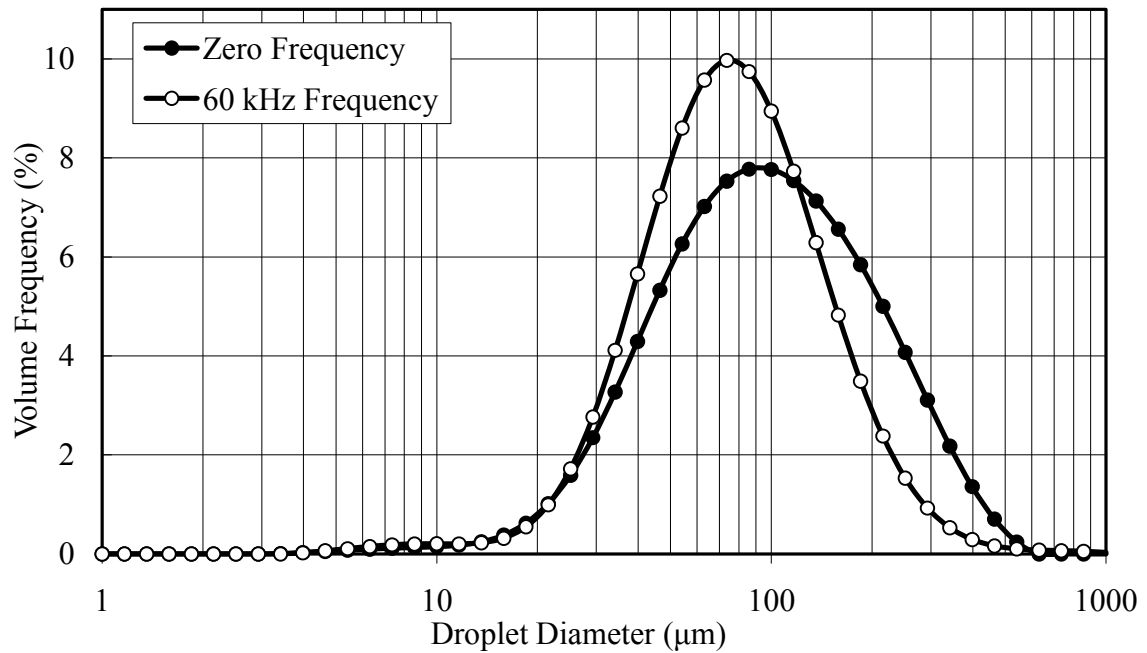


Figure 4.6 (a): The volume frequency vs. the droplet diameter at a liquid flow rate of 200 cc/min, with an ultrasonic frequency of 60 kHz, and a liquid injection pressure 4.1 MPa.

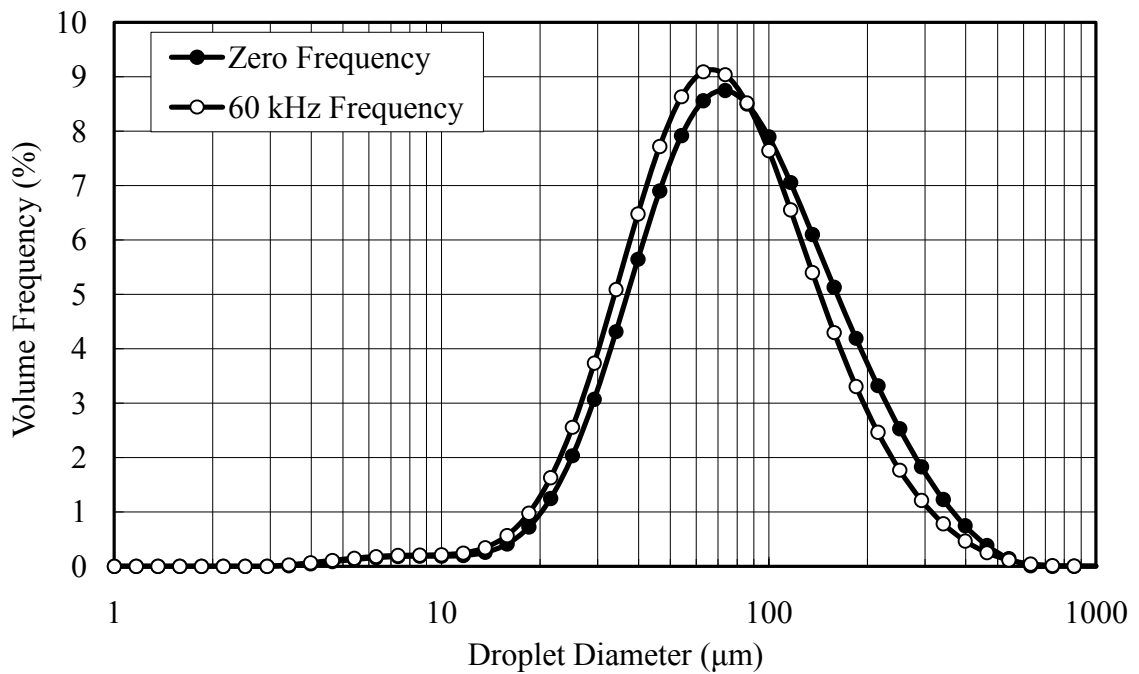


Figure 4.6 (b): The volume frequency vs. the droplet diameter at a liquid flow rate of 200 cc/min, with an ultrasonic frequency of 60 kHz, and a liquid injection pressure 4.8 MPa.

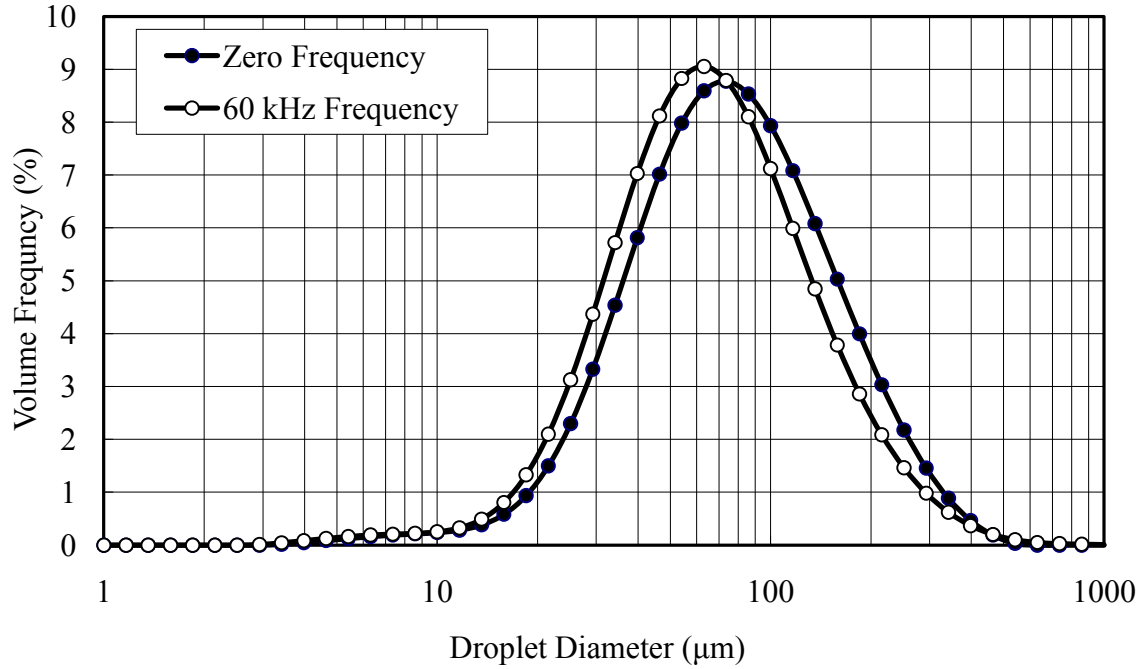


Figure 4.6 (c): The volume frequency vs. the droplet diameter at a liquid flow rate of 200 cc/min, with an ultrasonic frequency of 60 kHz, and a liquid injection pressure 5.5 MPa.

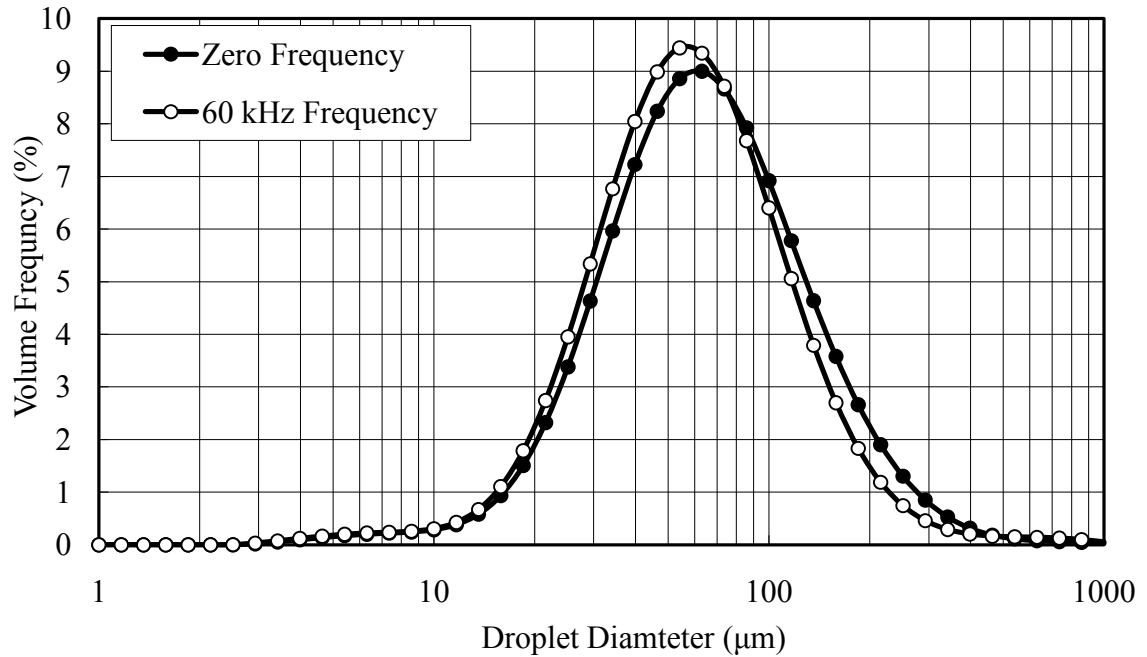


Figure 4.6 (d): The volume frequency vs. the droplet diameter at a liquid flow rate of 200 cc/min, with an ultrasonic frequency of 60 kHz, and a liquid injection pressure 6.2 MPa.

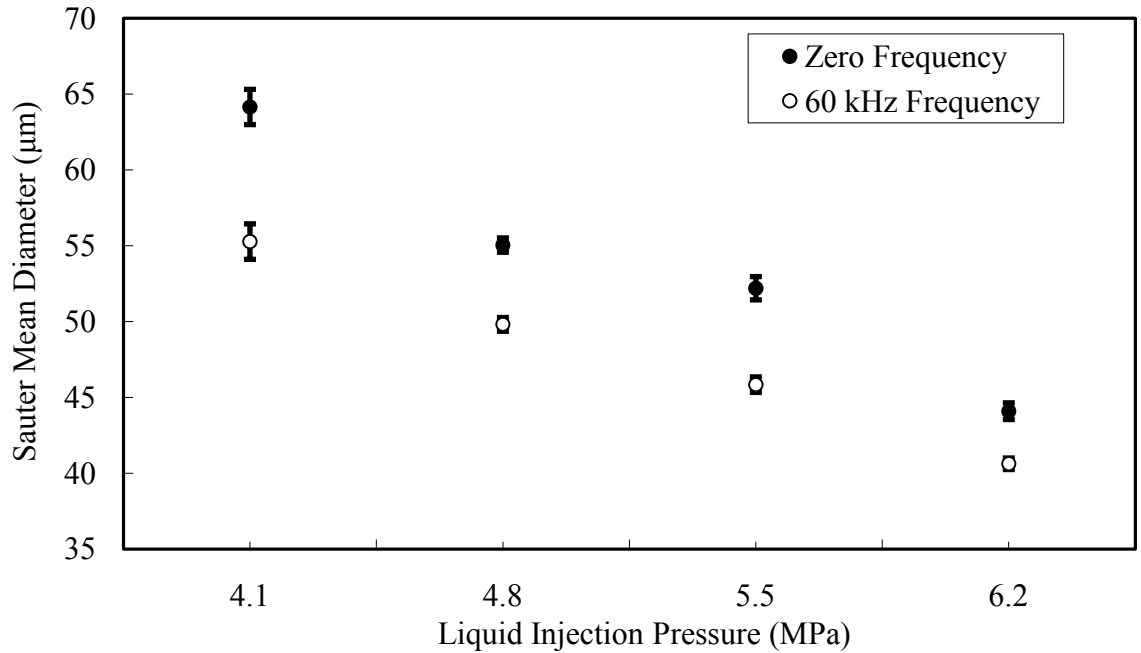


Figure 4.7: The Sauter mean diameter vs the liquid injection pressure at a liquid flow rate of 200 cc/min and ultrasonic frequencies of zero and 60 KHz.

Figure 4.8 shows a plot of the SMD against various ultrasonic frequencies at a liquid flow rate of 100 cc/min and a liquid injection pressure of 5.5 MPa. For the case of zero ultrasonic frequency, there is fluctuation of the SMD between 52 and 55 μm. The band of fluctuation of the SMD for 52-55 μm is considered at zero frequency and 5.5 MPa liquid injection pressure. Figure 4.8 demonstrates that the effect of ultrasonic cavitation and pressure modulation of the exiting liquid jet is minimal at all the frequencies tested except at the frequencies of 30 and 60 kHz. Only these two frequencies have a significant drop in the SMD outside of the band of fluctuation at zero ultrasonic frequency. However, 30 kHz has more variation in the SMD than 60 kHz. Thus, 60 kHz is the recommended operational frequency for this prototype.

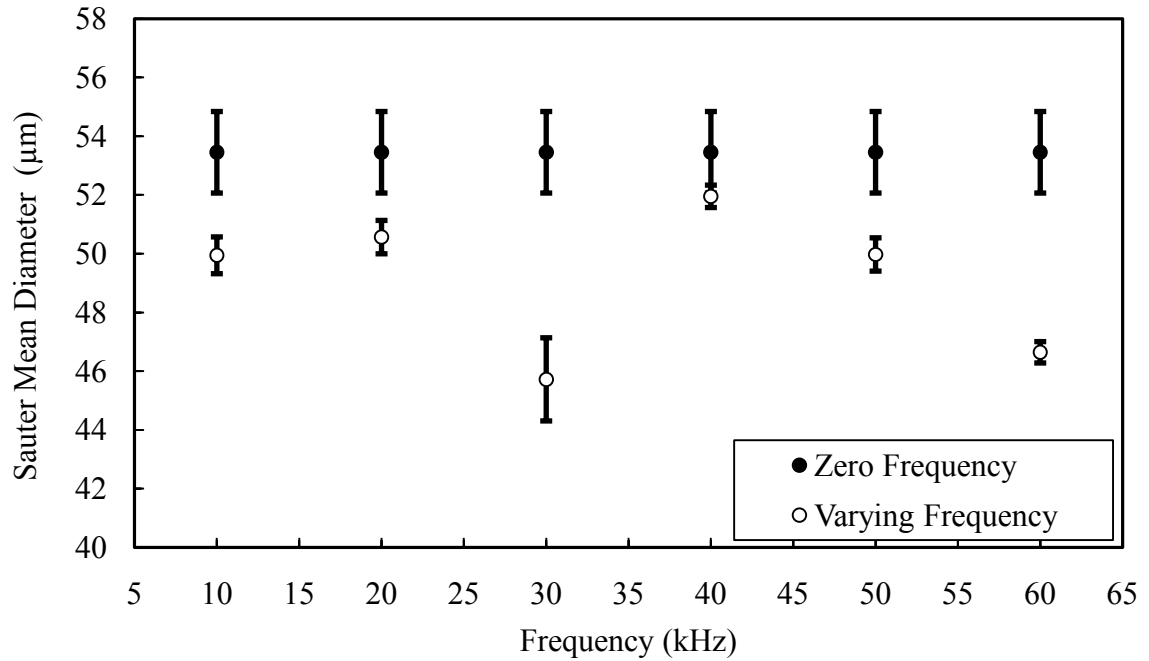


Figure 4.8: The sauter mean diameter vs the ultrasonic frequency at a liquid flow rate of 100 cc/min and liquid injection pressure of 5.5 MPa.

Figure 4.9 shows a time history of the SMD of the UCA prototype performance. For each liquid injection pressure setting the UCA was operated first without turning on the piezoelectric actuator and the SMD recorded. The piezoelectric actuator was turned on to monitor the effect of the cavitation and the pressure modulation phenomena on the spray atomization. The results show sudden drop in the SMD once the piezoelectric actuator is turned on for all liquid injection pressure settings.

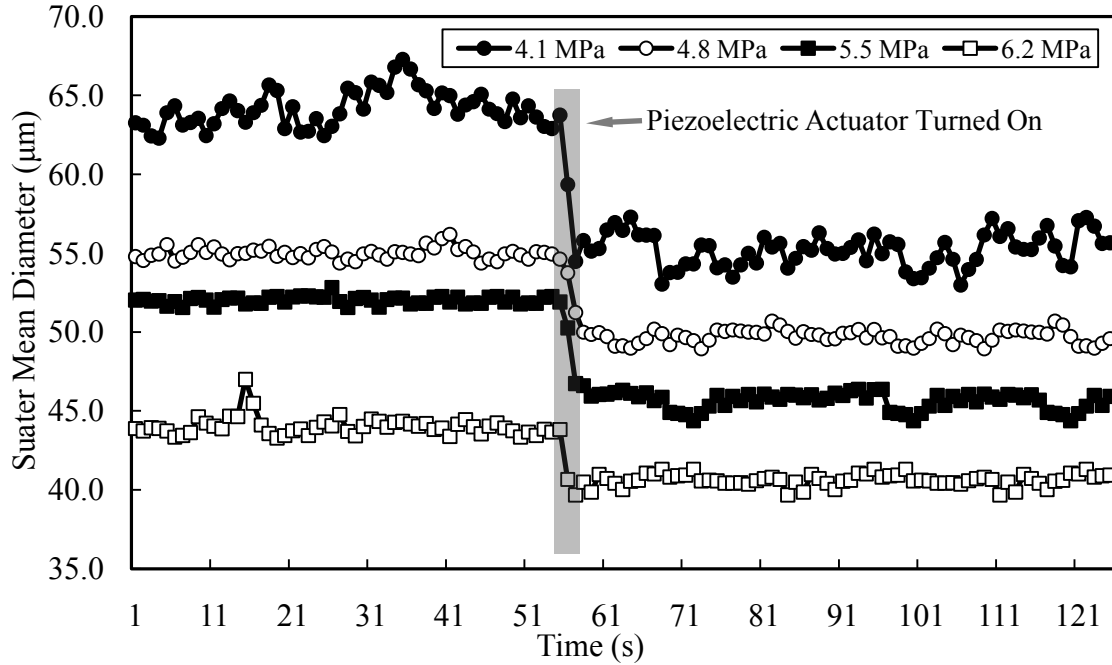


Figure 4.9: A time history of the sauter mean diameter with and without ultrasonic frequency of 60 kHz.

The result of the UCA which uses ultrasonic cavitation collapse energy and liquid pressure modulation to improve liquid jet disintegration to yield finer droplets have been offered. The tested parameters were horn frequency, liquid flow rate, and liquid injection pressure, and the results were presented. These results show that the UCA worked well in the reduction of the SMD at 60 kHz ultrasonic frequency, liquid injection pressure of 5.5 MPa and higher, and the liquid flow rates of 100 cc/min and 200 cc/min that were tested. The UCA demonstrated improvement in the disintegration of an axisymmetric liquid jet showing promise for a new type of spray atomizer driven by cavitation energy. This new type of atomizer can be more energy efficient than the current pressure driven atomizers, since the new atomizer requires lower pressure to achieve the same level of atomization.

The UCA's main design concept is the use of ultrasonic cavitation energy as a primary atomization mechanism. However, generation of cavitation bubbles at the ultrasonic horn tip was not explicitly measured in this experimental study. Thus a more detailed quantitative assessment on the role of cavitation on the atomization process within the UCA requires further study. From the UCA prototype characterization result, it can be surmised that the ultrasonic cavitation and pressure modulation have significant impact on the liquid jet disintegration.

4.2 INFRARED VISUALIZATION AND CHARACTERIZATION

The experimental procedure and results for the novel infrared thermography-based visualization and characterization technique developed for liquid sprays are presented in this section.

4.2.1 EXPERIMENTAL SETUP

A schematic of the experimental setup of the infrared thermography-based visualization and characterization technique is illustrated in Figure 4.10. The setup includes the paint applicator, the infrared camera, the radiation source, and a data processor. The infrared energy radiated by the background is attenuated by the spray, and the attenuated image is captured by the infrared camera.

To acquire high quality infrared images of the spray flow field, the blackbody background temperature was set at 30°C. This temperature setting was to allow for a

temperature difference between the coldest sections of the spray and the background not to exceed 10°C. This is necessary for excellent temperature contrast needed to view details of the spray flow field using infrared imaging. The working fluid was generally at room temperature, with the average temperature measured at 22°C. The background temperature was allowed to stabilize at the required temperature setting of 30°C before measurements are made. Once the background temperature stabilizes at 30°C, the atomizer was started, and the required operational conditions for which the measurements to be acquired are set. The spray was allowed to stabilize under these conditions before images are captured using the infrared camera.

The captured infrared images are later post-processed using the MATLAB image processing toolbox. The temperature map of the spray flow field is expressed as a map of radiant flux per unit surface area (W/m^2), using the following equation:

$$E = \varepsilon \sigma T^4 \quad (4.1)$$

where, ε is the emissivity of the blackbody background given as 0.96, σ is the Stefan-Boltzmann constant, given as $5.670 \times 10^{-8} \text{ W}/\text{m}^2 \cdot \text{K}^4$, and T the temperature measured by the infrared camera is express in Kelvin.

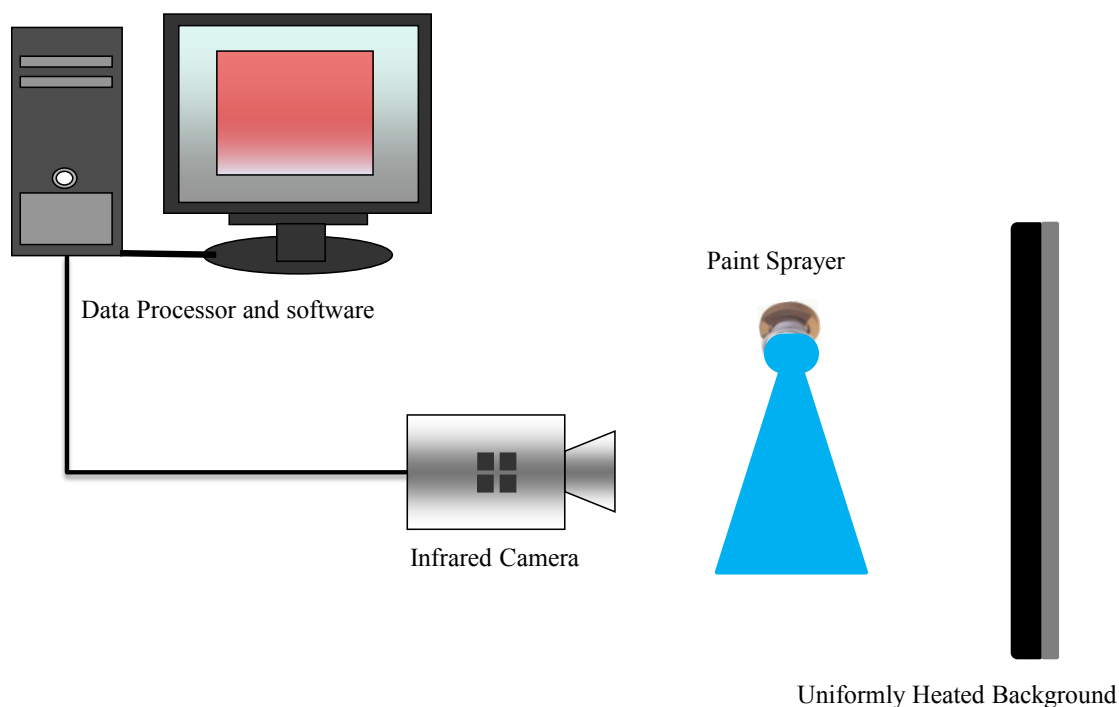


Figure 4.10: A schematic of the experimental setup for the infrared visualization and characterization technique.

For each of the three atomizers studied, several conditions were tested and both the visualization and characterizations results are offered in the following sections.

4.2.2 INFRARED VISUALIZATION RESULTS

This section presents the visualization results for the three atomizers studied. Note that the infrared wavelengths are attenuated less than the visible wavelengths by the spray (Labs and Parker, 2003, 2006). This is attributable to the fact that the attenuation of the electromagnetic wave within a scattering and an absorbing medium like a liquid spray

with the same size distribution will decrease with increasing wavelength within the electromagnetic spectrum.

4.2.2.1 HIGH-SPEED ROTARY BELL ATOMIZER VISUALIZATION RESULTS

The infrared thermography-based visualization results for the high-speed rotary bell atomizer for a liquid flow rate of 100 cc/min at bell cup rotation speeds of 20,000, 30,000, 40,000, and 50,000 rpm are shown in Figure 4.11a. Similar plots are repeated for a liquid flow rate of 200 cc/min in Figure 4.11b, a liquid flow rate of 300 cc/min in Figure 4.11c, and a liquid flow rate of 400 cc/min in Figure 4.11d.

The infrared images are captured at 300 frames/sec for each bell cup rotation speed. It can be observed from Figures 4.11a, 4.11b, 4.11c, and 4.11d that at 20,000 rpm the liquid droplets in the spray travels farther in the radial direction than the other rotation speeds. This behavior is explained in Figure 4.12. The shaping air, whose primary purposes are to support the transport of the paint droplets, stabilize the flow conditions around the atomizer, and permit a precise alignment of the spray pattern by limiting the atomizing cone, is supplied at a direction perpendicular to the trajectory of the liquid droplets.

The droplets follow a radial trajectory because of the centrifugal force used in generating them. As a result of the presence of the shaping air, the resultant trajectory of the droplets then becomes a function of the inertia of the droplets and the force of the shaping air. The radial travel distance of the droplets reduces with increasing bell cup

rotation speed, because the larger droplets have more inertia which resist the momentum force of the shaping airflow. As droplet size reduces with increasing bell cup rotation speed, the droplets become more affected by the shaping airflow, and thus their radial travel is curtailed. Note that the shaping airflow pressure was maintained constant, at 0.4 MPa, for all the conditions tested to simulate a practical operational condition.

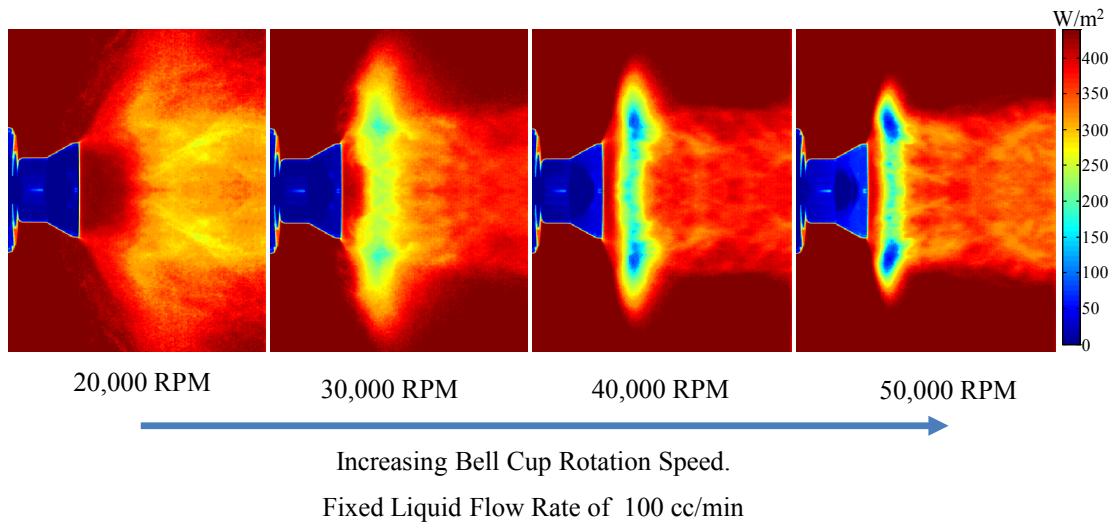


Figure 4.11a: Infrared visualization of the high-speed rotary bell atomizer showing increasing bell cup rotation speed for a liquid flow rate of 100 cc/min.

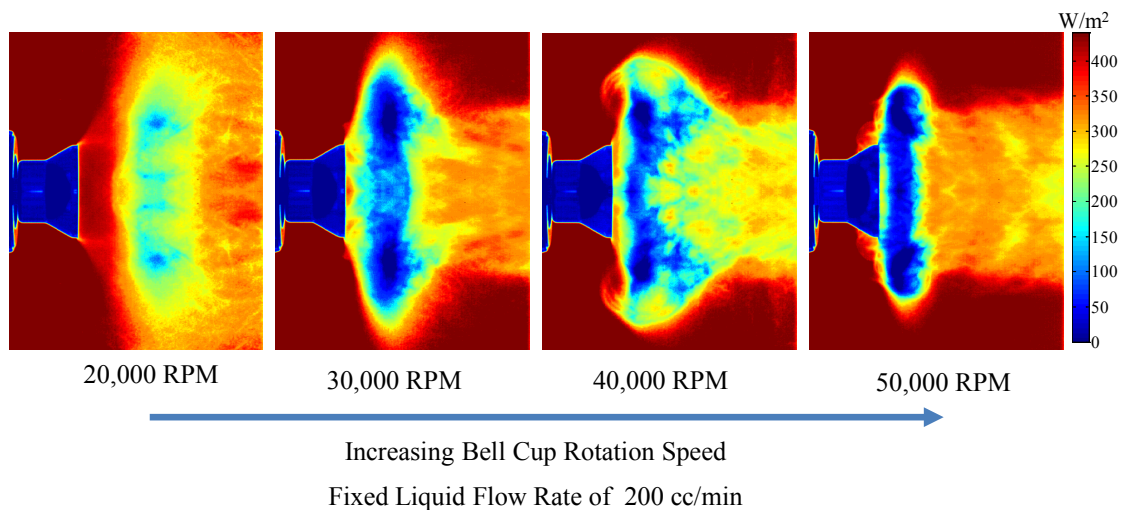


Figure 4.11b: Infrared visualization of the high-speed rotary bell atomizer showing increasing bell cup rotation speed for a liquid flow rate of 200 cc/min.

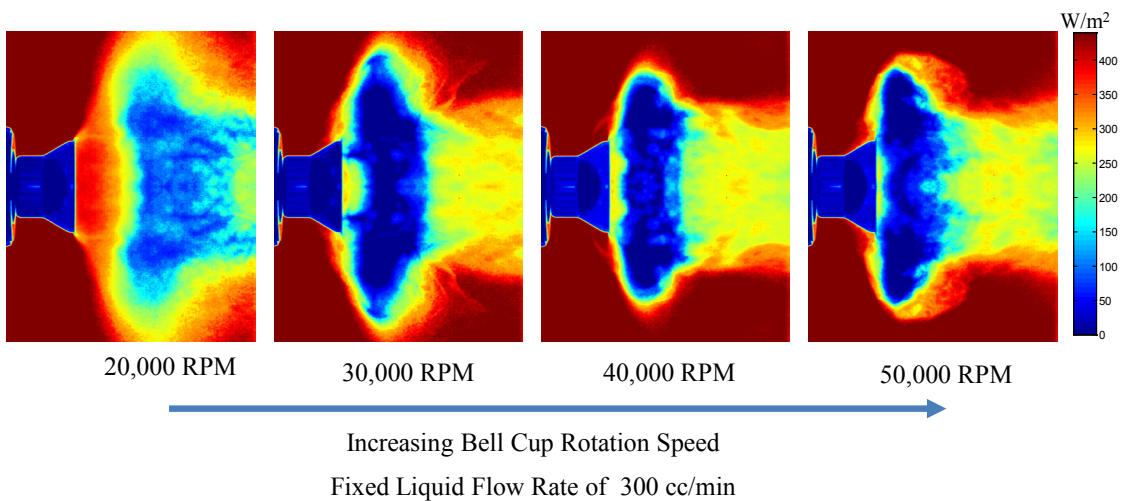


Figure 4.11c: Infrared visualization of the high-speed rotary bell atomizer showing increasing bell cup rotation speed for a liquid flow rate of 300 cc/min.

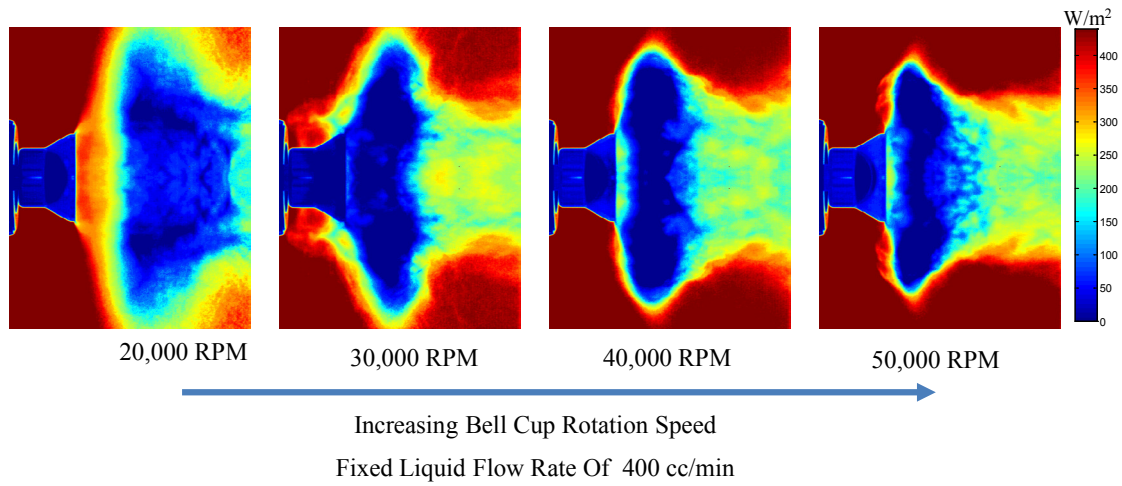


Figure 4.11d: Infrared visualization of the high-speed rotary bell atomizer showing increasing bell cup rotation speed for a liquid flow rate of 400 cc/min.

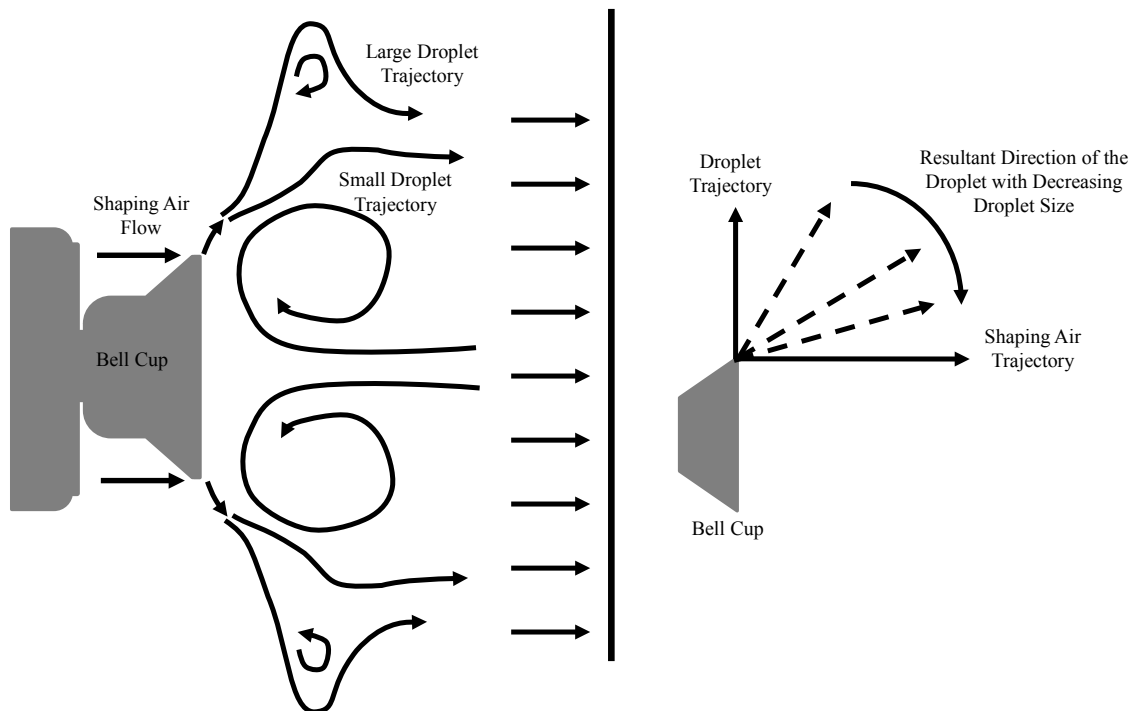


Figure 4.12: A schematic of the droplet trajectory in the high-speed rotary bell atomizer.

Figure 4.13 shows the SMD of the high-speed rotary bell atomizer for a liquid flow rate of 100cc/min as a function of bell cup rotation speed demonstrating that the SMD values decreases with increasing bell cup rotation speed. Figure 4.14 illustrates the plot of the droplet size distribution for a liquid flow rate of 100 cc/min at various bell cup rotation speeds. A leftward shift of the droplet size distribution is observed with increasing bell cup rotation speed, because the droplet size decreases with increasing bell cup rotation speed.

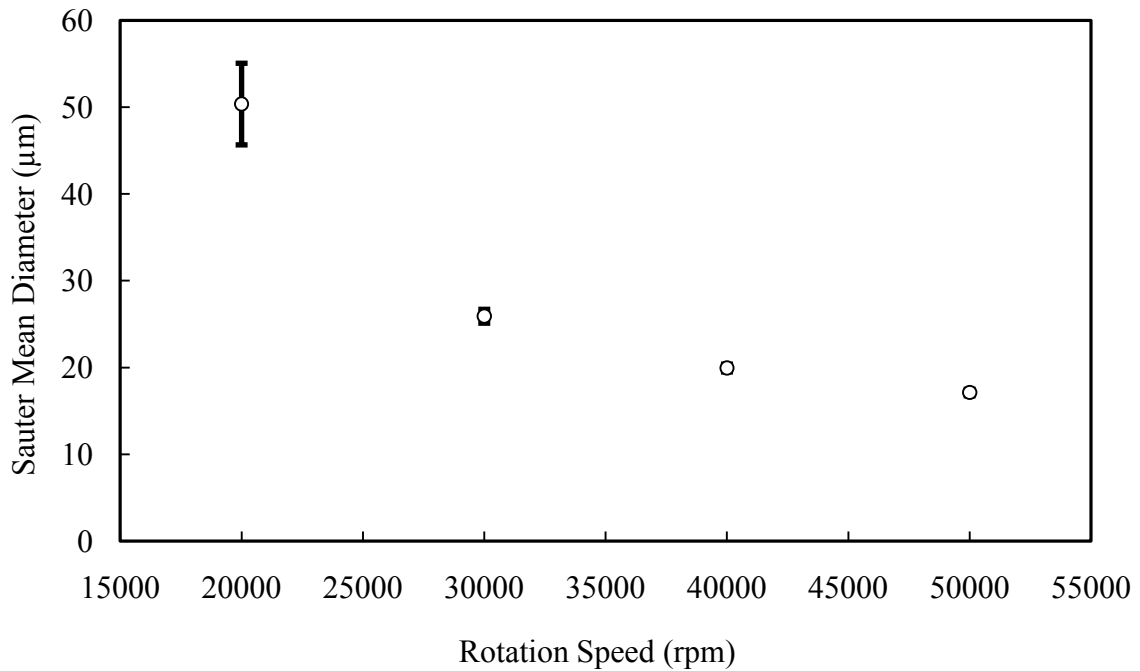


Figure 4.13: The Sauter mean diameter of the high-speed rotary bell atomizer for a liquid flow rate of 100cc/min at various bell cup rotation speeds.

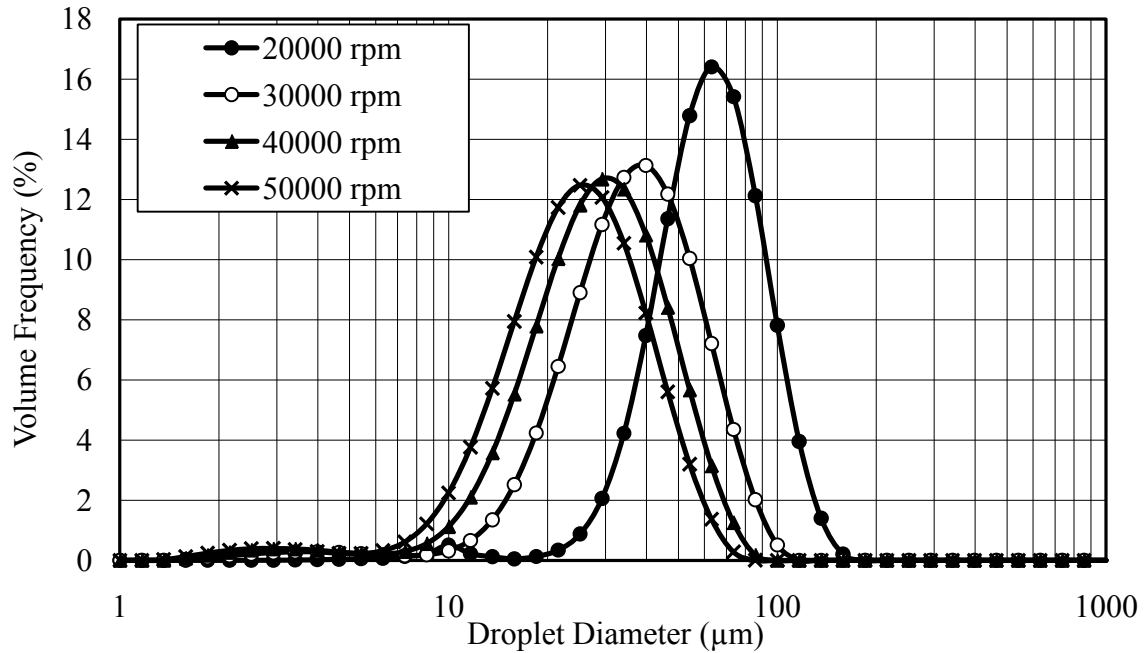


Figure 4.14: Droplet size distribution of the high-speed rotary bell atomizer for a liquid flow rate of 100 cc/min at various bell cup rotation speeds.

The SMD and the droplet size distribution plots are not repeated here for the other liquid flow rate condition tested because the trend is similar. Figures 4.11a, 4.11b, 4.11c, and 4.11d shows that under each bell cup rotation speed, the attenuation of the infrared energy increases with increasing liquid flow rates. Figure 4.15 shows the infrared thermographic image of the high-speed rotary bell atomizer with a fixed bell cup rotation speed of 40,000 rpm for increasing liquid flow rate.

The infrared thermographic image obtained is a function of the extinction of the infrared energy radiated by the source as it passes through the spray. The extinction is a function of the density of the participating medium (the spray). As the density of the portion of the spray increases, so does the attenuation of the infrared energy. Clearly shown in Figure 4.15, increase in liquid flow rate increases the density of the spray. The

corresponding plot of the SMD is shown in Figure 4.16 where the SMD increases with increasing liquid flow rate at a constant bell cup rotation speed. To maintain the same SMD at increasing liquid flow rate, the bell cup rotation speed must be increased accordingly.

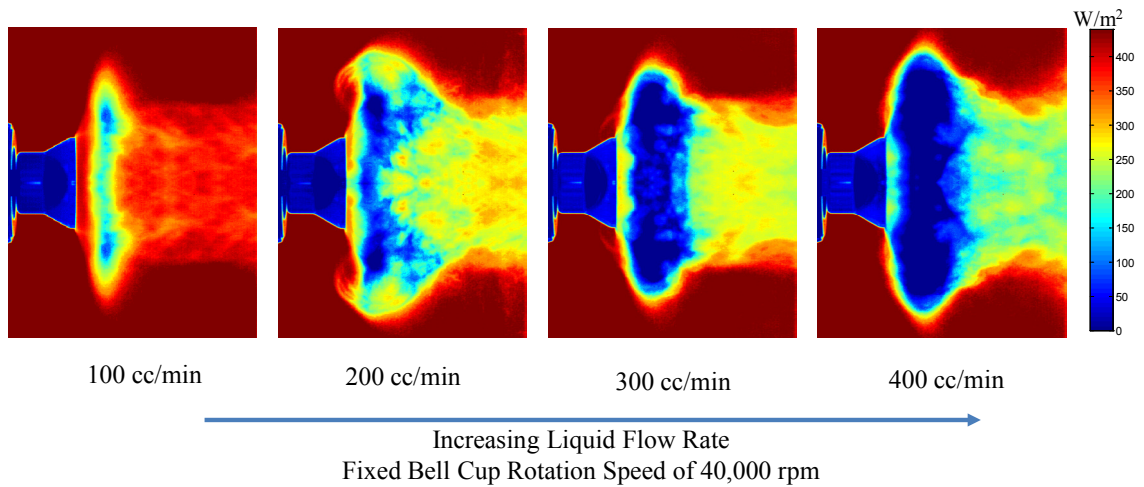


Figure 4.15: Infrared visualization of the high-speed rotary bell atomizer spray at a bell cup rotation speed of 40,000 rpm, showing increasing liquid flow rate.

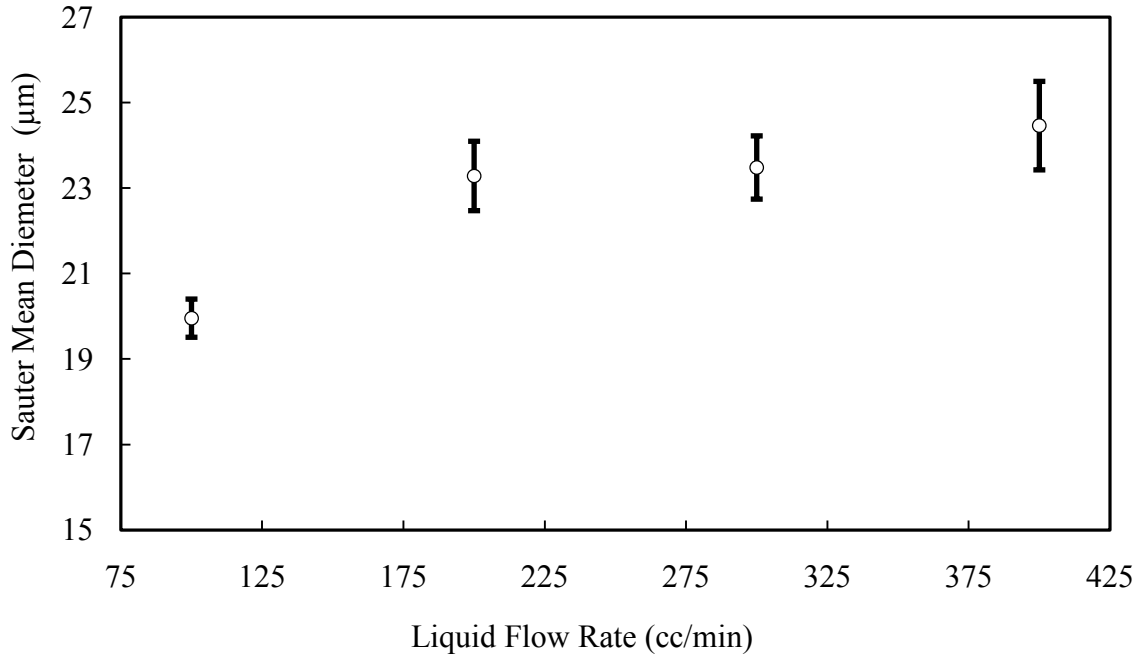


Figure 4.16: The Sauter mean diameter of the high-speed rotary bell atomizer spray at a bell cup rotation speed of 40,000 rpm, showing increasing liquid flow rate.

The high-speed rotary bell atomizer produces axisymmetric sprays, a cross section of which is illustrated in Figure 4.17. The cross-section at location *a* in Figure 4.17 has the appearance of a hollow spray; a closer look reveals a toroid shape ring, the detail of which is shown in Figure 4.18, where the infrared images are taken at an angle. The interaction between the liquid droplets and the shaping airflow generate vortices which form a toroid shaped ring. The illustration of the toroid vortex tube generated as a result of this interaction is shown in Figure 4.12. Figure 4.17 shows that the toroid shape collapses into a full spray in the cross-section at location *b* further downstream from location *a*.

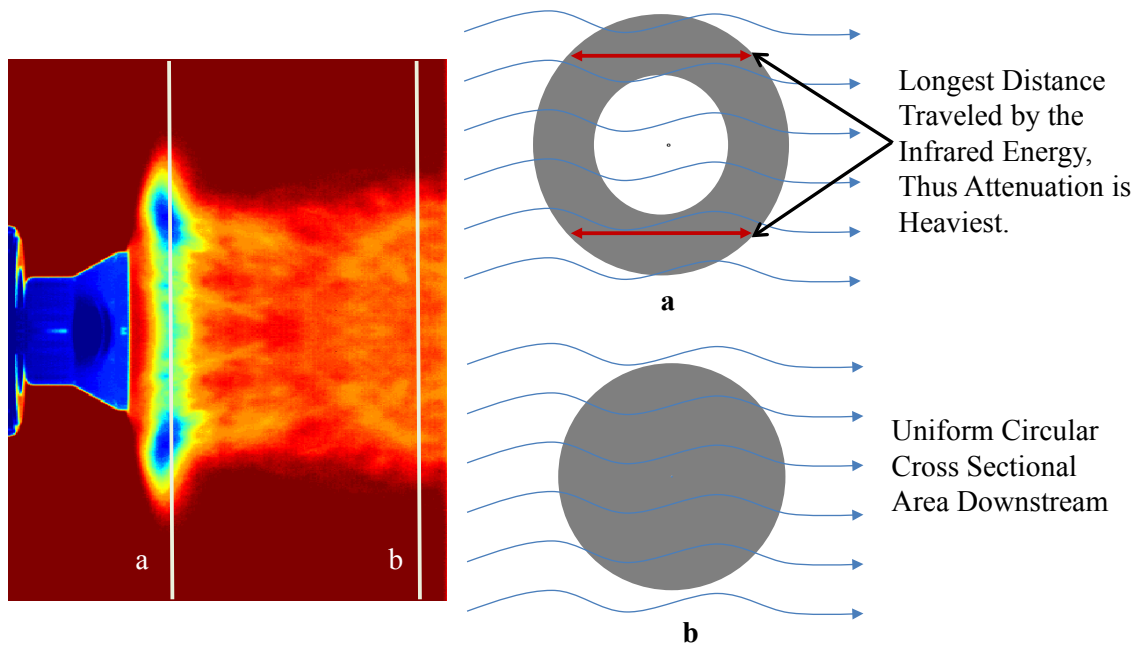


Figure 4.17: The cross-sectional area of the high-speed rotary bell atomizer spray.

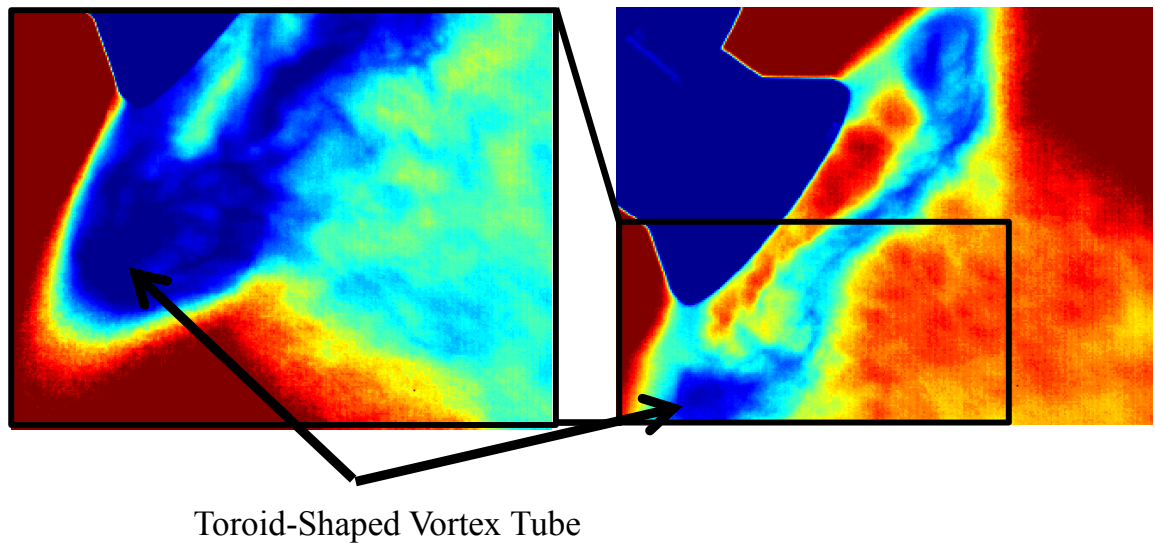


Figure 4.18: A detailed structure of the toroid-shape inside the high speed rotary bell atomizer spray.

The toroid shaped vortex ring observed in the high-speed rotary bell atomizer spray is formed as a result of the interactions between the shaping airflow and the liquid droplets. The interaction between these two high speed flows impinging perpendicularly on each other creates a vortex motion. This vortex motion forms the toroid shaped vortex ring which exhibits periodic vortex shedding illustrated in Figure 4.19. Vortex shedding is an unsteady flow that takes place in special flow velocities. In this flow, vortices develop around the toroid-shaped vortex tube, created as a result of the interaction between the shaping airflow and the liquid droplets which detach periodically from either side of the main vortex tube.

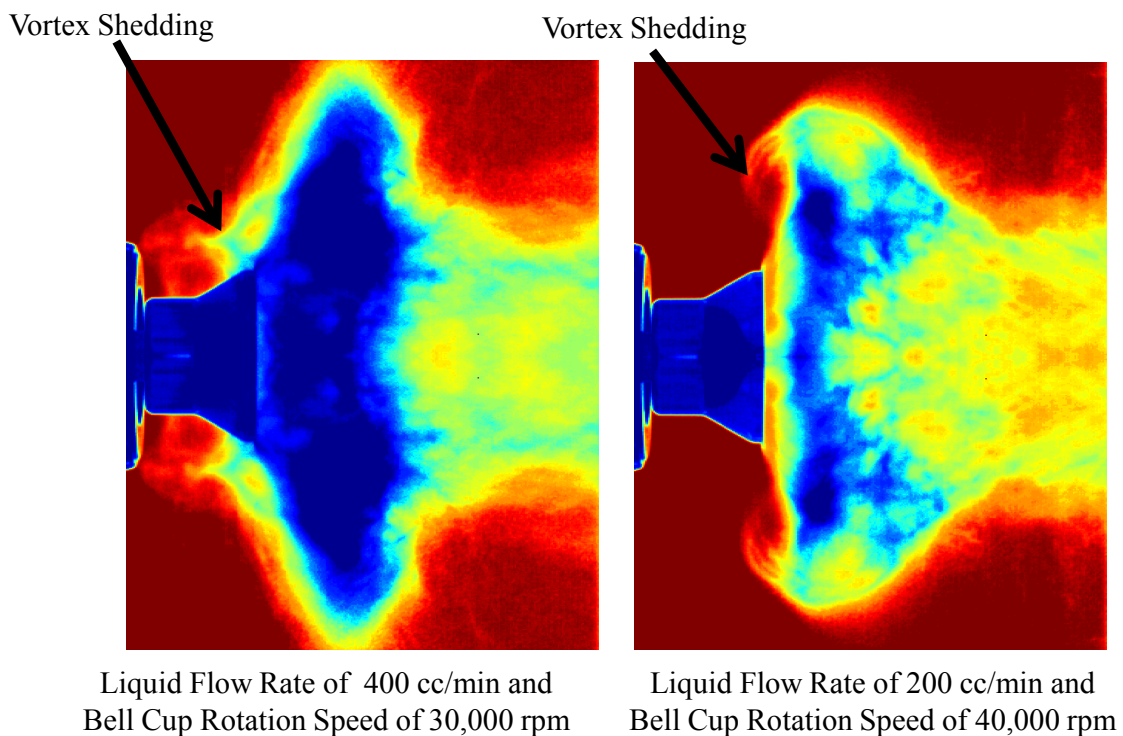


Figure 4.19: The infrared image showing vortex shedding from the toroid shaped vortex tube.

To visualize a cross-sectional structure of the toroid-shaped vortex tube, a laser light sheet generated by a continuous wave laser is passed through a cylindrical lens and expanded to penetrate the central axial plane of the spray. The Shimadzu HPV-1 high speed camera, which is capable of recording images at one million frames per second, was used to obtain visible images of the central axial plane with a liquid flow rate of 200 cc/min at various rotation speeds. The high speed images obtained at 125 frames/s are shown in Figure 4.20.

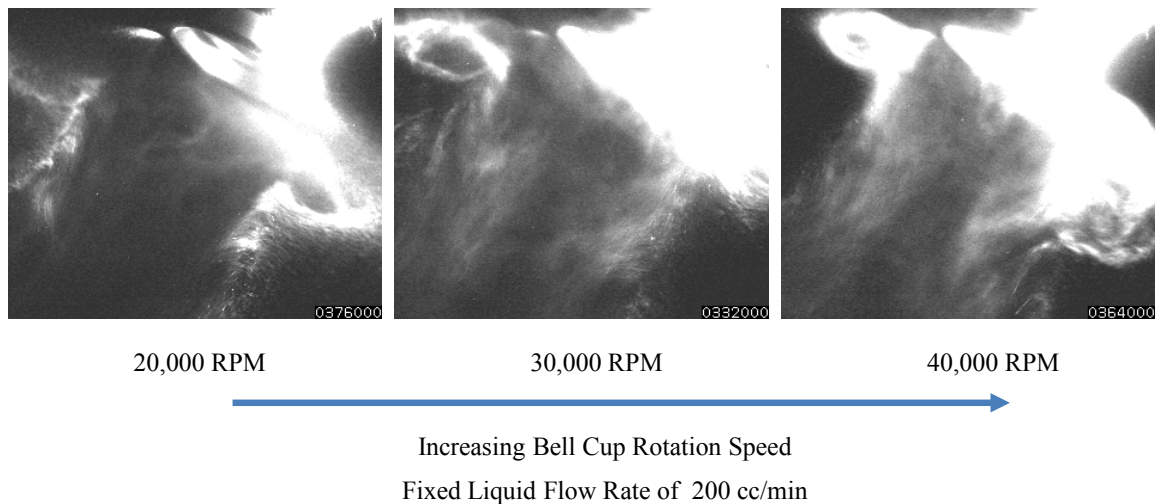


Figure 4.20: A high speed visual image of the high-speed rotary bell atomizer showing increasing bell cup rotation speed for a liquid flow rate of 200 cc/min.

4.2.2.2 HIGH VOLUME LOW PRESSURE AIR-ASSISTED ATOMIZER VISUALIZATION RESULTS

For the infrared visualization of the HVLP air-assisted atomizer, two measurement orientations are considered to fully describe the spray pattern: the

orientation of the measurement taken along the long axis of the fan-shaped spray (Figure 4.21a) and the orientation of the measurement taken along the short axis of the fan-shaped spray (Figure 4.21b).

Unlike the high-speed rotary bell atomizer which produces axisymmetric spray patterns, the HVLP air-assisted atomizer generates a fan-shaped spray. By taking measurements of both orientations and using edge detection technique, the values of the major axis of the assumed elliptical cross-sectional area of the fan-shaped spray are estimated along the spray axis. With the major axis obtained, the depth of the spray, b , can be computed along the spray axis. The value of b is needed to compute the liquid volume fraction and the droplet number density (Equations 2.33 and 2.34).

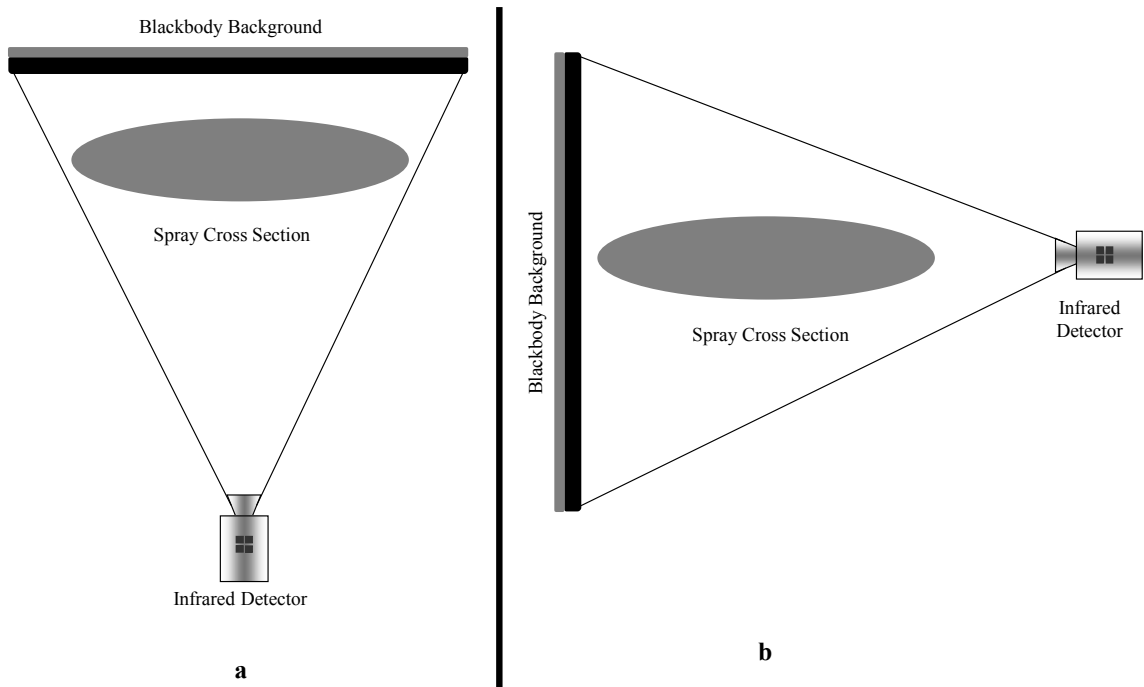


Figure 4.21: A schematic of the cross section of the flat spray and the measurement orientation: (a) orientation for the long axis, (b) orientation for the short axis.

The infrared visualizations of the long axis of the spray generated by the HVLP air-assisted atomizer are shown in Figure 4.22 for the increasing liquid flow rate with all other parameters maintained constant. The corresponding infrared visualizations of the short axis of the spray from the HVLP air-assisted atomizer are shown in Figure 4.23. The SMD and droplet size distribution for these conditions are respectively presented in Figures 4.24 and 4.25. Figure 4.22 shows that the spray angle opens up with an increase in the liquid flow rate and keeping all other operational parameters constant. Correspondingly, in Figure 4.24 the SMD increases almost linearly with an increase in the liquid flow rate. Figure 4.25 shows a rightward shift of the droplet size distribution with an increase in the liquid flow rate.

The infrared signal attenuation gets stronger as the droplet sizes and concentrations increase (Figure 4.23), demonstrated in the image of the short axis showing a much denser spray because the optical path length is longer. The increasing liquid flow rate shows a progressively denser core from a liquid flow rate of 100 cc/min to 400 cc/min, with the less dense core observed at a liquid flow rate of 100 cc/min, and the densest core observed at 400 cc/min.

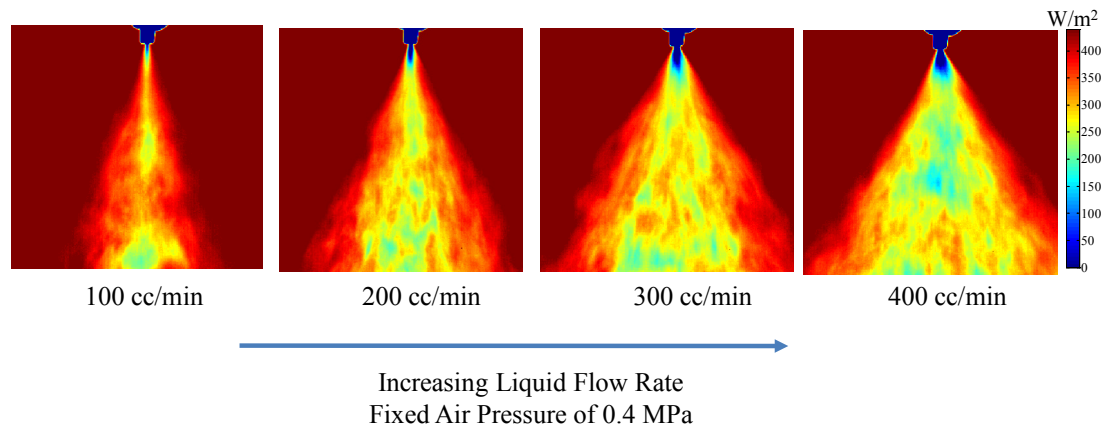


Figure 4.22: Infrared themographic images of the long axis of the HVLP air-assisted atomizer, with increasing liquid flow rate at a fixed air pressure of 0.4 MPa.

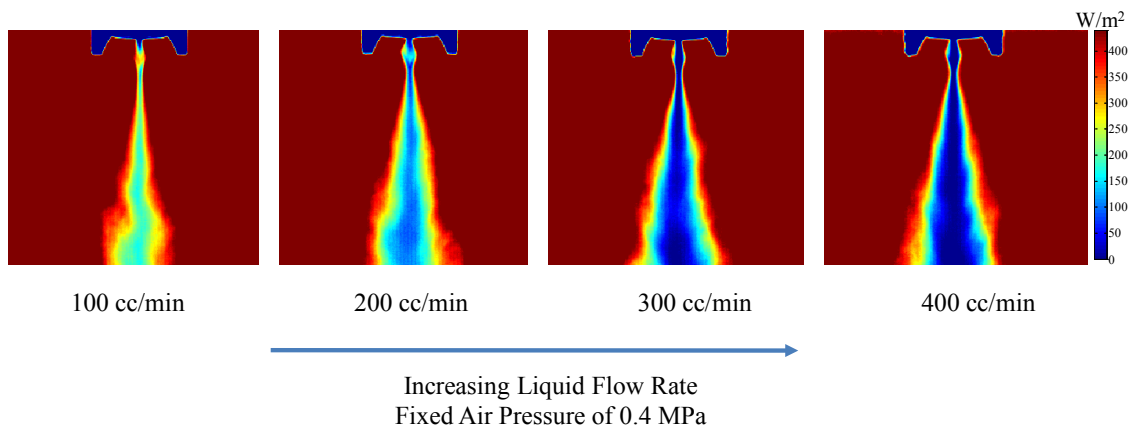


Figure 4.23: Infrared themographic images of the short axis of the HVLP air-assisted atomizer, with increasing liquid flow rate at a fixed air pressure of 0.4 MPa.

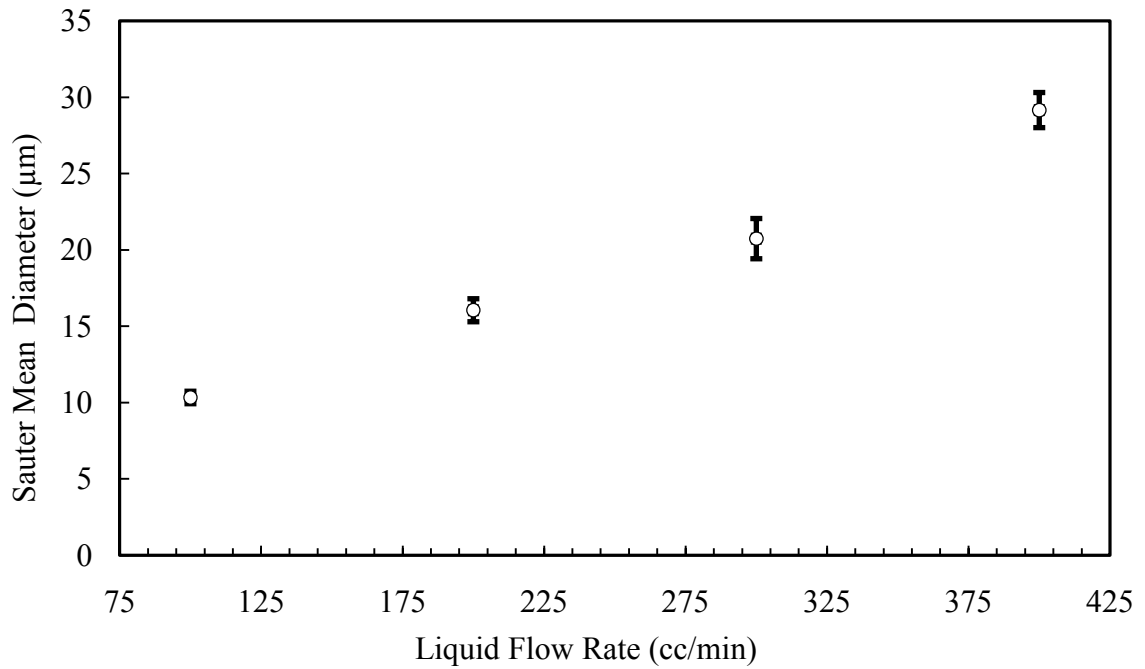


Figure 4.24: The Sauter mean diameter of the HVLP air-assisted atomizer with increasing liquid flow rate.

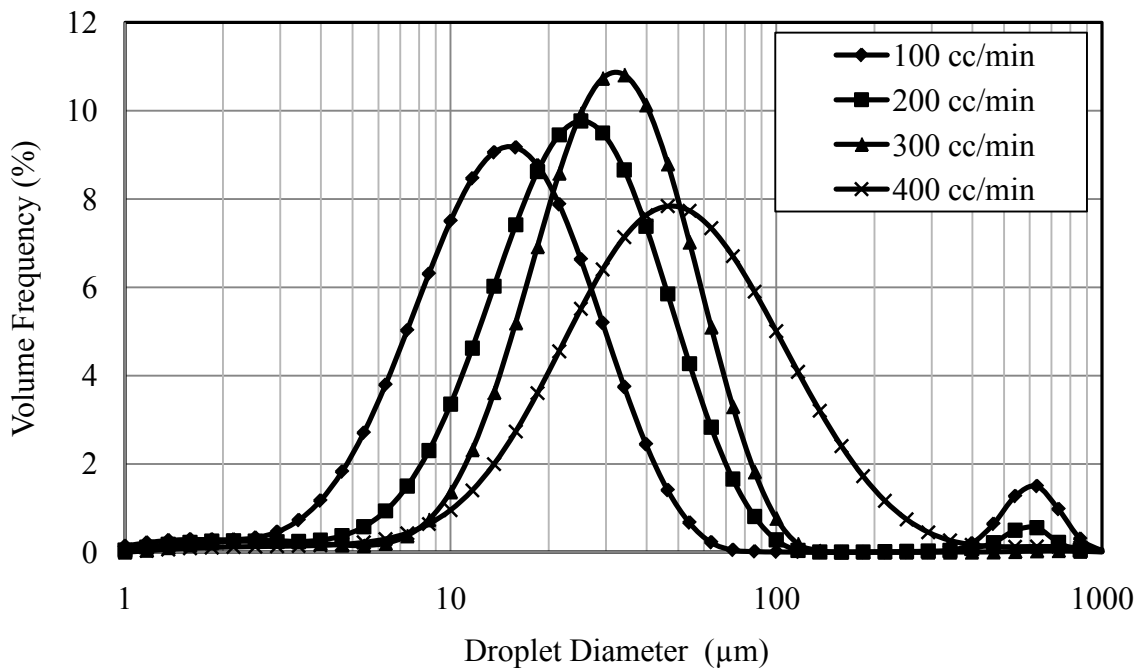


Figure 4.25: Droplet size distribution of HVLP air-assisted atomizer at various flow rates.

Figure 4.26 shows the infrared images for the HVLP air-assisted atomizer illustrating the increasing spray angle as a result of increasing liquid flow rates while maintaining all other operational parameters. The spray angle at a liquid flow rate of 100 cc/min was measured to be about 40°. For a liquid flow rate of 200 cc/min, the spray angle was determined to be about 50° and about 65° for a liquid flow rate of 300 cc/min. For a liquid flow rate of 400 cc/min, the spray angle was assessed to be about 70°.

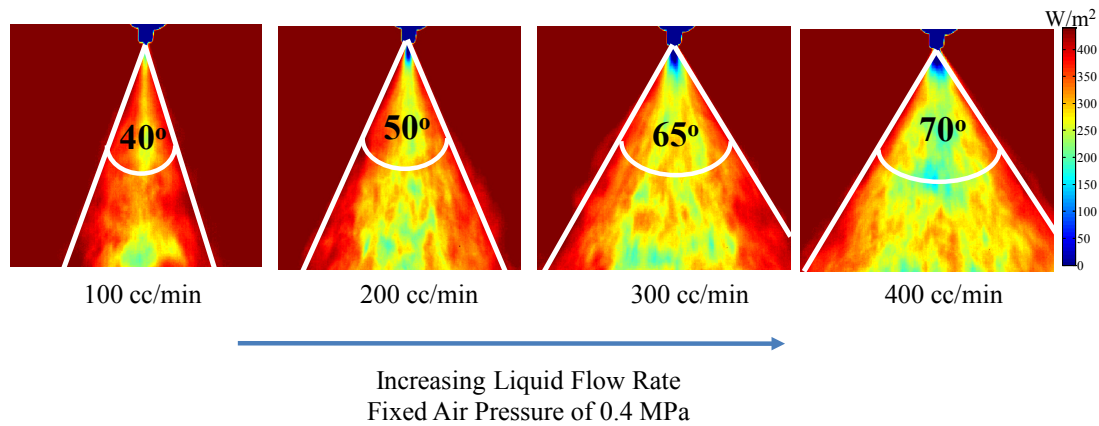


Figure 4.26: Infrared thermographic images of the long axis of the HVLP air-assisted atomizer, with increasing liquid flow rate at a fixed air pressure of 0.4 MPa showing increasing spray angle.

A careful observation of the infrared thermographic images obtained for the HVLP air-assisted atomizer measured along the short axis (Figure 4.23), reveals an expansion region just outside of the nozzle exit. The liquid jet emerging from the liquid nozzle opening comes into contact with the annulus atomizing air. Figure 4.27 show that the two-fluid mixture appears to expand just outside the nozzle exit, and then necking is observed before the spray begins to open up.

The lateral air supplied from both sides of the spray impinges on each other and is used to adjust the shape of the spray pattern. The impingement of the lateral pattern air creates a high pressure zone which forces the twin fluid mixture emerging from the nozzle to form a bottleneck at the region of the impingement. This constriction, as a result of an increased pressure zone, causes the jet upstream to expand creating the blob that is observed in Figure 4.27a and is explained by the illustration in Figure 4.27b.

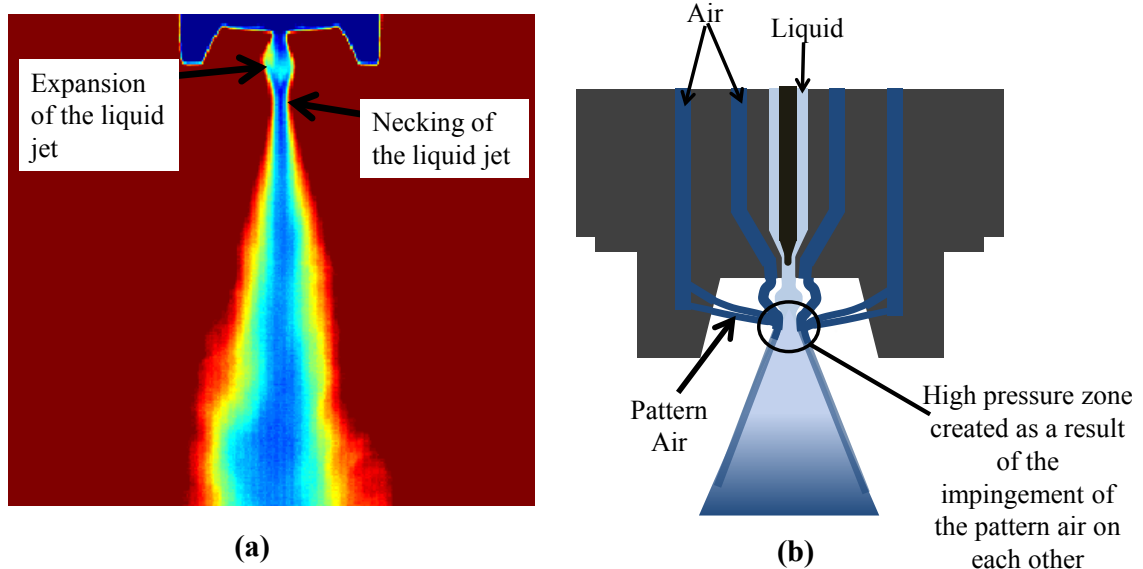


Figure 4.27: A schematic explanation of the expansion and necking in the infrared images along the short axis of the HVLP air-assisted atomizer: (a) the infrared image showing the bottleneck, (b) schematics explaining the phenomenon.

4.2.2.3 ULTRASONIC CAVITATING ATOMIZER RESULTS

The infrared thermographic images of the ultrasonic cavitating atomizer are shown in Figure 4.25 for a liquid flow rate of 100cc/min for an increasing atomizing pressure of 4.1, 4.8, 5.5, and 6.2 MPa. A similar plot for a liquid flow rate of 200 cc/min

is shown in Figure 4.26 for increasing atomizing pressure. The ultrasonic cavitating atomizer produces a full conical axisymmetric spray with circular cross-section. The spray is not entirely axisymmetric and slightly skewed to the right because, difficulty in micro-scale precision fabrication caused the ultrasonic horn to be slightly placed off center inside the nozzle head. However, this slight off-center placement of the horn inside the nozzle head did not cause any serious concerns for the use of this prototype to validate the concept of neither the UCA atomizer nor the infrared thermography visualization technique in spray behavior.

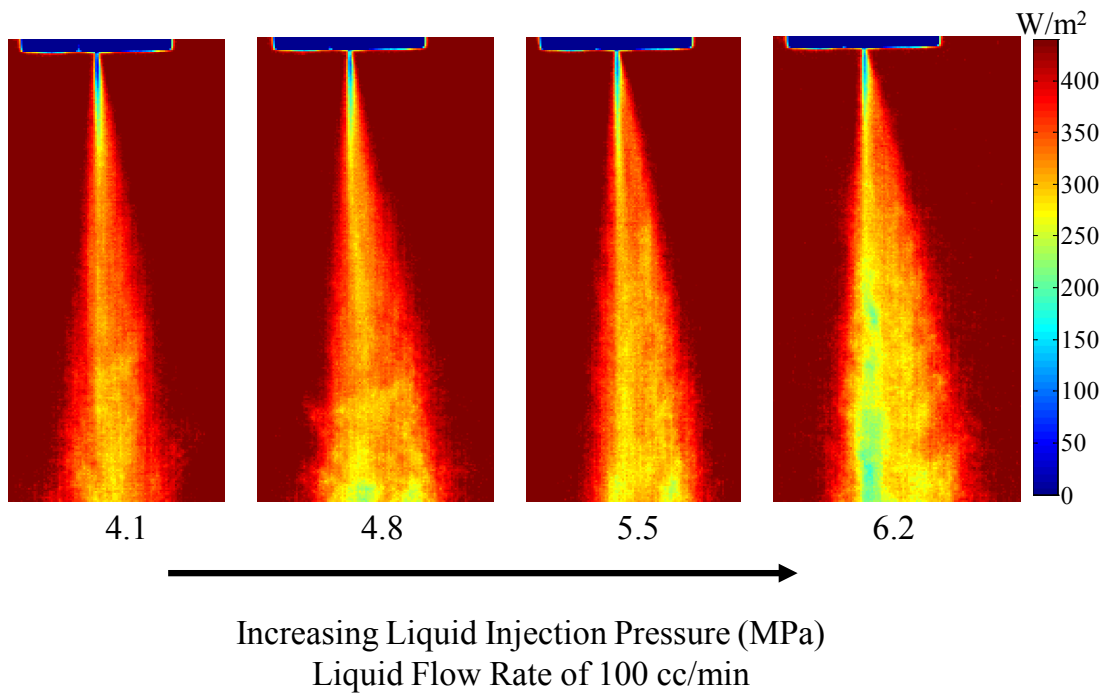


Figure 4.28: Infrared images of the UCA spray with increasing liquid injection pressure at a liquid flow rate of 100 cc/min.

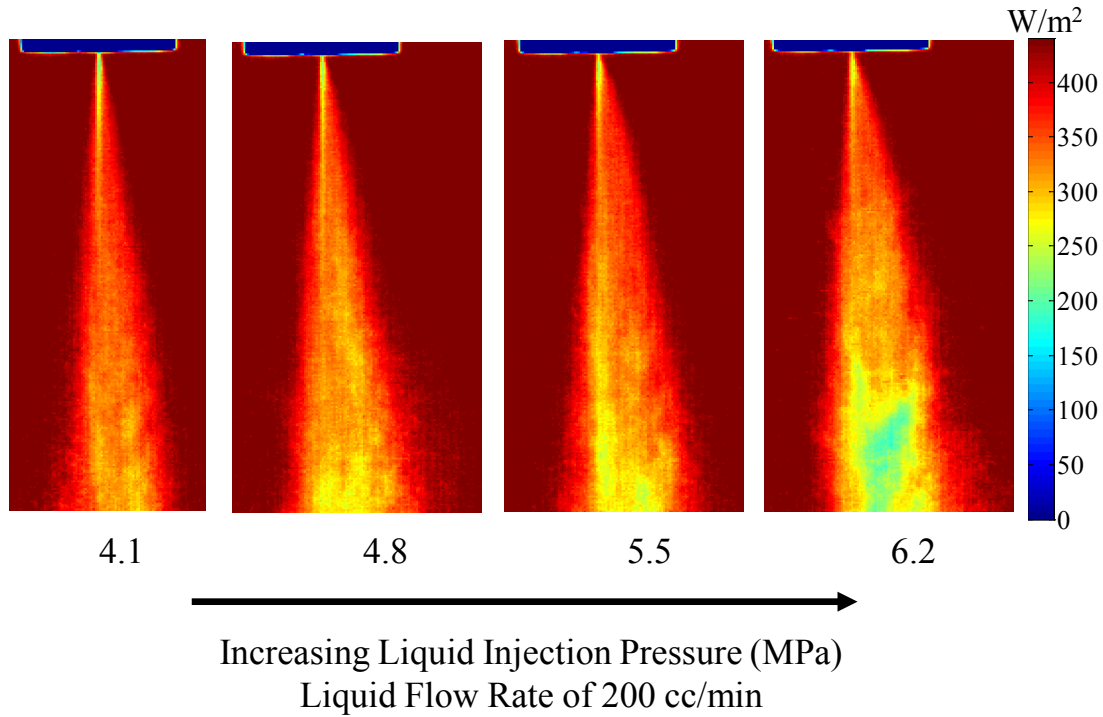


Figure 4.29: Infrared images of the UCA spray with increasing liquid injection pressure at a liquid flow rate of 200 cc/min.

The infrared thermography-based visualization technique for liquid spray was developed and its performance demonstrated for the visualization of the spray generated by the UCA prototype and two different types of automotive paint sprayers: the high-speed rotary bell atomizer and the HVLP air-assisted atomizer. Macroscopic features like spray pattern and angle, together with the flow structure in the entire spray flow field have been presented. Because the infrared band on the electromagnetic spectrum has a longer wavelength than visible light, allowing the infrared energy to be less attenuated in the spray than visible light for revealing more detailed information about the spray structure and concentration. This technique can be a useful tool in the development of new atomizers as well as in the understanding of the flow structure in existing ones.

4.2.3 VOLUME FRACTION AND NUMBER DENSITY RESULTS

The infrared thermography-based characterization data, which focuses primarily upon the estimation of the droplet number density and the liquid volume fraction inside the spray, is presented herein. To be able to estimate these two values, the droplet size information must be obtained via another method. Using Malvern Spraytec system to acquire this information, the droplet number density and the liquid volume fraction are obtained from the infrared images using equations derived earlier (Equations 2.33 and 2.34). The results are presented here for all three atomizers studied.

4.2.3.1 THE VOLUME FRACTION AND THE NUMBER DENSITY RESULTS FOR HIGH-SPEED ROTARY BELL ATOMIZER

The droplet size measurements are made along the spray center line 150 mm downstream from the rotary bell cup exit, using the Malvern Spraytec system. The images are analyzed at a pixel location corresponding to the measurement volume of the Malvern Spraytec system. With the SMD (D_{32}) obtained, the liquid volume fraction f_v is calculated at the chosen pixel location using Equation (2.31). The corresponding droplet number density is obtained from Equation (2.32). The data were processed and averaged in time over 900 frames obtained at 300 frames/s.

Figure 4.30 compares the liquid volume fraction and the SMD as a function of bell cup rotation speed at a pixel location on the spray centerline 150 mm from the rotating bell cup tip for a fixed liquid flow rate of 100 cc/min. Figure 4.31 compares the droplet number density and the SMD as a function of bell cup rotation speed at a pixel

location on the spray centerline 150 mm from the rotating bell cup tip for a fixed liquid flow rate of 100 cc/min. Similar results for a liquid flow rate of 400 cc/min are shown in Figures 4.32 and 4.33 for the liquid volume fraction and the droplet number density, respectively. The trend for both liquid flow rates was similar, with both the liquid volume fraction and the SMD decreasing while the bell cup rotation speed was increasing. On the other hand, the droplet number density increased with decreasing SMD and increasing bell cup rotation speed.

As the droplet size reduced, the liquid volume fraction f_v , which is defined as the ratio of equivalent volume of the liquid to a given volume of the gas and liquid mixture, decreased accordingly. This occurred because as the spray mixture became finer, air (which is the continuous medium) fills in between the droplets, consequently causing the volume fraction to reduce. Similarly, the droplet number density, which is defined as the number of liquid droplets per unit volume, increases with decreasing droplet size. This is attributable to the fact that as the spray becomes finer, the number of liquid droplets occupying a given volume in the spray increases as bigger droplets breakdown to form smaller droplets, the number count per unit area increases.

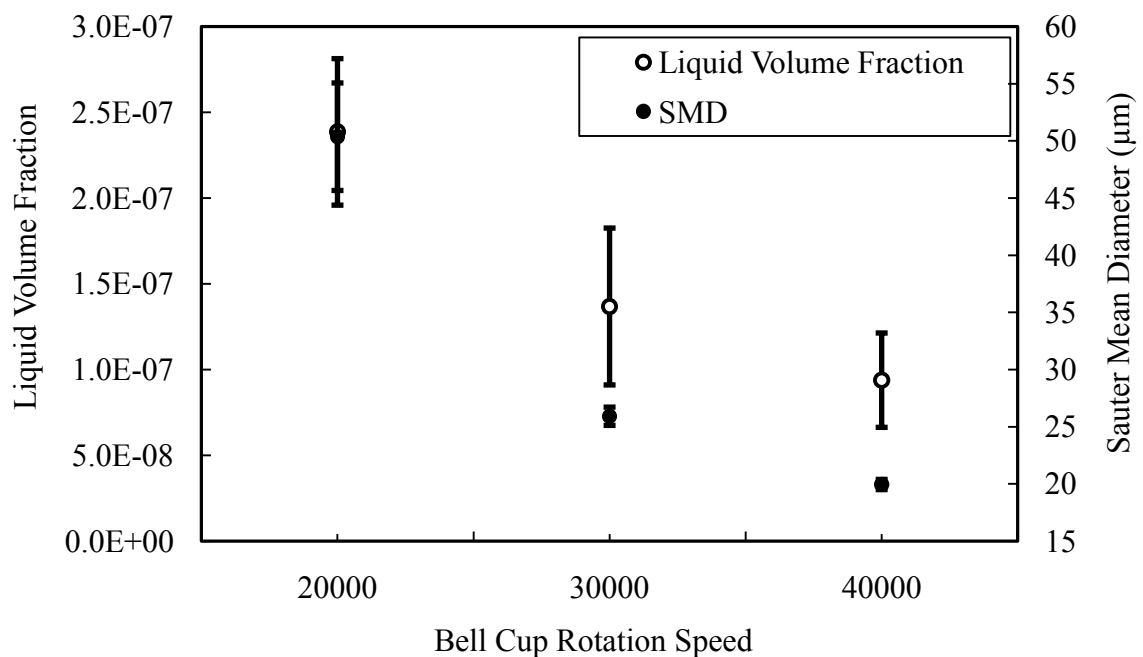


Figure 4.30: A comparison of the liquid volume fraction and the Sauter mean diameter for the high-speed rotary bell atomizer showing increasing bell cup rotation speed for a liquid flow rate of 100 cc/min.

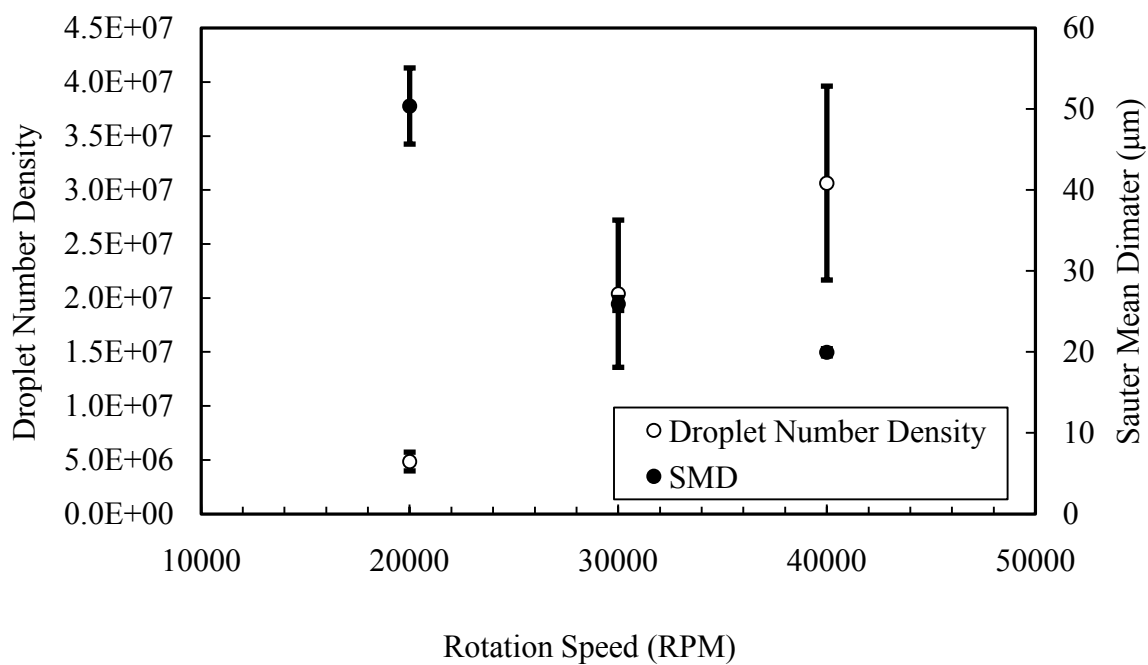


Figure 4.31: A comparison of the droplet number density and the Sauter mean diameter for the high-speed rotary bell atomizer showing increasing bell cup rotation speed for a liquid flow rate of 100 cc/min.

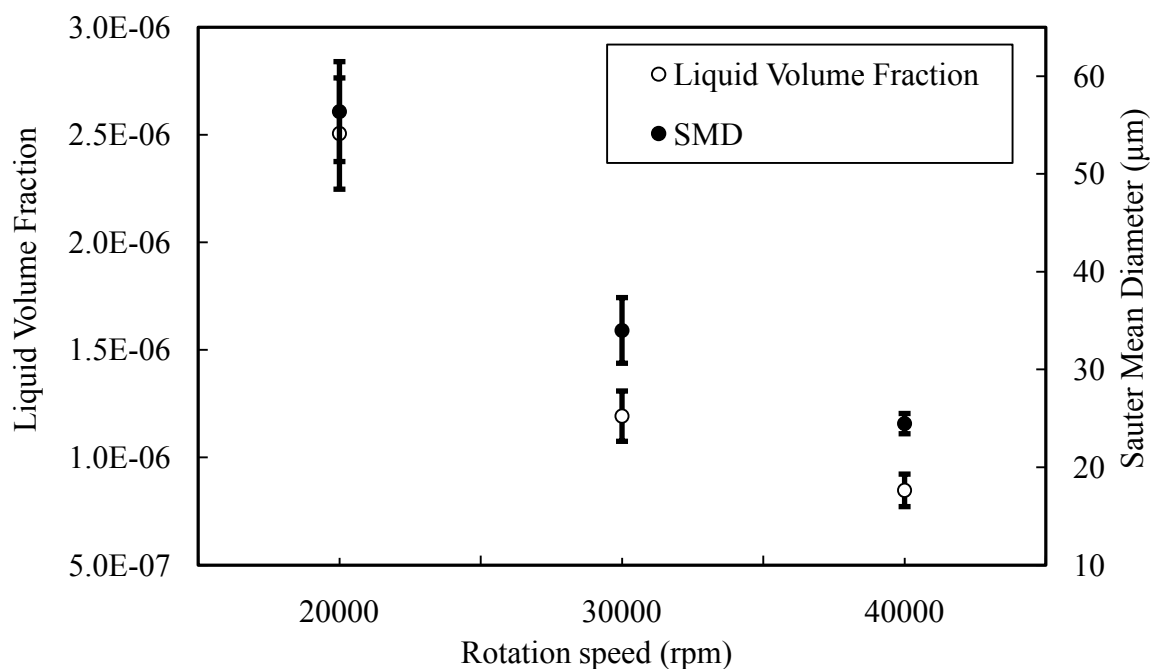


Figure 4.32: A comparison of the liquid volume fraction and the Sauter mean diameter for the high-speed rotary bell atomizer showing increasing bell cup rotation speed for a liquid flow rate of 400 cc/min.

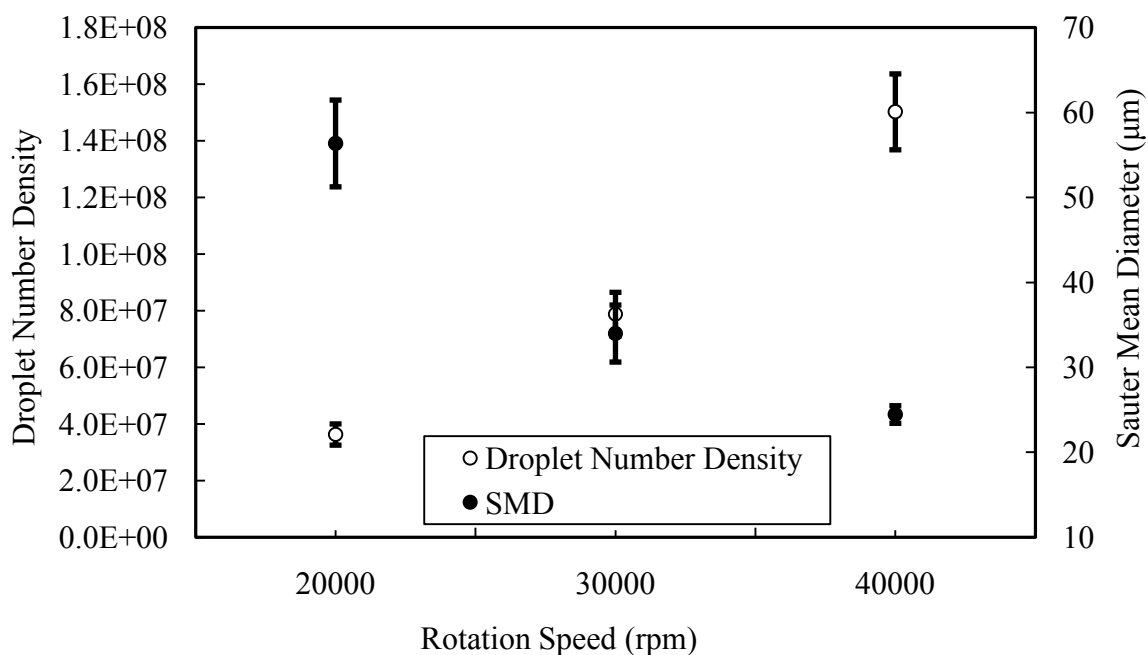


Figure 4.33: A comparison of the droplet number density and the Sauter mean diameter for the high-speed rotary bell atomizer showing increasing bell cup rotation speed for a liquid flow rate of 400 cc/min.

Figure 4.34, compares the liquid volume fraction and the SMD as a function of liquid flow rate at a pixel location on the spray centerline 150 mm from the rotating cup tip for a fixed bell cup rotation speed of 40,000 rpm. Similarly Figure 4.35 compares the droplet number density and the SMD as a function of liquid flow rate at a pixel location on the spray centerline at 150 mm from the rotating bell cup tip for a fixed bell cup rotation speed of 40,000 rpm. The SMD, the liquid volume fraction, and the droplet number density all increase with increasing liquid flow rate at a fixed bell cup rotation speed of 40,000 rpm.

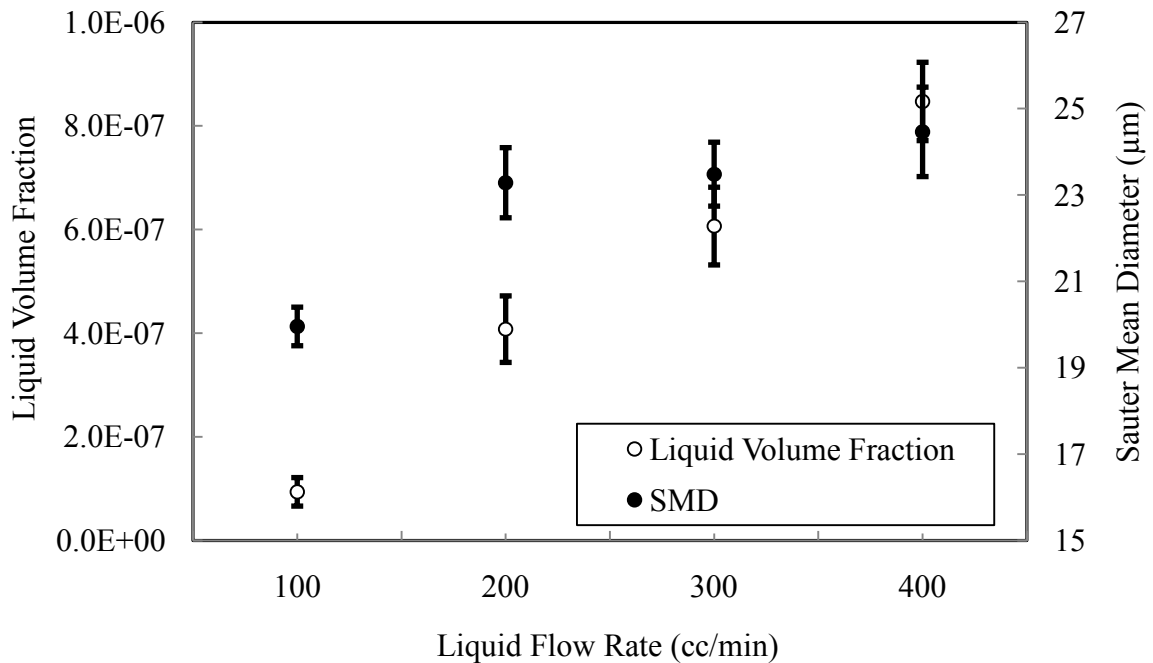


Figure 4.34: A comparison of the liquid volume fraction and the Sauter mean diameter for the high-speed rotary bell atomizer showing increasing liquid flow rate for a fixed bell cup rotation speed of 40,000 rpm.

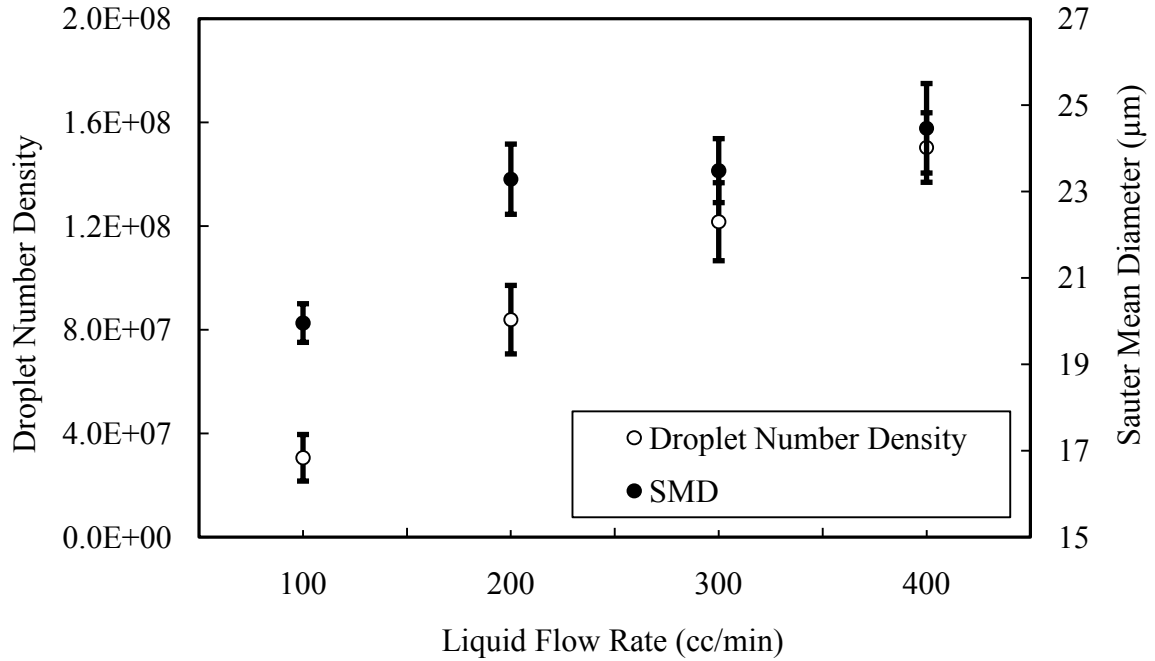


Figure 4.35: A comparison of droplet number density and the Sauter mean diameter for the high-speed rotary bell atomizer showing increasing liquid flow rate for a fixed bell cup rotation speed of 40,000 rpm.

4.2.3.2 VOLUME FRACTION AND NUMBER DENSITY RESULTS FOR HIGH VOLUME LOW PRESSURE AIR-ASSISTED ATOMIZER

As was in the case of the high-speed rotary bell atomizer, the droplet size measurements for the HVLP air-assisted atomizer are made along the spray center line of the longer cross sectional axis at 100 mm downstream from the nozzle exit using the Malvern Spraytec system. The infrared images are analyzed at a pixel location corresponding to the measurement volume of the Malvern Spraytec system. With the SMD obtained, the liquid volume fraction f_v is calculated at the chosen pixel location using Equation (2.31). The corresponding droplet number density is obtained from Equation (2.32). The data were processed and averaged in time over 900 frames obtained

at 300 frames/s. The standard deviations for the measurement are shown as error in the plot.

Figure 4.36 compares the average liquid volume fraction and the average SMD as a function of liquid flow rate at a pixel location on the spray centerline 100 mm from the nozzle exit for a fixed air pressure of 0.4 MPa. Similarly, Figure 4.37 compares the average droplet number density and the SMD as a function of liquid flow rate at a pixel location on the spray centerline at 100 mm from the nozzle exit for an air pressure of 0.4 MPa. The SMD and the liquid volume fraction increases with increasing liquid flow rate. The droplet number density, on the other hand, decreases with increasing liquid flow rate.

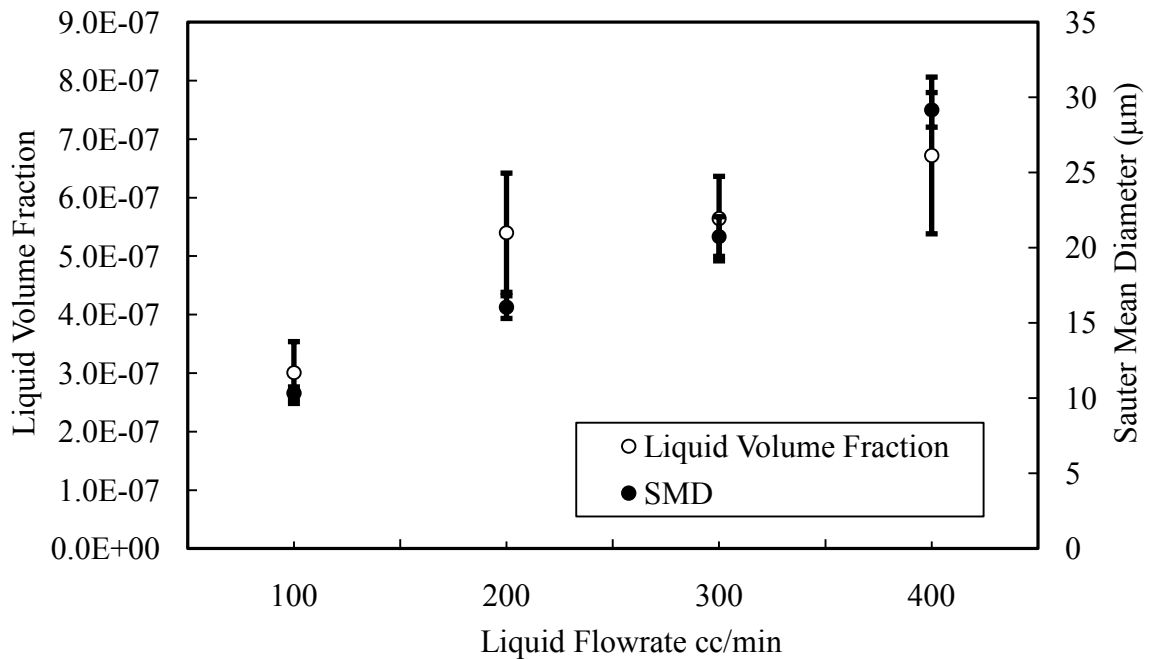


Figure 4.36: A comparison of the liquid volume fraction and the Sauter mean diameter for HVLP air-assisted atomizer showing increasing liquid flow rate at a fixed air pressure of 0.4 MPa.

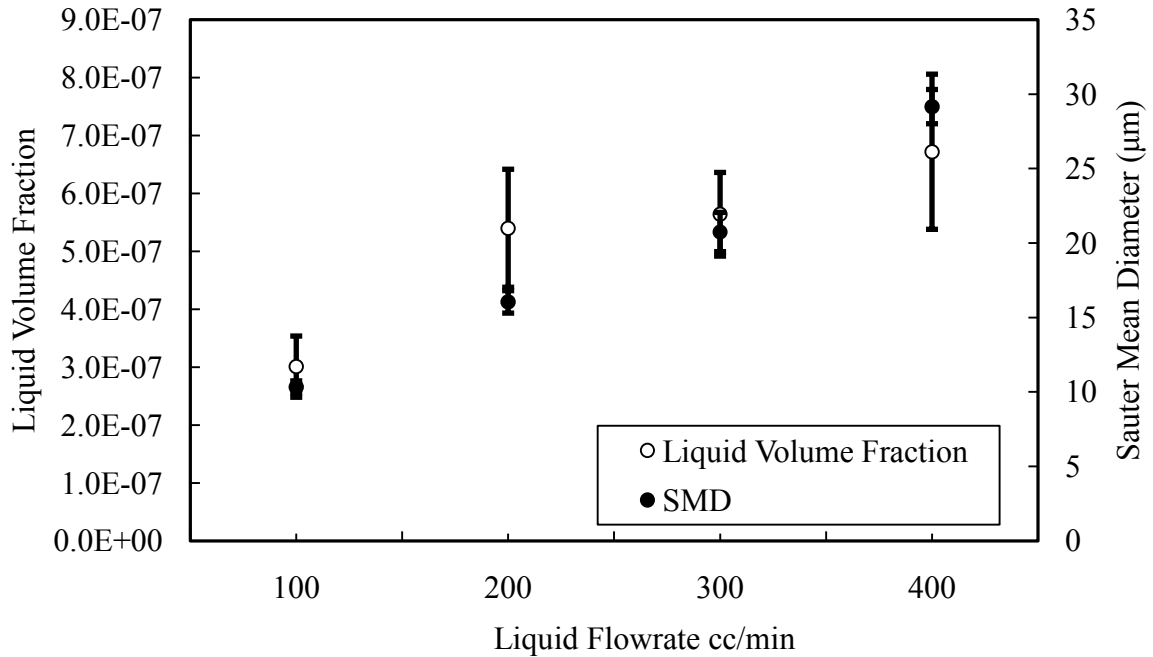


Figure 4.37: A comparison of the droplet number density and the Sauter mean diameter for HVLP air-assisted atomizer showing increasing liquid flow rate at a fixed air pressure of 0.4 MPa.

4.2.3.3 COMPARISON BETWEEN THE HIGH-SPEED ROTARY BELL ATOMIZER AND THE HVLP AIR-ASSISTED ATOMIZER

Figures 4.35 shows the average droplet number density and the average SMD as a function of liquid flow rate for the high-speed rotary bell atomizer and Figure 4.37 for the HVLP air-assisted atomizer. Comparison of these two-figure results indicates that the droplet number density and SMD increases with increasing flow rate in Figure 4.35 for the high-speed rotary bell atomizer, while the droplet number density decreases with increasing SMD and liquid flow rate for the HVLP air-assisted atomizer (Figure 4.37).

The explanation of the difference in the variation of droplet number densities with increasing liquid flow rates lies in the atomization mechanism resulting in the shape of

the spray produced by both atomizers. Infrared visualization of the spray from both atomizers with increasing liquid flow rate is shown in Figures 4.15 and for the high-speed rotary bell atomizer and in Figure 4.22 for the HVLP air-assisted atomizer. Figure 4.15 illustrates that with increasing liquid flow rate; the high-speed rotary bell atomizer generated, occupies about the same space and maintained its shape. Implying that the spray becomes denser and increasing droplet number densities with increasing flow rates. As the spray generated by the HVLP air-assisted atomizer opens up in Figure 4.22, the spray pattern becomes larger, and the spray angle grows from 40° at the liquid flow rate of 100 cc/min to 70° at a liquid flow rate of 400 cc/min. As a result, the area of the spray becomes larger with increasing liquid flow rate. Under this condition, with increasing droplet sizes and liquid flow rates, the spray becomes less dense, and decreases in droplet number density.

4.2.3.4 VOLUME FRACTION AND NUMBER DENSITY RESULTS FOR THE ULTRASONIC CAVITATING ATOMIZER

The droplet size measurements for the UCA were made along the spray center line axis at 75 mm downstream from the nozzle exit using the Malvern Spraytec system. The images are analyzed at a pixel location corresponding to the measurement volume of the Malvern Spraytec system. With the D_{32} obtained, the liquid volume fraction f_v is calculated at the chosen pixel location using Equation (2.31). The corresponding droplet number density is obtained from Equation (2.32). The data were processed and averaged

in time over 900 frames obtained at 300 frames/s. The standard deviations for the measurement are shown as error in the plot.

Figure 4.38 compares the average liquid volume fraction and the average SMD as a function of liquid injection pressure at a pixel location on the spray centerline 75 mm from the nozzle exit for a fixed liquid flow rate of 100 cc/min. Figure 4.39 compares the average droplet number density and the SMD as a function of the liquid injection pressure at a pixel location on the spray centerline at 75 mm from the nozzle exit for a liquid flow rate of 100 cc/min. Both the liquid volume fraction and the droplet number density increase with increasing liquid injection pressure and decreasing SMD. Figures 4.40 and 4.41 plot corresponding graphs for a liquid flow rate of 200 cc/min.

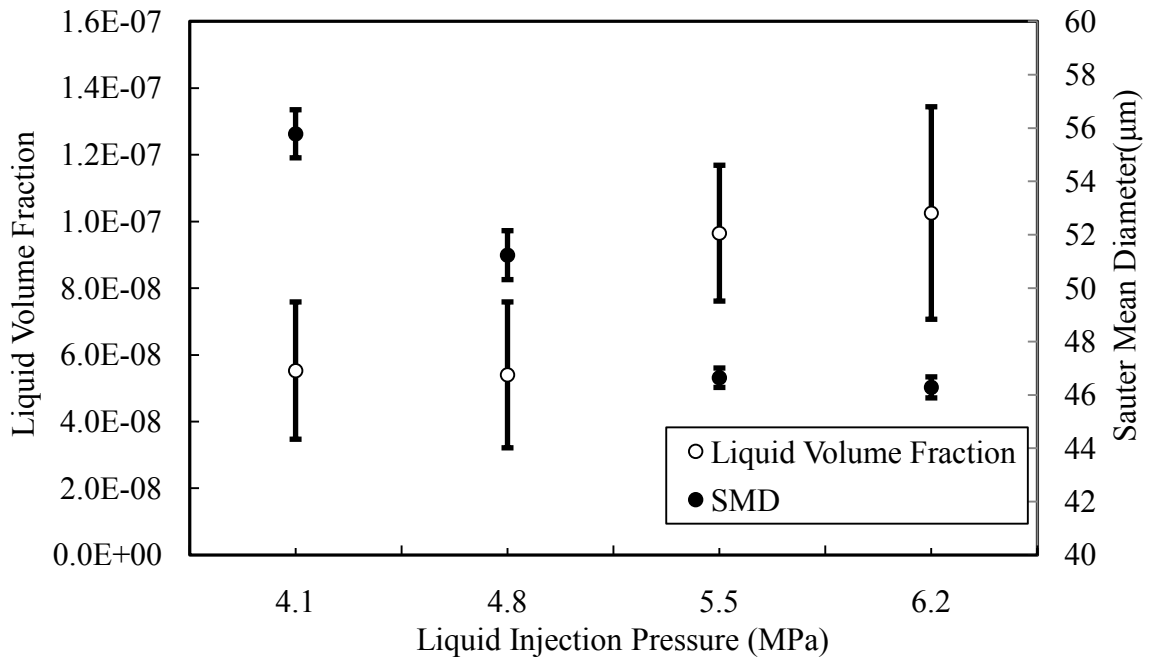


Figure 4.38: A comparison of the liquid volume fraction and the Sauter mean diameter for UCA atomizer showing increasing liquid injection pressure at a fixed liquid flow rate of 100 cc/min.

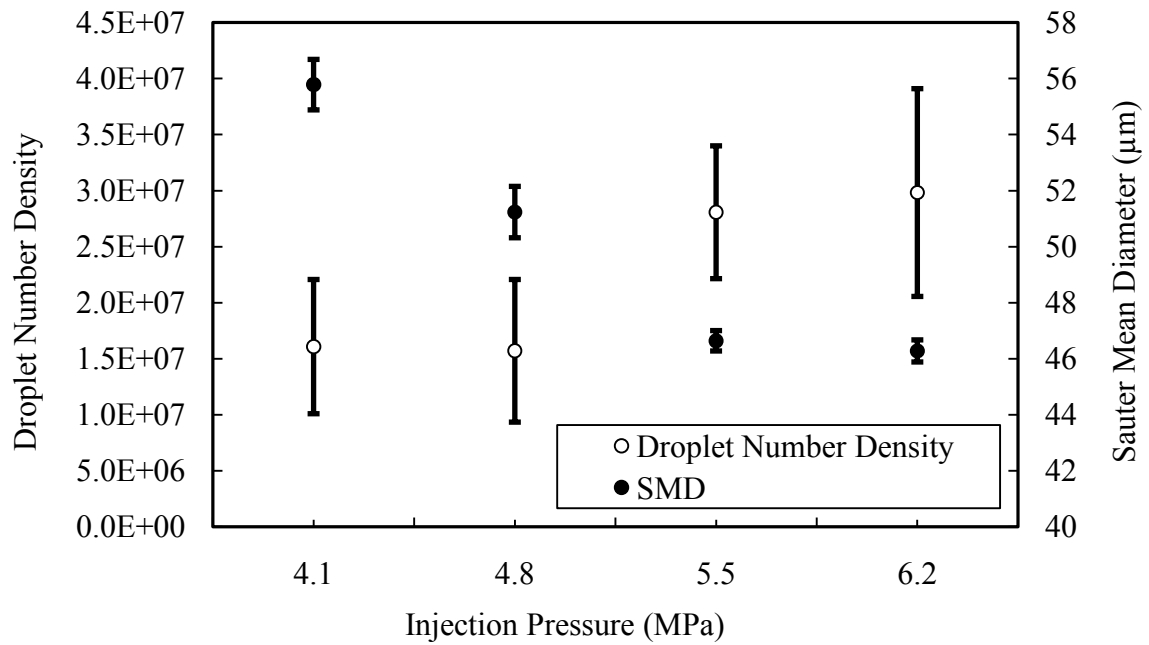


Figure 4.39: a comparison of the droplet number density and the Sauter mean diameter for UCA atomizer showing increasing liquid injection pressure at a fixed liquid flow rate of 100 cc/min.

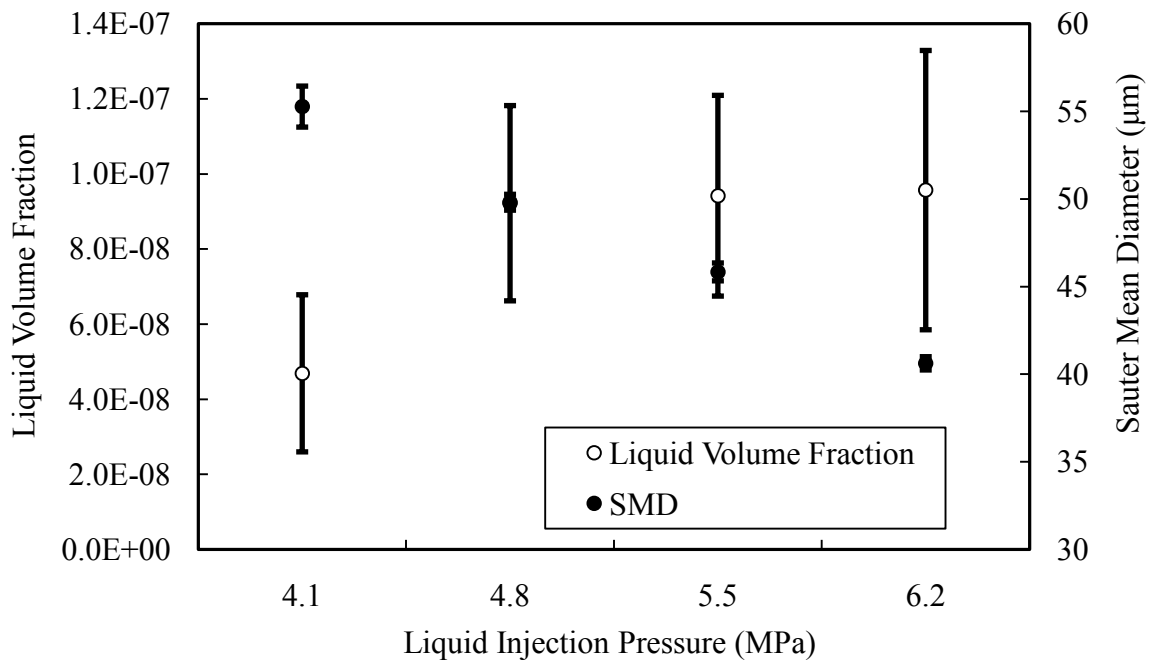


Figure 4.40: A comparison of the liquid volume fraction and the Sauter mean diameter for UCA atomizer showing increasing liquid injection pressure at a fixed liquid flow rate of 200 cc/min.

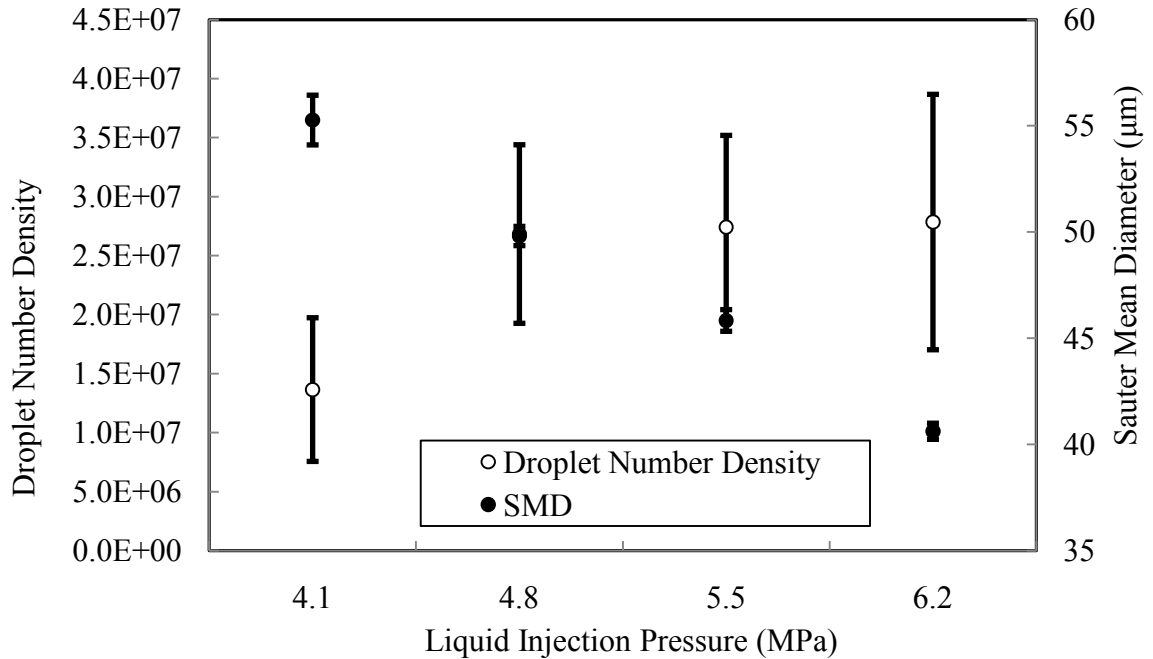


Figure 4.41: a comparison of the droplet number density and the Sauter mean diameter for UCA atomizer showing increasing liquid injection pressure at a fixed liquid flow rate of 200 cc/min.

The novel infrared-thermography-based visualization and characterization technique for liquid spray has been developed based on the extinction of the infrared energy emitted by a background which travels through the spray before reaching the detector. The technique was demonstrated on the three atomizers studied in this dissertation. The liquid volume fraction and the droplet number density of the sprays generated from these atomizers were estimated from the visualization data with the SMD acquired via the Malvern Spraytec system. The method presented here is a novel tool where qualitative information about the spray flow field is required.

CHAPTER FIVE

5.0 CONCLUSIONS AND RECOMMENDATIONS

In this dissertation the design, the fabrication, and the characterization of a new atomizer—the ultrasonic cavitating atomizer (UCA) was presented. In addition, a novel infrared thermography-based visualization and characterization technique for liquid sprays was developed and demonstrated on the UCA and two other automotive spray atomizers—the high-speed rotary bell atomizer and the high volume low pressure air-assisted atomizer. Section 5.1 summarizes the UCA atomizer design, fabrication, and characterization. Section 5.2 discusses the outcome of the infrared thermography-based visualization and characterization technique.

5.1 ULTRASONIC CAVITATION ATOMIZER FABRICATION AND CHARACTERIZATION

This dissertation offered the development and the characterization of an atomizer that uses pressure modulation and energy generated by the collapse of cavitation bubbles for the atomization of a low viscosity Newtonian liquid, such as water. In this context, a thorough review of the effect of cavitation, together with other influencing parameters, such as nozzle turbulence and geometric effects on the disintegration of round liquid jets were offered. To develop an energy efficient atomizer, the use of high frequency oscillations by means of an ultrasonic horn placed inside the nozzle, combined with cavitation phenomena were considered. The motion of the oscillating horn structure

induces pressure modulation on the exiting liquid jets. Details concerning the characteristic behavior of modulated jets were analyzed by deriving analytical relations of the oscillating pressure fields on the growth and collapse of cavitation bubbles.

Detailed design and fabrication of the prototype, the characterization and the visualization results were presented. These parameters—ultrasonic horn frequency, liquid flow rate, and liquid injection pressure—were varied, and the results were presented. The new atomizer offered improvement in the liquid jet disintegration process by reducing the Sauter Mean Diameter. Upon application of an ultrasonic frequency of 60 kHz and various liquid injection pressures, the Sauter Mean Diameter was observed to have been reduced by 10%, on average, for both liquid flow rates tested.

The UCA's main design concept is the use of ultrasonic cavitation energy as a primary atomization mechanism. However, the generation of cavitation bubbles at the ultrasonic horn tip was not explicitly measured in this experimental study. Thus, a more quantitative assessment on the role of cavitation on the atomization process within the UCA requires further study. The fabrication of the UCA also posts some difficulties that were not fully overcome in the current prototype presented in this dissertation. These difficulties include the complexity of manufacturing the nozzle section of the atomizer, the placement of the horn within the nozzle head in such a manner so as to ensure concentricity with the nozzle opening, and the ability to visualize the cavitation process.

The above mentioned difficulties are recommendations for future work on this atomizer. These difficulties, however, did not affect the initial motivation of creating an atomizer that utilizes the combined effects of pressure modulation and cavitation collapse energy on the disintegration of the cylindrical liquid jet.

5.2 INFRARED CHARACTERIZATION AND VISUALIZATION TECHNIQUE

A novel visualization and characterization technique that uses an infrared-thermography-based method was developed for liquid sprays. The method uses an infrared camera as a receiver and a uniformly heated background as a thermal radiation source. The technique provides images in which the value associated with each pixel accounts for the amount of infrared energy emitted by the source and attenuated by the spray. As a consequence of the scattering and absorption taking place, the attenuation of the infrared energy occurs, and the infrared detector receives a reduced signal.

The performance of the method was tested using three different types of atomizers: the high-speed rotary bell atomizer, the low pressure air atomizer, and the ultrasonic cavitating atomizer. Macroscopic features like spray pattern and angle, together with the flow structure in the entire spray flow field, were obtained and presented. Several theoretical and empirical correlations were derived from which the liquid droplet volume fraction and the liquid droplet number density of the spray were estimated from the visualization data with the SMD acquired via the Malvern Spraytec system.

The visualization method presented here has an advantage over visual photography in the sense that, radiation with wavelength in the visible band of the electromagnetic spectrum is attenuated more than radiation with wavelength in the infrared band. As a result, the method presented in this dissertation has the potential to reveal detailed structure inside a medium than visible photography. The new technique

offers a unique application of the infrared transmission mode widely used in non-destructive testing to view a multiphase medium.

In summary, the results presented herein demonstrate that this new technique has great promise in the qualitative characterization of sprays. As compared to other optical methods available, this new technique is easy to setup and takes very little time to acquire a high quality image of the spray. It can be applied in environments where current laser-based illumination photographic methods cannot be used, making a real-time and in-process imaging of spray transfer process possible.

5.3 CONTRIBUTION OF THIS DISSERTATION

In summary, this study provided the following contributions to the research community:

- (1) A novel atomization technique that uses the energy created by the collapse of ultrasonically generated cavitation bubbles together with the oscillation of the exiting liquid jet to enhance the disintegration the liquid jet.
- (2) A novel infrared thermography-based visualization method for the study of droplet transport within a spray. The method demonstrated the capability of revealing more internal structures of a liquid spray than any currently available visual photographic methods. This new method allows for real-time and in-process imaging of the spray droplet transfer process.

- (3) The research offers a novel infrared thermography-based particle characterization method for the estimation of the liquid volume fraction and the liquid droplet number density inside a spray.
- (4) The method demonstrates the use of infrared thermography in an area that has not been used before. Appendix B thus provides some suggested research areas in which this technique can be used. Some simple experiments were performed, and the results presented to demonstrate the concept.

Copyright © Nelson K. Akafuah 2009

APPENDICES

APPENDIX A: DETAIL DIAGRAM AND DIMENSIONS OF THE ULTRASONIC CAVITATING ATOMIZER

This appendix presents the detailed drawings and dimensions of the five main parts that makes up the ultrasonic cavitating atomizer. These parts are: part 1 – Cap, part 2 – Nozzle, part 3 – Body, part 4 – Support, and part 5 – End Cap.

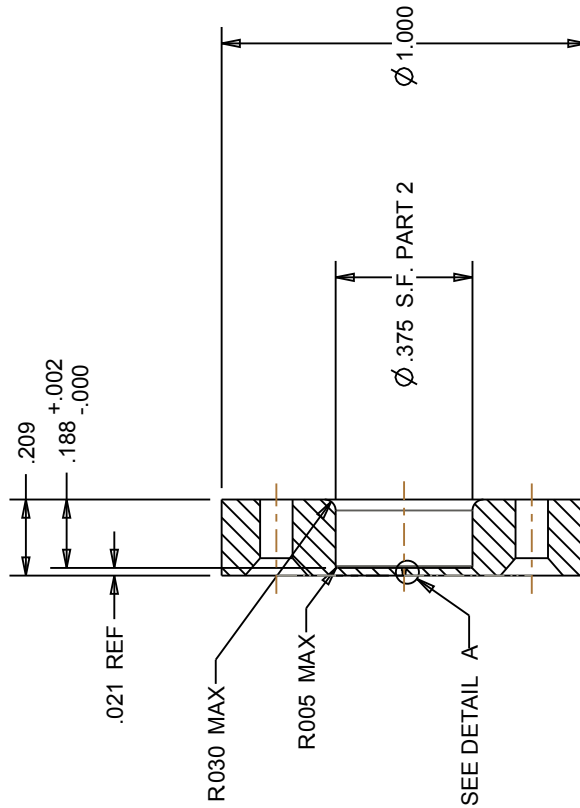
Technical drawing of a mechanical part, likely a valve or plug, showing a cross-section. The drawing includes dimensions and tolerances.

Top diameter: $\varnothing .012$ $^{+.001}_{-.000}$

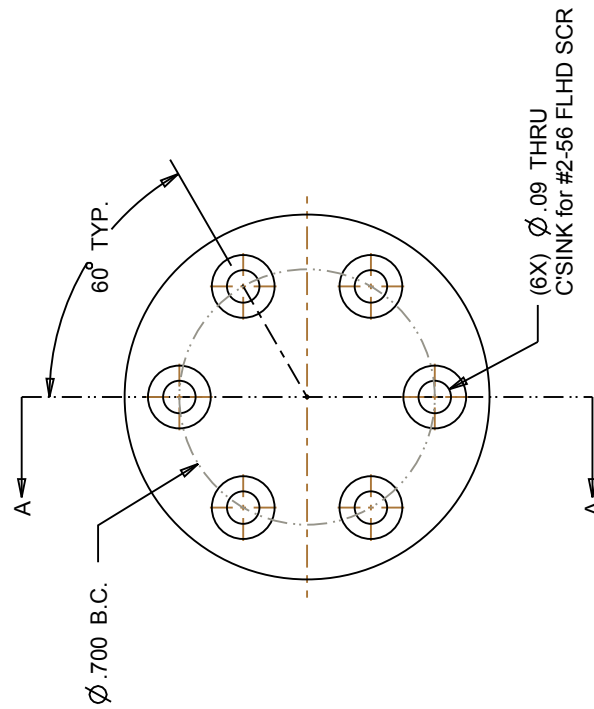
Bottom diameter: $\varnothing .008$ $^{+.001}_{-.000}$

Thickness: $.010 \pm .003$

Labels: DETAIL A, SCALE 12:1, NOTE 1 (two locations).

[illegible]

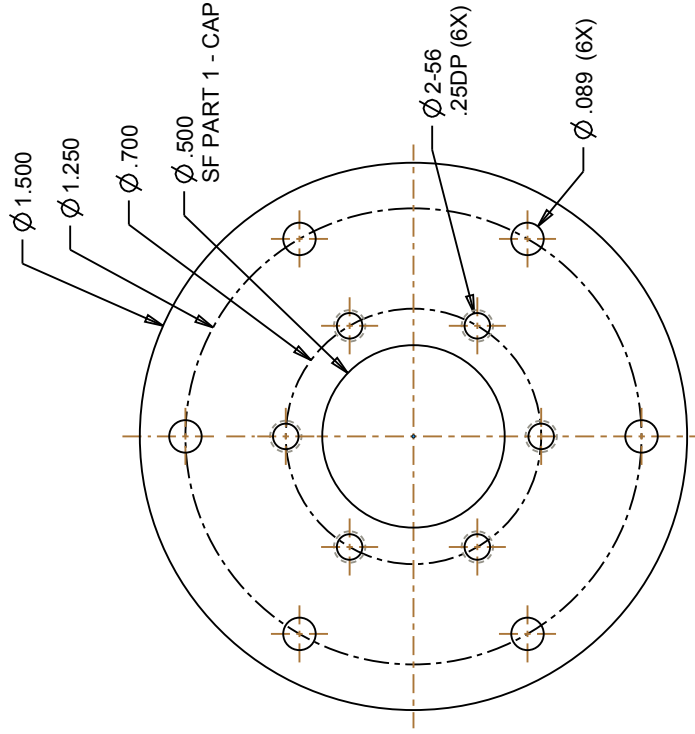
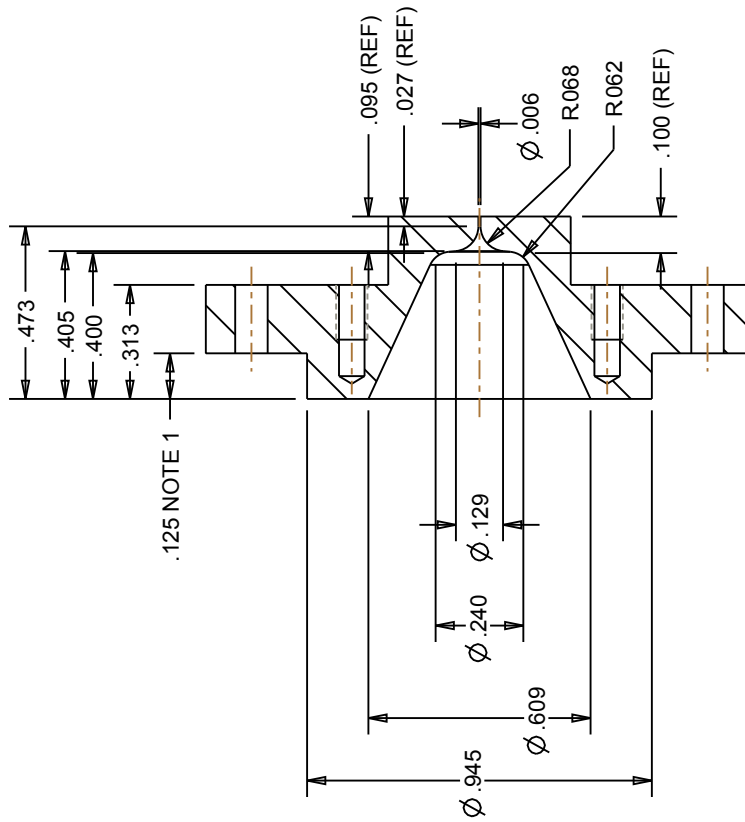
SECTION A-A



NOTE 1: BEST FINISH POSSIBLE

[illegible]

PART 2 - NOZZLE Stainless Steel



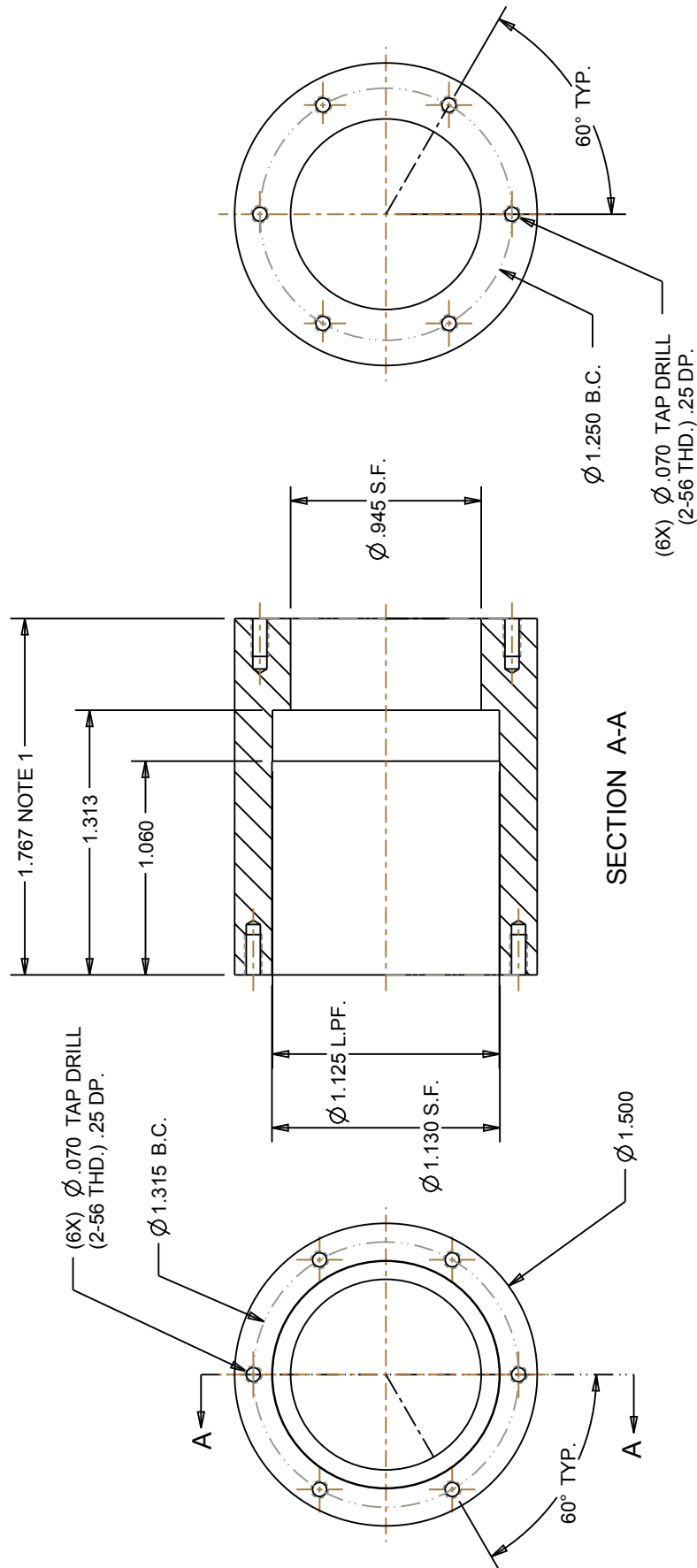
REVISIONS			
ECN	REV	DESCRIPTION	DATE

UNLESS OTHERWISE SPECIFIED DIMENSIONS ARE IN INCHES TOLERANCES ON		SIGNATURES	DATE
3% DECIMALS	.001	DRAWN AKAFUJAH	25-OCT-08
3% DECIMALS	.001	CHECKED	
ANGLES	0.5	APPROVED	
FRACTIONS	XXX		
CENTER FOR MANUFACTURING UNIVERSITY OF KENTUCKY		PART 2_NOZZLE	
SCALE		2,000	
PART		PART2A	
1 OF 1			

NOTE 1: DIMENSION BASED ON
HORN/TRANSDUCER ASSY LENGTH

PART 3 - BODY
Stainless Steel

REVISIONS				
EON	REV	DESCRIPTION	DATE	REVISED BY



SCALE 1.250

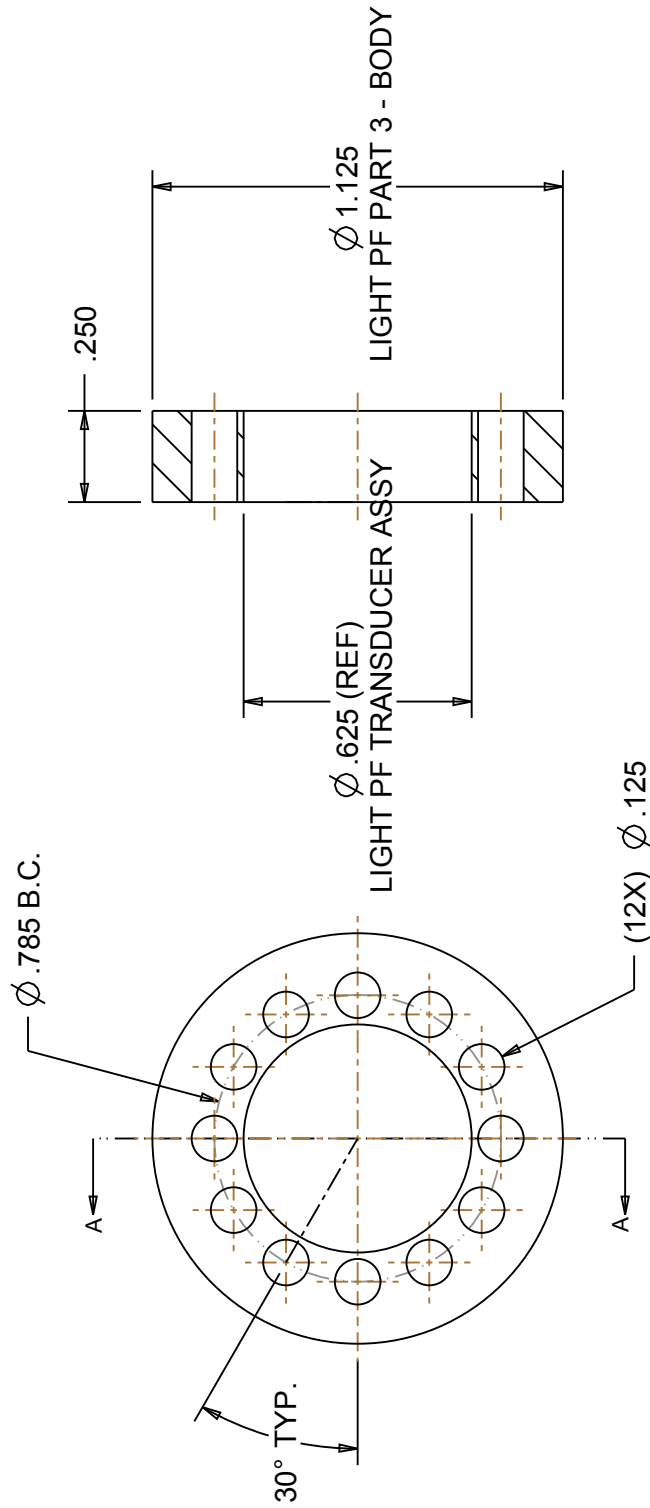
NOTE 1: DIMENSION BASED ON
HORN/TRANSDUCER ASSY LENGTH

UNLESS OTHERWISE SPECIFIED DIMENSIONS ARE IN INCHES TOLERANCE ON		SIGNATURES	DATE
2 1/2" DECIMALS	.001	DRAWN AKAFUJAH	25-OCT-08
2 1/2" DECIMALS	.001	CHECKED	
ANGLES	0.01	APPROVED	
FRACTIONS	XXX		
CENTER FOR MANUFACTURING UNIVERSITY OF KENTUCKY		SIZE A	SCALE 1.000
PART 3_BARREL		ISSUE PART	REV A
UNIVERSITY OF KENTUCKY COLLEGE OF ENGINEERING		DRAWN PART3	REV 1 OF 1



PART 4 - SUPPORT
Stainless Steel

REVISIONS				
ECN	REV	DESCRIPTION	DATE	REVISED BY




SECTION A-A

UNLESS OTHERWISE SPECIFIED		SIGNATURES	DATE	UNIVERSITY OF KENTUCKY	
DIMENSIONS IN INCHES		DRAWN AKAFUAH	25-OCT-08	COLLEGE OF ENGINEERING	
TOLERANCES		CHECKED		PART_4_SUPPORT	
3/16 DECIMALS	.001	APPROVED			
3/16 DECIMALS	.001				
ANGLES	0.5				
FRACTIONS	XXX				
CENTER FOR MANUFACTURING			SCALE	DRAWN BY	REV
UNIVERSITY OF KENTUCKY			2,000	AKAFUAH	X
			PART#	1 OF 1	

ECN	REV	FUNCTIONS			APPROVED
		DESCRIPTION	DATE	REVISED BY	



UNLESS OTHERWISE SPECIFIED DIMENSIONS ARE IN INCHES TOLERANCE ON		SIGNATURES	DATE
2 IN. DIMENSIONS	.001	DRAWN AKAFUHI	25-07-06
3 IN. DIMENSIONS	.001	CHECKED	
ANGLES	.05	APPROVED	
FRACTIONS	XXXX		



CENTER FOR MANUFACTURING
UNIVERSITY OF KENTUCKY

SIZE A	MODEL/TITLE PART	DRAWN BY DWYANE	REV X
-----------	---------------------	--------------------	----------

PART_5_END_CAP

UNIVERSITY OF KENTUCKY
COLLEGE OF ENGINEERING

DATE
1 OCT 1

APPENDIX B: SOME RESEARCH AREAS FOR INFRARED VISUALIZATION TECHNIQUE

The infrared thermography-based visualization technique developed in this dissertation is a useful tool in the visualization of thermal flow processes. Simple experiments were conducted to demonstrate the use of this technique in the visualization of buoyancy-driven and momentum-driven thermal plumes.

In the buoyancy driven thermal plume, buoyancy is induced by the combined presence of a fluid density gradient and a body force that is proportional to the density. In practice, the body force is usually gravitational, although it may be a centrifugal force in rotating fluid machinery or a Coriolis force in atmospheric and oceanic rotational motions. There are several ways in which a mass density gradient may arise in a fluid, but for the most part, it is the result of the presence of a temperature gradient. To demonstrate the ability of the technique developed in this work to visualize a buoyancy driven plume, we considered the following: (1) the thermal plume above a candle flame (Figure B-1), (2) the thermal plume above a butane lighter (Figure B-2), and (3) the thermal plume developed above a horizontally-placed soldering iron (Figure B-3).

The candle flame shown in Figure B-1a was enclosed to minimize disturbance of the airflow in the room. The infrared thermal image shows the plume above the candle flame to be laminar within the field-of-view (FOV). A candle flame is one of the oldest functional combustion systems developed primarily as a source of light. The candle flame is a model convective-diffusive flame in normal gravity theory and experiments. Figure

B-1b shows a contour plot of the candle flame, and Figure B-1c the visible image of the candle flame.

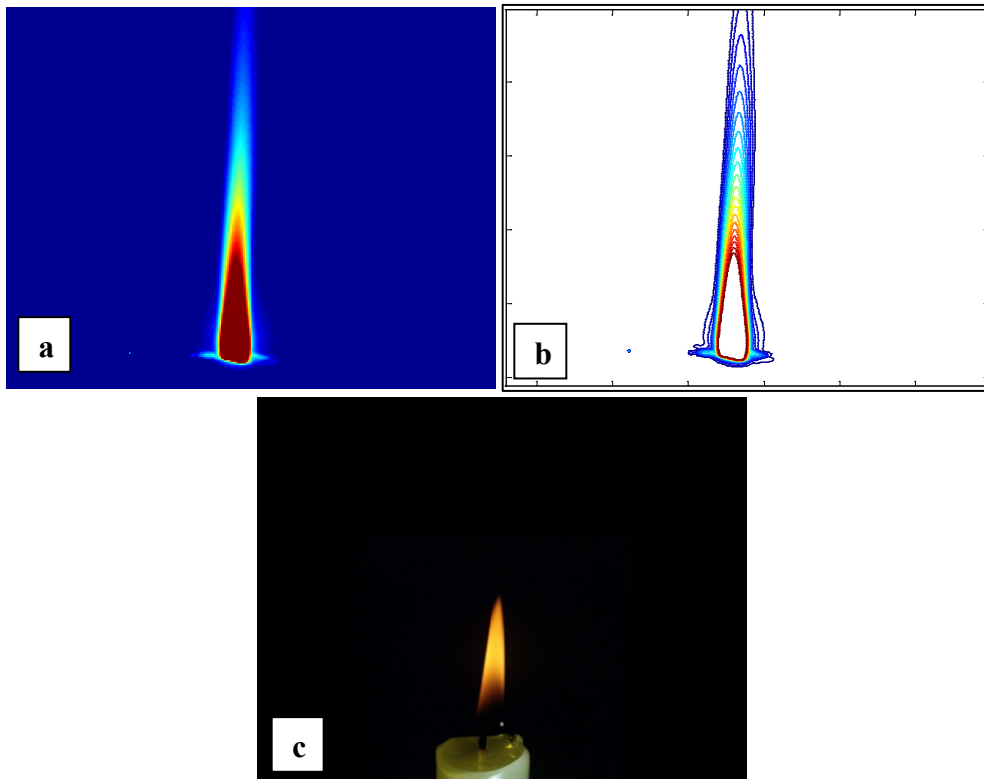


Figure B-1a: Infrared image of candle flame showing thermal plume, (b) contour plot of thermal image of candle flame, and (c) visible image of candle flame.

Figure B-2 shows the infrared thermal image of the flame from a disposable butane lighter. Unlike the candle flame, the butane lighter flame was not enclosed and the thermal plume generated above the flame quickly became turbulent. The turbulent behavior which is not observable in the visible image was captured by the infrared image. A coherent vertical motion can be seen above the flame. Figure B-2b shows a contour plot of the flame, and Figure B-2c illustrates the visible image.

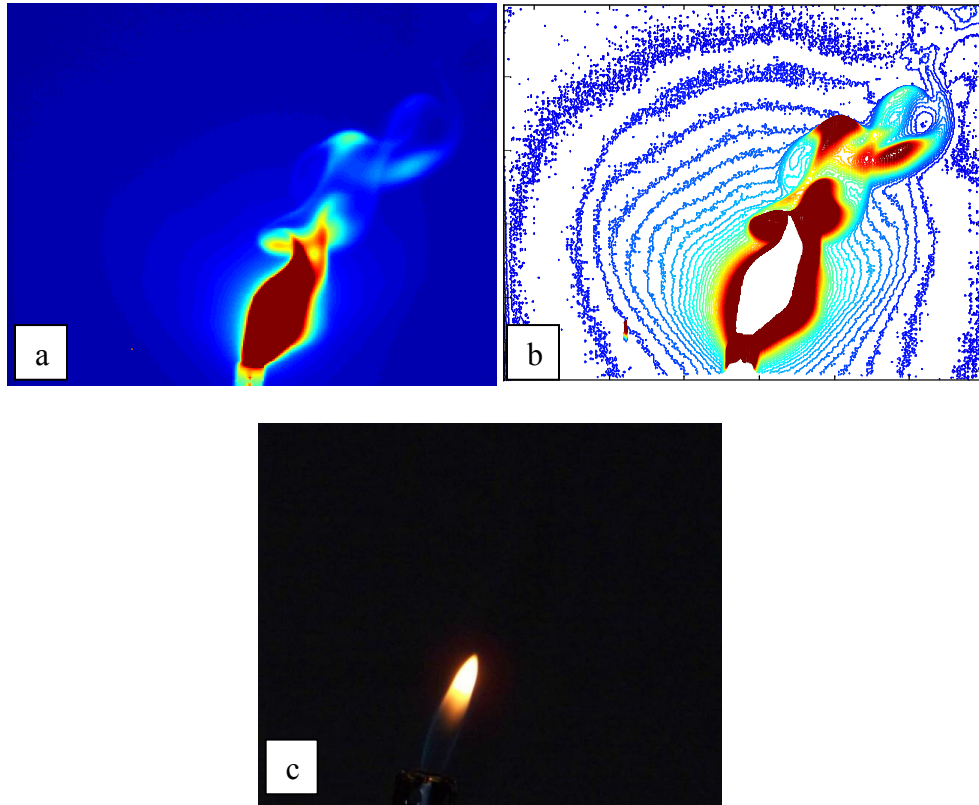


Figure B-2a: Infrared image of butane lighter showing thermal plume around flame, (b) contour plot of thermal image of butane lighter flame, and (c) visible image of butane lighter.

The third buoyancy-driven flow case considered was generated by a heated horizontally-placed soldering iron. Figure B-3a shows the thermal image, and the Figure B-3b reveals the contour plot of the image.

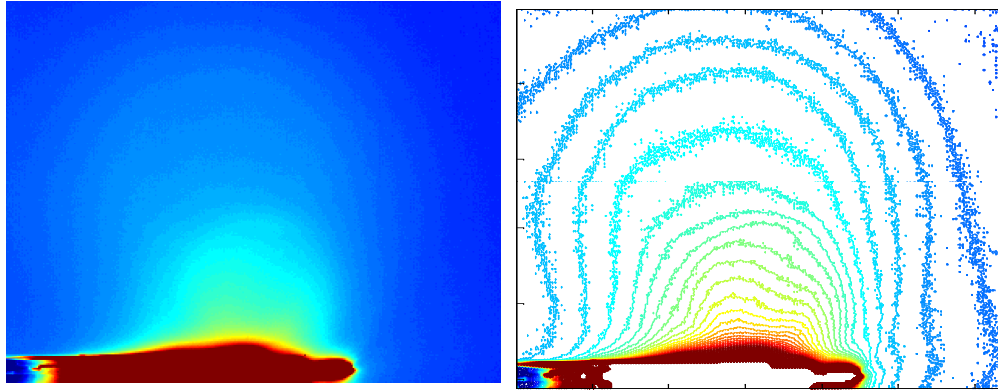


Figure B-3a: Infrared image of thermal plume above a horizontally-placed soldering iron and **(b)** contour plot of thermal image of thermal plume above a horizontal soldering iron.

For a momentum-driven thermal flow, a heat gun is used. A heat gun is a device used to emit a stream of hot air. They are superficially similar in shape and in construction to a hair dryer, although they run at much higher temperatures. Heat guns can be used to dry and strip paint, apply heat shrink tubing, apply shrink film, dry out damp wood, bend and weld plastic, soften adhesives, and thaw frozen pipes. They are also used in electronics to de-solder circuit board components. They typically output air at temperatures ranging from 100-550°C (200-1000°F) with some hotter models running around 760°C (1400°F). Some have a rest, so they can be activated and placed on a workbench, which frees the operator's hand. Heat guns can have nozzles which deflect their air for various purposes, such as concentrating the heat on one area, as in the case of thawing a pipe without heating up the wall behind.

When momentum effects are more important than density differences and buoyancy effects, the plume is usually described as a jet. In Figure B-4 we have the thermal jet from the heat gun at a low speed setting. Figure B-5 illustrates the effects for a

high speed setting. Figure B-4a demonstrates the thermal image, and Figure B-4b illustrates the contour plot. Similarly Figure B-5a and b demonstrates the thermal image and contour plot, respectively.

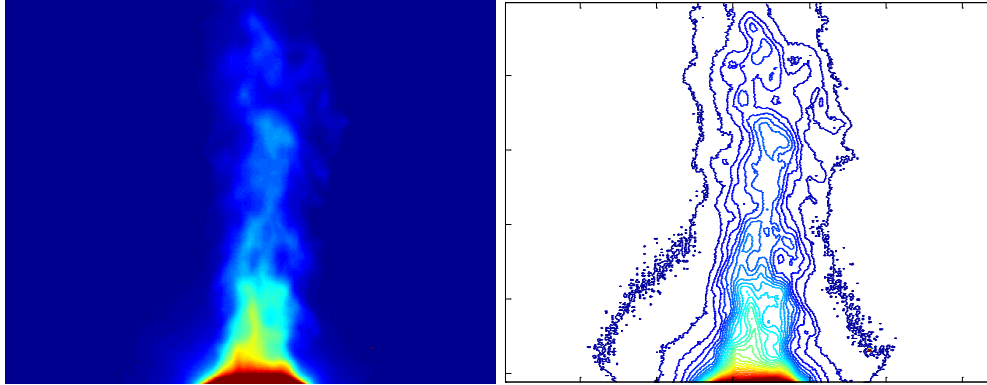


Figure B-4a: Infrared image of thermal jet from heat gun at low speed setting and **(b)** contour plot of thermal jet from heat gun at low speed setting

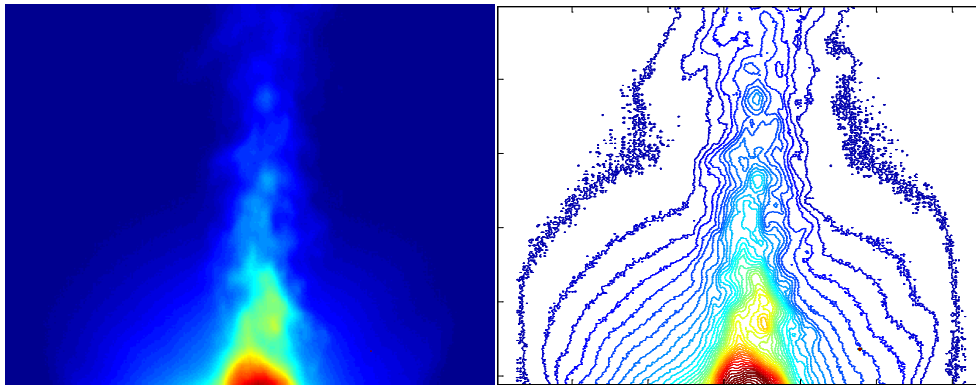


Figure B-5a: Infrared image of thermal jet from heat gun at high speed setting and **(b)** contour plot of thermal jet from heat gun at high speed setting

REFERENCES

- Agrawal, A. and Prasad, A. K. (2003). Integral Solution for the Mean Flow Profiles of Turbulent Jets, Plumes, and Wakes. *Journal of Fluids Engineering*, 125, 813-822.
- Arcoumanis, C. and Gavaises, M. (1998). Linking Nozzle Flow with Spray Characteristics in a Diesel Fuel Injection System. *Atomization and sprays*, 8, 307-347.
- Arcoumanis, C., Gavaises, M., Nouri, J. M., Abdul-Wahab, E., Horrocks, R.W. (1998) Analysis of the Flow in the Nozzle of a Vertical Multi Hole Diesel Engine Injector, *SAE transactions*, 107(3), 1245-1259
- Armaly, B.F., Durst, F., Pereira, J.C.F., Schönung, B. (1983). Experimental and Theoretical Investigation of Backward-Facing Step Flow. *Journal of Fluid Mechanics*, 127, 473-496.
- Astarita, Cardone, T. G. (2008). Convective Heat Transfer on a Rotating Disk with a Centred Impinging Round Jet. *International Journal of Heat and Mass Transfer*, 51, 1562-1572.
- Astarita, T., Cardone, G., Carlomagno, G. M., Meola, C. (2000). A Survey of Infrared Thermography for Convective Heat Transfer Measurements. *Optics and Laser Technology*, 32, 593-610.
- Ay, H., Jang, J. Y., Yeh, J-N. (2002). Local Heat Transfer Measurement of Plate Finned-Tube Heat Exchangers by Infrared Thermography. *International Journal of Heat and Mass Transfer*, 45, 4069-4078.
- Ayres, D., Caldas, M., Semiao, V., Da Graca Carvalho, M. (2001). Prediction of the Droplet Size and Velocity Joint Distribution for Sprays. *Fuel*, 80, 383-394.
- Bachalo, W. D. (1994). The Phase Doppler Method: Analysis, Performance Evaluations, and Applications. *Particle and Particle Systems Characterization*, 11, 73-83.

- Bae, C., Yu, J., Kang, J., and Kong, J. (2002). Effect of Nozzle Geometry on the Common-Rail Diesel Spray. *Society of Automotive Engineers, Technical Paper Series* 2002-01-1625.
- Balageas, D.L., Bouchardy, A-M. (1993) Application of Infrared Thermography in Fluid Mechanics. *Von Karman Institute for Fluid Dynamics Lecture Series; Lecture Series on Measurement Techniques*, 1993-05.
- Barkley, D., Gomes, M.G.M., Henderson, R.D. (2002). Three-Dimensional Instability in Flow Over a Backward-Facing Step. *Journal of Fluid Mechanics* 473, 167-190
- Barr, S., E. (1961). The Infrared Pioneers-I. Sir William Herschel. *Infrared Physics*, 1, 67-74
- Barr, S., E. (1962). The Infrared Pioneers-II. Macedonio Melloni. *Infrared Physics*, 2, 1-4
- Batchelor, G.K. (2000). *An Introduction to Fluid Dynamics*, Cambridge University Press
- Baur, T., Kongeter, J. (1998). The Three-Dimensional Character of Cavitation Structures in a Turbulent Shear Layer, *XIX IAHR International Symposium on Hydraulic Machinery and Cavitation*, 9-11, Singapore, September 1998.
- Bayvel, L. & Orzechowski, Z. (1993). *Liquid Atomization*. Taylor & Francis.
- Belahadji, B., Franc, J. P., Michel, J.M. (1995) Cavitation in the Rotational Structures of a Turbulent Wake. *Journal of Fluid Mechanics* 287, 383-403.
- Bellofiore, A., Ragucci, R., Di Martino, P. and Cavaliere A. (2007). Tailored Binarization of Spray Shadowgrams for Morphology Investigation. *2007 Annual Meeting of the Italian Section of the Combustion Institute*, 20-22 June, 2007, Napoli, Italy.
- Bergwerk, W. (1959). Flow Pattern in Diesel Nozzle Spray Holes. *Proceedings of the Institution of Mechanical Engineers*, 173, 655-660.

- Berour, N., Lacroix, d., Boulet, P., Jeandel, G. (2004). Radiative and Conductive Heat Transfer in Nongrey Semitransparent Medium. Application to Fire Protection Curtains. *Journal of Quantitative Spectroscopy and Radiative Transfer*, 86 (1), 9-30.
- Black, D. L., McQuay, M. Q. (2001). Laser-Based Particle Measurements of Spherical and on Spherical Particles. *International Journal of Multiphase Flow*, 27, 1333-1362.
- Black, D. L., McQuay, M. Q., Bonin, M. P. (1996). Laser-Based Techniques for Particle Size Measurement: A Review of Sizing Methods and their Industrial Applications. *Progress in Energy Combustion Science*, 22, 267-306.
- Borodin, V. A., Dityakin, Yu F., Klyachko, L. A., Yagodkin, V. I. (1967). *Raspylivanie Zhidkosti (Atomization of Liquids)*, Izd-VO Mashinostroenie Moscow
- Brennen, C.E. (1995). *Cavitation and Bubble Dynamics*, Oxford University Press
- Bruan, J. H., and Fields, D. P. (1994). Gloss of Paint Films: Effects of Pigment Size. *Journal of Coating and Technology*, 66, 93-98.
- Cao, J. (2002). On the Theoretical Prediction of Fuel Droplet Size Distribution in Nonreactive Diesel Sprays. *Journal of Fluids Engineering*, 124, 182-185.
- Castleman, R. A., Jr. (1931). The Mechanism of the Atomization of Liquids. *Bureau of Standards Journal of Research*, 369-376.
- Castleman, R. A., Jr. (1932). The Mechanism of Atomization Accompanying Solid Injection. *National Advisory Committee for Aeronautics, Technical Report*, No. 440.
- Chaves, H., Knapp, M., Kubitzek, A., Obermeier, F., Schneider, T. (1991). Experimental Study of Cavitation in the Nozzle Hole of Diesel Injectors Using Transparent Nozzles, *Society of Automotive Engineers, Paper No. 950290*, 645-657

- Collin, A., Boulet, P., Lacroix, D., and Jeandel, G. (2005). On Radiative Transfer in Water Spray Curtains Using the Discrete Ordinates Method. *Journal of Quantitative Spectroscopy and Radiative Transfer*, 92 (1), 85-110.
- Cornell, E. S. (1936). Early Studies in Radiant Heat. *Annals of Science*, 1, 217-225.
- Cornell, E. S. (1938 a). The Radiant Heat Spectrum from Herschel to Melloni. -I. The work of Herschel and His Contemporaries . *Annals of Science*, 3, 119-137.
- Cornell, E. S. (1938 b). The Radiant Heat Spectrum from Herschel to Melloni.-II. The Work of Melloni and His Contemporaries. *Annals of Science*, 3, 402-416
- Crane, L., Birch, S., McCormack, P.D. (1964) The Effect of Mechanical Vibration on the Breakup of a Cylindrical Water Jet In Air. *British Journal of Applied Physics*, 15, 743-750.
- Crum, L.A. (1979). Tensile Strength of Water. *Nature*, 278, 148-149
- Damaschke, N., Gouesbet, G., Grehan, G., Mignon, H., Tropea, C. (1997). Response of PDA Systems to Non-Spherical Droplets. *Proceedings of ILASS-Europe*, Florence, Italy: 382-388.
- DeJuhasz, K. J. (1960). *Spray Literature Abstracts, Vols. 1, 2, 3, 4*. New York: American Society of Mechanical Engineers.
- Dejuhasz, K.J. (1931). Dispersion of Sprays in Solid Injection Oil Engines. *Transaction of the ASME (OGP)*, 53, 65
- Dembele, S., Delmas, A., and Sacadura, J.-F. (1997). A Method for Modelling the Mitigation of Hazardous Fire Thermal Radiation by Water Spray Curtains. *Journal of Heat Transfer*, 119 (4), 746-753.
- Dembele, S., Wen, J. X., and Sacadura, J.-F. (2001) Experimental Study of Water Sprays for the Attenuation of Fire Thermal Radiation. *Journal of Heat Transfer*, 123(3), 534-543.

- Desideri, U., Rossi, G., Giovannozzi, A., and Maggiorana, P. (2004). High Resolution Infrared Thermography for Airfoils Boundary Layer Inspection in Passive Mode. *Proceeding of ASME Turbo Expo*, 14-17 June, 2004. Vienna, Austria, GT2004-53538
- Domann, R., Hardalupas, Y. (2000). Evaluation of the Planar Drop Sizing Technique. *Proceedings of ICLASS*, 16-20 July 2000, Pasadena, California.
- Dominick, J., and Thieme M. (2006). Atomization Characteristics of High-Speed Rotary Bell Atomizers. *Atomization and Sprays*, 16, 857-874.
- Dumouchel, C., Boyaval, S. (1999). Use of the Maximum Entropy Formalism to Determine Drop Size Distribution Characteristics. *Particles and Particle System Characterization*, 16, 177-184.
- Durst, F., Zare, M. (1975). Laser Doppler Measurements in Two Phase Flows. *Proceedings of the LDA-Symposium*, 25-28 August 1975, Copenhagen, Denmark: 403-429.
- Elrod, S. A., B. Hadimioglu, B. T. Khuri-Yakub, E. G. Rawson, E. Richley, and C. F. Quate. (1989). Nozzles Droplet Formation with Focused Acoustic Beams. *Journal of Applied Physics*, 65, 3441-3447.
- Farago', Z. and Chigier, N. (1992). Morphological Classification of Disintegration of Round Liquid Jets in a Coaxial Air Stream. *Atomization and Sprays*, 2, 137-153.
- Feldmann, O., Mayinger, E. H. F., and Gebhard, P. (1998). Evaluation of Pulsed Laser Holograms of Flashing Sprays by Digital Image Processing and Holographic Particle Image Velocimetry. *Nuclear Engineering and Design*, 184, 239-252.
- Feng, Z.C., Leal, L.G. (1997). Nonlinear Bubble Dynamics, *Annual Review of Fluid Mechanics*, 29, 201-43.

- FLIR Systems. (2009). *The Premier Infrared Solution for Advanced Industrial, Scientific and Military Applications*. Retrieved March, 31, 2009, from <http://www.flir.com.hk/Brochures/Sc6000%20XML%20ENG.pdf>
- Flynn, H.G. (1964). Physics of Acoustic Cavitation in Liquids. *Physical Acoustics*, 1B. Academic Press
- Frenkel, J. (1955). *Kinetic Theory of Liquids*. New York: Dover Publications
- Frohn, A., and Roth, N. (2000). *Dynamics of Droplet*. New York: Springer-Verlag.
- Fujimoto, H., Nishikori, T., Hojyo, Y., Tsukamoto, T., Senda, J. (1994). Modeling of Atomization and Vaporization Process in Flash Boiling Spray. *ICLASS 1994*, Rouen, France.
- Furness, R.A., Hutton, S.P. (1975) Experimental and Theoretical Studies of two Dimensional Fixed Cavities. *Journal of Fluids Engineering* 515-522.
- Gartenberg, E., Roberts Jr., A.S., McRee, G.J. (1989). Infrared Imaging and Tufts Studies of Boundary Layer Flow Regimes on a NACA 0012 Airfoil. *CH2762-3/89/0000-0168, IEEE*.
- Geschner, F., Chaves, H., Obermeier, F. (2001). Investigation of Different Phenomena of the Disintegration of a Sinusoidally Forced Liquid Jet. *ILASS-Europe 2001*, Zurich 2-6 September 2001.
- Geschner, F., Chaves, H., Obermeier, F. (2004). Non-Dimensional Map for the Appearance of Spray Structures of a Periodically Excited Liquid Jet, *DFG Schwerpunktprogramm Fluidzerst ubung und Spr uhvorg nge DFG-Priority Program Atomization and Spray Processes*, Dortmund, 18-19 March, 2004
- Giffen, E. and Muraszew, A. (1953). *The Atomization of Liquid Fuels*. New York: John Wiley & Sons.

- Gopalan, S., Katz, J. (2000) Flow Structure and Modeling Issues in the Closure Region of Attached Cavitation. *Physics of Fluids*, 12, 895-911.
- Hackett, B., H. and Settles, G., S. (1995). The Influence of Nozzle Design on HVOF Spray Particle Velocity and Temperature. *Proceedings of the 8th National Thermal Spray Conferenc*, 11-15 September, 1995, Houston, Texas.
- Hanson, A. R., Domich, E. G. & Adams, H. S. (1963). Shock Tube Investigation of the Break-Up of Drops by Air Blasts. *Physics of Fluids* 6, 1070-1080.
- Hansson, I., Kedrinskii, V.K., Morch, K.A. (1982). On the Dynamics of Cavity Clusters, *Journal of Physics D: Applied Physics*, 15, 1725-1734.
- Hansson, I., Morch, K.A. (1979 a) Some Aspects on the Initial Stage of Ultrasonically Induced Cavitation Erosion, *Ultrasonics International Conference and Exhibition, conference proceedings*, Kongress Zentrum Stefaniensaal, Graz, Austria, 15-17 May 1979
- Hansson, I., Morch, K.A. (1979 b). Comparison of the Initial Stage of Vibratory and Flow Cavitation Erosion, *Proceedings of the Fifth International Conference on Erosion by liquid and solid impact*, Cambridge University, England, September 3-6, 1979.
- Herbst, A. (2001). Droplet Sizing on Agricultural Sprays – A Comparison of Measurement Systems Using a Standard Droplet Sizing Classification Scheme. *Conference on Liquid Atomization and Spray Systems*, September 2001, Zurich, Switzerland.
- Herschel, W. (1800 a). Investigation of the Powers of the Prismatic Colours to Heat and Illuminate Objects; With Remarks, That Prove the Different Refrangibility of Radiant Heat. To which is Added, an Inquiry into the Method of Viewing the Sun Advantageously, with Telescopes of Large Aperture and High Magnifying Powers. *Philosophical Transactions, Royal Society of London*, 90, 255-283.

- Herschel, W. (1800 b). Experiments on the Refrangibility of the Invisible Rays of the Sun. *Philosophical Transactions, Royal Society of London*, 90, 284-292.
- Herschel, W. (1800 c) Experiments on the Solar, and on the Terrestrial Rays that Occasion Heat; with a Comparative View of the Laws to which Light and Heat, or Rather the Rays which Occasion them, are Subject, in order to Determine Whether they are the same, or Difference. *Philosophical Transactions, Royal Society of London*, 90, 293-326.
- Herschel, W. (1800 d). Observations Tending to Investigate the Nature of the Sun, in Order to Find the Causes or Symptoms of Its Variable Emission of Light and Heat; With Remarks on the Use That May Possibly Be Drawn from Solar Observations. *Philosophical Transactions, Royal Society of London*, 91, 265-318
- Hinze, J. O. (1949). Critical Speeds and Sizes of Liquid Globules. *Applied Science Research A1*, 273-288.
- Hinze, J. O. (1955). Fundamental of the Hydrodynamic Mechanism of Splitting in Dispersion Processes. *AIChE* 1-3, 289-295.
- Hirleman, E. D. (1988). Modeling of Multiple Scattering Effects in Fraunhofer Diffraction Particle Size Analysis. *Particle and Particle Systems Characterization*, 5(2), 57-65.
- Hiroyasu, H., Arai, M., and Shimizu, M. (1991). Breakup Length and Internal Flow in a Nozzle, *Proceedings of the International Conference on Liquid Atomization and Spray Systems-1991*, 275-282
- Im, K.-S., Lai, M.-C., Liu, Y., Sankagiri, N., Loch, T., and Nivi, H. (2001). Visualization and Measurement of automotive Electrostatic Rotary-Bell Paint Spray Transfer Processes. *Journal of Fluid Mechanics*, 123, 237-245.
- Infrared System Development Corp. (2009). IR-150/301 Blackbody System. Retrived March, 31, 2009, from <http://www.infraredsystems.com/Products/blackbody150.html>

- Ishii, M., and Hibiki, T. (2006). *Thermo-Fluid Dynamics of Two-Phase Flow*. New York: Springer-Verlag.
- Joseph, D. D., Belanger, J. & Beavers, G. (1999). Breakup of a Liquid Drop Suddenly Exposed to a High-Speed Airstream. *International Journal of Multiphase Flow* 25, 1263-1303.
- Kallio, K., Akedemi, A. (1996). *On the Mixture Model for Multiphase Flow*. Valtion Teknillinen Tutkimuskeskus, ESPOO, VTT Publications 288.
- Kashdan, J. T., Shrimpton, J. S., Booth, H. J. and Whybrew, A. (2000). Assessment of Particle Characterization via Phase Doppler Anemometry and Automated Particle Image Analysis Techniques. *Proceedings of the 10th International Symposium on Application of Laser Techniques to Fluid Mechanics*; 10-13 July 2000 Lisbon, Portugal.
- Kawanami, Y., Kato, H., Yamaguchi, H., Tagaya, Y., Tanimura, M. (1997). Mechanism and Control of Cloud Cavitation, *Journal of Fluids Engineering*, 119, 788-795.
- Kedrinskii, V.K. (1993). Nonlinear Problems of Cavitation Breakdown of Liquids Under Explosive Loading (Review), *Journal of Applied Mechanics and Technical Physics*, 34(3), 361-377
- Knapp, R.T, Daily, J.W., Hammitt, F.G. (1970). *Cavitation*, New York: McGraw-Hill
- Kolmogorov, A. N. (1949). On the Breakage of Drops in a Turbulent Flow (in Russian). *Dokl. Akad. Nauk SSSR* 66, 825-828.
- Krzeczkowski, S. A. (1980) Measurement of Liquid Droplet Mechanism. *International Journal of Multiphase Flow* 6, 227-239.
- Kubota, A., Kato, H., Yamaguchi H., Maeda, M. (1989) Unsteady Structure Measurement of Cloud Cavitation on a foil Section Using Conditional Sampling Technique. *Journal of Fluids Engineering*, 111, 204-210.

- Kubota, A., Kato, H., Yamaguchi H., Maeda, M. (1989) Unsteady Structure Measurement of Cloud Cavitation on a Foil Section Using Conditional Sampling Technique. *Journal of Fluids Engineering*, 111, 204-210.
- Kuo, K. K., (1995). *Recent Advances in Spray Combustion, Volume I: Spray Atomization and Drop Burning Phenomena*. American Institute of Aeronautics and Astronautics.
- Laberteaux, K.R, Ceccio, S. I. (2001). Partial Cavity Flows: Part 1—Cavities Forming on Models without Spanwise Variation. *Journal of Fluid Mechanics*, 431, 1-41
- Laberteaux, K.R, Ceccio, S.L., (2001). Partial Cavity Flows: Part 2—Cavities Forming On Test Objects With Spanwise Variation. *Journal of Fluid Mechanics*, 431, 43-63
- Labs, J., Parker T. (2003). Diesel Fuel Spray Droplet Sizes and Volume Fractions from the Region 25 mm Below the Orifice. *Atomization and Sprays*, 13 (5&6), 425-442
- Labs, J., Parker T. (2006). Two-Dimensional Droplet Size and Volume Fraction Distribution from the Near-Injector Region of High-Pressure Diesel Sprays. *Atomization and Sprays*, 16 (7), 425-442
- Lane, W. (1951). Shatter of Drops in Streams of Air. *Industrial and Engineering Chemistry*, 43, 1312-1317.
- Lang, R. J. (1962). Ultrasonic Atomization of Liquids. *Journal of the Acoustic Society of America*, 34(1), 6-8.
- Lapple, C. E., Henry, A. and Blake, D. E. (1967). Atomization Survey and Critique of the Literature. *Stanford Research Institute Report*, No. 6, AD 831-314.
- Lasheras, J., C. and Hopfinger, E. J. (2000). Liquid Jet Instability and Atomization in a Coaxial Gas Stream. *Annual Review of Fluid Mechanics* 32, 275-308

- Lasheras, J., Villiermaux, E. & Hopfinger, E. (1998). Breakup and Atomization of a Round Water Jet by a High-Speed Annular Jet. *Journal of Fluid Mechanics* 357, 351-379.
- Lee, S-W., Murata, Y., and Daisho, Y. (2005). Spray and Combustion Characteristics of Dimethyl Ether Fuel. *Proceedings of Institute of Mechanical Engineers Part D: Journal of Automobile Engineering*, 219, 97-102.
- Lefebvre, H. (1989). *Atomization and Sprays*. New York: Hemisphere Pub. Corp.
- Leroux, S., Dumouchel, C., Ledoux, M. (1996). The Stability Curve of Newtonian liquid Jets. *Atomization and sprays*, 6, 623-647.
- Levich, V. G. (1962). *Physicochemical Hydrodynamics*. Prentice Hall
- Li, X., and Tankin, R., S. (1987). Droplet Size Distribution: A Derivative of a Nukiyama-Tanasawa Type Distribution Function. *Combustion Science and Technology*, 56, 65-76.
- Li, X., and Tankin, R., S. (1988). Droplet Size Distribution in Sprays By Using Information Theory. *Combustion Science and Technology*, 60, 345-357.
- Lin S. P., and Reitz R., D. (1998). Droplet and Spray Formation from a Liquid Jet, *Annual Review of Fluid Mechanics*, 30, 85-105
- Lin, S. P., and D. R. Woods. (1991). A Branching Liquid Jet. *Physics of Fluids*, A3, 241-244.
- Liu, H. (2000). *Science and Engineering of Droplets: Fundamentals and Applications*. New York: Noyes publications.
- Malerba, M., Pirisinu, J., Rossi, G. L. (2006 a). Infrared Thermography for Shear Stress Field Measurement in Flows. *Proceedings of the 8th conference on Quantitative InfraRed Thermography*; 28-30 June 2006, Padova, Italy: QIRT 2006-018

- Malerba, M., Salviuolo, A., Rossi, G. L. (2006 b). Qualitative Fluid-Dynamic Analysis of Wing Profile by Thermographic Technique. *XIV A.I.VE.LA National Meeting*, 2006 November.
- Malvern Instruments Ltd. (2005). *Spraytec User Manual*. MAN0368, Issue 1.0, November , 2005, Worcestershire, United Kingdom.
- Manasse, U., Wriedt, T., bauckhage, K. (1992). Phase-Doppler Sizing of Optically Absorbing Liquid Droplets: Comparison between Mie Theory and Experiment. *Particle and Particle Systems Characterization*, 9, 176-185.
- Manasse, U., Wriedt, T., bauckhage, K. (1993). Phase Doppler Sizing of Optically Absorbent Single and Multicomponent Liquid Droplet Using Semiconductor Devices. *Measurement Science and Technology*, 4(3), 369-377.
- Mansour, A. & Chigier, N. (1994). Turbulence Characteristics in Cylindrical Liquid Jets. *Physics of Fluids*, 6, 3380-3391.
- Matzler, C. (2002). MATLAB Functions for Mie Scattering and Absorption, *Research Report No. 2002-08, Institut fur Angewandte Physik*.
- Mayinger, F. and Feldmann, O. (2001). *Optical Measurements, Techniques and Applications*. New York: Springer-Verlag.
- McCarthy, M. J. And Molloy, N. A. (1974). Review of Stability of Liquid Jets and the Influence of Nozzle Design. *The Chemical Engineering Journal*, 7(1), 1-20
- McCormack, P.D., Crane, L., Birch, S. (1965). An Experimental and Theoretical Analysis of Cylindrical Liquid Jets Subjected to Vibration. *British Journal of Applied Physics*, 16, 395-408,
- McKnight, M. E.; Martin, J. W. (1997). Advanced Methods and Models for Describing Coating Appearance. *Proc. of Organic Coatings – Waterborne; High Solids; Powder Coatings, 23rd International Conf.*, 7-11 July, 1997, Athens, Greece: 307-319.

- Meier, G.E.A., Loose, S., Stasicki, B. (1997). Unsteady Liquid Jets. *Applied Scientific Research*, 58, 207-216.
- Meimei, T. Z. (2000). Device Physics and State-Of-The-Art of Quantum Well Infrared Photodetectors and Arrays. *Materials Science and Engineering*, B74, 45-51
- Meola, C., Carlomagno, G. M. (2004). Recent Advances in the Use of Infrared Thermography. *Measurement Science and Technology*, 15, R27-R58.
- Modest, M. F. (1993). *Radiative Heat Transfer*. New York: McGraw-Hill, Inc
- Mugele, R. A., and Evans, H. D. (1951). Droplet Size Distribution in Sprays. *Industrial and Engineering Chemistry*, 43, 1317-1324.
- Narayanan, V., page, R.H., Seyed-Yagoobi, (2003). Visualization of airflow Using Infrared Thermography. *Journal of Experiments in Fluids*, 34, 275-284
- Nasr, G. G., Yule, A. J., Bending, L. (2000). *Industrial Sprays and Atomization*, London: Springer-Verlag London.
- Neppiras, E.A. (1980). Acoustic Cavitation. *Physics Report*, 61, 160-251
- Neppiras, E.A., Noltingk, B.E. (1951). Cavitation Produced by Ultrasonics: Theoretical Conditions for the Onset of Cavitation. *Proceedings of the Physical Society of London*, 64B, 1032-1038,
- Nishimura, A. and Assanis, D. N., (2000). A Model for Primary Diesel Fuel Atomization Based On Cavitation Bubble Collapse Energy. *ICLASS 2000, Pasadena, CA*, July 16 -20, 2000.
- Noltingk, B.E., Neppiras, E.A. (1950) Cavitation Produced by Ultrasonics. *Proceedings of the Physical Society of London*, 63B, 674-685.
- Northrup, R.P, (1951). *Flow Stability in Small Orifices*. New York: Technical Information service, American institute of aeronautics and astronautics.

- Nukiyama, S., and Tanasawa, Y. (1939). Experiments of the Atomization of Liquids in an Airstream. *Transaction of the Society of Mechanical Engineers Japan*, 5, 62-75.
- Nurick, W.H. (1976). Orifice Cavitation and its Effect on Spray Mixing. *Journal of Fluids Engineering*, 98, 681-687.
- Parent, G., Boulet, P., Gauthier, S., Blaise, J., and Collin, A. (2006). Experimental Investigation of Radiation Transmission through a Water Spray. *Journal of Quantitative Spectroscopy and Radiative Transfer*, 97 (1), 126-141.
- Park, S. H., Suh, H. K., and Lee, C. S. (2008). Effect of Cavitation Flow on the Flow and Fuel Atomization Characteristics of Biodiesel and Diesel Fuels. *Energy and Fuels*, 22, pp.605-613
- Peskin, R. L., and Raco, R. J. (1963). Ultrasonic Atomization of Liquids. *Journal of the Acoustic Society of America*, 35 (9), 1378-1381
- Pilch, M. & Erdman, C. (1987). Use of Breakup Time Data and Velocity History Data to Predict the Maximum Size of Stable Fragments for Acceleration-Induced Breakup Of A Liquid Drop. *International Journal of Multiphase Flow*, 13, 741-757.
- Pitcher, G., Wigley, G. (1992). A Study of the Break-up and Atomisation of a combusting Diesel Spray by Phase Doppler Anemometry. *Proceedings of the 6th International Symposium on Application of Laser Techniques to Fluid Mechanics*, Lisbon, Portugal.
- Pitcher, G., Wigley, G. (1994). Simultaneous Two-component Velocity and Drop-size Measurements in a Combusting Diesel Spray. *Proceedings of the 7th International Symposium on Application of Laser Techniques to Fluid Mechanics*, Lisbon, Portugal.
- Planck, M. (1901). Distribution of Energy in the Spectrum. *Annalen der physik*, 309, 553-563.

- Plateau, J. (1873). *Statique Exp'Erimentale Et Th'Eorique Des Liquides Soumis Aux Seules Forces Mol'Eculaires*. Gauthier Villars, Paris.
- Plesset, M.S. and Prosperetti, A. (1977). Bubble Dynamics and Cavitation. *Annual Review of Fluid Mechanics*, 9, 145-185
- Polidori, G., Henry, J. F., Fohanno, S. (2003). On the Simultaneous Use of Particle Streak Velocimetry and Infrared Thermography for the Study of Transient Separated Natural Convection Flow in Water. *Proceedings of PSFVIP-4*, 3-5 June, 2003, Chamonix, France: F4025, 14-17.
- Poritsky, M. (1951) The Collapse on Growth of a Spherical Bubble on Cavity in a Viscous Fluid. *Proceedings of the first U.S National Congress of Applied Mechanics held at the Illinois Institute of Technology*, June 11-16, 1951, 813-821, ASME.
- Prosperetti, A. (1982). Bubble Dynamics: A Review and Some Recent Results. *Applied Science Research*, 38, 145-164.
- Ranger, A. & Nicholls, J. (1969). Aerodynamic Shattering of Liquid Drops. *AIAA Journal*, 7, 285-290.
- Ranz, W.E. (1956). On Sprays and Spraying. *Department of Engineering Research, Pennsylvania State University, Bulletin*, 65.
- Rayleigh, Lord (1879). On the Stability of Jets. *Proceeding of the London Mathematics Society* 10, 4.
- Reitz, R.D (1978). *Atomization and Other Breakup Regimes of a Liquid Jet*, PhD Dissertation, Princeton University.
- Reitz, R.D., Bracco, F.V. (1982). Mechanism of Atomization of a Liquid Jet. *Physics of Fluids*, 25(10), 1730-1742

- Reitz, R.D., Bracco, F.V. (1986). Mechanisms of Breakup of Round Liquid Jets. *Encyclopedia of fluid mechanics*, Houston, Texas: Gulf Publishing Co.
- Sauter, J. (1929). Investigation of Atomization in Carburetors, *National Advisory Committee for Aeronautics, Technical Memorandum*, No. 518.
- Schick, R. J. (1997). *An Engineer's Practical Guide to Drop Size*. Wheaton, Illinois: Spraying Systems Co.
- Schick, R. J. *Spray Technology Reference Guide: Understanding Drop Size*. Wheaton, Illinois: Spraying Systems Co.
- Schmidt, D., P., Rutland, C., J., and Corradini, M. L. (1997) A Numerical Study of Cavitating Flow Through Various Nozzle Shapes, *Society of Automotive Engineers, Paper No. 971597*
- Schober, P., Meier, R., Schafer, O., and Wittig, S. (2002). Visualization and Phase Doppler Particle Analysis Measurement of Oscillating Spray Propagation of an Airblast Atomizer under Typical Engine Conditions. *Annals of the New York Academy of Science*, 972, 277-281.
- Schulz, A. (2000). Infrared Thermography as Applied to Film Cooling of Gas Turbine Components. *Measurement Science and Technology*, 11, 948-956.
- Schweitzer, P.H. (1937). Mechanism of Disintegration of Liquid Jets. *Journal of Applied physics*, 8, 513-521
- Semio V., Andare, P., and Carvalho, M., D-G. (1996). Spray Characterization: Numerical Prediction of Sauter Mean Diameter and Droplet Size Distribution. *Fuel*, 75, 1707-1714.
- Seno, T., Kageyama, S., Ito, R. (1997). Effect of Controlled Pulsation on Axi-Symmetric Behavior. *Journal of Chemical Engineering of Japan*, 20 (2), 128-133

- Setork, Ali. (1976). *Mathematical Models and their Numerical Solution for the Flow-Field of High Velocity Water Jets*. PhD Dissertation, Brown University.
- Settles, G. S. (1997). A Flow Visualization Study of Airless Spray Painting. *Proceedings of the 10th Annual Conference on Liquid Atomization and Spray Systems*. 18-21 May, 1997, Ottawa, Canada: 145-149.
- Settles, G., S. (2001). *Schlieren and Shawdograph Techniques, Visualizing Phenomena in Transparent Media*. New York: Springer-Verlag.
- Settles, G., S., Hackett, B., H., Miller, J., D., and Weinstein, L. M. (1995). Full-Scale Schlieren Flow Visualization. *Flow Visualization VII*, 2-13 September, 1995, Ed. J. P. Crowder, New York: Begell House.
- Shkadov, V. Ya. (1967). Wave Flow Regimes of a Thin Layer of Viscous Fluid Subject to Gravity. *Izv. AN SSSR. Mekhanika Zhidkosti i Gaza*, 2(1), 43-51.
- Siegel, R., and Howell, H. (2001). *Thermal Radiation Heat Transfer*. New York: Taylor & Francis.
- Sindayihebura, D., and Bolle, L. (1998). Ultrasonic Atomization of Liquid: Stability Analysis of the Viscous Liquid Film Free Surface. *Atomization Sprays*, 8, 217-233.
- Sirignano, W. A. (1993). Fluid Dynamics of Sprays – 1992 Freeman Scholar Lecture. *Journal of Fluid Engineering*, 115, 345-378.
- Sirignano, W. A. (1999). *Fluid Dynamics and Transport of Droplets and Sprays*. New York: Cambridge University Press.
- Smallwood, G. J., and Omer, L. G. (2000). Views on the Structure of Transient Diesel Sprays. *Atomization and Sprays*, 10(3-5), 511-527
- Sollner, K. (1936). Experiments to Demonstrate Cavitation Caused by Ultrasonic Waves. *Transactions of the Faraday Society*, 32, 1537–1538.

- Soteriou, R., Andrews, R., and Smith, M., (1995). Direct Injection Diesel Sprays and the Effect of Cavitation and Hydraulic Flip on Atomization, *Society of Automotive Engineers, Paper No. 950090*, 27-51
- Sou, A., Hosokawa, S., and Tomiyama, A. (2007). Effects of Cavitation in a Nozzle on Liquid Jet Atomization. *International Journal of Heat and Mass Transfer*, 50(17-18), 3575-3582.
- Sou, A., Tomiyama, A., Hosokawa, S., Nigorikawa, S., and Maeda, T. (2006). Cavitation in a Two-Dimensional Nozzle and Liquid Jet Atomization (LDV Measurement of Liquid Velocity in a Nozzle). *Japan Society of Mechanical Engineering International Journal, Series B*, 49(4), 1253-1259.
- Srinivasan, V. (2006). *A Numerical Study of a New Spray Applicator*. Ph.D. Dissertation, University of Kentucky.
- Srinivasan, V., Salazar, A., and Saito, K. (2008). Numerical Investigation on the Disintegration of Round Turbulent Liquid Jets Using LES/VOF Techniques. *Atomization and Sprays*, 18, 571-617.
- Srinivasan, V., Salazar, A., and Saito, K. (2009). Numerical Simulation of Cavitation Dynamics Using a Cavitation-Induced Momentum Defect Correction Approach. *Applied Mathematical Modeling*, 33, 1529-1559
- Srinivasan, V., Salazar, J. Saito, K. and Alloo, R. Systems and Method of Cavitation-Driven Atomizer. US patent pending.
- Stieglmeier, M., Tropea, C., Weiser, N., Nitsche, W. (1989). Experimental Investigation of the Flow through Axisymmetric Expansions. *Journal of Fluids Engineering*, 111(4), 464-471.
- Suh, H. K., Park, S. H., and Lee, C. S. (2008). Experimental Investigation of Nozzle Cavitation Flow Characteristics for Diesel and Biodiesel Fuels. *International Journal of Automotive Technology*, 9(2) pp. 217-224

- Swithenbank, J., Beer, J. M., Taylor, D. S., Abbot, D., McCreath, C. G. (1976). A Laser Diagnostic for the Measurement of Droplet and Particle Size Distribution. *14th American Institute of Aeronautics and Astronautics, Aerospace Sciences Meeting*, 26-28 January 1976, Washington, D.C: AIAA Paper; 76-99.
- Tamaki, N. (2009). Effects of Cavitation in a Nozzle Hole on Atomization of Spray and Development of High-Efficiency Atomization Enhancement Nozzle. *11th International Conference on Liquid Atomization and Spray Systems, Vail Colorado, USA*, 26-30 July, 2009
- Tamaki, N., Shimizu, M., Nishida, K., Hiroyasu. (1998). Effects of Cavitation and Internal Flow on Atomization of a Liquid Jet. *Atomization and Sprays*, 8(2), 179-197.
- Tate, R. W. (1969). Sprays, *Encyclopedia of Chemical Technology*, 18, 634
- Tien, C. L., and Drolen, B. L. (1987). Thermal Radiation in Particulate Media with Dependent and Independent Scattering. *Annual Review of Numerical Fluid Mechanics and Heat Transfer*, 1, 1-32.
- Tomita, Y., Shima, A. (1975). On the Impulse Pressure Accompanying Spherical Bubble Collapse in Liquids. *Rep. Inst. High speed Mech.*, 31, 281.
- Van de Hulst, H., C., (1981). *Light Scattering by Small Particles*, New York: John Wiley & Sons.
- Versteeg, H. K., Hargrave, G. K., and Kirby, M. (2006). Internal Flow and Near-Orifice Spray Visualization of a Model Pharmaceutical Pressurized Metered Dose Inhaler. *Journal of Physics: Conference Series*, 45, 207-213.
- Vijay, M. M. (1992). Ultrasonically Generated Cavitating or Interrupted Jet. *U. S. Patent No. 5,154,347*.

- Vijay, M.M. (1998). Design and Development of a Prototype Pulsed Water Jet Machine for the Removal of Hard Coatings. *Proceedings of the 14th International Conference on Jetting Technology*, 39-57.
- Wang, T.-C., Han, J.-S., Xie, X.-B., Lai, M.-C., Henein, N. A., Schwarz, E., Bryzok, W. (2003). Parametric Characterization of High-Pressure Diesel Fuel Injection Systems. *Journal of Engineering for Gas Turbines and Power*, 125, 412-426.
- Wang, Y.-C., Brennen, C. (1998). One-Dimensional Bubbly Cavitating Flows through a Converging-Diverging Nozzle. *Journal of Fluids Engineering*, 120(1), 166-170.
- Weber, C. (1931). Zum Zerfall eines Flüssigkeitsstrahles. *Z. Angew. Math. Mech.* 2, 136.
- Whybrew, A., Nicholls, T. R., Boaler, J. J., Booth, H. J. (1999). Diode Lasers – A Cost effective Tool for simultaneous visualization, Sizing and Velocity Measurements of Sprays. *Proceedings of ILASS-Europe*, 5-7 July 1999; Toulouse, France.
- Wien, W. (1894). Temperatur und Entropie der Strahlung. *Annalen der physik*, 288, 132-165.
- Woo, J., Roh, Y., Kang, K., Lee, S. (2006). Design and Construction of an Acoustic Horn for High Power Ultrasonic Transducers. *Proceedings of the 2006 IEEE International Ultrasonic Symposium*, 3-6 October 2006.
- Young T. (1802). An Account of Some Cases of the Production of Colors, not Hitherto Described. *Philosophical Transaction of the Royal Society of London*, 92, 387-397
- Young, F.R. (1989). *Cavitation*. McGraw-Hill Book Company.
- Yule, A. J., Chigier, N. A., Cox, N. W. (1978). Measurement of Particle Sizes in Sprays by the Automated Analysis of Spark Photographs. *Particle size analysis: Proceedings of a conference organized by the Analytical Division of the Chemical Society and held at the University of Salford*, 12-15 September 1977: 61-73, Heyden Press.

Zaleski, S., Li, J., Scardovelli, R. & Zanetti, G. (1996). Direct Simulation of Multiphase Flows with Density Variations. *In Colloque IUTAM on Variable Density Low Speed Turbulent Flows*, Marseille 8–10 Juillet 1996 (ed. L. Fulachier & F. Anselmet). Kluwer.

VITA

NELSON KUDZO AKAFUAH

Date of Birth: May 21, 1973.

Place of Birth: Accra, Ghana

EDUCATION

Master of Science in Mechanical Engineering, Thesis topic: *Uncertainty Analysis of Infrared Thermography in Convective Heat Transfer*, 2001-2003, University of New Orleans, New Orleans, Louisiana.

Bachelor of Science in Mechanical Engineering, Thesis topic: *Computer Simulation of the Takoradi Combine Cycle Thermal Power Plant*, 1995-1999, University of Science and Technology, Kumasi, Ghana,

AWARDS AND HONORS

Kentucky Graduate Scholarship, University of Kentucky, 2005 -2009

Crescent City Doctoral Scholarship, University of New Orleans, 2004-2005

Shell Foundation Scholarship, University of Science and Technology, Kumasi, Ghana 1995-1999

JOURNAL PUBLICATIONS

Akafuah, N. K., Salazar, A. J., Saito, K. Estimation of liquid volume fraction and droplet number density in automotive paint spray using infrared thermography-based visualization technique. *Atomization and Sprays*, Accepted

Akafuah, N. K., Salazar, A. J., Saito, K., Srinivasan, V. Infrared Thermography-Based Visualization of Droplet Transport in Liquid Sprays. *Infrared Physics and Technology*, Submitted

Akafuah, N. K., Salazar, A. J., Saito, K. Infrared Thermography: A Tool for Flow Visualization. *J. Visualization*, in preparation

PEER REVIEWED CONFERENCE PAPERS

Akafuah, N. K., Salazar, A. J., Saito. K. (2009). Infrared Visualization of Automotive Paint Spray Transfer Process. *ASME FEDSM2009-78033*, Vail, Colorado, USA.

Akafuah, N. K., Salazar, A. J., Saito, K., Srinivasan, V. (2009). Ultrasonically Driven Cavitating Atomizer: Prototype Fabrication and Characterization. *ASME FEDSM2009-78024*, Vail, Colorado, USA.

Akafuah, N. K., Hall, C. A., and Wang T. (2004). "Uncertainty Analysis of Infrared Thermography in Convective Heat Transfer", *HT-FED2004-56537, Proceedings of ASME HT-FED*, Charlotte, North Carolina, USA.

UNREVIEWED CONFERENCE PRESENTATIONS

Akafuah, N., K., Gharaibeh, B., and Saito, K., "Paint Color Effect on the Performance of Infrared Seed Inspection System for Automotive Applications" *Automotive Industry Advancement with NDT, an ASNT Topical Conference*, Greenville SC, 2009

Akafuah, N., K., Gharaibeh, B., and Saito, K., "Effect of Thermal Properties of Automotive Paint Color On The Performance Of Infrared Defect Detection" *Painting technology workshop*, Lexington, KY (2008)

Akafuah, N., K., Salazar, A., J., and Saito, K., "Influence of Cavitation and Ultrasonic Perturbation on Atomization," *Painting technology workshop*, Lexington, KY (2007)

TECHNICAL REPORTS

Akafuah, N., K., Salazar, A., J., and Saito, K., "Experimental Investigation and Validation of Computational Results of Ultrasonic Cavitating Atomizer (UCA) for Water" Final Report submitted to Toyota Motor Corporation, Japan, March 31, 2008

Wang, T., **Akafuah, N. K.,** and Hall, C.A., " Establishment of Research Capacity for Aerothermal Sciences and Engineering at UNO," ECCC Report 2004-08, Energy Conversion and Conservation Center, University of New Orleans, Final Report submitted to Louisiana Board of Regents, Award Number: LEQSF (2003-04)-ENH-TR-87, December 31, 2004.

Wang, T., Li, X., **and Akafuah, N.**, “Infrared Inspection of Energy Intensive Devices in the Dynegy Gas Processing Plant at Venice, Louisiana,” ECCC Report 2004-03, Energy Conversion and Conservation Center, University of New Orleans, Submitted to Dynegy, May 2004.

Akafuah, N. K. and Wang, T., "A Preliminary Examination of the Effect of Dimple Tape on the Performance of Two Wind Generators," ECCC Report 2004-02, Energy Conversion and Conservation Center, University of New Orleans, Submitted to Crescent Technology, April 2004

PATENTS

US Patent: Defect inspection in coated systems with variable colors, to be filed in 2009

US Patent: Infrared flow visualization techniques, to be filed in 2009

PROFESSIONAL MEMBERSHIP

Member, American Society of Mechanical Engineers

Member, American Society of Heating, Refrigerating and Air-conditioning Engineers

Member, National Society of Black Engineers

Member, American Institute of Aeronautics and Astronautics

Member, American Society of Non-Destructive Testing